Numerical Simulation of Aeroacoustics using the Variational Multiscale Method. Application to the problem of human phonation

Arnau Pont Ribas

Escola Tècnica Superior d'Enginyers de Camins, Canals i Ports de Barcelona
Universitat Politècnica de Catalunya (Barcelona Tech)

Doctoral Thesis
Structural Analysis Programme

Advisors:

Prof. Ramon Codina
Dr. Joan Baiges

February 2018

ACTA DE QUALIFICACIÓ DE LA TESI DOCTORAL

Reunit el tribunal integrat pels sota signants per jutjar la tesi doctoral:

Títol de la tesi: The Fixed-Mesh ALE method applied to multiphysics problems using stabilized formulations

Autor de la tesi: Joan Baiges

Acorda atorgar la qualificació de:

- ☐ No apte
- ☐ Aprovat
- ☐ Notable
- ☐ Excel·lent
- ☐ Excel·lent Cum Laude

Barcelona, ... de/d' ..... de .....

El President	El Secretari
.....	.....
(nom i cognoms)	(nom i cognoms)

El vocal	El vocal	El vocal
.....	.....	.....
(nom i cognoms)	(nom i cognoms)	(nom i cognoms)

Agraïments

Ara que estic tancant aquest fantàstic capítol de la meva vida, seria molt senzill presumir de totes les dificultats superades per arribar fins aquí. El cert és que de dificultats n'he patit ben poques, com a mínim no pas d'aquelles que siguin dignes de recordar. I això no és en absolut mèrit meu, sinó pel fet d'haver estat dirigit per dues persones, el Ramon Codina i el Joan Baiges, que m'han proporcionat plena confiança i llibertat a l'hora d'enfocar aquesta tesi. Aquest clima distès ha aconseguit, fins i tot, convertir quelcom tan propens al conflicte com la gestió d'un codi informàtic en un benefici per a tots els participants. En aquest sentit vull destacar la feina, l'ajuda i el tracte excel·lent que m'han dispensat el Camilo Bayona, el Ricardo Reyes, l'Ernesto Castillo, l'Héctor Espinoza, l'Álex Tello, l'Ángel Villota i la Laura Moreno. A tots ells moltes gràcies pel gran ambient de treball que han ajudat a construir al voltant de FEMUSS. D'altra banda, aquesta tesi no hagués estat possible sense la intensa colůlaboració amb l'Oriol Guasch, el Francesc Alias, el Marc Arnela i la Patricia Sánchez-Martín de La Salle - Universitat Ramon LLull. Es pot dir que tots plegats hem fet molta feina i, el que és més important, hem passat molt bones estones.

El meu agraïment no es limita a aquells amb qui he tingut el plaer de treballar. Vaig tenir la sort d'anar a parar al despatx C1-102, on a part de poder treballar braç a braç amb altres membres de l'equip FEMUSS, hi he tingut la sort de compartir moltes hores amb l'Ester Comellas i el Fermín Otero, que juntament amb l'Àlex Ferrer, em van fer sentir com a casa des del primer dia.

M'agradaria agrair especialment el suport financer rebut per part del Centre Internacional de Mètodes Numèrics en Enginyeria i de l'Agència de Gestió d'Ajuts Universitaris i de Recerca de la Generalitat de Catalunya a través de la beca predoctoral FI, així com l'oportunitat de treballar amb dues institucions del prestigi del departament de Resistència de Materials i Estructures a l'Enginyeria de la Universitat Politècnica de Catalunya i del CIMNE. Així mateix voldria donar les gràcies a la Rosa Maria Olea i a l'Alberto Burgos per la seva inestimable ajuda en dos dels temes més espinosos pels investigadors: l'administració i les averies dels sistemes informàtics.

"If you thought that science was certain –well, that is just an error on your part."

Richard Feynman

Abstract

The evolution of biomechanics and the huge growth of computational capacities in the past decades have enabled a wide application of computational mechanics to the analysis of human physiology. Amongst these problems, a very important and complex one is human phonation. Physically, voice involves complex interactions between laminar and turbulent airflow; vibrating, deforming, colliding elastic solids; and sound waves resonating in a contorting duct. So far, these mechanisms have had to be studied one at a time, using disparate tools and often gross approximations, for each of the subproblems. Traditionally, most of the works devoted to human voice focused on its sintetization for applications related to robotics, communication and security, but these advances have allowed the simulation of the physical phenomena behind the generation and propagation of human voice as a whole, which together with the availability of more precise monitoring and imaging techniques, can lead to very powerful tools for medical research in computer assisted surgery, but also for more everyday aspects of our life such as human sciences, pedagogy, linguistics and arts.

The solution of the human phonation problem applying computational mechanics is covered by several research branches, such as Computational Fluid Dynamics (CFD), biomechanics or acoustics among others. In the present thesis, the problem is approached from the Computational Aeroacoustics (CAA) point of view and the first main objective consists in developing numerical methods of general application that can take part in the solution of any scenario related to human phonation with affordable computational cost. In this sense, only the compressible Navier-Stokes equations can describe all flow and acoustic scales without any modelling, which is known as Direct Noise Calculation (DNC), but its computational cost is usually unaffordable. Even in the case of Large Eddy Simulations (LES), where the spatial discretization is coarse and the small scales are modelled, the cost can still be a handicap due to the complexity of the problem. This drawback worsens in the low Mach regime due to the large disparity between flow velocity and sound speed, which leads to an ill-conditioning of the system of equations to be solved, specially for conservative schemes. At this point, it makes sense to move towards the incompressible flow approx-

imation, bearing in mind the low velocities expected in human phonation problems.

Incompressible flows do not yield any acoustics, for which a second problem containing the propagation of the sound sources needs to be modelled and solved. These are the so called hybrid methods, which allow a better conditioning of the problem by segregating flow and acoustic scales. The first and most popular formulation within this family, Lighthill's analogy, has been taken as starting point for the present work, but its restriction to free-field scenarios has motivated the extension of the method to arbitrary geometries and non-uniform flows. The first development in this direction corresponds to a splitting of Lighthill's analogy into a quadrupolar and a dipolar component, which does not change the original problem but allows assessing the contribution of solid boundaries to the generation of sound. The second step consists in the development of a stabilized Finite Element (FEM) formulation for the Acoustic Perturbation Equations (APE's), which accounts for non-uniform mean flows and performs a complete filtering of the acoustic scales. The final step assumes the compressible approach but omitting the energy equation and thus considering both flow and acoustic propagation as isentropic. In this case the solver is unified and hence compatible boundary conditions for flow and acoustics need to be implemented. For this purpose a method combining weakly imposed essential and non-radiating boundary conditions has been developed. Finally, the numerical framework has been extended to dynamic phonation cases, such as syllables. The biomechanical aspects of the problem have not been taken into account, but the hypothetical deformation of the domain has been included in the formulations by expressing them in an Arbitrary Lagrangian Eulerian (ALE) frame of reference and by developing a novel remeshing strategy with conservative interpolation between meshes. In the present case, the syllable /sa/ has been simulated in a 2D simplified vocal tract geometry with both Lighthill's analogy and the isentropic compressible approach.

In the last chapter a challenging case in human phonation has been chosen for testing the developed computational framework: the fricative phoneme /s/. Unlike vowels, which are voiced sounds defined by a few characteristic frequencies called formants, fricatives cannot be simulated as the propagation of a known analytic solution (glottal pulse), because the sound sources correspond to a wide range of turbulent scales. Therefore, a CFD calculation is mandatory in order to capture all the relevant eddies behind the generation of sound. This problem is solved by using an LES formulation together with the Variational Multiscale (VMS) stabilization method as turbulence model, which is supplemented with several acoustic formulations in the case of the incompressible approach. The analysis of the results has focused on the numerical representation of turbulence and the acoustic signal

at the far-field, which has been compared against experimental recordings from an equivalent mechanical replica. Finally the role of the upper incisors in the generation of the fricative sound has been evaluated. All simulations have been run with the parallel multiphysics FEM code FEMUSS, based on Fortran Object-Oriented-Programming (OOP) and the OpenMPI parallel library.

Contents

Chapter 1

Introduction

1.1 Framework

This thesis was originally planned for developing a series of numerical models within Computational Aeroacoustics (CAA) using incompressible flow, the so called hybrid methods, which segregate the acoustic problem from the Computational Flow Dynamics (CFD) calculation. The main object of study was the generation of human unvoiced sounds from a turbulent flow, seen as an extension of the CFD solver implemented in the multiphysics code FEMUSS and widely tested in [149, 60, 57]. However, the scope of the work was progressively extended to a more general computational platform that can establish a solid base for more complex human phonation simulations. In this sense, apart from the original scope of the work, a formulation based on compressible flow has been derived and the computational tools for working with moving domains have also been developed.

To date, the numerical production of human voice using three dimensional vocal tract geometries has mainly focused on the generation of static vowel sounds. Simplified axisymmetric vocal tracts have lead to good quality synthesized vowels [see e.g., 173, 162, 6]. Yet the advantage of numerical methods, and in particular of the finite element method (FEM), is that one can directly deal with realistic vocal tracts obtained from magnetic resonance imaging (MRI) or computer tomography (CT) data, in its full complexity. This has offered the possibility of analyzing several aspects of vocal tract acoustics influencing the production of vowels, such as the role played by lateral cavities, like the valleculae and piriform fossae [see e.g., 166, 172, 165, 5], or the effects of lips [4], head geometry [9] and vocal tract high order modes [29, 30], on the radiated sound. Recently, the production of dynamic vowel sounds, like diphthongs, has been also addressed, see [89]. The situation becomes more complex because in this case one can no longer resort to the acoustic wave equation or its frequency domain counterpart, the Helmholtz

equation [90]. It is necessary to deal with the wave equation in mixed form for the acoustic pressure and acoustic particle velocity [48, 12], to account for waves propagating in a moving vocal tract that evolves from the shape of one vowel to another.

Aside from static and dynamic vowel sounds, few works can be found in literature addressing the numerical simulation of further voice sounds. The reason for that is probably the complex physics beneath their generation and the associated high computational cost. An exception that has received some attention is that of unvoiced sounds (see e.g., [126]) and in particular fricative sounds, for which some numerical works can be found. Fricative consonants are produced when air is forced to pass through a narrow channel made by placing two articulators (e.g., the tongue and the hard palate) close together. In [3] different Computational Fluid Dynamics (CFD) formulations were tested for fricative sound /sh/ using realistic two (2D) and three (3D) dimensional vocal tract geometries. The study compared the performance of a compressible CFD simulation, an incompressible large eddy simulation (LES) and a Reynolds averaged Navier-Stokes (RANS) approach. Though a rather coarse mesh was used, the study deemed interesting conclusions. As expected, the RANS simulation provided no reliable results but the compressible CFD and incompressible LES combined with an acoustic analogy yielded proper outputs. Another interesting and unexpected result was that although the flow field from 2D simulations did not match at all with the 3D one, that was not the case for the 2D acoustic pressure field, which was quite similar to the 3D one.

The computation of aerodynamic sound in the second step of a hybrid CAA approach is often performed by resorting to integral formulations like the Boundary Element Method (BEM) [135], though FEM is also common if the acoustic waves are to be computed at distances not too far from the source region. This is precisely the case of human phonation problems, but the main motivation for using FEM is the integration of several acoustic formulations in the multiphysics code FEMUSS for building a common CAA platform for a more general use. The other main characteristic of the numerical framework is the Variational Multiscale Method (VMS), which acts in three fronts: the stabilization of the convective term of the Navier-Stokes equations, the fulfillment of the Ladyzhenskaya-Babuska-Brezzi (LLB) stability condition and the modeling of the small turbulent scales that cannot be captured by the discretization in an LES.

1.2 Motivation

The present work has been mainly motivated by the EUNISON project $(2103-2016)$, which belonged to the FP7 framework of the European Com-

mission. This project had a double target: on the one hand the simulation of human voice by coupling fluid dynamics, acoustics, solid mechanics, and muscle activation inputs, and on the other, the construction of a mechanical replica of a human head for replicating voice only by injecting air. The International Centre for Numerical Methods in Engineering (CIMNE), the research institution where I have carried out this thesis, had the assignment of developing a parallel aeroacoustic solver which allowed reproducing the fricative phoneme /s/ and analyzing the physiological process that leads to the generation and propagation of this sound, and validating it against the experimental tests performed with the replica. In this sense, the task that has been mainly covered by this thesis corresponds to Computational Aeroacoustics (CAA) based on incompressible flow, although a formulation based on compressible flow has also been developed.

One of the main characteristics of fricative sounds is its fully turbulent spectrum, which means that the accuracy of the final results depends on the performance of the turbulence model of the CFD solver. For this reason, the Large Eddy Simulation (LES) requires a very fine grid in order capture all relevant flow scales. Moreover, the Variational Multiscale Method (VMS) method, whose main function consists in stabilizing the numerical approximation of the Navier-Stokes equations, must reproduce a physical turbulence pattern too. The validation of these features has been an important incentive, as well as the subsequent complexity of the whole problem, which has been extremely useful for testing the efficiency and the scalability of the multiphysics parallel code FEMUSS. Although these kind of analyses are out of the scope of this thesis, the performance of the code has been a constant concern during the implementation and calculation phases in order to ease the access to different High Performance Computing (HPC) clusters.

1.3 Objectives

Although Computational Aeroacoustics stems from the solution of a Computational Fluid Dynamics problem, the design of a proper numerical strategy to calculate the sound produced by a flow in motion after impacting against one or more obstacles is not as straightforward. In this framework only a few methods are available: Direct Numerical Simulation (DNS), where all flow scales are solved, Large Eddy Simulation (LES), where small scales cannot be captured by the spatial discretization and need to be modeled, and finally the Reynolds-Averaged-Navier-Stokes equations (RANS), which describe a mean flow solution and model the turbulent part. All three can be applied to the compressible flow equations and its incompressible counterpart, and their target application is very well defined. However, when we want to extract the aerodynamic sound from a CFD simulation several problems arise.

First of all, acoustics are only described by the compressible flow equations, which must be solved in any case when dealing with high speed flows. The conceptual discussion appears when the flow can be approximated as incompressible but we are still dealing with a big sized problem with a complex geometry like a 3D realistic vocal tract. Then, the acoustics will have to be properly modeled in a separate problem taking care of the computational cost.

Let us consider the compressible Navier-Stokes equations posed in a time interval $(0, T)$ and in a domain $\Omega \subset \mathbb{R}^d$, being d the number of space dimensions ($d = 2$ or 3). Let also $t \in (0, T)$ be a given time instant in the temporal domain, and $\boldsymbol{x} \in \Omega$ a given point in the spatial domain, Γ the boundary of the domain Ω, and $\boldsymbol{n}$ the geometric unit outward normal vector on Γ. Considering a compressible, Newtonian and viscous fluid, the governing equations are the conservation of mass (1.1), momentum (1.2), and energy (1.3) written in conservation form, which in turn need to be complemented with an equation of state for closing the problem. For this purpose, the specific formulation for the ideal gas law has been included:

$$\partial_t \rho + \partial_j \left(\rho u_j\right) = 0, \tag{1.1}$$

$$\partial_t \left(\rho u_i\right) + \partial_j \left(\rho u_j u_i\right) = \partial_j \left(\tau_{ji} - p\delta_{ji}\right) + \rho f_i, \tag{1.2}$$

$$\partial_t \rho \left(e + \frac{u_i u_i}{2}\right) + \partial_j \left(\rho u_j \left(e + \frac{u_i u_i}{2}\right)\right) = \partial_j \left(u_i(\tau_{ij} - p\delta_{ij}) - q_j\right) + \rho f_i u_i + \rho r, \tag{1.3}$$

where ∂_t and ∂_j refer to the Eulerian time derivative and $\partial/\partial x_j$, respectively. The usual summation convention is implied in the equation presented before, with indices running from 1 to d. In this relation ρ is the density, $\boldsymbol{u}$ is the velocity, p is the pressure, $\boldsymbol{\tau}$ is the viscous stress tensor, $\boldsymbol{I} = [\delta_{ij}]$ is the identity or *Kronecker* tensor, $\boldsymbol{f}$ is a body force vector, e is the internal energy, $\boldsymbol{q}$ is the heat flux vector, and r is a heat source/sink term.

The quantities conserved in the left hand side of equations (1.1), (1.2), and (1.3), are the so-called conservative variables; indeed, ρ is the density, $\boldsymbol{m} = \rho\boldsymbol{u}$ is the momentum, and e_{tot} is the total energy, which is defined as $e_{\text{tot}} = \rho\left(e + \boldsymbol{u} \cdot \boldsymbol{u}/2\right)$.

Hereafter, let us denote the transpose operation by the superscript $\top$. For Newtonian fluids considered in this work, the viscous stress tensor is defined as

$$\tau_{ij}\left(\boldsymbol{u}\right) = \mu\left(\frac{\partial u_i}{\partial x_j} + \frac{\partial u_j}{\partial x_i}\right) - \frac{2\mu}{3}\left(\frac{\partial u_l}{\partial x_l}\right)\delta_{ij}, \tag{1.4}$$

denoting by μ the viscosity of the fluid. We calculate the heat flux vector using Fourier's law,

$$q_i\left(T\right) = -\lambda\frac{\partial T}{\partial x_i}, \tag{1.5}$$

where λ is the thermal conductivity and T is the temperature of the fluid. The caloric equation $e = c_v(T)\,T$ and the ideal law for gases $p = \rho RT$ are used to calculate the pressure and the acoustic speed c. In these relations the specific heat at constant volume $c_v(T)$ and the specific heat at constant pressure $c_p(T)$ are thermodynamic properties of the fluid. We also define $\gamma = c_p/c_v$ for the ratio between the specific heats, and $R = c_p - c_v$ for the specific gas constant. The non-dimensional Mach number $M = |\boldsymbol{u}|/c$ is used to calculate the compressibility regime.

Although the compressible flow equations describe both aerodynamic and acoustic flow scales in a direct fashion without any need for modeling, their complexity and their poor numerical performance at the low-speed flow range, specially in conservative schemes [21], make them a very costly approach for the present problem. For this reason, an alternative version using primitive variables is often used to overcome the convergence problems at the low Mach limit and to reduce the complexity of the conservative approach [20]. In order to formulate the equations using primitive variables, we express the conservative unknowns $\boldsymbol{U}$ as a function of the primitive variables $\boldsymbol{Y} = (p, \boldsymbol{u}, T)^\top$:

$$\begin{aligned} \frac{D\rho}{Dt} + \rho\nabla\cdot\boldsymbol{u} &= 0, \\ \rho\frac{D\boldsymbol{u}}{Dt} + \nabla p &= \nabla\cdot(2\mu\epsilon'(\boldsymbol{u})) + \rho\boldsymbol{g}, \\ \rho c_p\frac{DT}{Dt} - \beta T\frac{Dp}{Dt} &= \nabla\cdot(k\nabla T) + \Phi + Q, \\ \rho &= F(p,T), \end{aligned} \tag{1.6}$$

where μ is the dynamic viscosity, ϵ' is the deviatoric part of the rate of deformation tensor, k is the heat conductivity, c_p is the specific heat at constant pressure, Q are the external energy volumetric sources, Φ are the Joule sources and F is the state function. In this work the ideal law for gases is used, so that the isothermal compressibility $\beta = 1/p$. This set of equations allows reaching the incompressible limit with an almost constant density. In spite of the improvements, the computational cost is still too high for a solver which will be mainly devoted to flows within the incompressible range. The reason for that is the huge disparity between the flow velocity and the wave propagation eigenvalues, which leads to a bad conditioning of the system. In order to overcome these numerical difficulties and taking into account the low velocities expected in human phonation problems, it makes sense to move towards the incompressible flow approximation. Chapter 2 is devoted to the development of a new acoustic model within the framework of hybrid methods based on incompressible flow, more specifically Lighthill's analogy. The main characteristic of hybrid methods is the segregation of the

aeroacoustic problem into a Computational Fluid Dynamics (CFD) calculation and an acoustic problem. On the one hand, these schemes overcome the numerical inconveniences of a DNS, such as the ill-conditioning of the problem, and allow a more flexible treatment of the problem according to the flow regime and the geometry of the domain, but on the other, the acoustic scales must be partly modeled and thus simplistic assumptions might be taken. In this sense, Lighthill's analogy has been the most popular option for unbounded flows [130]. First, an incompressible CFD simulation is carried out and the double divergence of the Reynolds tensor is computed from it as an approximation to Lighthill's tensor (see [63, 153, 161] for a detailed justification). The latter is propagated with a wave operator to get the acoustic pressure radiated by flow motion. This allows one to identify the problem of flow noise emission with that of sound radiation by a distribution of quadrupoles in free space. It can be easily derived from the mass and momentum conservation equations (1.1)(1.2) as follows:

$$\partial_t \rho + \partial_j \left(\rho u_j\right) = 0, \tag{1.7}$$

$$\partial_t \left(\rho u_i\right) + \partial_j \left(\rho u_j u_i\right) = \partial_j \left(\tau_{ji} - p\delta_{ji}\right) + \rho f_i. \tag{1.8}$$

Taking the time derivative of the mass conservation equation and subtracting it from the divergence of the momentum equation, the following equality is obtained:

$$\partial_{tt}\rho - \partial_j\partial_i p\delta_{ji} \; + \partial_j\partial_i\tau_{ji} = \partial_j\partial_i \left(\rho u_j u_i\right). \tag{1.9}$$

Then, subtracting $c_0^2\partial_j\partial_i\rho\delta_{ji}$ on both sides of the previous equation, the following wave equation in terms of ρ appears:

$$\partial_{tt}\rho - c_0^2\partial_j\partial_i\rho\delta_{ji} = \partial_j\partial_i \left(\rho u_j u_i - \tau_{ji} + \left(p - c_0^2\rho\right)\delta_{ji}\right), \tag{1.10}$$

which can be compacted defining $T_{ji} = \rho u_j u_i - \tau_{ji} + \left(p - c_0^2\rho\right)\delta_{ji}$ as the Lighthill turbulence stress tensor:

$$\partial_{tt}\rho - c_0^2\partial_j\partial_i\rho\delta_{ji} = \partial_j\partial_i T_{ji}. \tag{1.11}$$

At this point, the previous equations is still exact if it is used together with a compressible flow solver, since no simplifications have been made yet. Although it sounds contradictory, acoustic analogies and other hybrid methods that will be presented next, are also used in the context of compressible flows [179], mainly for two reasons: for a better visualization of the acoustic field and for a higher flexibility in the separate modelization and domain discretization of the flow (e.g. LES) and the acoustic problem. However, in the incompressible case, it is necessary to express the wave equations in terms of the pressure instead of the density. For this purpose, we can express

ρ as a function of p using $p - p_0 = c_0^2 (\rho - \rho_0)$, where p_0 and ρ_0 are the pressure and the density at stagnation state. This is a realistic approximation in the low-Mach regime, as well as neglecting the effects of viscosity in the generation of sound. However, the first important simplification consists in considering that $p >> p_0$, which implies the hypothesis of propagation in a medium at rest, yielding

$$c_0^{-2} \partial_{tt} p - \partial_j \partial_i p \delta_{ji} = \rho_0 \partial_j \partial_i u_j u_i. \tag{1.12}$$

Therefore (1.12) can only be deployed with full precision in scenarios where the wave propagation takes place in a free field. Another disadvantage of not having any control on the mean flow variables has to do with the visualization of the acoustic field, because at the near field the noise produced by mean flow oscillations (pseudosound) will be captured by the acoustic pressure, although these fluctuations do not yield any wave propagation. Moreover, the role of solid boundaries in the generation and propagation of sound will not be assessed by the method, since the model does not include the separate contribution of dipolar sources. Though Lighthill is indeed the most celebrated acoustic analogy, many other analogies have been derived. Some emphasize the role of vorticity in aerodynamic noise production [148, 105, 139], while others attempt at transferring mean flow effects from Lighthill's source term to the wave operator (see e.g., [131] for a review and also [85]). Approaches standing on Acoustic Perturbation Equations (APE) (e.g., [73, 111, 97]) derived from linearization of the Euler equations (e.g., [161, 16]) are also quite common.

All the strategies in the precedent paragraph are intended for aerodynamic sound propagation in the free field. To consider the effects of bodies within the flow on aerodynamic noise, one could proceed analogously to what is done for Lighthill's acoustic analogy, but convolving the source term with a tailored Green's function that accounts for the body boundary conditions. The problem is that for complex geometries tailored Green's functions are not available. Curle [65] proposed a way out to this difficulty by identifying the influence of rigid bodies with that of a distribution of surface dipoles. The free-space Green's function can be used instead of the tailored one, though at the price of taking into account a new source of sound in the simulations. Curle's formulation was extended for non-rigid bodies in the well-known Ffowcs Williams-Hawkings equation [178]. Unfortunately, when applied to low Mach number aeroacoustics, Curle's formulation presents a problem. The dipole surface integral term involves the gradient of the total pressure in the normal direction to the boundary of the rigid body. The total pressure includes the acoustic fluctuations, which cannot be obtained from an incompressible CFD simulation. Recently, it has been proposed to surpass this difficulty by just considering the gradient of the incompressible

flow pressure and by replacing the wave equation Green's function with that of the Laplacian operator [138]. Another strategy will be followed hereafter. This is based on the observation that Curle's analogy is actually a sharp way to account for aerodynamic noise generated by surfaces, though what it is really happening, from a physical point of view, is that waves generated by flow motion get diffracted by the rigid body [66, 61, 84]. For this reason, the first main objective of this thesis consists in developing alternatives which overcome these drawbacks without paying an excessive computational cost. In this first step, a decomposition strategy of Lighthill's analogy into two different problems has been developed for domains which do not fulfill the free field condition. The output will be two components of the acoustic pressure which will capture the noise generated by quadrupolar and dipolar sources separately. This will bring several important advantages: on the one hand, it will reproduce Curle's strategy without any further implementation of a dipolar source term, and on the other, it will provide a clearer representation of the acoustic field radiated by the solid boundaries. The method has been tested and validated with a 2D benchmark of the aeolian tones and with a 3D simplified geometry of a vocal tract emulating the fricative phoneme /s/. The latter has been intended as a first approach towards the evaluation of the contribution of specific parts of the vocal tract to the generation of fricative sound.

The previous method overcomes one of the main issues of Lighthill's analogy, but does not improve the basic assumptions of the model. The next step consists in exploring other formulations within hybrid methods which yield a more accurate acoustic solution at near-field regions by accounting for effects of non-quiescent flow areas on the propagation of aerodynamic noise. For this purpose, convective and refraction effects have to be extracted from the acoustic source term and included in the wave operator (see e.g., [17]), which has led to the development of more sophisticated analogies (see e.g., [131, 85]) and to alternatives such as the linearized Euler equations (LEE) [16]. This also means a better separation of the acoustic oscillations from the mechanical ones, leading to a better visualization of the wave propagation. In this sense, the incompressible-acoustic split method presented in [99, 160] enriches the incompressible flow equations with a variable density linked to pressure perturbations. Then, the time derivative of this perturbed density is translated into isentropic fluctuations of velocity and pressure that are propagated using a purely acoustic compressible solver after subtracting the incompressible component of the flow field. In a similar way, some formulations propagate the near field flow information to the far field with the aforementioned Linearized Euler Equations (LEE) [33, 19, 158] or with the Acoustic Perturbation Equations (APE) [74, 125], which consist in an acoustic filtering of the LEE source term. Chapter 3 of this thesis is precisely

devoted to the development of a stabilized FEM formulation of the APE's [97] and its application to the 2D aeolian tones case with the aim of evaluating the effects of flow convection on the propagation of acoustic waves, as well as the filtering of the acoustic solution from the scales captured by the CFD calculation.

The APE's manage indeed to solve most of the problems listed in the previous paragraphs, since they account for non-uniform flows and they provide a purely acoustic solution. However, the implementation cost in a FEM code and the computational complexity, including the numerical stabilization, of this approach have turned to be rather demanding. In Chapter 4 a last formulation has been developed in order to reduce the complexity of CAA calculations without losing the accuracy gained with the APE's. This last formulation aims for a simplification of CAA based on compressible flows and proposes a general framework that can be applied to any geometry, spatial discretization or flow regime below the transonic range. It consists in a compressible formulation with primitive variables without solving for the energy equation, since both flow and acoustic propagation are considered isentropic, which after condensing the density field becomes a system of two equations in terms of the velocity and the pressure, like in incompressible flow solvers. As a consequence, the implementation cost is very low when one departs from an already implemented incompressible flow solver, since the formulation reminds the artificial compressibility schemes [42]. Also, the computational cost is reduced with respect to other methodologies due to the following reasons: getting rid of the fully compressible approach and solving only for velocity and pressure, solving all scales at once without acoustic analogies and improving the condition number of the system for the incompressible limit. This formulation provides two important advantages respect to the acoustic analogies and other hybrid methods presented in the previous paragraph: first, it takes into account the acoustic feedback on the flow scales and second, the validity of the acoustic field will not depend on the motion of the flow or the presence of obstacles. These are precisely the main and only advantages of a Direct Noise Computation (DNC). In fact, for flows with $M \longrightarrow 0$ this solver is expected to converge to the solution of a DNC, but with a much lower computational cost. The only drawback of such a unified system will be, again like in a DNC, the lack of visualization of the acoustic fluctuations at the near field, where the aerodynamic scales are totally dominant and the wave propagation cannot be extracted like in [154, 97, 96]. As in all compressible flow models, an adequate equation of state needs to be chosen, in this case relating only density and pressure. For simplicity the ideal gas law has been used to close the problem, but the formulation can be easily extended to any other equation of state. Another typical challenge related to compressibility is the prescription of appropriate

boundary conditions. In this case, compatible flow and acoustic boundary conditions have been imposed in a weak sense [53, 71] so the acoustic waves can exit the domain through Dirichlet boundaries. In order to validate the formulation in all its application range, two benchmarks have been computed: first, the 2D aeolian tones case presented in [90] for checking the performance in the incompressible limit and the convergence to a DNC, and second a 3D NACA0012 airfoil with a Mach number of 0.4 [179].

At this point, the numerical framework for simulating phonemes involving aeroacoustic noise in fixed geometries has been completed. However, the general character of the proposed methods has motivated the extension of the previous framework to dynamic phonation cases, such as syllables. In this case, the irreducible second order wave equation is not appropriate for taking into account the domain motion and it must be replaced by the wave equation in mixed form, which can be directly derived from (1.1) and (1.2) keeping the first order of the derivatives and taking the same simplification of (1.12):

$$c_0^{-2}\partial_t p + \rho_0 \partial_j \hat{u}_j = 0, \tag{1.13}$$

$$\rho_0 \partial_t \hat{u}_i + \partial_j \left(p\delta_{ji}\right) = -\rho_0 \partial_j u_j u_i, \tag{1.14}$$

where $\hat{\boldsymbol{u}}$ is the acoustic velocity. The biomechanical aspects of the problem have not been taken into account, but the hypothetical deformation of the domain has been included in the formulations by expressing them in an Arbitrary Lagrangian Eulerian (ALE) setting [67]. This reference allows the computational grid to adapt its shape according to the motion of the domain, but this progressive deformation of the mesh might lead to an excessive distortion of the elements, specially in cases with irregular boundaries and large deformations. Since this is precisely the expected scenario in the simulation of a syllable, a novel remeshing strategy has also been developed. This formulation has been conceived for general use and consists in a point-by-point Lagrangian interpolation from a deformed mesh to a new one followed by an a posteriori correction based on [104]. The method imposes the conservation of relevant physical quantities, such as mass, momentum or energy, through Lagrange multipliers in an optimization problem which in turn minimizes the L^2-norm between the corrected solution and the interpolated one. Chapter 5 is completely devoted to the presentation of this remeshing strategy in the context of flow problems in an ALE reference with large domain deformations, establishing a solid ground towards a robust and accurate calculation of CAA cases in moving domains, such as syllables, provided the proper geometry and the deformation mapping are given. Furthermore, Chapter 2 has been extended with Lighthill's analogy using the mixed form of the wave equation in an ALE frame of reference [89], and its decomposition in quadrupolar and dipolar components as an alternative to the

Ffowcs-Williams-Hawkings method [178]. Analogously, Chapter 4 has been completed with the ALE formulation of the isentropic compressible solver. This feature has been tested in two cases with moving domains which have been computed with both compressible and incompressible aeroacoustic formulations: a 2D version of the NACA0012 airfoil with a bounded oscillation of the trailing edge and $M = 0.2$ and a 3D simulation of the syllable /sa/ using a simplified vocal tract geometry with one-dimensional vertical opening motion.

After having developed and tested the whole theoretical CAA framework for both fixed and mobile domains, the main application of the thesis is presented in Chapter 6. It consists in a large-scale simulation of the fricative phoneme /s/ using a 3D realistic vocal tract geometry obtained with MRI and the formulations presented previously, except the APE's, whose cost has not been affordable in regard to the available computational hours. A sibilant fricative /s/ is generated when the turbulent jet in the narrow channel between the tongue blade and the hard palate is deflected downwards through the incisors' space, and impinges the inter-space between the lower incisors and the lower lips. The flow eddies in that region become a source of direct aerodynamic sound, which is also diffracted by the upper incisors and radiated outwards. The numerical simulation of this phenomenon is complex. The spectrum of an /s/ typically peaks between $4-10$ kHz, which implies using very fine computational meshes to capture the eddies producing such high frequencies. In this work, the computation has been performed resorting to two different acoustic analogies based on an incompressible LES using the VMS stabilization method as turbulence model: Lighthill's analogy and its filtered version presented in [154]. It is to be noted that 3D LES simulations of flow passing around teeth-shaped obstacles to better understand the underlying physics of /s/ were already reported in [176, 175] and in [43]. Simulations of flow passing through simplified geometries with constrictions of different sizes have also been conducted [44]. [142] also resorted to LES to analyze the flow dynamics of /s/ in a realistic vocal tract geometry. As said before, more recently, [181] presented simulations on a 3D realization of the geometry in [106]. Also, the numerical strategy presented in Chapter 2 which allows determining, in a single computational run, the separate contributions from the direct turbulent sound and the sound diffracted by the upper incisors, has been applied to the radiated sibilant /s/. Results are presented for points located close to the mouth exit showing the relative influence of the sources of sound depending on frequency, and finally compared to experimental data from an equivalent mechanical replica [81]. Moreover, the same case has been calculated again with the isentropic compressible formulation using the same LES-VMS approach and the results have been compared to those obtained with the incompressible acoustic analogies.

1.4 Articles

This thesis has been structured in self-contained chapters that correspond to published or submitted scientific articles. The following list summarizes the connection between contents:

- Chapter 2 contains the material presented in two papers: "Oriol Guasch, Arnau Pont, Joan Baiges, and Ramon Codina. Concurrent finite element simulation of quadrupolar and dipolar flow noise in low Mach number aeroacoustics, 133:129-139, *Computers Fluids* (2016)", and its ALE extension "Oriol Guasch, Arnau Pont, Joan Baiges, and Ramon Codina. Simultaneous finite element computation of direct and diffracted flow noise in domains with moving walls", which has been published as a proceeding at the FLINOVIA II symposium and is currently being extended for submitting a journal article.

- Chapter 3 corresponds entirely to "Oriol Guasch, Patricia Sánchez-Martín, Arnau Pont, Joan Baiges, and Ramon Codina. Residual-based stabilization of the finite element approximation to the acoustic perturbation equations for low Mach number aeroacoustics, 82:839-857, *International Journal for Numerical Methods in Fluids*, (2016).", which has been mainly developed and implemented by Dr. Patricia Sánchez and Prof. Oriol Guasch. The main contribution of the author has consisted in providing the underlying CFD calculation and analyzing the effect of non-quiescent flows on the propagation of acoustic waves in the aeolian tones case.

- Chapter 4 contains the article "Arnau Pont, Ramon Codina, Joan Baiges, Oriol Guasch. Unified solver for fluid dynamics and aeroacoustics in isentropic gas flows", submitted to the *Journal of Computational Physics*, and a small part of "Simultaneous finite element computation of direct and diffracted flow noise in domains with moving walls" corresponding to the ALE extension of the isentropic compressible formulation.

- Chapter 5 corresponds entirely to "Arnau Pont, Ramon Codina, Joan Baiges. Interpolation with restrictions between finite element meshes for flow problems in an ALE setting, 110:1203-1226, *International Journal for Numerical Methods in Engineering* (2017)".

- Chapter 6 presents the main results of the thesis and corresponds to the paper "Arnau Pont, Oriol Guasch, Joan Baiges, Ramon Codina, Annemie van Hirtum. Computational aeroacoustics to identify sound sources in the generation of sibilant /s/", submitted to Biomechanics

and Modeling in Mechanobiology. A final section is added to this work in order to include the equivalent results using the formulation presented in Chapter 4.

Chapter 2

Concurrent finite element simulation of quadrupolar and dipolar flow noise in low Mach number aeroacoustics

The computation of flow-induced noise at low Mach numbers usually relies on a two-step hybrid methodolgy. In the first step, an incompressible fuid dynamics simulation (CFD) is performed and an acoustic source term is derived from it. The latter becomes the inhomegenous term for an acoustic wave equation, which is solved in the second step, often resorting to boundary integral formulations. In the presence of rigid bodies, Curle's acoustic analogy is probably the most extended approach. It has been shown that Curle's boundary dipolar noise contribution does in fact correspond to the diffraction of the quadrupolar aerodynamic noise generated by the flow past the rigid body. In this work, advantage is taken from this fact to propose an alternative computational methodology to get the individual quadrupolar and dipolar contributions to the total acoustic pressure. For any linear acoustic wave operator, the unknown acoustic pressure can be split into its incident and diffracted components and be computed simultaneously to the incompressible flow field, in a single finite element computational run. This circumvents the problem found in Curle's analogy of needing the total pressure at the body's boundary, which include the acoustic pressure fluctuations. The latter cannot be obtained from an incompressible CFD simulation. The proposed unified strategy could be beneficial for a large variety problems such as those involving noise generated from duct terminations, or those related with the simulation of fricatives in numerical voice production, among many others. The whole method will be also adapted to aeroacoustic problems in moving domains by using an Arbitrary Lagrangian

Eulerian (ALE) frame of reference.

2.1 Background

In the direct noise computation (DNC) approach to aeroacoustics (see e.g., [32]), aerodynamic noise is straightforwardly obtained as a bypass product of the unsteady and/or turbulent flow motion, driven by the compressible Navier-Stokes equations. However, DNC is only feasible for academic cases, and a few industrial ones, due to its high computational cost. As a consequence, most computational aeroacoustics (CAA) strategies to date have relied on hybrid approaches [17], which can be applied whenever there is no important feedback from the acoustic field to the aerodynamic one. Hybrid approaches usually consist of a first finite element (FEM), or finite volume, computational fluid dynamics (CFD) simulation to obtain the aerodynamic velocity and pressure fields, from which some acoustic sources can be derived. The latter are set as the inhomogeneous term of a wave equation that is solved to get the acoustic pressure field in a second numerical simulation. The acoustic pressure is usually computed with the boundary element method (BEM) if the sound pressure is to be found at long distances from the source region, though FEM is also feasible if the computational domain is not too large [143, 91, 92, 124, 15].

In this work, focus is placed on aeroacoustics at low Mach numbers. The most popular option for unbounded flows probably is that of making use of Lighthill's acoustic analogy [130]. First, an incompressible CFD simulation is carried out and the double divergence of the Reynolds tensor is computed from it as an approximation to Lighthill's tensor (see [63, 153, 161] for a detailed justification). The latter is convolved with the free-space Green function for the wave equation to get the acoustic pressure radiated by flow motion. This allows one to identify the problem of flow noise emission with that of sound radiation by a distribution of quadrupoles in free space. Though the most celebrated acoustic analogy is that of Lighthill, many other analogies have been derived. Some emphasize the role of vorticity in aerodynamic noise production [148, 105, 139] while others attempt at transferring mean flow effects from Lighthill's source term to the wave operator (see e.g., [131] for a review and also [85]). Approaches standing on acoustic perturbation equations (e.g., [73, 111, 97]) derived from linearization of the Euler equations (e.g., [161, 16]) are also quite common.

All the strategies in the precedent paragraph are intended for aerodynamic sound propagation in free field. To consider the effects of bodies within the flow on aerodynamic noise, one could proceed analogously to what is done for Lighthill's acoustic analogy, but convolving the source term with a tailored Green function that accounts for the body boundary condi-

tions. The problem is that for complex geometries tailored Green functions are not available. Curle [65] proposed a way out to this difficulty by identifying the influence of rigid bodies with that of a distribution of surface dipoles. The free-space Green function can be used instead of the tailored one, though at the price of taking into account a new source of sound in the simulations. Curle's formulation was extended for non-rigid bodies in the well-known Ffowcs Williams-Hawkings equation [178].

Unfortunately, when applied to low Mach number aeroacoustics, Curle's formulation presents a problem. The dipole surface integral term involves the gradient of the total pressure in the normal direction to the boundary of the rigid body. The total pressure includes the acoustic fluctuations, which cannot be obtained from an incompressible CFD simulation. Recently, it has been proposed to surpass this difficulty by just considering the gradient of the incompressible flow pressure and by replacing the wave equation Green function with that of the Laplacian operator [138]. Another strategy will be followed hereafter. This is based on the observation that Curle's analogy is actually a sharp way to account for aerodynamic noise generated by surfaces, though what it is really happening, from a physical point of view, is that waves generated by flow motion get diffracted by the rigid body [66, 61, 84].

In this chapter, we take advantage of this fact and propose a methodology for the simultaneous computation of the flow field, and of the turbulent and surface diffracted contributions to the total acoustic pressure field. At each time step of the simulation, the flow incompressible aerodynamic velocity and pressure are obtained by solving the incompressible Navier-Stokes equations, and input into a wave equation for the acoustic pressure, as if no rigid body was present. This computed acoustic pressure generated by the wake past the body has a quadrupolar character and plays the role of an incident pressure field on the rigid body boundary. Therefore, the incident pressure is used in turn to solve a wave equation for the acoustic pressure diffracted by the rigid body, at the same computational time step. In this way, the complete time evolution of the separate contributions to the acoustic pressure generated by flow motion (quadrupolar) and by surface diffraction (dipolar) is obtained at the end of the simulation. All the partial differential equations involved in this methodology have been solved by means of FEM, resorting to stabilization strategies when necessary. A preliminary, short version of this work can be found in [95].

The chapter is organized as follows. The basic theory and problem statement, as well as the continuous and discrete formulation using FEM for static domains (Eulerian reference) are presented in Section 2. A reminder is made of Curle's analogy as a diffraction problem and the proposed methodology for flow noise computation is detailed for general wave operators, then the weak formulation of the equations is first exposed and finally we proceed

to their space and time discretization. Section 3 focuses on the numerical approximation of the Navier-Stokes and wave equations in an ALE frame of reference, reminding first the Ffowcs-Williams-Hawkings method (FWH) as the extension of Curle's analogy for moving surfaces. In section 4, four numerical examples are presented. The first one, used for verification and testing purposes, deals with aerodynamic noise generated by flow past a two-dimensional cylinder (aeolian tones). The second one concerns noise produced by flow past a sharp constraint at the exit of a three-dimensional rectangular duct. This second example is of importance to analyze the physics involved, for instance, in the generation of voice sibilant sounds like /s/. The third one consists in an oscillating 2D NACA0012 airfoil and the last one presents a schematic example of a syllable in a simplified vocal tract in opening motion. Conclusions close the chapter in section 5.

2.2 Problem statement for fixed domains

2.2.1 Curle's analogy as a diffraction problem

As a motivation for this work, let us first review the connection between Curle's analogy and the diffraction of aerodynamic sound by a rigid body. We will closely follow [84] for that purpose. Consider the situation depicted in Fig. 2.1, where a low Mach, high Reynolds number gas flow impinges on a rigid body Ω_b and as a result, a wake develops past the body. The evolution of the aerodynamic velocity $\boldsymbol{u}^0(x,t)$ and the aerodynamic pressure $p^0(x,t)$ will be driven to a good extent by the incompressible Navier-Stokes equations. These are to be solved in a computational domain $\Omega_{NS} \subset \mathbb{R}^d$ (where $d = 2, 3$ is the number of space dimensions) with boundary $\partial\Omega_{NS}$ and prescribed initial and boundary conditions. Splitting $\partial\Omega_{NS}$ into three disjoint sets $\partial\Omega_{NS} = \Gamma_b \cup \Gamma_D \cup \Gamma_N$, the mathematical problem to be faced reads

$$\partial_t \boldsymbol{u}^0 - \nu\Delta\boldsymbol{u}^0 + \boldsymbol{u}^0 \cdot \nabla\boldsymbol{u}^0 + \nabla p^0 = \boldsymbol{f} \quad \text{in } \Omega_{NS},\ t > 0, \tag{2.1a}$$

$$\nabla \cdot \boldsymbol{u}^0 = 0 \quad \text{in } \Omega_{NS},\ t > 0, \tag{2.1b}$$

$$\boldsymbol{u}^0(\boldsymbol{x}, 0) = \boldsymbol{u}_0^0(\boldsymbol{x}) \quad \text{in } \Omega,\ t = 0, \tag{2.1c}$$

$$\boldsymbol{u}^0(\boldsymbol{x}, t) = \boldsymbol{0} \quad \text{on } \Gamma_b,\ t > 0, \tag{2.1d}$$

$$\boldsymbol{u}^0(\boldsymbol{x}, t) = \boldsymbol{u}_D^0(\boldsymbol{x}, t) \quad \text{on } \Gamma_D,\ t > 0, \tag{2.1e}$$

$$\boldsymbol{n} \cdot \boldsymbol{\sigma}(\boldsymbol{x}, t) = \boldsymbol{t}_N(\boldsymbol{x}, t) \quad \text{on } \Gamma_N,\ t > 0, \tag{2.1f}$$

where ν stands for the kinematic viscosity and $\boldsymbol{f}$ for the external force. $\boldsymbol{\sigma}$ is the Cauchy stress tensor, and $\boldsymbol{n}$ and $\boldsymbol{t}_N$ respectively denote the outward normal at the boundary and the traction. ∂_t denotes the first order time derivative. In his celebrated work, Lighthill [130] reordered the compressible

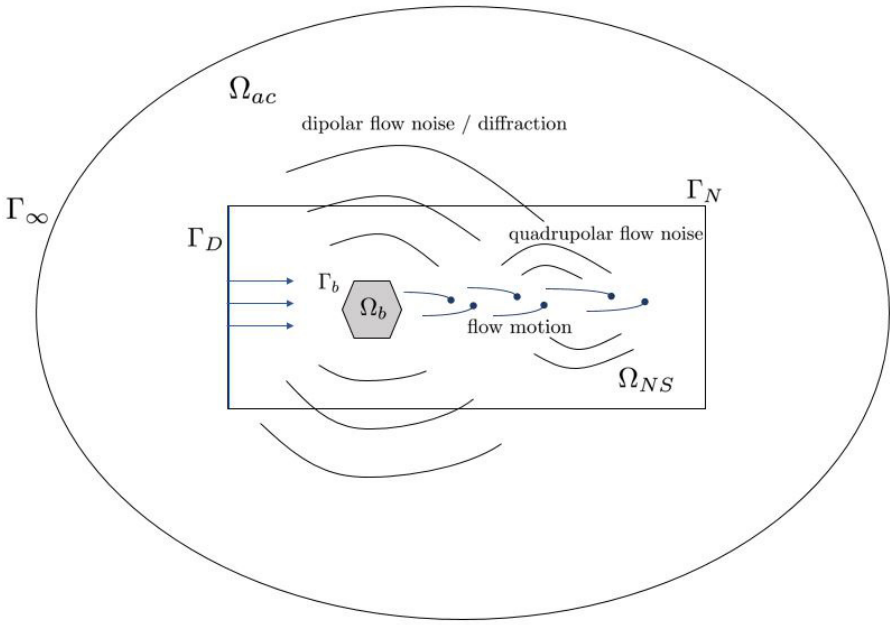

Figure 2.1: Flow noise problem. The dipolar contribution from the rigid body Ω_b in Curle's analogy corresponds to the diffraction of the quadrupolar flow noise generated at the wake past the body

Navier-Stokes equations into a wave equation whose source term involved the double divergence of the so-called Lighthill's tensor, T_{ij}. In the particular case of low Mach and high Reynolds numbers one can neglect viscous dissipation and refraction in T_{ij}, and approximate the tensor solely in terms of the incompressible velocities

$$T_{ij} \approx \rho_0 u_i^0 u_j^0, \tag{2.2}$$

with ρ_0 standing for the flow constant density. According to Lighthill's acoustic analogy we can then obtain the flow induced noise by solving the wave equation

$$\partial_{tt}^2 p - c_0^2 \nabla^2 p = \rho_0 \partial_{ij}^2 (u_i^0 u_j^0) \quad \text{in } \Omega_{ac},\ t > 0, \tag{2.3a}$$

$$\nabla p \cdot \boldsymbol{n} = 0 \quad \text{on } \Gamma_b,\ t > 0, \tag{2.3b}$$

$$\nabla p \cdot \boldsymbol{n} = c_0^{-1} \partial_t p \quad \text{on } \Gamma_\infty,\ t > 0, \tag{2.3c}$$

$$p(\boldsymbol{x}, 0) = 0,\ \partial_t p(\boldsymbol{x}, 0) = 0 \quad \text{in } \Omega_{ac},\ t = 0. \tag{2.3d}$$

In (2.3), p represents the acoustic pressure and c_0 the speed of sound. Γ_∞ corresponds to the outer boundary where a Sommerfeld like condition is to be imposed to avoid waves propagating outwards to reflect back into the computational domain. Besides, it is assumed for the time being that the

source term in the r.h.s of (2.3a) vanishes outside $\Omega_{NS} \subset \Omega_{ac}$ (see section 2.3 for further considerations). The flow is therefore at rest in $\Omega_{ac} - \Omega_{NS}$. On the other hand, we have used ∂_i to denote the first order spatial derivative with respect to coordinate x_i, i.e., $\partial_i \equiv \partial/\partial x_i$. The summation convention for repeated indices is also assumed in what follows unless explicitly specified.

An integral solution to (2.3) could be found provided a tailored Green function $G(\boldsymbol{x}, t \mid \boldsymbol{y}, \tau)$ satisfying the boundary conditions at Γ_b was known. This would result in the acoustic pressure field

$$p\,(\boldsymbol{x}, t) = \rho_0 \int_{-\infty}^{\infty} \int_{\Omega_{ac}} G(\boldsymbol{x}, t \mid \boldsymbol{y}, \tau) \partial_{ij}^2 (u_i^0 u_j^0) d^3\boldsymbol{y} d\tau. \tag{2.4}$$

Unfortunately, tailored Green functions are only available for bodies with very simple geometrical shapes. In the particular case of the typical wavelength of the generated sound being larger than the body principal dimension, one can make use of compact Green functions [108] and extend the number of situations where (2.4) could be applied in practice. Nonetheless, for more general applications it would be desirable to find a way out to solve (2.3) making use of the more simple free space Green function for the wave equation

$$G_F(\boldsymbol{x}, t \mid \boldsymbol{y}, \tau) = \frac{1}{4\pi|\boldsymbol{x} - \boldsymbol{y}|} \delta \left(t - \tau - \frac{|\boldsymbol{x} - \boldsymbol{y}|}{c_0} \right), \tag{2.5}$$

where δ stands for the Dirac delta function. This was achieved by Curle [65] using an ingenious procedure, which allowed one to identify the rigid body contribution to flow noise with that of a dipole source distribution radiating into free space. Curle's final integral formulation for the acoustic pressure reads

$$p\,(\boldsymbol{x}, t) = \rho_0 \partial_{ij}^2 \int_{\Omega_{ac}} \frac{1}{4\pi|\boldsymbol{x} - \boldsymbol{y}|} \left[u_i^0 u_j^0 \right]_{t'} d^3\boldsymbol{y} - \partial_i \int_{\Gamma_b} \frac{1}{4\pi|\boldsymbol{x} - \boldsymbol{y}|} [p'_{ij}]_{t'} n_j d^2\boldsymbol{y}, \tag{2.6}$$

with $p'_{ij} = P\delta_{ij} - \sigma_{ij}$, P denoting the full compressible pressure to be evaluated at the body's boundary. As said, we are considering high Reynolds numbers so that $p'_{ij} \approx P\delta_{ij}$ and the second term in the r.h.s of (2.6) simplifies to $\partial_i \int_{\Gamma_b} (4\pi|\boldsymbol{x}-\boldsymbol{y}|)^{-1} [P]_{t'} n_i d^2\boldsymbol{y}$. As usual for retarded potentials, the squared brackets in (2.6) denote evaluation at the retarded time $t' := t - |\boldsymbol{x} - \boldsymbol{y}|/c_0$.

According to (2.6), the acoustic pressure at a far field point in $\Omega_{ac} - \Omega_{NS}$ has two contributions, namely the quadrupolar one directly stemming from flow motion (volume integral term in the r.h.s of (2.6)), and the dipolar one due to the presence of the rigid body Ω_b within the flow domain (surface integral term in the r.h.s). However, as commented in the Introduction, a

severe difficulty appears for low Mach number flows if the acoustic source term is derived from an incompressible CFD computation. Whereas the incompressible velocity in the volume integral of (2.6) can be readily obtained from the solution of (2.1), this is not the case for the source term in the surface integral, because the integrand P involves not only the aerodynamic pressure at Γ_b but also the acoustic pressure fluctuations on it. In [138], an approximation was proposed to circumvent this problem that consists in making use of the incompressible pressure at the surface Γ_b and in replacing the free field Green function for the wave equation (2.5) by that of the Poisson equation. An alternative to that approach will be proposed hereafter that involves less assumptions. This is based on the fact that, as noted by several authors (see e.g. [66, 61, 84]), the acoustic pressure contribution of the surface integral in (2.6) corresponds to the diffraction of the aerodynamic noise produced, in the case of Fig. 2.1, by the flow wake past the rigid body.

The tailored Green function in (2.4) can be decomposed as

$$G(\boldsymbol{x}, t \mid \boldsymbol{y}, \tau) = G_F(\boldsymbol{x}, t \mid \boldsymbol{y}, \tau) + G_D(\boldsymbol{x}, t \mid \boldsymbol{y}, \tau), \tag{2.7}$$

with G_F being the free-space Green function in (2.5) and G_D its diffracted (read also scattered) field correction that accounts for the presence of boundaries. Substituting (2.7) into (2.4) results in

$$p\,(\boldsymbol{x}, t) = \rho_0 \partial_{ij}^2 \int_{\Omega_{ac}} \frac{1}{4\pi|\boldsymbol{x}-\boldsymbol{y}|} \left[u_i^0 u_j^0\right]_{t'} d^3\boldsymbol{y} + \rho_0 \int_{-\infty}^{\infty} \int_{\Omega_{ac}} G_D \partial_{ij}^2 (u_i^0 u_j^0) d^3\boldsymbol{y} d\tau. \tag{2.8}$$

A direct comparison with (2.6) allows one to identify

$$-\partial_i \int_{\Gamma_b} \frac{1}{4\pi|\boldsymbol{x}-\boldsymbol{y}|} [P]_{t'} n_i d^2\boldsymbol{y} = \rho_0 \int_{-\infty}^{\infty} \int_{\Omega_{ac}} G_D \partial_{ij}^2 (u_i^0 u_j^0) d^3\boldsymbol{y} d\tau. \tag{2.9}$$

It becomes then apparent that the Curle surface integral, which represents an acoustic dipole source distribution, does in fact correspond to the body diffraction of the turbulent noise generated by the flow wake.

2.2.2 Proposed methodology

In view of (2.8), one may consider the possibility of obtaining the individual flow quadrupolar turbulent contribution as well as the dipolar one due to diffraction all at once, as the outputs of a single FEM computational run. This would prove very useful in some aeroacoustics situations where the influence of each type of sources is needed, for example, for noise reduction remedial purposes, or for a better understanding of the underlying noise generation mechanisms of a given physical phenomenon.

Let us split the total acoustic pressure into its incident and diffracted components $p = p_i + p_d$ in (2.3), as commonly done for diffraction problems. This results in the two wave equations,

$$\partial_{tt}^2 p_i - c_0^2 \nabla^2 p_i = \rho_0 \partial_{ij}^2 (u_i^0 u_j^0) \quad \text{in } \Omega_{ac} \cup \ \Omega_b, \ t > 0, \tag{2.10a}$$

$$\nabla p_i \cdot \boldsymbol{n} = c_0^{-1} \partial_t p_i \quad \text{on } \Gamma_\infty, \ t > 0, \tag{2.10b}$$

$$p_i(\boldsymbol{x}, 0) = 0, \ \partial_t p_i(\boldsymbol{x}, 0) = 0 \quad \text{in } \Omega_{ac} \cup \ \Omega_b \ t = 0, \tag{2.10c}$$

and

$$\partial_{tt}^2 p_d - c_0^2 \nabla^2 p_d = 0 \quad \text{in } \Omega_{ac}, \ t > 0, \tag{2.11a}$$

$$\nabla p_d \cdot \boldsymbol{n} = -\nabla p_i \cdot \boldsymbol{n} \quad \text{on } \Gamma_b, \ t > 0, \tag{2.11b}$$

$$\nabla p_d \cdot \boldsymbol{n} = c_0^{-1} \partial_t p_d \quad \text{on } \Gamma_\infty, \ t > 0, \tag{2.11c}$$

$$p_d(\boldsymbol{x}, 0) = 0, \ \partial_t p_d(\boldsymbol{x}, 0) = 0 \quad \text{in } \Omega_{ac}, \ t = 0. \tag{2.11d}$$

Instead of resorting to an integral formulation, it is herein proposed to solve the problem of aerodynamic sound generation by solving (2.1), (2.10) and (2.11) all together, in a single simulation. The weak form of these equations will be discretized in space using FEM and in time using finite difference schemes. At each time step of the simulation the incompressible velocity obtained from (2.1) will be used in (2.10) to compute the incident acoustic pressure field (i.e., the direct quadrupolar contribution), which in turn will be used in (2.11) to compute the diffracted pressure field (i.e., the direct dipolar surface contribution). This strategy avoids the problem of having to deal with the total pressure in the surface integral of Curle's analogy and independently provides the contributions p_i and p_d to the total acoustic pressure p, which could not have been obtained from the direct FEM solution of (2.3). Alternatively, one could also attempt at solving (2.3) and (2.10) and obtain the diffracted contribution by subtracting the incident acoustic pressure field from the total one.

2.2.3 Generalization to other wave operators and sound sources

Though posing Curle's analogy as a diffraction problem has motivated the approach in the preceding section to compute the quadrupolar and dipolar contributions to aerodynamic sound, that methodology can be generalized to other linear wave operators and source terms that include phenomena neglected in Lighthill's tensor approximation (2.2). Let us denote by L a generic linear wave operator acting on the acoustic pressure p defined in Ω_{ac}, B_b a linear operator defining the boundary conditions at the rigid body (including e.g., a prescribed impedance value at Γ_b) and B_∞ a linear

operator describing a non-reflecting boundary condition at Γ_∞. Q will stand for a generic aerodynamic source term obtained from an incompressible CFD computation solving (2.1). Then, the aerodynamic noise problem of solving

$$Lp = Q \quad \text{in } \Omega_{ac},\ t > 0, \tag{2.12a}$$
$$\nabla p \cdot \boldsymbol{n} = B_b p \quad \text{on } \Gamma_b,\ t > 0, \tag{2.12b}$$
$$\nabla p \cdot \boldsymbol{n} = B_\infty p \quad \text{on } \Gamma_\infty,\ t > 0, \tag{2.12c}$$
$$p(\boldsymbol{x}, 0) = 0,\ \partial_t p(\boldsymbol{x}, 0) = 0 \quad \text{in } \Omega_{ac},\ t = 0. \tag{2.12d}$$

can always be split using $p = p_i + p_d$ as

$$Lp_i = Q \quad \text{in } \Omega_{ac} \cup \Omega_b,\ t > 0, \tag{2.13a}$$
$$\nabla p_i \cdot \boldsymbol{n} = B_\infty p_i \quad \text{on } \Gamma_\infty,\ t > 0, \tag{2.13b}$$
$$p_i(\boldsymbol{x}, 0) = 0,\ \partial_t p_i(\boldsymbol{x}, 0) = 0 \quad \text{in } \Omega_{ac} \cup \Omega_b\ t = 0, \tag{2.13c}$$

and

$$Lp_d = 0 \quad \text{in } \Omega_{ac},\ t > 0, \tag{2.14a}$$
$$\nabla p_d \cdot \boldsymbol{n} - B_b p_d = -\nabla p_i \cdot \boldsymbol{n} + B_b p_i \quad \text{on } \Gamma_b,\ t > 0, \tag{2.14b}$$
$$\nabla p_d \cdot \boldsymbol{n} = B_\infty p_d \quad \text{on } \Gamma_\infty,\ t > 0, \tag{2.14c}$$
$$p_d(\boldsymbol{x}, 0) = 0,\ \partial_t p_d(\boldsymbol{x}, 0) = 0 \quad \text{in } \Omega_{ac},\ t = 0. \tag{2.14d}$$

Equations (2.3), (2.10) and (2.11) are nothing but a particular case of (2.12), (2.13) and (2.14). Another example, could be that of identifying L with the convective wave equation $L \equiv [c_0^{-2}(\partial_t + U_0 \cdot \nabla)^2 - \nabla^2]$ to account for the effects of a uniform mean flow velocity U_0 in the wave operator. With regard to the source term, one could consider, for instance, the double time derivative of the incompressible pressure instead of the double divergence of (2.2) as a source term, i.e., $Q \equiv c_0^{-1}\partial_{tt}^2 p^0$ (see e.g., [155]). The boundary condition operator B_b could involve the admittance coefficient at the surface, μ, and be identified e.g., with $B_b \equiv -\mu c_0^{-1}\partial_t$. Besides, one could also attempt to extend the above procedure for the wave equation in mixed form [49], or for the more complex acoustic perturbation equations [73], though this is out of the scope of the present work.

Finally, we would like to note that in the case of dealing with N diffracting disjoint bodies instead of just one the problem becomes totally analogous to (2.13) and (2.14) if one is interested in knowing their quadrupolar and dipolar contributions as a whole. One simply has to consider that for such situations $\Omega_b = \bigcup_{j=1\ldots N} \Omega_{bj}$ with $\bigcap_{j=1\ldots N} \bar{\Omega}_{bj} = \emptyset$, each Ω_{bj} representing the j-th diffracting or scattering body (depending on the relation between wavelength and object characteristic size). An example of such a type would be that of determining the noise generated by a grille at the exit of a ventilation system, or knowing the influence of the upper and lower incisors in the voice generation of a fricative sound like /s/.

2.2.4 Numerical discretization

Continuous weak formulation

To present the numerical discretization of the proposed methodology we will focus on equations (2.1), (2.10) and (2.11). Resorting to a FEM approach for the spatial discretization of these equations demands working with their corresponding weak forms. Let us introduce some notation for that purpose. In what follows, for any two functions (or distributions) f and g, the integral of their product over the computational domain will be designated by $(f,g) \equiv \int_\Omega fg d\Omega$. This integral will typically represent a scalar product or a duality pair. A subscript will indicate that the integral is performed on a boundary, e.g., $(f,g)_{\Gamma_b}$. As usual, $L^p(0,T|X)$ will stand for the space of time dependent vector functions such that their X-norm is $L^p(0,T)$, L^p denoting the space of functions whose p-power ($1 \leq p < \infty$) is integrable within Ω. On the other hand, $H^m(\omega)$ will represent the space of functions whose distributional derivatives up to $m \geq 0$ (m integer) belong to $L^2(\Omega)$. The subspace of functions in $H^m(\Omega)$ that vanish on $\partial\Omega$ will be designated by $H_0^m(\Omega)$. The vector counterparts of all these spaces will be indicated by bold letters. Let us finally also identify $\boldsymbol{\mathcal{V}} := \boldsymbol{H}^1(\Omega)$ ($\mathcal{V} := H^1(\Omega)$), $\boldsymbol{\mathcal{V}_0} := \boldsymbol{H}_0^1(\Omega)$ ($\mathcal{V}_0 := H_0^1(\Omega)$) and $\mathcal{L}_0 := L^2(\Omega)/\mathbb{R}$. The weak form of the Navier-Stokes equations (2.1) is found as usual by multiplying them by a test function $\boldsymbol{v}^0$ for the velocity and q^0 for the pressure, and integrating over the computational domain Ω_{NS}. The variational problem to be solved is that of finding $[\boldsymbol{u}^0, p^0] \in \boldsymbol{L}^2(0,T|\boldsymbol{\mathcal{V}}) \times L^\infty(0,T|\mathcal{L}_0)$ such that

$$\begin{aligned}(\partial_t \boldsymbol{u}^0, \boldsymbol{v}^0) + (\boldsymbol{u}^0 \cdot \nabla \boldsymbol{u}^0, \boldsymbol{v}^0) + \nu(\nabla \boldsymbol{u}^0, \nabla \boldsymbol{v}^0) - (p^0, \nabla \cdot \boldsymbol{v}^0) \\ = (\boldsymbol{f}, \boldsymbol{v}^0) + (\boldsymbol{t}_N, \boldsymbol{v}^0)_{\Gamma_N}, \qquad (2.15a)\\ (q^0, \nabla \cdot \boldsymbol{u}^0) = 0, \qquad (2.15b)\end{aligned}$$

for all $[\boldsymbol{v}^0, q^0] \in \boldsymbol{\mathcal{V}_0} \times \mathcal{L}_0$, and supplemented with the weak form of the initial conditions in (2.29c). Analogously, multiplying (2.10) by the test function q and integrating now over the domain $\Omega_{ac} \cup \Omega_b$ we get the variational problem of obtaining the incident acoustic pressure $p_i \in C^2(0,T|\mathcal{L}_0) \cap C^0(0,T|\mathcal{V})$ which fulfills

$$(\partial_{tt}^2 p_i, q) + c_0^2(\nabla p_i, \nabla q) - c_0(\partial p_i, q)_{\Gamma_\infty} = (\boldsymbol{u}^0 \cdot \nabla \boldsymbol{u}^0, \nabla q), \qquad (2.16)$$

for all $q \in \mathcal{V}_0$. Note that it has been reasonably assumed that $\boldsymbol{u}^0$ vanishes on $\partial\Omega_{NS}$, and, again, the weak forms of the initial conditions (2.10c) are to be considered to solve the problem. Finally, the weak formulation for the diffracted acoustic pressure problem (2.11) becomes that of getting the pressure $p_d \in C^2(0,T|\mathcal{L}_0) \cap C^0(0,T|\mathcal{V})$ such that

$$(\partial_{tt}^2 p_d, q) + c_0^2(\nabla p_d, \nabla q) - c_0(\partial p_d, q)_{\Gamma_\infty} = c_0^2(\nabla p_i \cdot \boldsymbol{n}, q)_{\Gamma_b}, \qquad (2.17)$$

for all $q \in \mathcal{V}_0$. In this case volume integrals take place over Ω_{ac} and initial conditions (2.11d) have to be also appended to the variational form.

Spatial discretization

A FEM approach has been applied for the space discretization of all the involved variational equations in the preceding section. Let us first focus on the weak form of the Navier-Stokes equation in (2.15). For this case, it is well-known that the standard Galerkin FEM solution suffers from many numerical problems. On the one hand, a compatibility inf-sup condition has to be satisfied to control the pressure that does not allow one to use equal interpolations for the incompressible velocity and pressure fields. On the other hand, instabilities also appear in the case of strong convection as happens for high Reynolds number flows. Numerical instabilities may also trigger at the early stage of evolutionary processes when using small time steps.

It is possible to solve the above difficulties by resorting to stabilized finite element approaches. In particular, the subgrid scale stabilization methods (also known as variational multiscale or residual-based stabilization methods) [113, 46] are of special interest for the simulation of turbulent flows. This is so because, if well designed, they not only allow one to circumvent the above mentioned numerical problems, but also act as implicit large eddy simulation models [46, 103, 22, 59, 94]. The basic idea of subgrid scale methods is that of splitting the problem unknowns, $\boldsymbol{u}^0$ and p^0 for (2.15), and the test functions, $\boldsymbol{v}^0$ and q^0, into large scale components, $\boldsymbol{u}_h^0$ and p_h^0 (h refers to the mesh size), which can be resolved by the computational mesh and small scale components, $\tilde{\boldsymbol{u}}^0$ and $\tilde{p}^0$, which cannot be captured and whose effects onto the large scales have to be modeled. Substituting $\boldsymbol{u}^0 = \boldsymbol{u}_h^0 + \tilde{\boldsymbol{u}}^0$, $p^0 = p_h^0 + \tilde{p}^0$, $\boldsymbol{v}^0 = \boldsymbol{v}_h^0 + \tilde{\boldsymbol{v}}^0$ and $q^0 = q_h^0 + \tilde{q}^0$ in (2.15) yields two coupled equations, one driving the dynamics of the large scales but containing the influence of the small scales, and the other one governing the dynamics of the subscales, which in turn depend on the large scales. The solution to the latter is usually approximated considering the subscales to be directly proportional to the residual (in the algebraic subgrid scale (ASGS) version [113, 115]) or taking the residual component perpendicular to the finite element space (in the orthogonal subgrid scale (OSS) approach [46]). The proportionality is characterized by means of a matrix of the so-called stabilization parameters.

For the simulations in the present work we have resorted to the ASGS formulation, assumed quasi-static subscales and neglected the influence of the pressure subscales. The space-discrete variational problem for the large scales then becomes that of finding $[\boldsymbol{u}_h^0, p_h^0] \in \boldsymbol{L}^2(0,T|\boldsymbol{\mathcal{V}_h} \subset \boldsymbol{\mathcal{V}}) \times L^\infty(0,T|\mathcal{L}_{0h} \subset$

$\mathcal{L}_0$) such that

$$(\partial_t \boldsymbol{u}_h^0, \boldsymbol{v}_h^0) + (\boldsymbol{u}_h^0 \cdot \nabla \boldsymbol{u}_h^0, \boldsymbol{v}_h^0) + \nu(\nabla \boldsymbol{u}_h^0, \nabla \boldsymbol{v}_h^0) - (p_h^0, \nabla \cdot \boldsymbol{v}_h^0) + (q_h^0, \nabla \cdot \boldsymbol{u}_h^0) + (\boldsymbol{t}_N, \boldsymbol{v}_h^0)_{\Gamma_N} - (\boldsymbol{f}, \boldsymbol{v}_h^0) + (\tilde{\boldsymbol{u}}^0 \cdot \nabla \boldsymbol{u}_h^0, \boldsymbol{v}_h^0) - (\tilde{\boldsymbol{u}}^0, \tilde{\boldsymbol{u}}^0 \cdot \nabla \boldsymbol{v}_h^0) - \sum_{\Omega_{el}} (\tilde{\boldsymbol{u}}^0, \nu \triangle \boldsymbol{v}_h^0 + \boldsymbol{u}_h^0 \cdot \nabla \boldsymbol{v}_h^0 + \nabla q_h^0)_{\Omega_{el}} = 0, \tag{2.18}$$

for all $[\boldsymbol{v}_h^0, q_h^0] \in \boldsymbol{\mathcal{V}}_{0h} \times \mathcal{L}_{0h} \subset \boldsymbol{\mathcal{V}}_0 \times \mathcal{L}_0$. The incompressible velocity subscales $\tilde{\boldsymbol{u}}^0$ in (2.18) which solve the small scales equation are computed as

$$\tilde{\boldsymbol{u}}^0 = \tau(\boldsymbol{f} - \partial_t \boldsymbol{u}_h^0 - \boldsymbol{u}_h^0 \cdot \nabla \boldsymbol{u}_h^0 + \nu \triangle \boldsymbol{u}_h^0 - \nabla p_h^0), \tag{2.19}$$

with the stabilization parameter τ being given by

$$\tau = \left[c_1 \frac{\nu}{h^2} + c_2 \frac{|\boldsymbol{u}_h^0|}{h} \right]^{-1}, \tag{2.20}$$

and c_1 and c_2 in (2.15) standing for algorithmic parameters. From numerical experiments the values $c_1 = 4$ and $c_2 = 2$ have been deemed appropriate for them. The influence of the subscales $\tilde{\boldsymbol{u}}^0$ has been neglected in the non-linear term of the residual in (2.19), and in the stabilization parameter as well.

Observe that the first line of (2.18) is nothing but the Galerkin FEM approach to the variational Navier-Stokes problem whereas the second line contains the subscale contributions to the material derivative, as well as the stabilization terms which mitigate the numerical problems mentioned above. The notation $(f, g)_{\Omega_{el}}$ in the second line refers to integration within an element domain (subscales are assumed to vanish at the interelement boundaries). The reader is referred to [59] for a detailed derivation of the above equations. These arise as a particular case of the most general situation in which subscales are tracked in time and all its non-linear contributions retained.

In what concerns the wave equations, (2.16) and (2.17) do not present special spatial discretization difficulties because they only involve the Laplacian operator. A standard Galerkin FEM proves accurate enough. The spatial discrete version of (2.16) is that of finding $p_{ih} \in C^2(0, T|\mathcal{L}_{0h} \subset \mathcal{L}_0) \cap C^0(0, T|\mathcal{V}_h \subset \mathcal{V})$ which satisfies

$$(\partial_{tt}^2 p_{ih}, q_h) + c_0^2(\nabla p_{ih}, \nabla q_h) - c_0(\partial p_{ih}, q_h)_{\Gamma_\infty} = (\boldsymbol{u}_h^0 \cdot \nabla \boldsymbol{u}_h^0, \nabla q_h), \tag{2.21}$$

for all $q_h \in \mathcal{V}_{h0} \subset \mathcal{V}_0$. Analogously, the spatial discrete version of (2.17) consists in obtaining the diffracted pressure $p_{dh} \in C^2(0, T|\mathcal{L}_{0h} \subset \mathcal{L}_0) \cap C^0(0, T|\mathcal{V}_h \subset \mathcal{V}$ such that

$$(\partial_{tt}^2 p_{dh}, q_h) + c_0^2(\nabla p_{dh}, \nabla q_h) - c_0(\partial p_{dh}, q_h)_{\Gamma_\infty} = c_0^2(\nabla p_{ih} \cdot \boldsymbol{n}, q_h)_{\Gamma_b}, \tag{2.22}$$

for all $q_h \in \mathcal{V}_{h0} \subset \mathcal{V}_0$.

The main numerical difficulties with (2.21) and (2.22) usually arise from its time discretization (to be dealt with in the forthcoming subsection) or from undesired reflections at the boundary of the finite computational domain. Although simple Sommerfeld radiation conditions have proved precise enough for the numerical tests in the present study, the use of perfectly matched layers (PML) for the irreducible wave equation is certainly recommendable [110, 123, 6].

Finally, we point out that to get the matrix versions of the above equations one has to expand as usual the unknowns $\boldsymbol{u}_h^0$, p_h^0, p_{ih}, p_{dh}, and their corresponding test functions, as linear combinations of polynomial basis functions and nodal unknowns, and rearrange (2.18), (2.21) and (2.22). Needless to say that the equations are to be supplied with the corresponding discrete initial conditions in weak form.

Fully discretized numerical scheme in space and time

To approximate the first and second order time derivatives in (2.18), (2.21) and (2.22) second order backward finite difference schemes (BDF2) have been used. Let us partition the time interval $[0, T]$ into N equal time steps of size $\delta t := t^{n+1} - t^n$ so that $0 \equiv t^0 < t^1 < \ldots < t^n < \ldots < t^N \equiv T$. Given a generic time dependent function $g(t)$, the following notation will be used for the BDF2 approximation to the first time derivative,

$$\partial_t g|_{t^n} \approx \delta_t g^n := \frac{1}{2\delta t}(3g^n - 4g^{n-1} + g^{n-2}), \tag{2.23}$$

whilst the BDF2 second order time derivative will be designated by

$$\partial_{tt}^2 g|_{t^n} \approx \delta_{tt}^2 g^n := \frac{1}{(\delta t)^2}(2g^n - 5g^{n-1} + 4g^{n-2} - g^{n-3}). \tag{2.24}$$

As usual, g^n denotes evaluation of g at time step t^n.

Given that the proposed concurrent FEM formulation for aeroacoustics is not intended for sound propagation at very far distances (for which an integral approach would probably be more efficient), the above BDF2 time discretization schemes prove accurate enough. Otherwise, if acoustic wave propagation was required for distances involving several tenths or hundreds of wavelengths, one should resort to high-order schemes (e.g., fourth order Runge-Kutta [2, 132]) or to symplectic integrators (e.g. of the Verlet-type).

At an arbitrary time step of the numerical simulation, the final fully discretized implicit scheme in space and time proposed to solve equations (2.3), (2.10) and (2.11) reads as follows. From known $\boldsymbol{u}_h^{0,n-2}$ and $\boldsymbol{u}_h^{0,n-1}$, compute the incompressible velocity and pressure at time step t^n, $[\boldsymbol{u}_h^{0,n}, p_h^{0,n}] \in$

$\boldsymbol{\mathcal{V}_h} \times \mathcal{L}_{0h}$ such that

$$(\delta_t \boldsymbol{u}_h^{0,n}, \boldsymbol{v}_h^0) + (\boldsymbol{u}_h^{0,n} \cdot \nabla \boldsymbol{u}_h^{0,n}, \boldsymbol{v}_h^0) + \nu(\nabla \boldsymbol{u}_h^{0,n}, \nabla \boldsymbol{v}_h^0) - (p_h^{0,n}, \nabla \cdot \boldsymbol{v}_h^0) + (q_h^0, \nabla \cdot \boldsymbol{u}_h^{0,n}) - (\boldsymbol{f}^n, \boldsymbol{v}_h^0) + (\boldsymbol{t}_N^n, \boldsymbol{v}_h^0)_{\Gamma_N} + (\tilde{\boldsymbol{u}}^{0,n} \cdot \nabla \boldsymbol{u}_h^{0,n}, \boldsymbol{v}_h^0) - (\tilde{\boldsymbol{u}}^{0,n}, \tilde{\boldsymbol{u}}^{0,n} \cdot \nabla \boldsymbol{v}_h^0) - \sum_{\Omega_{el}} (\tilde{\boldsymbol{u}}^{0,n}, \nu \triangle \boldsymbol{v}_h^0 + \boldsymbol{u}_h^{0,n} \cdot \nabla \boldsymbol{v}_h^0 + \nabla q_h^0)_{\Omega_{el}} = 0, \quad (2.25)$$

for all $[\boldsymbol{v}_h^{0,n}, q_h^{0,n}] \in \boldsymbol{\mathcal{V}_{h0}} \times \mathcal{L}_{0h}$. Then, from known $\boldsymbol{u}_h^{0,n}$, p_{ih}^{n-3}, p_{ih}^{n-2} and p_{ih}^{n-1}, find the incident acoustic pressure at time step t^n, $p_{ih}^n \in \mathcal{V}_h$ that satisfies

$$(\delta_{tt}^2 p_{ih}^n, q_h) + c_0^2(\nabla p_{ih}^n, \nabla q_h) - c_0(\partial p_{ih}^n, q_h)_{\Gamma_\infty} = (\boldsymbol{u}_h^{0,n} \cdot \nabla \boldsymbol{u}_h^{0,n}, \nabla q_h), \quad (2.26)$$

for all $q_h \in \mathcal{V}_{h0}$. Finally, from p_{ih}^n, p_{dh}^{n-3}, p_{dh}^{n-2} and p_{dh}^{n-1} compute the diffracted acoustic pressure at time t^n, $p_{dh} \in \mathcal{V}_h$ such that

$$(\delta_{tt}^2 p_{dh}^n, q_h) + c_0^2(\nabla p_{dh}^n, \nabla q_h) - c_0(\partial p_{dh}^n, q_h)_{\Gamma_\infty} = c_0^2(\nabla p_{ih}^n \cdot \boldsymbol{n}, q_h)_{\Gamma_b}, \quad (2.27)$$

for all $q_h \in \mathcal{V}_{h0}$.

Usually, knowing the acoustic field generated by the initial transients of the NS equations is of no interest at all, so the acoustic module in the above scheme (equations (2.26) and (2.27)) gets activated after a certain period of time. On the other hand, note that at each time step of the simulation a linearization process is needed for the convective term in the NS equations. This can be achieved either by means of a simple Picard's scheme or by a Newton-Raphson's one.

Finally, it is worth mentioning that the proposed strategy presents a somehow tricky point because the computational domains for the variational NS equation (2.25) and for the two wave equations (2.26) and (2.27) are not the same. At each time step of the simulation, after solving (2.25) the domain Ω_b has to be *switched on* and included for the computation of the incident acoustic pressure in (2.26), and then *switched off* to compute the diffracted sound field in (2.27). Besides, it should be noted that special care should be taken when interpolating the results from the CFD domain to the acoustic one to avoid spurious errors [137, 128, 64].

2.3 Problem statement for moving domains

Next, a complete aeroacoustic formulation based on incompressible flow is presented. As stated in the Introduction, one of the main objectives is the derivation and implementation of numerical methods that can take part in a coupled simulation of any human phonation case, which includes dynamic sounds such as diphthongs and syllables. First, the incompressible Navier-Stokes equations are reformulated in an ALE frame of reference in

the parallel FEMUSS code following the example of [102]. In Chapter 4, the isentropic compressible equations will undergo the same procedure. Moreover, Lighthill's analogy and the splitting of the acoustic pressure into a quadrupolar and a dipolar component will also be formulated and implemented departing from [89].

2.3.1 Incompressible flow problem in an Arbitrary Lagrangian Eulerian frame of reference

The arbitrary Lagrangian-Eulerian (ALE) description [67] is intended to profit from the advantages of the two classical kinematic descriptions, the Lagrangian and the Eulerian, while minimizing considerably their drawbacks. In the Lagrangian formulation each node of the computational mesh follows the motion of the material particle it represents. This description is very suitable for structural mechanics and specific applications related to the tracking of free surfaces and interfaces between different materials. However, it is not capable to absorb large deformations of the domain unless a remeshing strategy is implemented. On the other hand Eulerian algorithms consider a fixed mesh with respect to the moving continuum, which allows large irregularities in the motion of the material. For this reason they are basically used in fluid mechanics. However, it is not able to capture with precision interfaces and other details of the flow. In the ALE description, the nodes may either follow the continuum in a Lagrangian fashion, or be held fixed in an Eulerian manner, or they can even be prescribed a completely independent velocity, for instance in case of a flow motion driven by deformation of the physical domain. Therefore, this approach admits larger distortions of the continuum than a purely Lagrangian method and offers a higher resolution than a purely Eulerian description. These considerations do not affect the numerical calculation of static speech sounds, like the sibilant fricative /s/ presented in chapter 6. However, when the object of study is a diphthong or a syllable, like the present case, the kinematics of the domain must be taken into account in both the flow and the acoustic problem.

Following the change of reference operation presented in [67], the material derivative for any magnitude f in an ALE frame of reference will be

$$\begin{aligned} \frac{Df}{Dt} &= \frac{\partial f}{\partial t} + (\mathbf{c} \cdot \nabla) f, \\ \boldsymbol{c} &= \boldsymbol{u} - \boldsymbol{u}_{\mathrm{dom}}, \end{aligned} \tag{2.28}$$

where $\boldsymbol{c}$ is the advection velocity in the new reference, $\boldsymbol{u}$ is the velocity in the Eulerian reference and $\boldsymbol{u}_{\mathrm{dom}}$ refers to the motion of the domain.

Once the nodal displacements of the mesh have been computed, the mesh velocity $\boldsymbol{u}_{\text{dom}}$ is computed by time derivation and sent to the physical problems to be solved in an ALE frame of reference. As shown previously, the ALE frame of reference modifies the second term of the material derivative of a certain magnitude, which in turn affects the convective term of the incompressible Navier-Stokes problem. This involves both the momentum equation and the stabilization terms. Moreover, boundary conditions must be also adapted to the new reference by adding the domain velocity to the Dirichlet prescribed values and recomputing the external normal of the boundaries for the Neumann conditions. Departing from the incompressible flow problem presented in section 2.2.1 and using the same notation, the ALE formulation of the continuous problem will be

$$\partial_t \boldsymbol{u}^0 - \nu \Delta \boldsymbol{u}^0 + \left(\boldsymbol{u}^0 - \boldsymbol{u}_{\text{dom}}\right) \cdot \nabla \boldsymbol{u}^0 + \nabla p^0 = \boldsymbol{f} \quad \text{in } \Omega_{NS},\ t > 0, \tag{2.29a}$$

$$\nabla \cdot \boldsymbol{u}^0 = 0 \quad \text{in } \Omega_{NS},\ t > 0, \tag{2.29b}$$

$$\boldsymbol{u}^0(\boldsymbol{x}, 0) = \boldsymbol{u}_0^0(\boldsymbol{x}) \quad \text{in } \Omega,\ t = 0, \tag{2.29c}$$

$$\boldsymbol{u}^0(\boldsymbol{x}, t) = \boldsymbol{u}_{\text{dom}}(\boldsymbol{x}, t) \quad \text{on } \Gamma_b,\ t > 0, \tag{2.29d}$$

$$\boldsymbol{u}^0(\boldsymbol{x}, t) = \boldsymbol{u}_D^0(\boldsymbol{x}, t) + \boldsymbol{u}_{\text{dom}}(\boldsymbol{x}, t) \quad \text{on } \Gamma_D,\ t > 0, \tag{2.29e}$$

$$\boldsymbol{n} \cdot \boldsymbol{\sigma}(\boldsymbol{x}, t) = \boldsymbol{t}_N(\boldsymbol{x}, t) \quad \text{on } \Gamma_N,\ t > 0, \tag{2.29f}$$

The fully discrete formulation of the problem using FEM can be easily derived as in 2.2.4. For the sake of conciseness it will not be presented again.

In spite of using an ALE reference which follows the deformation of the domain, an excessive distortion of the mesh elements might take place in cases with large displacements or when dealing with geometries that tend to localize deformation in small regions. For this reason a remeshing strategy which allows a conservative transmission of results between computational grids will be presented in Chapter 5. For the cases presented next, which consist in a bounded rotation of a 2D NACA0012 airfoil and the opening of a 2D simplified vocal tract emulating the syllable /sa/, the regularity of the geometry and its simple motion do not require any remeshing stage if the mesh undergoes a virtual elastic problem presented in [39]. Unlike the Poisson problem, which yields a smooth and homogeneous propagation of the prescribed displacements from the boundary to the interior nodes of the mesh, this method allows minimizing element distortion by adapting the mechanical properties of each mesh element at every time step. In a first run, after prescribing the motion of the domain boundaries, the principal stresses and strains resulting from the mesh deformation are computed locally using a uniform Young's modulus $\bar{E}$, from which the distortion energy density is derived. This scalar field will then be used in a second and definitive elastic

problem to modify Young's modulus at each element E:

$$E = \frac{\bar{E}}{12\,(1+\nu)}\left[(\epsilon_1-\epsilon_2)^2+(\epsilon_2-\epsilon_3)^2+(\epsilon_3-\epsilon_1)^2\right], \tag{2.30}$$

where ν is Poisson's ratio and ϵ_i are the principal strains at each element.

2.3.2 FWH analogy as a diffraction problem

The main goal now consists in showing how to extend the above splitting procedure to the case of flow noise generated in domains with moving walls. The previously presented Curle's analogy accounts for the contribution of rigid fixed walls. For moving or flexible surfaces one has to resort to the Ffowcs-Williams-Hawkings method (FWH) [178], which also departs from Lighthill's analogy and includes both dipolar and monopolar source terms in the form of surface integrals. The first one can be also found in [65], whereas the second describes sound generated by a pulsating displacement of air produced by a moving surface:

$$\begin{aligned} Hc_0^2\,(\rho-\rho_0) = {} & \frac{\partial^2}{\partial x_i \partial x_j}\int_{V(\Omega)}[T_{ij}]\,\frac{dV}{4\pi\mid \boldsymbol{x}-\boldsymbol{y}\mid} \\ & -\frac{\partial}{\partial x_i}\int_{S(\Omega)}\left[\rho v_i\,(v_i-\bar{v}_j)+p'_{ij}\right]\frac{dS_j\,(\boldsymbol{y})}{4\pi\mid \boldsymbol{x}-\boldsymbol{y}\mid} \\ & +\frac{\partial}{\partial t}\int_{S(\Omega)}\left[\rho v_i\,(v_i-\bar{v}_j)+\rho_0\bar{v}_j\right]\frac{dS_j\,(\boldsymbol{y})}{4\pi\mid \boldsymbol{x}-\boldsymbol{y}\mid}. \end{aligned} \tag{2.31}$$

If the surface $S\,(\Omega)$ is rigid, then $v_j=\bar{v}_j$ on $S\,(\Omega)$ and the terms can be rearranged as follows:

$$\begin{aligned} Hc_0^2\,(\rho-\rho_0) = {} & \frac{\partial^2}{\partial x_i \partial x_j}\int_{V(\Omega)}[T_{ij}]\,\frac{dV}{4\pi\mid \boldsymbol{x}-\boldsymbol{y}\mid}-\frac{\partial}{\partial x_i}\int_{S(\Omega)}\left[p'_{ij}\right]\frac{dS_j\,(\boldsymbol{y})}{4\pi\mid \boldsymbol{x}-\boldsymbol{y}\mid} \\ & +\frac{\partial}{\partial t}\int_{S(\Omega)}\left[\rho_0\bar{v}_j\right]\frac{dS_j\,(\boldsymbol{y})}{4\pi\mid \boldsymbol{x}-\boldsymbol{y}\mid}, \end{aligned} \tag{2.32}$$

where the first term corresponds to Lighthill's quadrupolar sources, the second one to the dipolar sources and the final one to the monopolar noise. Like in Curle's analogy, the problem can be separated into a free field Green's function (G) and a diffracted component (G_D), which now will include a monopolar term.

Once again, this methodology has the problem of Curle's when using an incompressible flow solver, which is not able to provide the acoustic pressure fluctuations on $S\,(\Omega)$. Therefore, the same strategy is applied to this case, but taking into account that it becomes no longer possible to resort to the

acoustic wave equation in irreducible form when dealing with acoustic waves propagating in moving domains. The linearized continuum and momentum conservation equations used to derive the latter need to be expressed in an ALE frame of reference, which precludes obtaining a scalar wave equation for the acoustic pressure [89]. One is then forced to work with the linearized momentum and continuity equations, sometimes referred to as the wave equation in mixed form (see e.g., [49]). This reads

$$\frac{1}{\rho_0 c_0^2}\partial_t p + \nabla \cdot \boldsymbol{u} = Q, \tag{2.33a}$$

$$\rho_0 \partial_t \boldsymbol{u} + \nabla p = \boldsymbol{f}, \tag{2.33b}$$

where p stands anew for the acoustic pressure while $\boldsymbol{u}$ represents the acoustic particle velocity. Q denotes a volume source distribution and $\boldsymbol{f}$ an external body force per unit volume.

To express (2.33) in an ALE domain one follows the same procedure applied to (2.29) obtaining

$$\frac{1}{\rho_0 c_0^2}\partial_t p - \frac{1}{\rho_0 c_0^2}\boldsymbol{u}_{\text{dom}} \cdot \nabla p + \nabla \cdot \boldsymbol{u} = Q, \tag{2.34a}$$

$$\rho_0 \partial_t \boldsymbol{u} - \rho_0 \boldsymbol{u}_{\text{dom}} \cdot \nabla \boldsymbol{u} + \nabla p = \boldsymbol{f}. \tag{2.34b}$$

The source terms corresponding to Lighthill's analogy and the acoustic filtered version in [155] are given by,

- Lighthill's analogy: $f_i = -\rho_0 \partial_j (u_i^0 u_j^0)$, $Q = 0$
- Filtered Lighthill: $\boldsymbol{f} = \boldsymbol{0}$, $Q = -(1/\rho_0 c_0^2)\left[\partial_t p^0 - \boldsymbol{u}_{\text{dom}} \cdot \nabla p^0\right]$

To solve (2.34) in a computational domain $\Omega_{ac}(t),\ t > 0$, we need to supplement the equation with appropriate boundary conditions and initial conditions. Assuming again a rigid body for simplicity we get,

$$\boldsymbol{u} \cdot \boldsymbol{n} = 0 \quad \text{on } \Gamma_b(t)\ \ t > 0 \tag{2.35a}$$

$$\boldsymbol{u} \cdot \boldsymbol{n} = \frac{1}{Z_0} p \quad \text{on } \Gamma_\infty\ \ t > 0 \tag{2.35b}$$

$$p\,(\boldsymbol{x}, 0) = 0\ \boldsymbol{u}\,(\boldsymbol{x}, 0) = \boldsymbol{0}, \quad \text{in } \Omega_{ac}(t),\ t = 0 \tag{2.35c}$$

where (2.35b) is the Sommerfeld radiation condition for the wave equation in mixed form (see e.g., [72]) and $Z_0 = \rho_0 c_0$.

2.3.3 Proposed methodology

We can next apply the splitting strategy into incident and diffracted fields for the ALE mixed wave equation (2.34). Notice that the general linear

operator $\mathcal{L}$ in (2.12) herein acts both on the acoustic pressure p and on the acoustic particle velocity $\boldsymbol{u}$. Taking $\boldsymbol{u} = \boldsymbol{u}_i + \boldsymbol{u}_d$ and $p = p_i + p_d$ in (2.34) we get the incident field problem

$$\frac{1}{\rho_0 c_0^2}\partial_t p_i - \frac{1}{\rho_0 c_0^2}\boldsymbol{u}_{\text{dom}} \cdot \nabla p_i + \nabla \cdot \boldsymbol{u}_i = Q \quad \text{in } \Omega_{ac}(t) \cup \Omega_b(t),\ t > 0, \tag{2.36a}$$

$$\rho_0 \partial_t \boldsymbol{u}_i - \rho_0 \boldsymbol{u}_{\text{dom}} \cdot \nabla \boldsymbol{u}_i + \nabla p_i = \boldsymbol{f} \quad \text{in } \Omega_{ac}(t) \cup \Omega_b(t),\ t > 0, \tag{2.36b}$$

$$\boldsymbol{u}_i \cdot \boldsymbol{n} = \frac{1}{Z_0} p_i \quad \text{on } \Gamma_\infty,\ t > 0, \tag{2.36c}$$

$$p_i(\boldsymbol{x}, 0) = 0,\ \boldsymbol{u}_i(\boldsymbol{x}, 0) = \boldsymbol{0}, \quad \text{in } \Omega_{ac}(t) \cup \Omega_b(t),\ t = 0, \tag{2.36d}$$

and the diffracted field one,

$$\frac{1}{\rho_0 c_0^2}\partial_t p_d - \frac{1}{\rho_0 c_0^2}\boldsymbol{u}_{\text{dom}} \cdot \nabla p_d + \nabla \cdot \boldsymbol{u}_d = 0 \quad \text{in } \Omega_{ac}(t),\ t > 0, \tag{2.37a}$$

$$\rho_0 \partial_t \boldsymbol{u}_d - \rho_0 \boldsymbol{u}_{\text{dom}} \cdot \nabla \boldsymbol{u}_d + \nabla p_d = \boldsymbol{0} \quad \text{in } \Omega_{ac}(t),\ t > 0, \tag{2.37b}$$

$$\boldsymbol{u}_d \cdot \boldsymbol{n} = -\boldsymbol{u}_i \cdot \boldsymbol{n} \quad \text{on } \Gamma_b(t),\ t > 0, \tag{2.37c}$$

$$\boldsymbol{u}_d \cdot \boldsymbol{n} = \frac{1}{Z_0} p_d \quad \text{on } \Gamma_\infty,\ t > 0, \tag{2.37d}$$

$$p_d(\boldsymbol{x}, 0) = 0,\ \boldsymbol{u}_d(\boldsymbol{x}, 0) = \boldsymbol{0}, \quad \text{in } \Omega_{ac}(t),\ t = 0. \tag{2.37e}$$

Our goal consists in solving equations (2.36) and (2.37) together with the Navier-Stokes equations (also in an ALE framework) to get the source terms, using a finite element approach.

2.3.4 Numerical discretization

Continuous weak form

The FEM discretization of equations (2.36) and (2.37) rely on their weak formulation rather than on the differential one. The continuous weak forms of the equations can be found multiplying equations (2.36a) and (2.37a) with a scalar test function q, and equations (2.36b) and (2.37b) with a vector test function $\boldsymbol{v}$, and then integrating over the respective computational domains $\Omega_{ac}(t) \cup \Omega_b(t)$ and $\Omega_{ac}(t)$. Assuming that we want to solve the problem in a given time interval $[0, T]$, the variational problems for the incident and diffracted acoustic pressure and velocity can be posed as follows.

First, find $p_i \in \mathcal{W}_p([0,T], \mathcal{V}_p)$ and $\boldsymbol{u}_i \in \boldsymbol{\mathcal{W}}_{\boldsymbol{u}}([0,T], \boldsymbol{\mathcal{V}}_{\boldsymbol{u}})$ such that

$$\frac{1}{\rho_0 c_0^2}(\partial_t p_i, q) - \frac{1}{\rho_0 c_0^2}(\boldsymbol{u}_{\text{dom}} \cdot \nabla p_i, q) + (\nabla \cdot \boldsymbol{u}_i, q) = (Q, q) \quad \forall\ q \in \mathcal{V}_p, \tag{2.38a}$$

$$\rho_0(\partial_t \boldsymbol{u}_i, \boldsymbol{v}) - \rho_0(\boldsymbol{u}_{\text{dom}} \cdot \nabla \boldsymbol{u}_i, \boldsymbol{v}) + (\nabla p_i, \boldsymbol{v}) = (\boldsymbol{f}, \boldsymbol{v}) \quad \forall\ \boldsymbol{v} \in \boldsymbol{\mathcal{V}}_{\boldsymbol{u}}, \tag{2.38b}$$

where $\mathcal{W}_p$, $\boldsymbol{\mathcal{W}}_{\boldsymbol{u}}$, $\mathcal{V}_p$ and $\boldsymbol{\mathcal{V}}_{\boldsymbol{u}}$ denote appropriate functional spaces not to be detailed herein (see e.g., [89] for more details). As for the diffracted fields we will have to find $p_d \in \mathcal{W}_p([0,T],\mathcal{V}_p)$ and $\boldsymbol{u}_d \in \boldsymbol{\mathcal{W}}_{\boldsymbol{u}}([0,T],\boldsymbol{\mathcal{V}}_{\boldsymbol{u}})$ such that

$$\frac{1}{\rho_0 c_0^2}(\partial_t p_d, q) - \frac{1}{\rho_0 c_0^2}(\boldsymbol{u}_{\text{dom}} \cdot \nabla p_d, q) + (\nabla \cdot \boldsymbol{u}_d, q) = 0 \quad \forall\, q \in \mathcal{V}_p, \tag{2.39a}$$

$$\rho_0(\partial_t \boldsymbol{u}_d, \boldsymbol{v}) - \rho_0(\boldsymbol{u}_{\text{dom}} \cdot \nabla \boldsymbol{u}_d, \boldsymbol{v}) + (\nabla p_d, \boldsymbol{v}) = \boldsymbol{0} \quad \forall\, \boldsymbol{v} \in \boldsymbol{\mathcal{V}}_{\boldsymbol{u}}. \tag{2.39b}$$

The Dirichlet boundary conditions (2.36c), (2.37c) and (2.37d) are to be imposed strongly on $\Gamma_b(t)$ and Γ_∞. Alternatively, one could integrate the terms $(\nabla\cdot\boldsymbol{u}_i, q)$ in (2.38a) and $(\nabla\cdot\boldsymbol{u}_d, q)$ in (2.39a) to impose the conditions weakly. The consequences of such an option are detailed in [13].

Finite element spatial discretization

The Galerkin FEM solution to variational mixed problems like (2.38) and (2.39) is known to exhibit strong oscillations if equal order interpolations are used for the pressure and velocities (see e.g., [49, 54, 89]). Moreover, the ALE frame of reference introduces a convective term which also needs to be stabilized. One could prevent them by resorting to stabilized FEM strategies like the variational multiscale method (VMM) in [113, 115]. In this work, orthogonal subgrid scales (OSS), see [46, 59], will be used to stabilize the Galerkin FEM approach to (2.38) and (2.39), following the strategy depicted in [89].

Let us consider the finite element spaces $\mathcal{V}_{p_h} \subset \mathcal{V}_p$ and $\boldsymbol{\mathcal{V}}_{\boldsymbol{u}_h} \subset \boldsymbol{\mathcal{V}}_{\boldsymbol{u}}$. The discrete stabilized FEM approach to the incident problem (2.38) consists in finding $p_{i_h} \in \mathcal{W}_p([0,T],\mathcal{V}_{p_h})$ and $\boldsymbol{u}_{i_h} \in \boldsymbol{\mathcal{W}}_{\boldsymbol{u}}([0,T],\boldsymbol{\mathcal{V}}_{\boldsymbol{u}_h})$ such that

$$\begin{aligned}
&\frac{1}{\rho_0 c_0^2}(\partial_t p_{i_h}, q_h) - \frac{1}{\rho_0 c_0^2}(\boldsymbol{u}_{\text{dom}} \cdot \nabla p_{i_h}, q_h) + (\nabla \cdot \boldsymbol{u}_{i_h}, q_h) \\
&+ \sum_{\Omega_{el}} (\tau_p \mathcal{P}\big[- \frac{1}{\rho_0 c_0^2}\boldsymbol{u}_{\text{dom}} \cdot \nabla p_{i_h} + \nabla \cdot \boldsymbol{u}_{i_h} - Q\big], \\
&- \frac{1}{\rho_0 c_0^2}\boldsymbol{u}_{\text{dom}} \cdot \nabla q_{i_h} + \nabla \cdot \boldsymbol{v}_h)_{\Omega_e(t^n)} = (Q^{n+1}, q_h),
\end{aligned} \tag{2.40a}$$

$$\begin{aligned}
&\rho_0(\partial_t \boldsymbol{u}_{i_h}, \boldsymbol{v}_h) - \rho_0(\boldsymbol{u}_{\text{dom}} \cdot \nabla \boldsymbol{u}_{i_h}, \boldsymbol{v}_h) + (\nabla p_{i_h}, \boldsymbol{v}_h) \\
&+ \sum_{\Omega_{el}} (\tau_{\boldsymbol{u}} \mathcal{P}\big[- \rho_0 \boldsymbol{u}_{\text{dom}} \cdot \nabla \boldsymbol{u}_{i_h} + \nabla p_{i_h} - \boldsymbol{f}\big], \\
&- \rho_0 \boldsymbol{u}_{\text{dom}} \cdot \nabla \boldsymbol{v}_h + \nabla q_h)_{\Omega_e(t^n)} = (\boldsymbol{f}, \boldsymbol{v}_h),
\end{aligned} \tag{2.40b}$$

for all $q_h \in \mathcal{V}_{p_h}$ and $\boldsymbol{v}_h \in \boldsymbol{\mathcal{V}}_{\boldsymbol{u}_h}$.

The first and fourth rows in the above equations contain the Galerkin FEM terms, whereas the second and fifth rows account for the stabilization

terms. $\mathcal{P}$ in (2.40) stands for a projection to be applied either to scalars or vectors depending on the argument. In the OSS method $\mathcal{P}$ it is computed as $\mathcal{P} = \boldsymbol{I} - \Pi_h$, with $\boldsymbol{I}$ being the identity and Π_h being the L^2-projection onto the corresponding finite element space. On the other hand, the following expressions can be obtained for the stabilization parameters τ_p and $\tau_{\boldsymbol{u}}$, (see [89])

$$\begin{aligned}\tau_{\boldsymbol{u}} &= \frac{h}{C_1\rho_0|\boldsymbol{u}_h| + \rho_0 c_0 C_2},\\ \tau_p &= \frac{\rho_0 c_0^2 h}{C_1|\boldsymbol{u}_h| + c_0 C_2},\end{aligned} \tag{2.41}$$

with C_1 and C_2 being constants to be determined from numerical experiments (a value of $C_1 = C_2 = 100$ was taken in [89]). Analogously, the discrete stabilized FEM approach to the diffraction problem (2.39) is that of finding $p_{d_h} \in \mathcal{W}_p([0,T], \mathcal{V}_{p_h})$ and $\boldsymbol{u}_{d_h} \in \boldsymbol{\mathcal{W}}_{\boldsymbol{u}}([0,T], \boldsymbol{\mathcal{V}}_{\boldsymbol{u}_h})$ such that

$$\begin{aligned}&\frac{1}{\rho_0 c_0^2}(\partial_t p_{d_h}, q_h) - \frac{1}{\rho_0 c_0^2}(\boldsymbol{u}_{\text{dom}} \cdot \nabla p_{d_h}, q_h) + (\nabla \cdot \boldsymbol{u}_{d_h}, q_h)\\ &+ \sum_{\Omega_{el}} (\tau_p \mathcal{P}\big[- \frac{1}{\rho_0 c_0^2}\boldsymbol{u}_{\text{dom}} \cdot \nabla p_{d_h} + \nabla \cdot \boldsymbol{u}_{d_h}\big], -\frac{1}{\rho_0 c_0^2}\boldsymbol{u}_{\text{dom}} \cdot \nabla q_h + \nabla \cdot \boldsymbol{v}_h)_{\Omega_e(t^n)}\\ &= 0,\end{aligned} \tag{2.42a}$$

$$\begin{aligned}&\rho_0(\partial_t \boldsymbol{u}_{d_h}, \boldsymbol{v}_h) - \rho_0(\boldsymbol{u}_{\text{dom}} \cdot \nabla \boldsymbol{u}_{d_h}, \boldsymbol{v}_h) + (\nabla p_{d_h}, \boldsymbol{v}_h)\\ &+ \sum_{\Omega_{el}} (\tau_{\boldsymbol{u}} \mathcal{P}\big[- \rho_0 \boldsymbol{u}_{\text{dom}} \cdot \nabla \boldsymbol{u}_{d_h} + \nabla p_{d_h}\big], -\rho_0 \boldsymbol{u}_{\text{dom}} \cdot \nabla \boldsymbol{v}_h + \nabla q_h)_{\Omega_e(t^n)} = \boldsymbol{0},\end{aligned} \tag{2.42b}$$

for all $q_h \in \mathcal{V}_{p_h}$ and $\boldsymbol{v}_h \in \boldsymbol{\mathcal{V}}_{\boldsymbol{u}_h}$.

Fully discrete numerical scheme

To get the final numerical scheme, we need to discretize equations (2.40) and (2.42) in time. We use again a second order backward differentiation formula (BDF2) to approximate the first order time derivative of $\boldsymbol{u}$ and p.

The time discrete version of the incident problem (2.40) then becomes

$$\begin{aligned}
&\frac{1}{\rho_0 c_0^2}(\delta_t p_{i_h}^{n+1}, q_h) - \frac{1}{\rho_0 c_0^2}(\boldsymbol{u}_{\text{dom}} \cdot \nabla p_{i_h}^{n+1}, q_h) + (\nabla \cdot \boldsymbol{u}_{i_h}^{n+1}, q_h) \\
&+ \sum_{\Omega_{el}} (\tau_p \mathcal{P}\big[- \frac{1}{\rho_0 c_0^2} \boldsymbol{u}_{\text{dom}} \cdot \nabla p_{i_h}^{n+1} + \nabla \cdot \boldsymbol{u}_{i_h}^{n+1} - Q^{n+1}\big], \\
&- \frac{1}{\rho_0 c_0^2} \boldsymbol{u}_{\text{dom}} \cdot \nabla q_h + \nabla \cdot \boldsymbol{v}_h)_{\Omega_e(t^n)} = (Q^{n+1}, q_h), \qquad (2.43a) \\
&\rho_0(\delta_t \boldsymbol{u}_{i_h}^{n+1}, \boldsymbol{v}_h) - \rho_0(\boldsymbol{u}_{\text{dom}} \cdot \nabla \boldsymbol{u}_{i_h}^{n+1}, \boldsymbol{v}_h) + (\nabla p_{i_h}^{n+1}, \boldsymbol{v}_h) \\
&+ \sum_{\Omega_{el}} (\tau_{\boldsymbol{u}} \mathcal{P}\big[- \rho_0 \boldsymbol{u}_{\text{dom}} \cdot \nabla \boldsymbol{u}_{i_h}^{n+1} + \nabla p_{i_h}^{n+1} - \boldsymbol{f}^{n+1}\big], \\
&- \rho_0 \boldsymbol{u}_{d_h}^{n+1} \cdot \nabla \boldsymbol{v}_h + \nabla q_h)_{\Omega_e(t^n)} = (\boldsymbol{f}^{n+1}, \boldsymbol{v}_h). \qquad (2.43b)
\end{aligned}$$

Note that $\mathcal{P}(\delta_t p_h) = 0$ and $\mathcal{P}(\delta_t \boldsymbol{u}_h) = 0$ in (2.43) because we are considering orthogonal subscales. Similarly, the time discrete version of the diffraction problem (2.42) is given by

$$\begin{aligned}
&\frac{1}{\rho_0 c_0^2}(\delta_t p_{d_h}^{n+1}, q_h) - \frac{1}{\rho_0 c_0^2}(\boldsymbol{u}_{\text{dom}} \cdot \nabla p_{d_h}^{n+1}, q_h) + (\nabla \cdot \boldsymbol{u}_{d_h}^{n+1}, q_h) \\
&+ \sum_{\Omega_{el}} (\tau_p \mathcal{P}\big[- \frac{1}{\rho_0 c_0^2} \boldsymbol{u}_{\text{dom}} \cdot \nabla p_{d_h}^{n+1} + \nabla \cdot \boldsymbol{u}_{d_h}^{n+1}\big], \\
&- \frac{1}{\rho_0 c_0^2} \boldsymbol{u}_{\text{dom}} \cdot \nabla q_h + \nabla \cdot \boldsymbol{v}_h)_{\Omega_e(t^n)} = 0, \qquad (2.44a) \\
&\rho_0(\delta_t \boldsymbol{u}_{d_h}^{n+1}, \boldsymbol{v}_h) - \rho_0(\boldsymbol{u}_{\text{dom}} \cdot \nabla \boldsymbol{u}_{d_h}^{n+1}, \boldsymbol{v}_h) + (\nabla p_{d_h}^{n+1}, \boldsymbol{v}_h) \\
&+ \sum_{\Omega_{el}} (\tau_{\boldsymbol{u}} \mathcal{P}\big[- \rho_0 \boldsymbol{u}_{\text{dom}} \cdot \nabla \boldsymbol{u}_{d_h}^{n+1} + \nabla p_{d_h}^{n+1}\big], - \rho_0 \boldsymbol{u}_{d_h}^{n+1} \cdot \nabla \boldsymbol{v}_h + \nabla q_h)_{\Omega_e(t^n)} \\
&= \boldsymbol{0}. \qquad (2.44b)
\end{aligned}$$

Finally, let us mention that the motion of the computational mesh in the numerical examples of the forthcoming sections has been driven through the solution of an elastic problem [39]. Though efficient remeshing strategies are currently available (see e.g., [146]), they can be avoided if the deformations are not very large, which saves a considerable amount of computational cost.

2.4 Numerical examples

2.4.1 Aeolian tones

To test the above proposed methodology we will first address the classical case of aeolian tones induced by flow vortex shedding past a cylinder. The

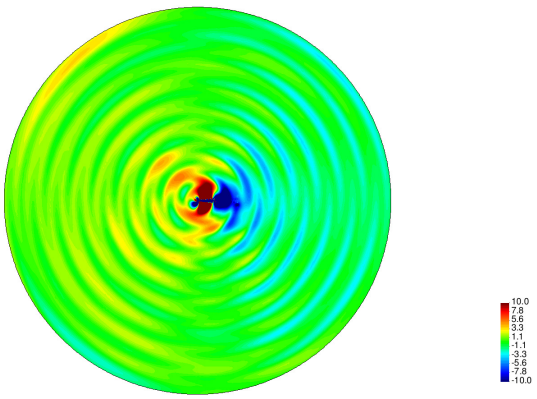

(a) Quadrupolar incident pressure

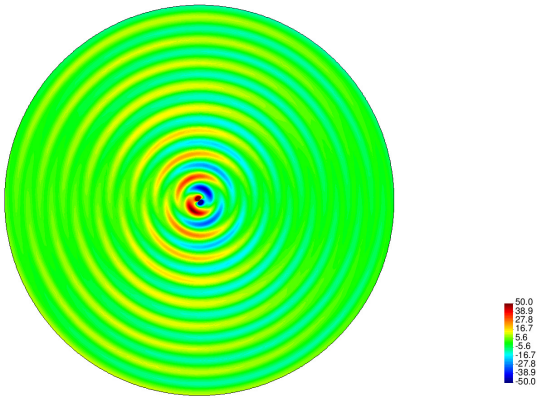

(b) Dipolar diffracted pressure

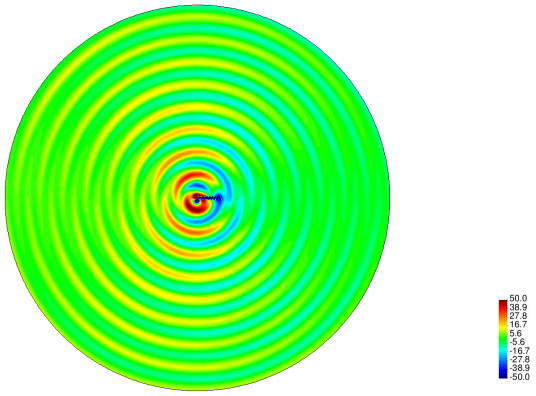

(c) Total acoustic pressure

Figure 2.2: Snapshots of the quadrupolar incident (a), dipolar diffracted (b) and total (c) acoustic pressure fields at time instant $t = 0.3$ s. The total pressure in (c) is obtained from the summation of the incident and diffracted pressure fields in (a) and (b). The colour scale has not been kept constant for better visualization of the weak quadrupolar radiation.

characteristic Reynolds number of the problem is $\mathrm{Re} = \rho_0 U^0 D/\mu$, with U^0 denoting the mean velocity impinging on the cylinder and D its diameter. As long as Re is increased from an almost zero value, a set of bifurcations take place until the flow past the cylinder becomes fully turbulent at high enough Reynolds numbers (see e.g., [68]). Our interest is on that range of Re where the flow first loses its steadiness and a set of periodic vortices form behind the cylinder, known as the Von Kármán vortex street. The vortices are shed at an approximate frequency of $f_{sh} = S_t U^0/D$, with S_t denoting the Strouhal number that slightly depends on Re as $S_t = 0.198(1 - 19.7/\mathrm{Re})$ (see e.g., [107]). The wake of vortices generate aerodynamic quadrupolar noise which is diffracted by the cylinder. The diffracted noise exhibits a strong dipolar character that clearly determines the acoustic pressure in the far field. The emitted sound has a dominant frequency of f_{sh}. Aeolian tones can be appreciated in practice when wind impinges power transmission lines and are also emitted, for instance, by train pantographs and tubular heat exchangers.

For the simulations we have considered a two-dimensional cylinder with diameter $D = 0.1$ m embedded in a circular acoustic computational domain Ω_{ac} that has a diameter of $D_{\Omega_{ac}} = 50$ m. An inner rectangular domain Ω_{NS} of dimensions 5 m $\times$ 10.4 m has been used for the CFD computation. An inlet flow velocity of $U^0 = 50$m/s has been prescribed in the horizontal direction on its Dirichlet boundary, which has resulted in a vortex shedding and emitted sound frequency of 120 Hz. We have considered a sound speed of $c_0 = 343$ m/s. The two-dimensional mesh for Ω_{NS} consists of 55.881 linear finite elements while 194.322 linear elements have been used for the acoustic domain Ω_{ac}. A time step of $\triangle t = 10^{-4}$ s has been chosen for the time evolution. The variational equations (2.15), (2.16) and (2.17) have been solved following the explanations in sections 3.2 and 3.3.

Representative snapshots at time instant $t = 0.3$ s of the generated acoustic pressure field have been plotted in Fig. 2.2. In Fig. 2.2a we present the incident acoustic pressure field generated by the vortex wake which exhibits a clear quadrupolar directivity pattern. We remind that this computation is done in $\Omega_{ac} \cup \Omega_b$ as if the cylinder was absent. The incident acoustic pressure is diffracted by the cylinder which emits aerodynamic sound with a dipole pattern. The colour scale in Fig. 2.2a has been set different from that in Fig. 2.2b to better observe the quadrupolar radiation. It is to be noted that the amplitude of the diffracted sound turns to be $\sim 6-7$ times stronger than the incident one, which is in accordance with the fact that the dipolar contribution is of order M^{-1} times the quadrupolar one (see e.g., [84]). In the present example the Mach number is $M \approx 0.146$.

The total acoustic field has been plotted in Fig. 2.2c. As observed, except for the area just past the cylinder, the results in Fig. 2.2c almost totally

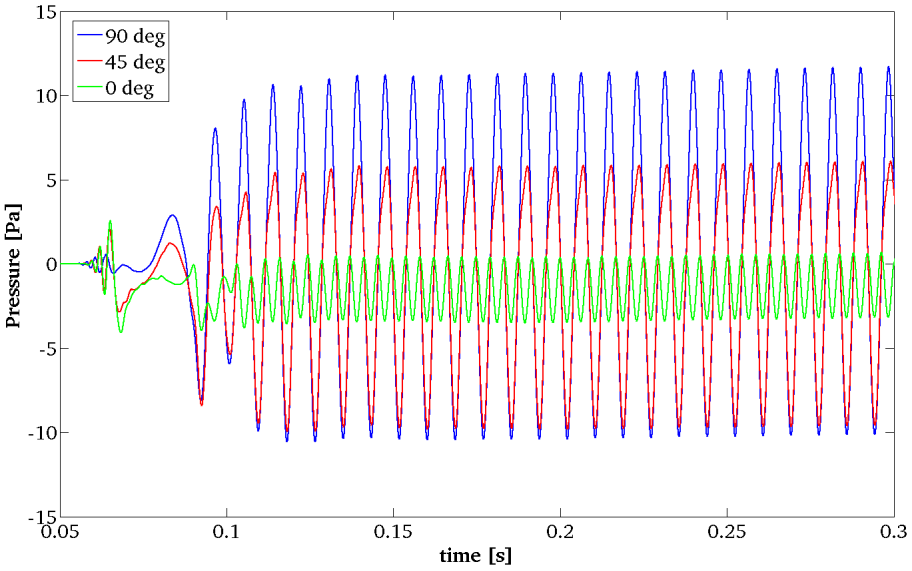

Figure 2.3: Evolution of the diffracted pressure at points $(20\ \text{m}, 0°)$, green line, $(20\ \text{m}, 45°)$, blue line and $(20\ \text{m}, 90°)$, red line.

match those in Fig. 2.2b confirming that the far field is governed by the dipolar diffracted noise. This can also be appreciated in Fig. 2.3, where we have plotted the acoustic pressure evolution at three points located at distances and angles $(20\ \text{m}, 0°)$, $(20\ \text{m}, 45°)$ and $(20\ \text{m}, 90°)$ from the center of the cylinder. The acoustic pressure takes its maximum amplitude at the axis perpendicular to the inlet inflow direction.

2.4.2 3D duct exit with sharp constraint

The second application case focuses on the validation of the presented method for a benchmark test employed for better understanding the aeroacoustics in the generation of the sibilant sound /s/. The test consists of a duct with a sharp edge obstacle stuck at the end, which may be roughly viewed as a very idealized representation of a vocal tract and the teeth [43]. When the flow passes through the gap left by the constriction a turbulent wake develops driven by a shedding frequency. This results in the generation of aerodynamic noise which becomes diffracted by the teeth. As it will be shown, it will be again this diffracted noise component the one that dominates the far field acoustics. The computational domain for both, the CFD and acoustic computations, consists of a three dimensional rectangular duct with dimensions $10.2\ \text{cm} \times 2.5\ \text{cm} \times 2.5\ \text{cm}$ and a hemisphere at its exit, 15 cm in radius, to account for outward acoustic wave propagation. The teeth is placed close to the duct exit leaving a gap of $0.15\ \text{cm} \times 2.5\ \text{cm}$ which corresponds to

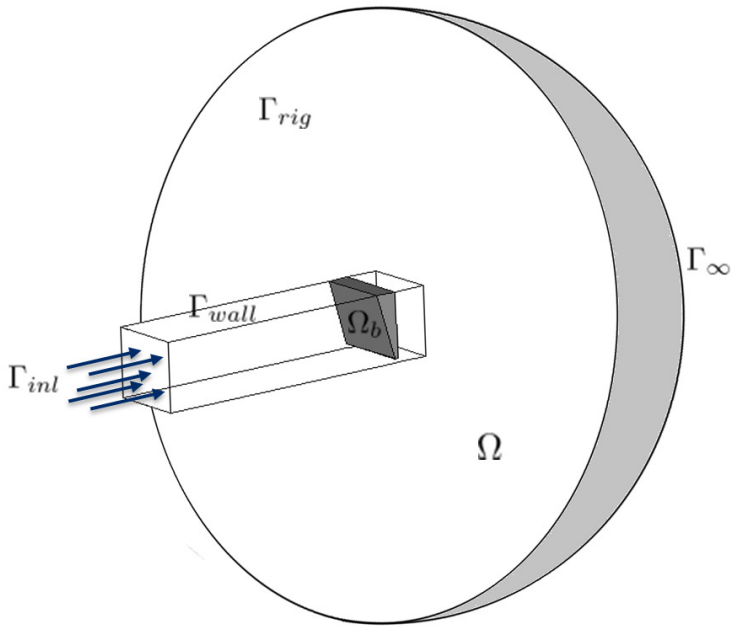

Figure 2.4: Sketch of the computational domain for the 3D duct with sharp constraint

6% of the duct section (see Fig. 2.4). The thickness of the edge of the teeth is 1.25 mm. As regards the CFD computation, an inlet velocity of $(2.4, 0, 0)^\top$ m/s is imposed for the air at the duct entrance whereas a no-slip boundary condition is prescribed on its walls. The Reynolds number according to the height of the teeth gap and the inlet velocity is $\mathrm{Re} = 300$. In what concerns the acoustic simulations, the duct walls have been assumed to be

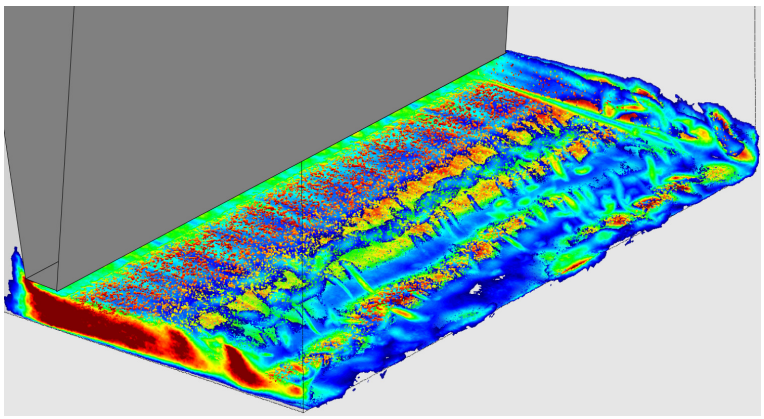

Figure 2.5: 3D isovorticity surfaces

rigid and a Sommerfeld boundary condition has been imposed at the outer surface of the hemisphere. The computational mesh is made of 42 550 677 P1/P1 finite elements with 6 798 782 nodes. A second order fractional step scheme has been used to solve the incompressible Navier Stokes equations, using a biconjugate gradient solver with a Hypre Pilut preconditioner for the velocity and a Trilinos ML one for the pressure. The later has been also used for the acoustic computations. In what refers the time discretization, a BDF3 scheme has been used for the CFD simulations and a BDF2 for the wave equation. The time step is given by $\Delta t = 2 \times 10^{-6}$s. The CFD has been first run for 1000 steps to surpass the initial transients without triggering the acoustic module. Both, CFD and acoustic results have been then computed from the subsequent 2 000 time steps. All simulations have been performed using 1024 processors of a PDC Beskow machine at the KTH (Kungliga Tekniska Högskolan) supercomputing center.

As a result of the CFD computation, and as mentioned above, a turbulent wake develops past the teeth with some dominating shedding frequencies, the most important one taking place at 6 kHz. In Fig. 2.5 we show a snapshot of the isovorticity surfaces of the flow just past the teeth where the formation of coherent vortex structures can be appreciated. In Figs. 2.6a and c, we respectively present a vertical cut (at $z = 0.0125$m) and a horizontal cut (at $y = 0.0032$m) for the velocity modulus, whereas the analogous ones for the aerodynamic pressure are given in Figs. 2.6b and d. All of them are plotted for $t = 0.006$s. In Fig. 2.7 we show the pressure spectrum E_{pp} in a log-log plot for a point located at the flow wake. According to Kolmogorov's theory, $E_{pp} \sim k^{-7/3}$, k being the wavenumber, and making use of the frozen-turbulence approximation (Taylor's hypothesis) it can be shown that the dependency with frequency also becomes $E_{pp} \sim f^{-7/3}$ (see e.g., [101, 147]). The slope $-7/3$ is plotted as a red line in Fig. 2.7. As it can be observed, the computed spectrum closely matches the Kolmogorov pressure spectrum prediction for fully developed isotropic turbulence. The generated aerodynamic sound results in acoustic waves propagating outside the duct exhibiting a spherical directivity pattern (see Fig. 2.8). In Fig. 2.10a and b we respectively plot the incident and diffracted acoustic pressure for the plane located at $y = 0.0032$m. The influence of the wake is apparent for the incident field whereas it is logically absent for the diffracted acoustic field. Again, we should remind that the incident acoustic field computation is carried out by removing the teeth from the computational domain. By the way, it is to be noted that Lighthill's source term becomes strongly concentrated at the wake past the teeth and quickly smears out when the flow leaves the duct (see Fig. 2.9).

One can easily check that it is the noise diffracted by the teeth the one that governs the acoustics at the far field, in accordance with theoretical

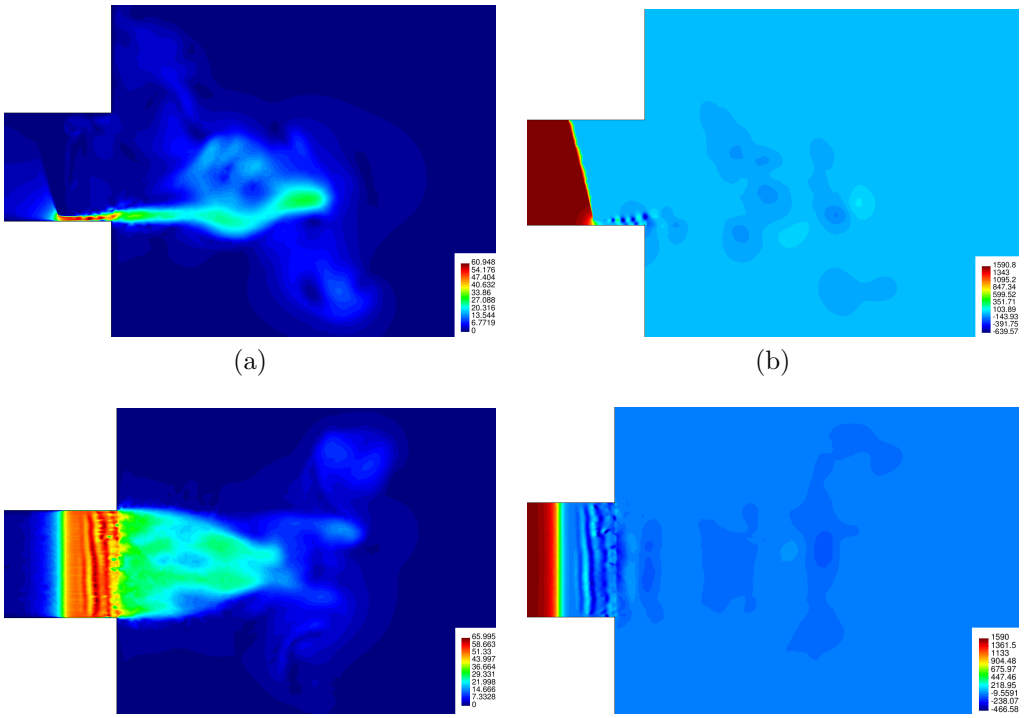

Figure 2.6: Velocity profile at $z = 0.0125$m (a), velocity profile at $y = 0.0032$m (b), pressure profile at $z = 0.0125$m (c) and pressure profile at $y = 0.0032$m (d) at t=0.006s.

models for sibilant sound production (see e.g., [106]). In Fig. 2.11a we have plotted a sample of the total, incident and diffracted time history for the acoustic pressure at a point located at the far field $((x, y, z)^\top)$. As observed, the diffracted component almost justifies the total acoustic pressure at this point. In Fig. 2.11b we present the Fourier transform for the incident and diffracted acoustic pressure evolution. The diffracted spectrum presents a clear peak at 6 kHz, corresponding to the dominant shedding frequency in the turbulent wake (see Fig. 2.7). This frequency determines the main oscillations observed in the diffracted and total pressure evolution in Fig. 2.11a. This result is in accordance with experimental data presented in [141], where several frequency spectra of the phoneme /s/ were recorded for different different languages, syllables, ages and gender. In this study, the peak can be found at $6.8 - 8$ kHz and the spectra are continuous and no characteristic frequencies can be identified, which is not the case of the present work because the simplified geometry is totally symmetric and regular. However, in both cases the main contribution to the sound generation takes place within the range of $2 - 10$ kHz.

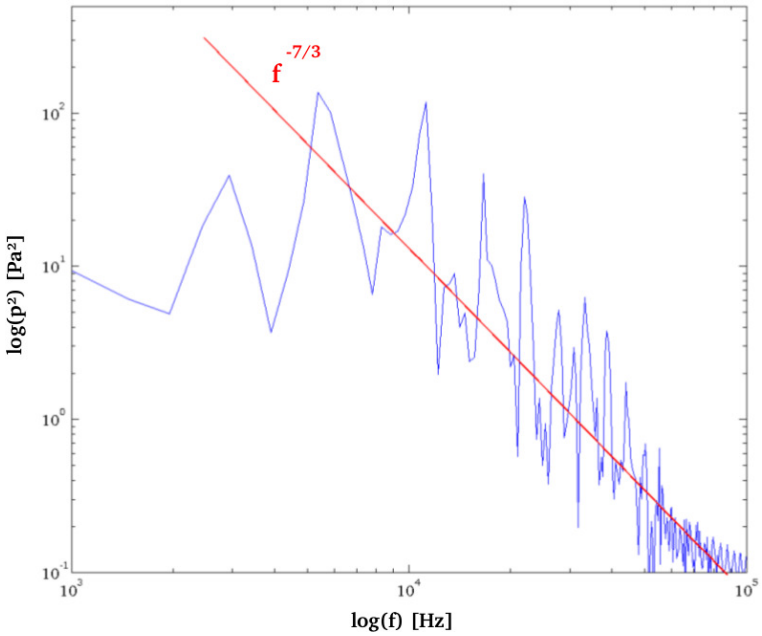

Figure 2.7: Point pressure spectrum E_{pp} in [Pa^2] versus frequency f in Hz.

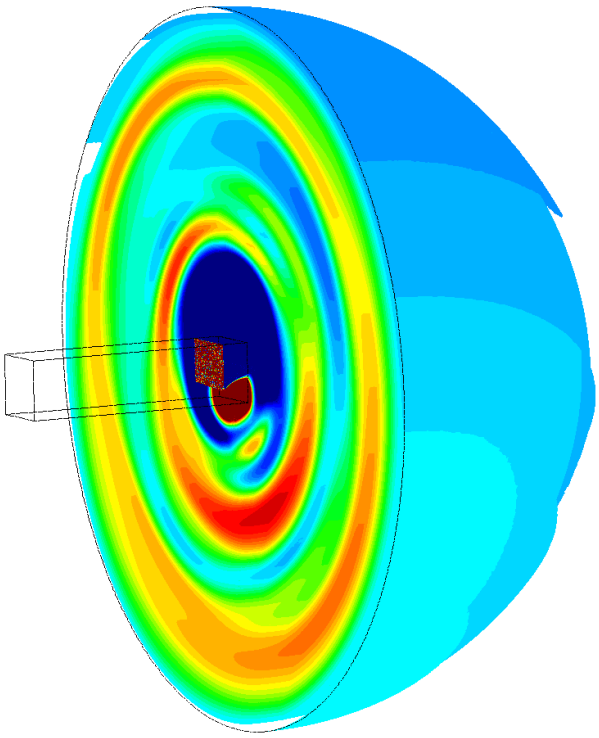

Figure 2.8: Total acoustic pressure front waves

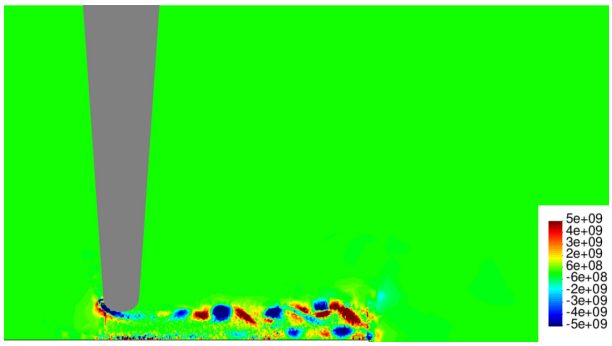

Figure 2.9: Lighthill source term $\rho_0 \partial_{ij}^2 (u_i^0 u_j^0)$ at plane $z = 0.0125$m.

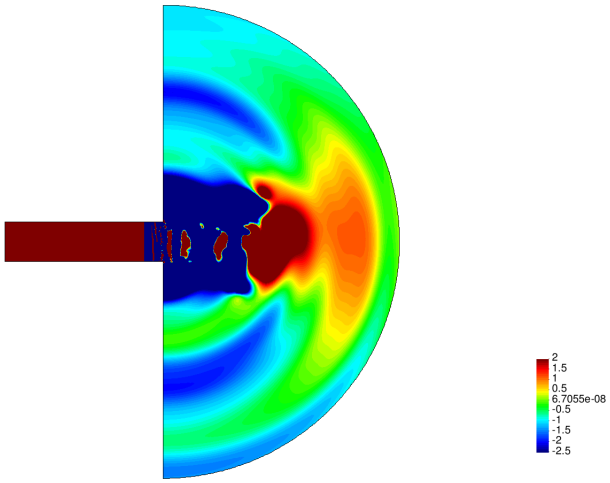

(a)

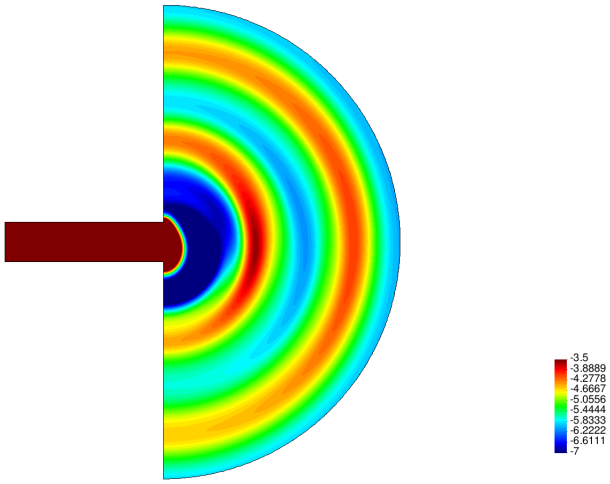

(b)

Figure 2.10: Incident acoustic pressure at $y = 0.0032$m (a) and diffracted acoustic pressure at $y = 0.0032$m (b) for t=0.006s.

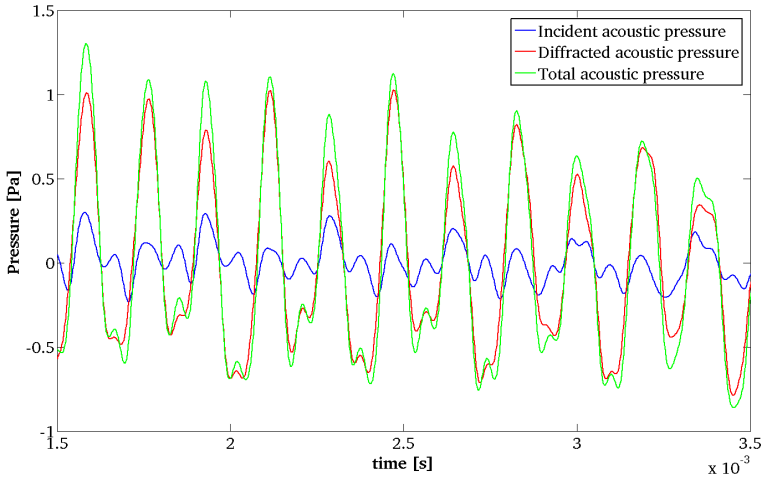

(a)

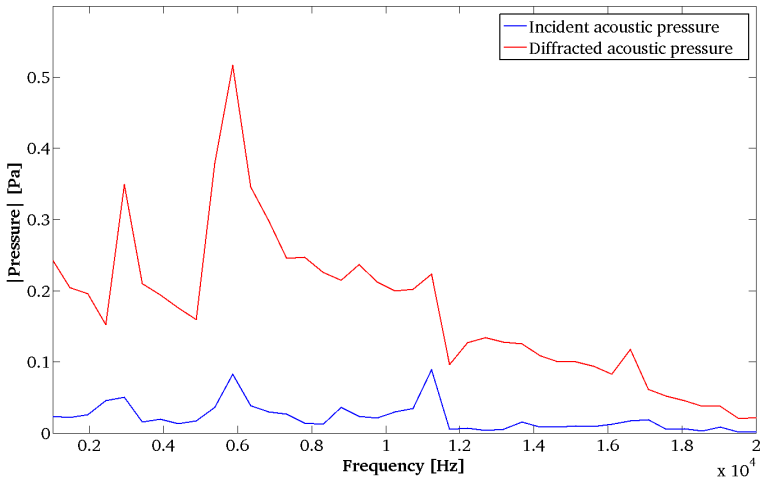

(b)

Figure 2.11: Time history for the total, incident and diffracted acoustic pressure at a far field point (a) and Fourier transform of the incident and diffracted acoustic components (b).

2.4.3 Aeroacoustics of an oscillating 2D NACA0012 airfoil. $\mathbf{M} = 0.1$

To demonstrate the extended splitting approach for domains with moving boundaries (see section 2.3), and to test as well the numerical proposal in section 4, we have considered a two-dimensional example of a flow around a NACA 0012 airfoil with an initial angle of attack of 5 degrees [179]. The flow Reynolds number based on the airfoil chord ($d = 0.1524$) is $\mathrm{Re}_c = 102,000$, whereas the incident Mach number is $\mathrm{M} = 0.1$. The problem has been solved in an unstructured mesh of nearly $600,000$ tetrahedral linear elements using

equal interpolation spaces for velocity and pressure, with a size of $4 \cdot 10^{-5}$ m on the airfoil surface (all units are in SI). The case has been run up to 0.045 s with a time step $\delta t = 10^{-5}$ s, departing from an initial incompressible solution in order to ease the initial convergence of the solver.

The airfoil rotates around the leading edge, which in turn corresponds to the origin of coordinates, with an angular frequency $\omega = 40$ rad/s. The consequent mesh deformation is calculated and minimized with the method presented in [39] and the grid motion is taken into account by the flow dynamics and the acoustics through the previously presented ALE formulations. At a first stage, the airfoil reaches the horizontal position and the first picture of the flow velocity and the two components of the acoustic pressure are obtained, see Figs. 2.12a, 2.13a and 2.14a. After that, the tail reaches its maximum height in see Figs. 2.12b, 2.13b and 2.14b, where it can be clearly observed that the boundary layer detaches earlier from the wall leading to an increase of the turbulent quadrupolar sound radiation (incident component). Finally, the airfoil passes through the original position until the tail reaches its minimum height in Figs. 2.12c, 2.13c and 2.14c. At that point, the profile has already suffered a considerable aerodynamic loss, for which the intensity of both components of the noise increase.

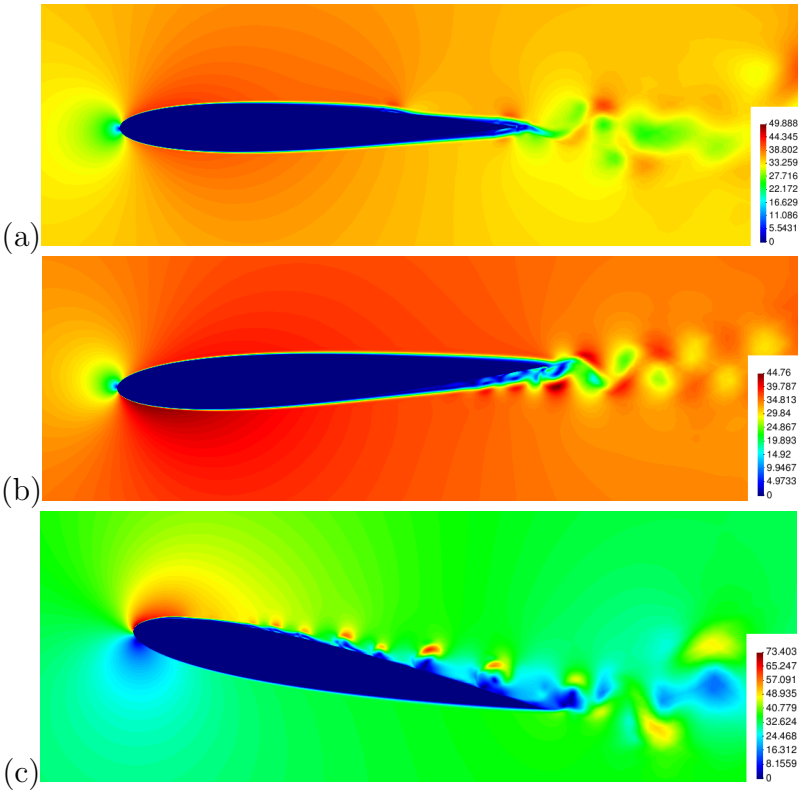

Figure 2.12: Velocity profiles at three different positions of the airfoil.

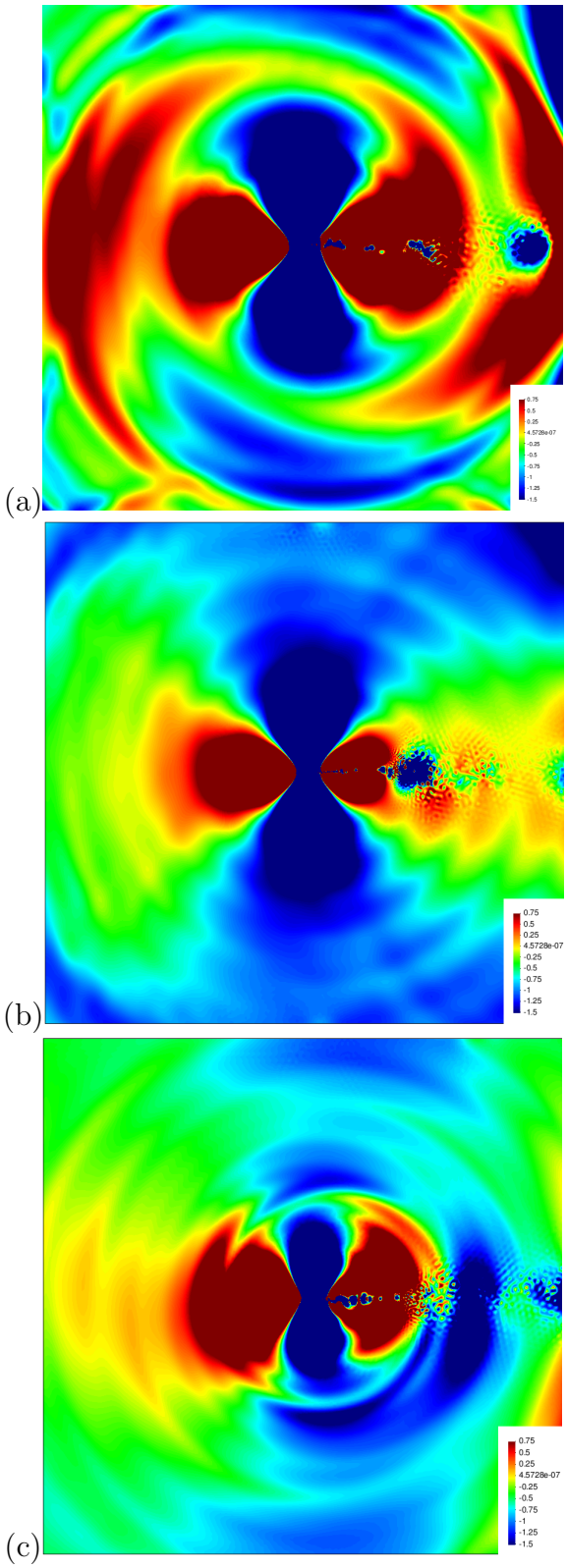

Figure 2.13: Incident acoustic pressure profiles at three different positions of the airfoil.

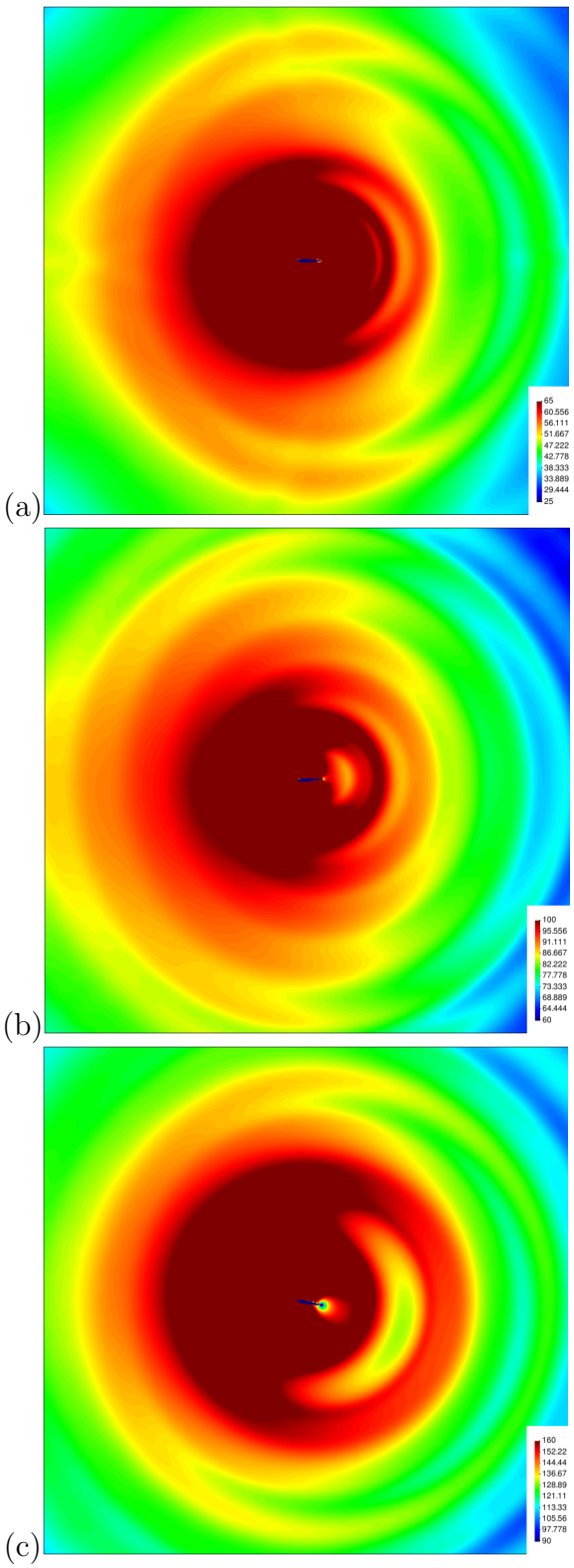

Figure 2.14: Diffracted acoustic pressure profiles at three different positions of the airfoil.

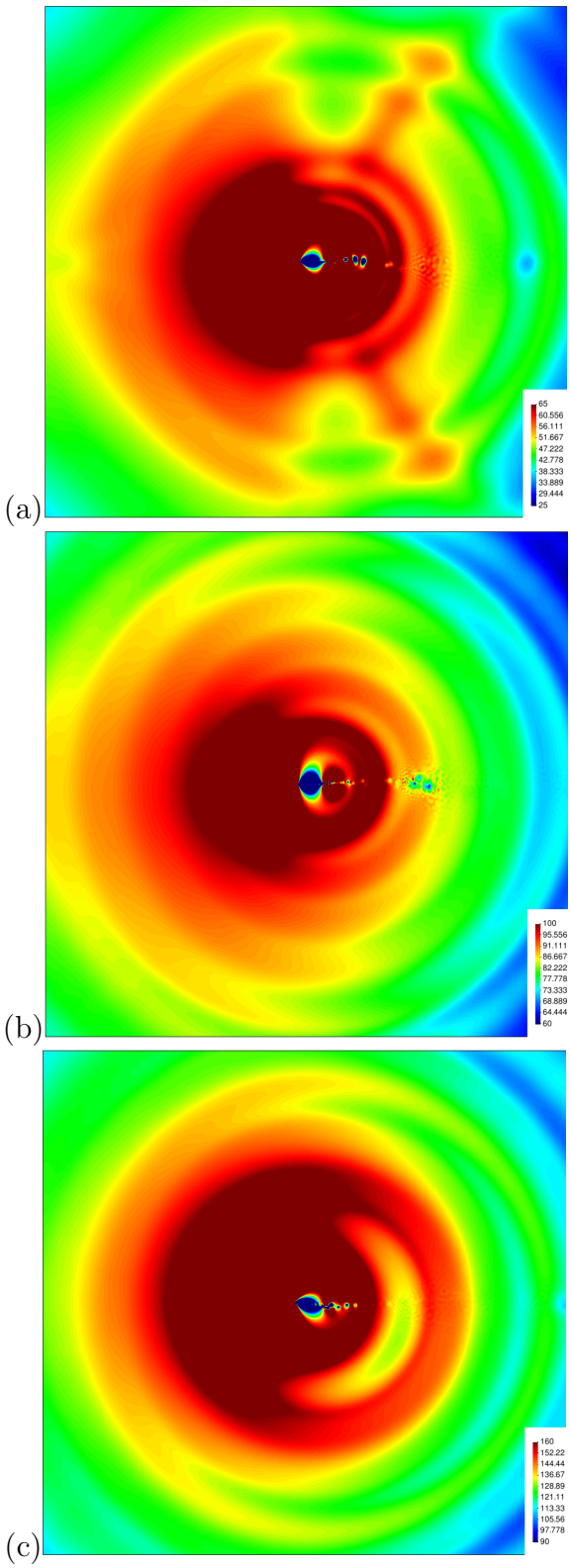

Figure 2.15: Total acoustic pressure profiles at three different positions of the airfoil.

One relevant aspect of the simulation is the continuous growth of the diffracted acoustic pressure and subsequently the total one, see Figs. 2.13 and Fig. 2.15. This is a numerical issue related to the acoustic pressure undetermination, since no Dirichlet boundary conditions are deployed in the acoustic problem. The side effect is an unclear visualization of the acoustic field due to the presence of a variable offset which does not allow a proper scaling of the propagation. As no satisfactory solution has been found within the numerical method, the time history of these two variables has been modified in a post-processing stage by computing a third order regression polynomial and subtracting the latter from the former. In this way, a clean oscillating signal has been obtained for a proper frequency analysis. For this purpose, four points at the far-field have been selected: $P1 = (-1.4, 0.0)^\top$, $P2 = (0.0, 1.4)^\top$, $P3 = (1.4, 0.0)^\top$ and $P4 = (0.0, -1.4)^\top$. The importance of satisfying the far-field condition lies on two facts: first, the hypothesis of flow at rest for a valid wave propagation using Lighthill's analogy, and second for proving the dominance of the diffracted acoustic pressure (dipolar source) over the turbulent noise (quadrupolar source). In this sense, Figs. 2.16, 2.17, 2.18, 2.19 show, like in the previous static cases, the expected result. For $P2$ and $P4$, which are placed on the perpendicular axis to the flow, there is a difference of approximately 30 dB between the two components along the whole frequency range. For $P1$, which is located upstream, the offset decreases for high frequencies, whereas for $P3$, which lies on the wake, the quadrupolar sources are relevant at low frequencies (large eddies).

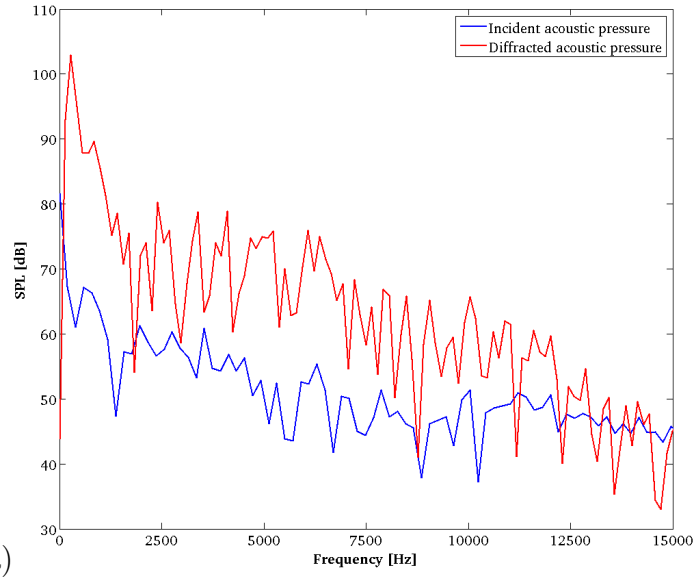

(a)

Figure 2.16: Incident and diffracted acoustic pressure frequency spectra at P1.

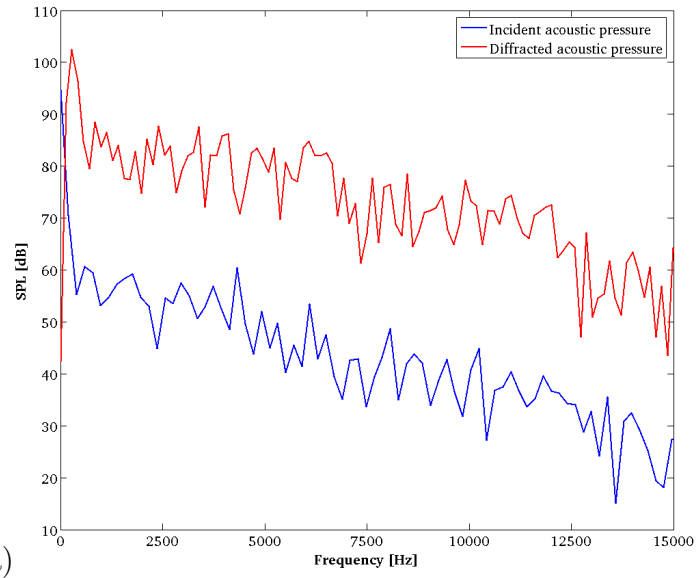

(a)

Figure 2.17: Incident and diffracted acoustic pressure frequency spectra at P2.

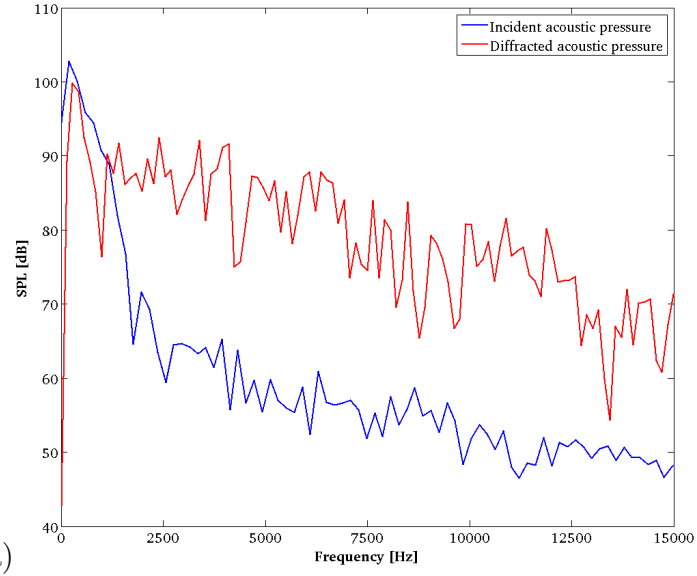

(a)

Figure 2.18: Incident and diffracted acoustic pressure frequency spectra at P3.

Next, Fig. 2.20 shows a time history of the total acoustic pressure at the four selected points and the corresponding frequency spectrum. The quantitative analysis and the subsequent validation of the results will be performed in Chapter 4, where the same case will be computed with the isentropic compressible formulation.

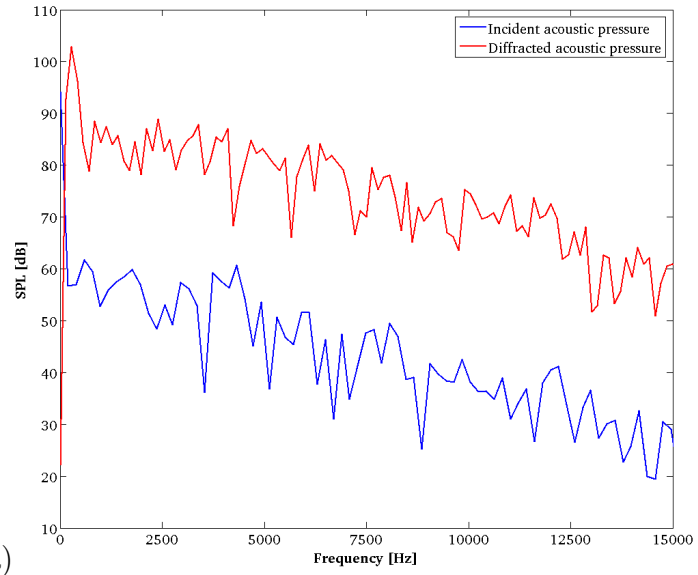

(a)

Figure 2.19: Incident and diffracted acoustic pressure frequency spectra at P4.

2.4.4 Aeroacoustics of a 2D opening teeth-shaped obstacle

The second example of application problem with acoustics in moving domains intends to show the degree of maturity of the formulation for simulating dynamic phonemes provided the proper biomechanical background. The application to diphthongs using glottal pulses as acoustic source instead of Lighthill's stress tensor has already been presented in [89]. Now the approach is extended with the inclusion of a CFD calculation for any syllable, which would allow the simulation of the sound /sa/. In fact, the present case aims for a schematic representation of this syllable. The domain motion is prescribed with a velocity ramp that opens the gap between incisors from 3 mm to a final distance of 18 mm, see Fig. 2.21. Since the analysis focuses on the contribution of the incisors along the whole simulation, the opening starts at $t = 0.03$ s, allowing the flow and the propagation to be fully developed. Then the opening takes place progressively until $t = 0.06$ s. Finally, the geometry is left open up to the end at $t = 0.09$ s for obtaining a new stationary state. For simplicity, the same flow configuration of 2.4.2 has been used with a time step $\delta t = 10^{-5}$ s. The initial occlusion causes a turbulent airjet which leads to the propagation of a wide range of frequencies and to a high level of noise, see Figs. 2.22a, 2.23a and 2.24a. At $t = 0.045$ the partial opening of the vocal tract has notably dissipated the airjet and decreased the sound intensity, Figs. 2.22b, 2.23b and 2.24b. It is important to remark that the incident component suffers a bigger loss

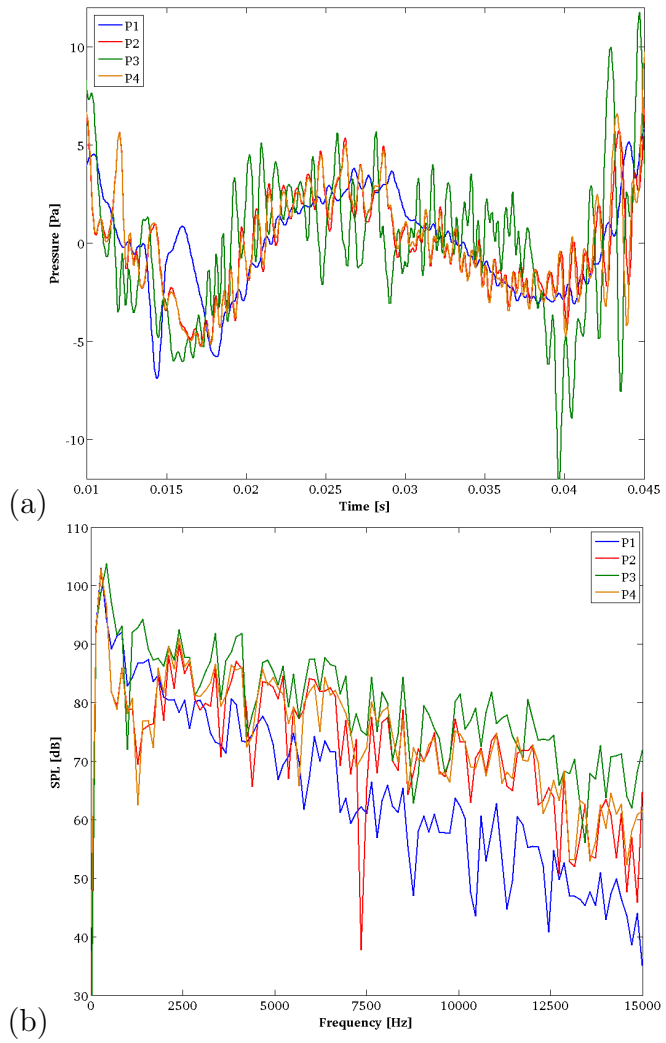

Figure 2.20: Total acoustic pressure time history (a) and frequency spectrum (b) at the four selected points.

than the diffracted one, since the quadrupolar sources are directly tied to the level of turbulence. Finally, at $t = 0.06$ and $t = 0.09$, which correspond to the final open position, the flow has become laminar except for some old vortices which still feed the incident component of the acoustic pressure at a very low level, see Figs. 2.22c, 2.23c,d and 2.24c,d. On the other hand, the diffracted component does not capture any propagation during this stage.

In order to evaluate the evolution and contribution of both acoustic pressure components, the time history of a point placed at the upper left corner of the outer domain is presented, see Fig 2.25. Unlike the airfoil case, where the far-field conditions are clearly met, the present case does not show a clear dominance of the dipolar sources over the quadrupolar ones, mainly due to

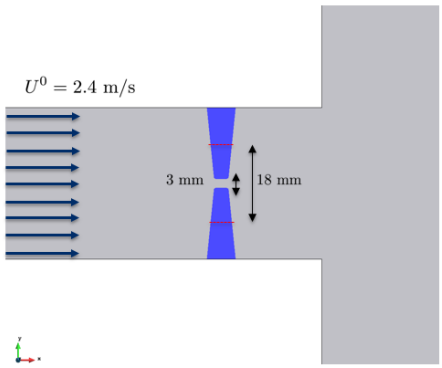

Figure 2.21: Scheme of the computational domain close to the duct exit. The obstacle evolves from minimum to maximum opening.

the small size of the domain. Another important difference that can explain this fact is the confined character of this flow, which leads to the generation of secondary vortices. Translated to the acoustics of the problem, it means new sources of quadrupolar noise for the incident component. Once again, the diffracted component is affected by the numerical issue of the evolving offset.

2.5 Conclusions

This chapter suggests a methodology to obtain the turbulent quadrupolar contribution to aerodynamic flow noise, as well as the dipolar one due to the influence of rigid body surfaces, as a direct output of a single finite element computational run. To that purpose use is made of Lighthill's acoustic analogy, although as shown, the procedure can be extended to any other acoustic linear wave operator and acoustic source term. Instead of directly solving the wave equation for the acoustic pressure, the latter becomes split into an incident component, due to flow motion, plus a diffracted one, due to the presence of bodies within the flow. At each time step of the simulation, the incompressible Navier-Stokes equations are solved and an approximation to Lighthill's tensor is derived from them. This source term is inserted in a wave equation for the incident pressure that is solved as if the rigid body was absent for that time step. This provides the quadrupolar flow noise contribution. The value of the incident pressure at the boundary of the rigid body is then used to compute the dipolar acoustic pressure contribution due to the body's diffraction. The proposed approach avoids the problem of the standard Curle formulation for low Mach number aeroacoustics, of knowing the acoustic pressure fluctuations in the surface integral, not just

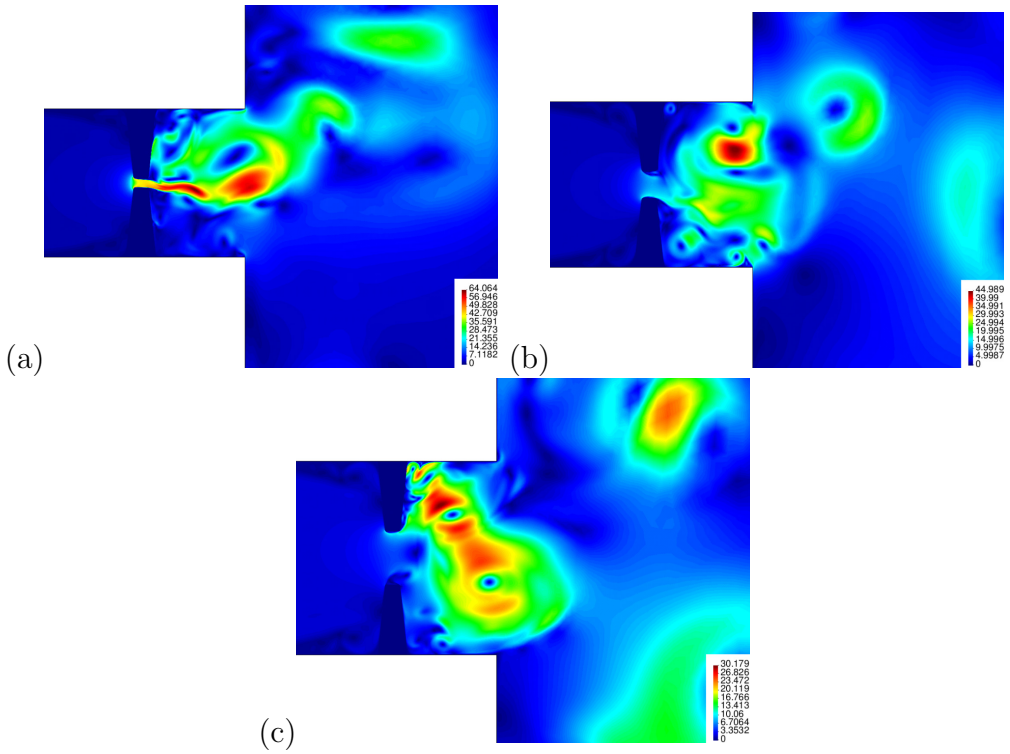

Figure 2.22: Evolution of the flow velocity: $t = 0.03$ (a), $t = 0.045$ (b), $t = 0.06$ (c).

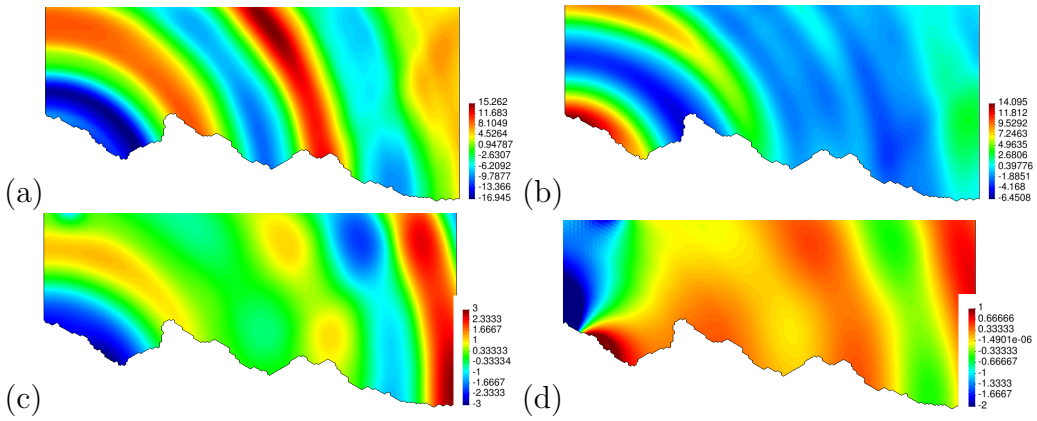

Figure 2.23: Evolution of the incident component of the acoustic pressure: $t = 0.03$ (a), $t = 0.045$ (b), $t = 0.06$ (c), $t = 0.09$ (d).

the incompressible pressure that could stem from an incompressible CFD simulation.

The extension to moving domains has also been derived departing from the stabilized mixed wave equation in an ALE reference presented in [89]. In spite of the considerable complexity jump respect to the fixed version, the

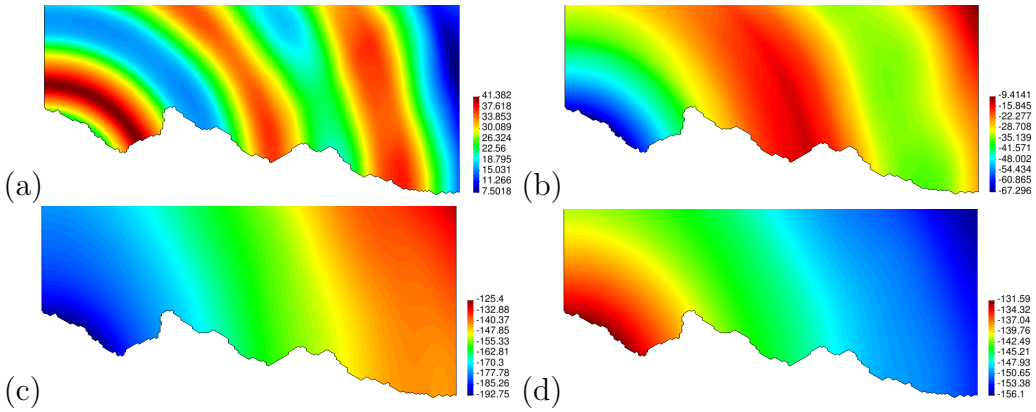

Figure 2.24: Evolution of the diffracted component of the acoustic pressure: $t = 0.03$ (a), $t = 0.045$ (b), $t = 0.06$ (c), $t = 0.09$ (d).

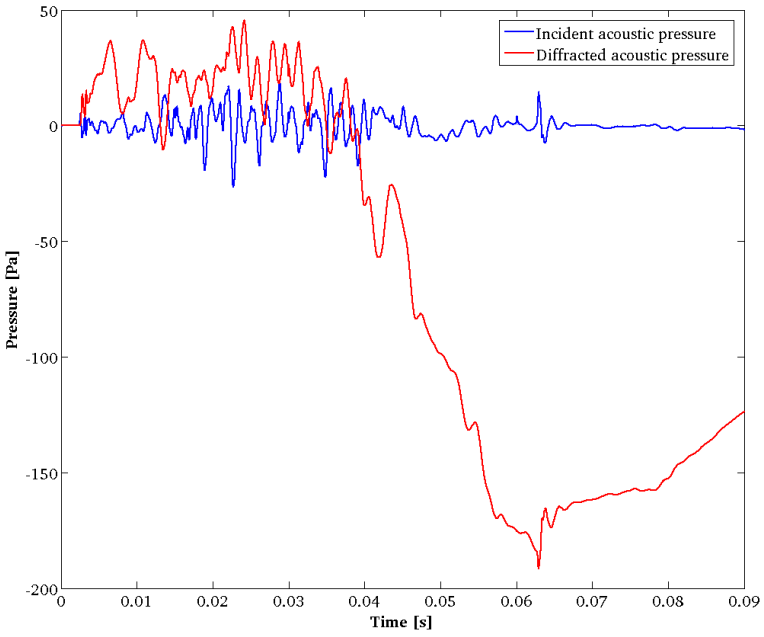

Figure 2.25: Time history of the incident and diffracted components of the acoustic pressure at the far-field.

method has been able to simulate complex scenarios and could be used in more complex dynamic phonation cases provided the availability of realistic geometries and deformation mappings.

Chapter 3

Residual-based stabilization of the finite element approximation to the acoustic perturbation equations for low Mach number aeroacoustics

The acoustic perturbation equations (APE) are suitable to predict aerodynamic noise in the presence of a non-uniform mean flow. As for any hybrid computational aeroacoustics approach, a first computational fluid dynamics simulation is carried out from which the mean flow characteristics and acoustic sources are obtained. In a second step, the APE are solved to get the acoustic pressure and particle velocity fields. However, resorting to the finite element method (FEM) for that purpose is not straightforward. Whereas mixed finite elements satisfying an appropriate inf-sup compatibility condition can be built in the case of no mean flow, i.e., for the standard wave equation in mixed form, these are difficult to implement and their good performance is yet to be checked for more complex wave operators. As a consequence, strong simplifying assumptions are usually considered when solving the APE with FEM. It is possible to avoid them by resorting to stabilized formulations. In this work, a residual-based stabilized FEM is presented for the APE at low Mach numbers, which allows one to deal with the APE convective and reaction terms in its full extent. The key of the approach resides in the design of the matrix of stabilization parameters. The performance of the formulation and the contributions of the different terms in the equations are tested for an acoustic pulse propagating in sheared solenoidal and non-solenoidal mean flows, and for the aeolian tone generated by flow past a two-dimensional cylinder.

3.1 Background

In this work, a stabilized finite element method (FEM) is proposed to solve the acoustic perturbation equations (APE). These equations can account for aerodynamic sound propagation in areas with non-uniform mean flow. In particular, we will herein focus on the low Mach number APE in [73], which are derived after source filtering the linearized Euler equations (LEE) to get rid of the vorticity and entropy modes, while leaving the acoustic ones.

The APE constitute a particular case of the so called hybrid methods in computational aeroacoustics (CAA). These separate the computation of aerodynamic sound into two steps. In the first one, a computational fluid dynamics (CFD) simulation is carried out to obtain the acoustic source terms from the aerodynamic velocity and pressure fields. In the second one, the source terms are input into an acoustic wave operator. The latter can directly be, for example, the standard linear wave equation in irreducible or mixed form, their convective counterparts, or more complex operators like the ones involved in the LEE.

The best known hybrid approaches are those in the category of acoustic analogies, being Lighthill's the most celebrated one [130]. Lighthill's analogy states the problem of aerodynamic sound radiation into a quiescent medium as that of noise radiated by a distribution of quadrupoles in free space. For low Mach number flows, Lighthill approximates the source of sound by the double divergence of the Reynolds tensor, which is built from the products of the components of the aerodynamic velocity vector. Other analogies place their emphasis on the role of vorticity in the generation of sound [148, 105, 139]. Besides, it should be remarked that the influence of rigid bodies within the flow on noise radiation was considered since the birth of acoustic analogies (see [65]) and later generalized to flexible bodies in [178].

As long as one aims to compute aerodynamic sound propagation in non-quiescent flow areas, convective and refraction effects have to be extracted from the acoustic source term and included in the wave operator (see e.g., [17]). This led to the development of more sophisticated analogies (see e.g., [131, 85]) and to alternatives such as the linearized Euler equations [16], or resorting to perturbation equations [73, 161]. As mentioned above, in this work we will attempt at solving the low Mach number formulation of the APE in [73] using FEM. Refraction effects will be neglected for simplicity.

The computation of aerodynamic sound in the second step of a hybrid CAA approach is often performed by resorting to integral formulations, though FEM is also common if the acoustic waves are to be computed at distances not too far from the source region. Most aeroacoustic FEM works

to date have dealt with Lighthill's acoustic analogy, [143, 92, 124, 15], yet convection effects have also been taken into account. In [91] the convective Helmholtz equation flow was considered, while a mixed convection wave equation with uniform mean flow was considered in [111] as a simplification of the APE in [73].

The numerical difficulties associated to the FEM solution of the various wave operators involved in CAA are of a very different nature. Whereas for the standard linear wave equation for the acoustic pressure most efforts are placed on the time discretization schemes, given that the spatial discretization presents no serious difficulties (the Laplacian is a well-behaved operator), this is not the case for its Fourier transform, the Helmholtz equation. The latter may become non-positive definite for large wavenumbers and the standard Galerkin FEM approach fails to solve it. A large amount of stabilization strategies have been devised to prevent the pollution error associated to the Helmholtz equation [98]. With regard to mixed formulations like the APE, which involve both, the acoustic pressure and the acoustic particle velocity, the situation gets more intricate. In the case of no convection the APE simply reduces to the wave equation in mixed form. The variational formulation of the latter has to satisfy a compatibility inf-sup condition for the problem to be well posed, which is not inherited by the standard Galerkin FEM approach to it. It therefore becomes necessary to work with finite elements having different interpolations for the acoustic pressure and velocity fields to avoid the appearance of spurious oscillations in the numerical solution [23, 24, 25]. An alternative to circumvent the discrete inf-sup condition and consider the same interpolation fields for the acoustic pressure and velocity is that of resorting to stabilization strategies, such as the residual based multiscale methods [113, 115, 46]. These were applied to the mixed wave equation in [49]. It was proved in [13] that the solution to the problem is then bounded by the data in an energy norm that involves all additional stabilization terms.

The situation worsens when one considers the presence of a mean flow. As far as the authors know, it has not been checked yet whether the tailored finite elements for the mixed wave equation could perform well in the presence of convection. Even if this was the case, their implementation is not an easy task. Stabilized FEM offer a way out to these problems. A first simplification to the APE is that of assuming a uniform mean flow so that they reduce to the convective mixed wave equation. As previously commented, this occurrence was addressed in [111], where a stabilizing flux term (as in the discontinuous Galerkin method) and a penalization term were incorporated in the formulation. However, in the case of a non-uniform mean flow, not only the convective terms in the APE become more complex, but one also has to deal with a reaction term. With regard to the former, analogous

non-uniform convective terms appear in the linearized modified Boussinesq equation for shallow waters. The Galerkin FEM approach to it exhibits high frequency oscillations [129, 134] that can be overcome by resorting to stabilization strategies [100, 54]. The same type of instabilities are found when setting the wave equation in mixed form in an arbitrary Lagrangian-Eulerian (ALE) frame of reference, to deal with wave propagation in moving domains [89].

In this chapter, a residual-based stabilized FEM will be proposed to solve the APE equations that include the effects of the non-uniform convection and of the reaction term due to the mean velocity gradient. This stabilization strategy relies on splitting the problem unknowns into large scales that can be resolved by the computational mesh, and small scales whose effects onto the large scales have to be modelled. The key for the good performance of the method depends upon the design of a proper matrix of stabilization parameters, which can be achieved through a Fourier analysis of the subscale equation [49, 54, 89].

The chapter is organized as follows. In section 2, we disclose the APE equations, set them in matrix form and work out their variational formulation. In section 3, we proceed to discretization. The residual-based stabilized FEM approach is presented and the derivation of the matrix of stabilization parameters is exposed in detail. The fully discretized numerical scheme in time and space close the section. Three numerical examples are finally given in section 4. These consist of three benchmark tests dealing with the wave-front propagation in solenoidal sheared mean flows and in non-solenoidal shear mean flows, and with the generation of an aeolian tone by flow past a two-dimensional cylinder.

3.2 Problem statement

3.2.1 An acoustic perturbation equation for low Mach numbers

Our starting point will be the acoustic perturbation equations (53)-(55) derived in [73], in the particular case of only considering vortex sound for low Mach numbers and neglecting the linear coupling between acoustic and vorticity modes. These equations read

$$\partial_t \rho' + \nabla \cdot (\rho' \bar{\boldsymbol{u}} + \bar{\rho} \boldsymbol{u}^a) = 0, \tag{3.1a}$$

$$\partial_t \boldsymbol{u}^a + \nabla(\bar{\boldsymbol{u}} \cdot \boldsymbol{u}^a) + \nabla\Big(\frac{p^a}{\bar{\rho}}\Big) = \boldsymbol{0}, \tag{3.1b}$$

$$\partial_t p^a - \bar{c}^2 \partial_t \rho' = -\partial_t p^h, \tag{3.1c}$$

and are obtained from manipulation of the linearized Euler equations for the enthalpy and velocity fields (the reader is referred to [73] for details). ∂_t stands for the first order time derivative and $\bar{c}$ denotes the speed of sound. The above equations are based on the following decompositions for the compressible velocity $\boldsymbol{u}$, pressure p and density ρ,

$$\boldsymbol{u} = \bar{\boldsymbol{u}} + \boldsymbol{u}' \quad \text{with} \quad \boldsymbol{u}' := \boldsymbol{u}^h + \boldsymbol{u}^a, \tag{3.2a}$$

$$p = \bar{p} + p' \quad \text{with} \quad p' := p^h + p^a, \tag{3.2b}$$

$$\rho = \bar{\rho} + \rho' \quad \text{with} \quad \rho' := \rho^h + \rho^a. \tag{3.2c}$$

In (3.1)-(3.2) an overbar indicates a time averaged mean quantity i.e., $\overline{g(\boldsymbol{x})} := \lim_{T\to\infty}(1/T)\int_{t_0}^{t_0+T} g(\boldsymbol{x},t)dt$, with t_0 standing for the initial time of the averaging process and T for its total duration. The mean values are independent of t_0 once the initial transients of a simulation/measurement have been surpassed. Likewise, a prime $g(\boldsymbol{x},t)'$ denotes a perturbation from the mean value. The velocity fluctuation $\boldsymbol{u}'$ in (3.2a) becomes split into two components, a hydrodynamic solenoidal perturbation $\boldsymbol{u}^h$ and an irrotational acoustic perturbation $\boldsymbol{u}^a$. Similarly, the pressure and density fluctuations p' and ρ' in (3.2b)-(3.2c) consist of two terms, a hydrodynamic component p^h and ρ^h responsible for the production of pseudo-sound, and an acoustic component p^a and ρ^a that will propagate as acoustic waves outwards the source region.

Equation (3.1) can be further simplified if we neglect sound refraction by assuming that neither the time averaged sound speed nor the time averaged density have a spatial dependence, i.e., $\bar{c} \equiv c_0$ and $\bar{\rho} \equiv \rho_0$. Assuming $p' = c_0^2\rho'$, this allows one to express (3.1) solely in terms of the velocity and pressure variables

$$\frac{1}{\rho_0 c_0^2}\partial_t p^a + \frac{1}{\rho_0 c_0^2}\,\bar{\boldsymbol{u}}\cdot\nabla p^a + \nabla\cdot\boldsymbol{u}^a + \frac{1}{\rho_0 c_0^2}\,p^a\nabla\cdot\bar{\boldsymbol{u}} = -\frac{1}{\rho_0 c_0^2}\partial_t p^h - \frac{1}{\rho_0 c_0^2}\bar{\boldsymbol{u}}\cdot\nabla p^h - \frac{1}{\rho_0 c_0^2}p^h\nabla\cdot\bar{\boldsymbol{u}} =: Q, \tag{3.3a}$$

$$\rho_0\partial_t\boldsymbol{u}^a + \rho_0\,\bar{\boldsymbol{u}}\cdot\nabla\boldsymbol{u}^a + \nabla p^a + \rho_0\,\boldsymbol{u}^a\cdot\nabla\bar{\boldsymbol{u}} = \boldsymbol{0}. \tag{3.3b}$$

In the event that $\bar{\boldsymbol{u}}$ and p^h are obtained from a previous computational fluid dynamics (CFD) simulation, (3.3) will provide the solution for the acoustic field taking into account the convection of acoustic disturbances by the mean flow. Given that we are dealing with low Mach numbers, we can resort to an incompressible CFD simulation to do so, so that $\bar{\boldsymbol{u}} \equiv \bar{\boldsymbol{u}}_{\text{inc}}$ and $p^h \equiv p^h_{\text{inc}} = p_{\text{inc}} - \bar{p}_{\text{inc}}$, subscript inc standing for incompressible. In such

situation we get $\nabla \cdot \bar{\boldsymbol{u}}_{\text{inc}} = 0$ and (3.3) further simplifies to

$$\frac{1}{\rho_0 c_0^2}\partial_t p^a + \frac{1}{\rho_0 c_0^2}\ \bar{\boldsymbol{u}}_{\text{inc}} \cdot \nabla p^a + \nabla \cdot \boldsymbol{u}^a = -\frac{1}{\rho_0 c_0^2}\partial_t p_i^h - \frac{1}{\rho_0 c_0^2}\bar{\boldsymbol{u}}_{\text{inc}} \cdot \nabla p_i^h, \quad (3.4a)$$

$$\rho_0 \partial_t \boldsymbol{u}^a + \rho_0\ \bar{\boldsymbol{u}}_{\text{inc}} \cdot \nabla \boldsymbol{u}^a + \nabla p^a + \rho_0\ \boldsymbol{u}^a \cdot \nabla \bar{\boldsymbol{u}}_{\text{inc}} = \boldsymbol{0}. \quad (3.4b)$$

3.2.2 Differential matrix problem and variational formulation

It is possible to rewrite equations (3.3a) and (3.3b) in matrix form for convenience as

$$\boldsymbol{\mu}\partial_t \boldsymbol{u} + \boldsymbol{A}_i \partial_i \boldsymbol{u} + \boldsymbol{S}\boldsymbol{u} = \boldsymbol{F}, \quad (3.5)$$

where the summation convention over repeated indexes is assumed hereinafter. The index i will run from 1 to the number of spatial dimensions with ∂_i standing for the first order spatial derivatives. The following vector and matrix identifications have been made

$$\boldsymbol{u} = \begin{pmatrix} p^a \\ u_1^a \\ u_2^a \\ u_3^a \end{pmatrix},\ \boldsymbol{F} = \begin{pmatrix} Q \\ f_1 \\ f_2 \\ f_3 \end{pmatrix},\ \boldsymbol{\mu} = \begin{pmatrix} \mu_p & 0 & 0 & 0 \\ 0 & \mu_{\boldsymbol{u}} & 0 & 0 \\ 0 & 0 & \mu_{\boldsymbol{u}} & 0 \\ 0 & 0 & 0 & \mu_{\boldsymbol{u}} \end{pmatrix},$$

$$\boldsymbol{A}_1 = \begin{pmatrix} \mu_p \bar{u}_1 & 1 & 0 & 0 \\ 1 & \mu_{\boldsymbol{u}} \bar{u}_1 & 0 & 0 \\ 0 & 0 & \mu_{\boldsymbol{u}} \bar{u}_1 & 0 \\ 0 & 0 & 0 & \mu_{\boldsymbol{u}} \bar{u}_1 \end{pmatrix},\ \boldsymbol{A}_2 = \begin{pmatrix} \mu_p \bar{u}_2 & 0 & 1 & 0 \\ 0 & \mu_{\boldsymbol{u}} \bar{u}_2 & 0 & 0 \\ 1 & 0 & \mu_{\boldsymbol{u}} \bar{u}_2 & 0 \\ 0 & 0 & 0 & \mu_{\boldsymbol{u}} \bar{u}_2 \end{pmatrix},$$

$$\boldsymbol{A}_3 = \begin{pmatrix} \mu_p \bar{u}_3 & 0 & 0 & 1 \\ 0 & \mu_{\boldsymbol{u}} \bar{u}_3 & 0 & 0 \\ 0 & 0 & \mu_{\boldsymbol{u}} \bar{u}_3 & 0 \\ 1 & 0 & 0 & \mu_{\boldsymbol{u}} \bar{u}_3 \end{pmatrix},$$

$$\boldsymbol{S} = \begin{pmatrix} \mu_p \nabla \cdot \bar{\boldsymbol{u}} & 0 & 0 & 0 \\ 0 & \mu_{\boldsymbol{u}} \partial_1 \bar{u}_1 & \mu_{\boldsymbol{u}} \partial_2 \bar{u}_1 & \mu_{\boldsymbol{u}} \partial_3 \bar{u}_1 \\ 0 & \mu_{\boldsymbol{u}} \partial_1 \bar{u}_2 & \mu_{\boldsymbol{u}} \partial_2 \bar{u}_2 & \mu_{\boldsymbol{u}} \partial_3 \bar{u}_2 \\ 0 & \mu_{\boldsymbol{u}} \partial_1 \bar{u}_3 & \mu_{\boldsymbol{u}} \partial_2 \bar{u}_3 & \mu_{\boldsymbol{u}} \partial_3 \bar{u}_3 \end{pmatrix}. \quad (3.6)$$

The parameters $\mu_p \equiv (\rho_0 c_0^2)^{-1}$ and $\mu_{\boldsymbol{u}} \equiv \rho_0$ satisfying $c_0 = (\mu_p \mu_{\boldsymbol{u}})^{-1/2}$ in (3.6) have been introduced to ease the notation and $\bar{u}_i$, $i = 1, 2, 3$, designate the components of the time averaged mean velocity vector. Note also that, for completeness, we have included the possibility of an external force acting on the momentum equation by means of the components f_i.

Problem (3.5) is to be solved in a computational domain Ω whose boundary $\partial\Omega$ can be considered to be made from the union of two disjoint sets: Γ_p where we will prescribe the acoustic pressure and $\Gamma_{\boldsymbol{u}}$ where the normal component of the acoustic particle velocity is to be imposed. For simplicity, we shall take homogeneous Dirichlet conditions on them in the forthcoming expressions, i.e., $p^a = 0$ on Γ_p, $\quad t > 0$ and $\boldsymbol{u}^a \cdot \boldsymbol{n} = 0$ on $\Gamma_{\boldsymbol{u}}$, $\quad t > 0$, with $\boldsymbol{n}$ standing for the outward normal of the domain's boundary. Equation (3.5) needs also to be suplemmented with initial conditions $p^a(\boldsymbol{x}, 0) = p_0^a(\boldsymbol{x})$ and $\boldsymbol{u}^a(\boldsymbol{x}, 0) = \boldsymbol{u}_0^a(\boldsymbol{x})$ in Ω.

Additionally, let us introduce the functional spaces $V_p = \{q \in H^1(\Omega) | \bar{\boldsymbol{u}} \cdot \nabla q \in L^2(\Omega),\ q = 0 \text{ on } \Gamma_p\}$ and $\boldsymbol{V_u} = \{\boldsymbol{v}b \in \boldsymbol{L}^2(\Omega) | \nabla \cdot \boldsymbol{v}b \in L^2(\Omega), \bar{\boldsymbol{u}} \cdot \nabla \boldsymbol{v}b \in \boldsymbol{L}^2(\Omega), \boldsymbol{v}b \cdot \boldsymbol{n} = 0 \text{ on } \Gamma_{\boldsymbol{u}}\}$ and use (f, g) to denote the integral of the product of two arbitrary functions f and g, i.e., $(f, g) := \int_\Omega f g d\Omega$. Next, consider a test function q for the acoustic pressure and $\boldsymbol{v}b$ for the acoustic velocity. The weak form of (3.5) is found multiplying it by a vector test function $\boldsymbol{v} \equiv [q, \boldsymbol{v}b]^\top$ and integrating over the computational domain Ω. Defining the spaces $\mathcal{L} \equiv L^2 \times \boldsymbol{L}^2$ and $\mathcal{V} \equiv V_p \times \boldsymbol{V_u}$, the problem becomes that of finding $\boldsymbol{u} \equiv [p^a, \boldsymbol{u}^a]^\top \in C^1([0, T], \mathcal{L}) \cap C^0([0, T], \mathcal{V})$ such that

$$(\boldsymbol{\mu}\partial_t \boldsymbol{u}, \boldsymbol{v}) + (\boldsymbol{A}_i \partial_i \boldsymbol{u}, \boldsymbol{v}) + (\boldsymbol{S}\boldsymbol{u}, \boldsymbol{v}) = (\boldsymbol{F}, \boldsymbol{v}) \quad \forall\ \boldsymbol{v} \in \mathcal{V}. \tag{3.7}$$

3.3 Numerical approximation

3.3.1 Residual-based stabilized finite element method

The standard discretized conforming Galerkin FEM approach to solve problem (3.7) aims at finding a finite element solution $\boldsymbol{u}_h \in C^1([0, T], \mathcal{L}_h \subset \mathcal{L}) \cap C^0([0, T], \mathcal{V}_h \subset \mathcal{V})$ such that

$$(\boldsymbol{\mu}\partial_t \boldsymbol{u}_h, \boldsymbol{v}_h) + (\boldsymbol{A}_i \partial_i \boldsymbol{u}_h, \boldsymbol{v}_h) + (\boldsymbol{S}\boldsymbol{u}_h, \boldsymbol{v}_h) = (\boldsymbol{F}, \boldsymbol{v}_h) \quad \forall\ \boldsymbol{v}_h \in \mathcal{V}_h. \tag{3.8}$$

Here, $\mathcal{L}_h$, $\mathcal{V}_h$ represent finite dimensional spaces built from a finite element partition $\{\Omega_e\}$ of Ω. The index e ranges from 1 to the total number of elements n_{el} in the computational mesh. However, the Galerkin FEM formulation (3.8) is known to suffer from numerical instabilities which can be overcome by resorting to a variational multiscale stabilization approach. The latter basically consists in splitting the exact solution $\boldsymbol{u}$ into a large component $\boldsymbol{u}_h$ that can be captured by the finite element computational mesh, plus a small component $\boldsymbol{u}'$, which cannot be resolved by the mesh. $\boldsymbol{u}'$ is usually referred to as the subscale. The effects of the subscales onto the large scales have to be modeled. The procedure to do so give rise to different stabilization methods.

Substituting $\boldsymbol{u} = \boldsymbol{u}_h + \boldsymbol{u}'$ into (3.7) results in two equations. The first one governs the dynamics of the large scales and is given by

$$\begin{aligned}&(\boldsymbol{\mu}\partial_t \boldsymbol{u}_h, \boldsymbol{v}_h) + (\boldsymbol{\mu}\partial_t \boldsymbol{u}', \boldsymbol{v}_h) + (\boldsymbol{A}_i\partial_i \boldsymbol{u}_h, \boldsymbol{v}_h) + (\boldsymbol{A}_i\partial_i \boldsymbol{u}', \boldsymbol{v}_h)\\ &+ (\boldsymbol{S}\boldsymbol{u}_h, \boldsymbol{v}_h) + (\boldsymbol{S}\boldsymbol{u}', \boldsymbol{v}_h) = (\boldsymbol{F}, \boldsymbol{v}_h).\end{aligned} \tag{3.9}$$

To better account for the influence of the subscales in the large scale equation we can integrate the convective term by parts. Furthermore, if we assume the subscales to be quasi-static, i.e., $\partial_t \boldsymbol{u}' \approx \boldsymbol{0}$, equation (3.9) becomes

$$\begin{aligned}&(\boldsymbol{\mu}\partial_t \boldsymbol{u}_h, \boldsymbol{v}_h) + (\boldsymbol{A}_i\partial_i \boldsymbol{u}_h, \boldsymbol{v}_h) + (\boldsymbol{S}\boldsymbol{u}_h, \boldsymbol{v}_h)\\ &- (\boldsymbol{u}', \boldsymbol{A}_i^\top \partial_i \boldsymbol{v}_h) + (\boldsymbol{u}', \partial_i \boldsymbol{A}_i^\top \boldsymbol{v}_h) + (\boldsymbol{u}', \boldsymbol{S}^\top \boldsymbol{v}_h) = (\boldsymbol{F}, \boldsymbol{v}_h).\end{aligned} \tag{3.10}$$

Notice that the first line in (3.10) contains the terms of the standard Galerkin approach in (3.8), whereas the second line discloses the subscale stabilization terms. The term $(\boldsymbol{u}', \partial_i \boldsymbol{A}_i^\top \boldsymbol{v}_h)$ in the second line plays the role of an additional reaction weighted by the subscales.

On the other hand, the second equation driving the dynamics of $\boldsymbol{u}'$ has the expression

$$(\boldsymbol{\mu}\partial_t \boldsymbol{u}_h, \boldsymbol{v}') + (\boldsymbol{A}_i\partial_i \boldsymbol{u}_h, \boldsymbol{v}') + (\boldsymbol{A}_i\partial_i \boldsymbol{u}', \boldsymbol{v}') + (\boldsymbol{S}\boldsymbol{u}_h, \boldsymbol{v}') + (\boldsymbol{S}\boldsymbol{u}', \boldsymbol{v}') = (\boldsymbol{F}, \boldsymbol{v}'), \tag{3.11}$$

which corresponds to the L^2-projection of $\boldsymbol{\mu}\partial_t \boldsymbol{u}_h + \boldsymbol{A}_i\partial_i \boldsymbol{u}_h + \boldsymbol{A}_i\partial_i \boldsymbol{u}' + \boldsymbol{S}\boldsymbol{u}_h + \boldsymbol{S}\boldsymbol{u}' = \boldsymbol{F}$ onto the space of subscales. If we use $\mathcal{P}$ to denote this projection, (3.11) can be rewritten as

$$\mathcal{P}(\boldsymbol{A}_i\partial_i \boldsymbol{u}' + \boldsymbol{S}\boldsymbol{u}') = \mathcal{P}[\boldsymbol{F} - (\boldsymbol{\mu}\partial_t \boldsymbol{u}_h + \boldsymbol{A}_i\partial_i \boldsymbol{u}_h + \boldsymbol{S}\boldsymbol{u}_h)] =: \mathbb{R}_h, \tag{3.12}$$

where the residual $\mathbb{R}_h$ of the finite element approximation onto the subscale space has been introduced. The goal of the residual-based stabilization approaches is to find an approximate solution to (3.12), which yields an expression for $\boldsymbol{u}'$ that could be substituted in (3.10) resulting in enhanced stabilization properties.

A legitimate option consists in taking the subscales proportional to the residual i.e., $\boldsymbol{u}' = \boldsymbol{\tau}\mathbb{R}_h$, which is analogous to saying that $\mathcal{P}(\boldsymbol{A}_i\partial_i \boldsymbol{u}' + \boldsymbol{S}\boldsymbol{u}') \approx \boldsymbol{\tau}^{-1}\boldsymbol{u}'$, see [49, 54]. Here, $\boldsymbol{\tau}$ stands for a symmetric, positive-definite matrix of stabilization parameters that has to be determined. Once this has been done, $\boldsymbol{u}' = \boldsymbol{\tau}\mathbb{R}_h$ can be substituted into the large scale equation (3.10) that becomes

$$\begin{aligned}&(\boldsymbol{\mu}\partial_t \boldsymbol{u}_h, \boldsymbol{v}_h) + (\boldsymbol{A}_i\partial_i \boldsymbol{u}_h, \boldsymbol{v}_h) + (\boldsymbol{S}\boldsymbol{u}_h, \boldsymbol{v}_h)\\ &+ \sum_{e=1}^{n_{el}} (\boldsymbol{\tau}\mathcal{P}[\boldsymbol{F} - (\boldsymbol{\mu}\partial_t \boldsymbol{u}_h + \boldsymbol{A}_i\partial_i \boldsymbol{u}_h + \boldsymbol{S}\boldsymbol{u}_h)], -\boldsymbol{A}_i\partial_i \boldsymbol{v}_h + \partial_i \boldsymbol{A}_i \boldsymbol{v}_h + \boldsymbol{S}^\top \boldsymbol{v}_h)_{\Omega_e}\\ &= (\boldsymbol{F}, \boldsymbol{v}_h).\end{aligned} \tag{3.13}$$

Note that we have used the fact that the convective matrices $\boldsymbol{A}_i$ are symmetric in the above expression. With regard to the projection operator $\mathcal{P}$ different options exist. In the more classical ASGS (Algebraic Subgrid Scale) formulation, the projection is taken as the identity matrix over the space of finite element residuals, i.e., $\mathcal{P} =$. Alternatively, in the OSS (Orthogonal Subgrid Scale) method the subscales are assumed to be orthogonal to the finite element space and consequently, $\mathcal{P} = -\Pi_h$, with Π_h standing for the L^2-projection onto the former [46, 59]. Let us also mention that the subscales are presumed to be local and vanish at the interelemental boundaries. When integrating over Ω, the integrals containing subscales are evaluated as a summation of integrals over the finite element domains Ω_e (as explicitly indicated in (3.13)).

3.3.2 Dimensional rescaling considerations

To complete the stabilized formulation in (3.13), the crucial step of finding an appropriate expression for the stabilization matrix $\boldsymbol{\tau}$ remains to be done. However, before addressing such an issue some considerations are to be made concerning the scalar products in the variational formulations (3.6) and (3.13). The r.h.s (right hand side) of these equations involves products of the type $\boldsymbol{u}^\top \boldsymbol{F} = p^a Q + u_1^a f_1 + u_2^a f_2 + u_3^a f_3$ (see (3.6)). If we use $[\cdot]$ to denote a dimensional group, it becomes necessary that $[p^a Q] = [u_i^a f_i]$. From the dimensions of the terms in the r.h.s of (3.3) it can readily be checked that $[p^a Q] = [u_i^a f_i] = MLT^{-3}$, with M, L and T standing for dimensions of mass, length and time respectively. Yet, when deriving an appropriate expression for $\boldsymbol{\tau}$ in the next subsection we will have to deal with products like $\boldsymbol{F}^\top \boldsymbol{F}$ or $\boldsymbol{u}^\top \boldsymbol{u}$, which are not dimensionally well defined. For instance, $\boldsymbol{F}^\top \boldsymbol{F} = Q^2 + f_1^2 + f_2^2 + f_3^2$ but $[Q^2] \neq [f_i^2]$. Similarly, $\boldsymbol{u}^\top \boldsymbol{u} = p^{a2} + u_1^{a2} + u_2^{a2} + u_3^{a2}$ but again $[p^{a2}] \neq [u_i^{a2}]$. Consequently, and as quoted in [49, 54], it becomes necessary to rescale the original differential equations for these products to make sense.

This is tantamount to introducing the weighting matrix $\boldsymbol{M}$ (see [49]),

$$\boldsymbol{M} = \begin{pmatrix} m_p & 0 & 0 & 0 \\ 0 & m_{\boldsymbol{u}} & 0 & 0 \\ 0 & 0 & m_{\boldsymbol{u}} & 0 \\ 0 & 0 & 0 & m_{\boldsymbol{u}} \end{pmatrix}, \; m_p := \sqrt{\mu_{\boldsymbol{u}}/\mu_p} = \rho_0 c_0, \tag{3.14}$$

$$m_{\boldsymbol{u}} := \sqrt{\mu_p/\mu_{\boldsymbol{u}}} = \frac{1}{\rho_0 c_0}, \tag{3.15}$$

to define the weighted scalar product $\boldsymbol{F}^\top \boldsymbol{M} \boldsymbol{F} \equiv |\boldsymbol{F}|^2_{\boldsymbol{M}}$ which can be shown to be dimensionally correct given that $[m_p Q^2] = [m_{\boldsymbol{u}} f_i^2] = ML^{-2}T^{-3}$. Analogoulsy, the inverse of $\boldsymbol{M}$ can be used to correctly define the product $\boldsymbol{u}^\top \boldsymbol{M}^{-1} \boldsymbol{u} \equiv |\boldsymbol{u}|^2_{\boldsymbol{M}^{-1}}$. That is so because $[m_p^{-1} p^{a2}] = [m_{\boldsymbol{u}}^{-1} u_i^{a2}] = MT^{-3}$.

Therefore, $\boldsymbol{M}$ and $\boldsymbol{M}^{-1}$ are the appropriate weighthing matrices to define products between any two force vectors $\boldsymbol{F}_1^\top \boldsymbol{M}\boldsymbol{F}_2$ and unknowns $\boldsymbol{u}_1^\top \boldsymbol{M}^{-1}\boldsymbol{u}_2$. We can also define an $\boldsymbol{M}$-weighted product between two arbitrary matrices $\boldsymbol{B}_1$ and $\boldsymbol{B}_2$ as $\boldsymbol{B}_1^\top \boldsymbol{M}\boldsymbol{B}_2$. The squared $\boldsymbol{M}$-pointwise norm of a matrix $\boldsymbol{B}$ will be given by $|\boldsymbol{B}|^2_{\boldsymbol{M}} = \sup\{\boldsymbol{X}^\top \boldsymbol{B}^\top \boldsymbol{M}\boldsymbol{B}\boldsymbol{X}\}$, $\forall\ \boldsymbol{X}; |\boldsymbol{X}|_{\boldsymbol{M}^{-1}} = 1$. For regular enough force vector functions it is also possible to introduce the following vector function $\boldsymbol{M}$-weighted scalar products,

$$(\boldsymbol{u}, \boldsymbol{F}) = \int_\Omega \boldsymbol{u}^\top \boldsymbol{F} d\Omega,\ (\boldsymbol{F}_1, \boldsymbol{F}_2)_{\boldsymbol{M}} := \int_\Omega \boldsymbol{F}_1^\top \boldsymbol{M}\boldsymbol{F}_2 d\Omega,\ (\boldsymbol{u}_1, \boldsymbol{u}_2)_{\boldsymbol{M}^{-1}} := \int_\Omega \boldsymbol{u}_1^\top \boldsymbol{M}^{-1}\boldsymbol{u}_2 d\Omega, \quad (3.16)$$

whose induced norms are designated by $\|\cdot\|$, $\|\cdot\|_{\boldsymbol{M}}$ and $\|\cdot\|_{\boldsymbol{M}^{-1}}$.

3.3.3 The matrix $\boldsymbol{\tau}$ of stabilization parameters

A fruitful way to derive an expression for the matrix of stabilization parameters $\boldsymbol{\tau}$ is from the spatial Fourier transform of the subscale equation (3.12). Let us identify the linear operator $\mathscr{L} := \boldsymbol{A}_i\partial_i + \boldsymbol{S}$ and use a hat symbol for Fourier transformed functions. Equation (3.12) can therefore be expressed in the wavenumber domain as (hereafter k_i denotes the i-th component of the wavenumber adimensionalized by the characteristic mesh size h),

$$\hat{\mathscr{L}}(\boldsymbol{k})\hat{\boldsymbol{u}}' = -\mathrm{i}\frac{1}{h}k_j\boldsymbol{A}_j\hat{\boldsymbol{u}}' + \boldsymbol{S}\hat{\boldsymbol{u}}' = \hat{\mathbb{R}}_h, \quad (3.17)$$

with squared $\boldsymbol{M}$-norm

$$\hat{\boldsymbol{u}}'^\top \hat{\mathscr{L}}(\boldsymbol{k})^\top \boldsymbol{M}\hat{\mathscr{L}}(\boldsymbol{k})\hat{\boldsymbol{u}}' = \hat{\boldsymbol{u}}'^\top \Big(\frac{1}{h^2}k_l k_j \boldsymbol{A}_l^\top \boldsymbol{M}\boldsymbol{A}_j + 2\frac{\mathrm{i}}{h}k_l[\boldsymbol{A}_l\boldsymbol{M}\boldsymbol{S}]_A + \boldsymbol{S}^\top \boldsymbol{M}\boldsymbol{S}\Big)\hat{\boldsymbol{u}}' = \hat{\mathbb{R}}_h^\top \boldsymbol{M}\hat{\mathbb{R}}_h. \quad (3.18)$$

Here, $[\boldsymbol{A}_l\boldsymbol{M}\boldsymbol{S}]_A$ stands the skew-symmetric part of $\boldsymbol{A}_l^\top \boldsymbol{M}\boldsymbol{S}$. The induced norm for the residual (see (3.16)) fulfills

$$\begin{aligned}
\|\hat{\mathbb{R}}_h\|^2_{\boldsymbol{M}} &= \int |\hat{\mathbb{R}}_h|^2_{\boldsymbol{M}} d\boldsymbol{k} = \int |\hat{\mathscr{L}}(\boldsymbol{k})\hat{\boldsymbol{u}}'|^2_{\boldsymbol{M}} d\boldsymbol{k} \le \int |\hat{\mathscr{L}}(\boldsymbol{k})|^2_{\boldsymbol{M}} |\hat{\boldsymbol{u}}'|^2_{\boldsymbol{M}^{-1}} d\boldsymbol{k} \\
&= \int |\hat{\mathscr{L}}(\boldsymbol{k}^0)|^2_{\boldsymbol{M}} |\hat{\boldsymbol{u}}'|^2_{\boldsymbol{M}^{-1}} d\boldsymbol{k} = |\hat{\mathscr{L}}(\boldsymbol{k}^0)|^2_{\boldsymbol{M}} \|\hat{\boldsymbol{u}}'\|^2_{\boldsymbol{M}^{-1}} \\
&= \rho(\hat{\mathscr{L}}(\boldsymbol{k}^0)^\top \boldsymbol{M}\hat{\mathscr{L}}(\boldsymbol{k}^0))\|\hat{\boldsymbol{u}}'\|^2_{\boldsymbol{M}^{-1}} \\
&\le \Big[\rho\Big(\frac{1}{h^2}k_l^0 k_j^0 \boldsymbol{A}_l^\top \boldsymbol{M}\boldsymbol{A}_j\Big) + \rho\Big(2\frac{\mathrm{i}}{h}k_l^0[\boldsymbol{A}_l\boldsymbol{M}\boldsymbol{S}]_A\Big) + \rho(\boldsymbol{S}^\top \boldsymbol{M}\boldsymbol{S})\Big]\|\hat{\boldsymbol{u}}'\|^2_{\boldsymbol{M}^{-1}},
\end{aligned} \quad (3.19)$$

where the existence of $\boldsymbol{k}^0$ in the second line is guaranteed by the mean value theorem and $\rho(\boldsymbol{B})$ denotes the spectral radius of an arbitrary matrix $\boldsymbol{B}$ arising from the solution of the generalized eigenvalue problem $\boldsymbol{B}\boldsymbol{u} = \lambda\boldsymbol{M}^{-1}\boldsymbol{u}$, λ being an eigenvalue. All spectral radii in the fourth line of (3.19) will be shown to be real (note that $[\boldsymbol{A}_l\boldsymbol{M}\boldsymbol{S}]_A$ is totally skew-symmetric and therefore has imaginary eigenvalues).

On the other hand, from the Fourier transform of the approximation for the subscales $\boldsymbol{u}' = \boldsymbol{\tau}\mathbb{R}_h$, we can get the bound

$$\|\hat{\mathbb{R}}_h\|^2_{\boldsymbol{M}} \leq |\boldsymbol{\tau}^{-1}|^2_{\boldsymbol{M}}\|\hat{\boldsymbol{u}}'\|^2_{\boldsymbol{M}^{-1}}. \tag{3.20}$$

The combination of (3.19) and (3.20) provides one way to find an expression for the stabilization matrix given that

$$\rho(\boldsymbol{\tau}^{-1}\boldsymbol{M}\boldsymbol{\tau}^{-1}) \leq \rho\Big(\frac{1}{h^2}k_l^0k_j^0\boldsymbol{A}_l^\top\boldsymbol{M}\boldsymbol{A}_j\Big) + \rho\Big(2\frac{\mathrm{i}}{h}k_l^0[\boldsymbol{A}_l\boldsymbol{M}\boldsymbol{S}]_A\Big) + \rho(\boldsymbol{S}^\top\boldsymbol{M}\boldsymbol{S}). \tag{3.21}$$

Without loss of generality, hereafter we will derive the stabilization matrix for a two dimensional case, its extension to the three dimensional one being straightforward. Let us first compute the spectral radii for the three terms in the r.h.s (3.21). Taking into account the definitions of $\boldsymbol{A}_i$ in (3.6) and of the scaling matrix $\boldsymbol{M}$ in (3.15), the matrix in the first term of (3.21) reads

$$\frac{1}{h^2}k_i^0k_j^0\boldsymbol{A}_i^\top\boldsymbol{M}\boldsymbol{A}_j = \frac{1}{h^2}\times \begin{pmatrix} m_{\boldsymbol{u}}|\boldsymbol{k}^0|^2 + \beta_p|\boldsymbol{k}^0\cdot\bar{\boldsymbol{u}}|^2 & \alpha k_1^0(\boldsymbol{k}^0\cdot\bar{\boldsymbol{u}}) & \alpha k_2^0(\boldsymbol{k}^0\cdot\bar{\boldsymbol{u}}) \\ \alpha k_1^0(\boldsymbol{k}^0\cdot\bar{\boldsymbol{u}}) & m_p(k_1^0)^2 + \beta_{\boldsymbol{u}}|\boldsymbol{k}^0\cdot\bar{\boldsymbol{u}}|^2 & k_1^0k_2^0m_p \\ \alpha k_2^0(\boldsymbol{k}^0\cdot\bar{\boldsymbol{u}}) & k_1^0k_2^0m_p & m_p(k_2^0)^2 + \beta_{\boldsymbol{u}}|\boldsymbol{k}^0\cdot\bar{\boldsymbol{u}}|^2 \end{pmatrix} \tag{3.22}$$

with

$$\alpha \equiv (m_p\mu_p + m_{\boldsymbol{u}}\mu_{\boldsymbol{u}}), \quad \beta_p \equiv m_p\mu_p^2, \quad \beta_{\boldsymbol{u}} \equiv m_{\boldsymbol{u}}\mu_{\boldsymbol{u}}^2. \tag{3.23}$$

The spectrum of $k_i^0k_j^0\boldsymbol{A}_i^\top\boldsymbol{M}\boldsymbol{A}_j$ can be analytically worked out and is given by

$$\mathrm{Spec}_{\boldsymbol{M}^{-1}}(k_i^0k_j^0\boldsymbol{A}_i^\top\boldsymbol{M}\boldsymbol{A}_j) = \left\{\left(\frac{\boldsymbol{k}^0\cdot\bar{\boldsymbol{u}}}{c_0} + |\boldsymbol{k}^0|\right)^2, \left(\frac{\boldsymbol{k}^0\cdot\bar{\boldsymbol{u}}}{c_0}\right)^2, \left(\frac{\boldsymbol{k}^0\cdot\bar{\boldsymbol{u}}}{c_0} - |\boldsymbol{k}^0|\right)^2\right\}. \tag{3.24}$$

The spectral radius of $\Big(\frac{1}{h^2}k_l^0 k_j^0 \boldsymbol{A}_l^\top \boldsymbol{M}\boldsymbol{A}_j\Big)$ corresponds to the maximum eigenvalue

$$\rho\Big(\frac{1}{h^2}k_l^0 k_j^0 \boldsymbol{A}_l^\top \boldsymbol{M}\boldsymbol{A}_j\Big) = \frac{1}{h^2}\left(\frac{\boldsymbol{k}^0\cdot\bar{\boldsymbol{u}}}{c_0} + |\boldsymbol{k}^0|\right)^2 \equiv \frac{1}{h^2}\left(\frac{C_2|\bar{\boldsymbol{u}}|}{c_0} + C_1\right)^2 = \frac{1}{h^2}\Big(C_1 + C_2 M\Big)^2, \quad (3.25)$$

where $M = |\bar{\boldsymbol{u}}|/c_0$ stands for the flow local Mach number (do not confuse the scalar Mach number M with the weighthing matrix $\boldsymbol{M}$). Since $\boldsymbol{k}^0$ is an unknown dimensionless number, we have taken $\boldsymbol{k}^0\cdot\bar{\boldsymbol{u}} = |\boldsymbol{k}^0||\bar{\boldsymbol{u}}|\cos\theta \equiv C_2|\bar{\boldsymbol{u}}|$ and $|\boldsymbol{k}^0| \equiv C_1$ in the r.h.s of (3.25), C_1 and C_2 being constants that have to be determined from numerical experiments.

Next, considering the expressions for $\boldsymbol{A}_i$ and $\boldsymbol{S}$ in (3.6) and for $\boldsymbol{M}$ in (3.15), we get for the matrix in the second term of (3.21)

$$2\frac{\mathrm{i}}{h}k_l^0[\boldsymbol{A}_l\boldsymbol{M}\boldsymbol{S}]_A = \frac{\mathrm{i}}{h}\times \quad (3.26)$$

$$\begin{pmatrix} 0 & m_{\boldsymbol{u}}\mu_{\boldsymbol{u}}\boldsymbol{k}^0\cdot\partial_1\bar{\boldsymbol{u}} - m_p\mu_p k_1^0\nabla\cdot\bar{\boldsymbol{u}} & m_{\boldsymbol{u}}\mu_{\boldsymbol{u}}\boldsymbol{k}^0\cdot\partial_2\bar{\boldsymbol{u}} - m_p\mu_p k_2^0\nabla\cdot\bar{\boldsymbol{u}} \\ m_p\mu_p k_1^0\nabla\cdot\bar{\boldsymbol{u}} - m_{\boldsymbol{u}}\mu_{\boldsymbol{u}}\boldsymbol{k}^0\cdot\partial_1\bar{\boldsymbol{u}} & 0 & -\beta_{\boldsymbol{u}}\boldsymbol{k}^0\cdot\bar{\boldsymbol{u}}(\partial_1\bar{u}_2 - \partial_2\bar{u}_1) \\ m_p\mu_p k_2^0\nabla\cdot\bar{\boldsymbol{u}} - m_{\boldsymbol{u}}\mu_{\boldsymbol{u}}\boldsymbol{k}^0\cdot\partial_2\bar{\boldsymbol{u}} & \beta_{\boldsymbol{u}}\boldsymbol{k}^0\cdot\bar{\boldsymbol{u}}(\partial_1\bar{u}_2 - \partial_2\bar{u}_1) & 0 \end{pmatrix}. \quad (3.27)$$

The spectrum of this matrix is given by

$$\mathrm{Spec}_{\boldsymbol{M}^{-1}}(2\frac{\mathrm{i}}{h}k_l^0[\boldsymbol{A}_l\boldsymbol{M}\boldsymbol{S}]_A) = \left\{\frac{1}{h}\Big[(c^2+b^2) + m_{\boldsymbol{u}}d^2\Big]^{1/2}, 0, -\frac{1}{h}\Big[(c^2+b^2) + m_{\boldsymbol{u}}d^2\Big]^{1/2}\right\}, \quad (3.28)$$

with

$$\begin{aligned} c^2+b^2 &= \frac{1}{c_0^2}|\boldsymbol{k}^0|^2(\nabla\cdot\bar{\boldsymbol{u}})^2 + \frac{1}{c_0^2}\Big[(\boldsymbol{k}^0\cdot\partial_1\bar{\boldsymbol{u}})^2 + (\boldsymbol{k}^0\cdot\partial_2\bar{\boldsymbol{u}})^2\Big] \\ &\quad - \frac{2}{c_0^2}\nabla\cdot\bar{\boldsymbol{u}}\Big[k_1^0(\boldsymbol{k}^0\cdot\partial_1\bar{\boldsymbol{u}}) + k_2^0(\boldsymbol{k}^0\cdot\partial_2\bar{\boldsymbol{u}})\Big] \\ &\le \frac{2}{c_0^2}|\boldsymbol{k}^0|^2(\nabla\cdot\bar{\boldsymbol{u}})^2 + \frac{2}{c_0^2}\Big[(\boldsymbol{k}^0\cdot\partial_1\bar{\boldsymbol{u}})^2 + (\boldsymbol{k}^0\cdot\partial_2\bar{\boldsymbol{u}})^2\Big] \\ &\le \frac{2}{c_0^2}|\boldsymbol{k}^0|^2(\nabla\cdot\bar{\boldsymbol{u}})^2 + \frac{2}{c_0^2}|\boldsymbol{k}^0|^2\Big[(\partial_1\bar{\boldsymbol{u}})^2 + (\partial_2\bar{\boldsymbol{u}})^2\Big] \le \frac{4}{c_0^2}|\boldsymbol{k}^0|^2|\nabla\bar{\boldsymbol{u}}|_F^2, \\ m_{\boldsymbol{u}}^2 d^2 &= m_{\boldsymbol{u}}^2\beta_{\boldsymbol{u}}(\boldsymbol{k}^0\cdot\bar{\boldsymbol{u}})^2(\partial_1\bar{u}_2 - \partial_2\bar{u}_1)^2 \le \frac{1}{c_0^4}|\boldsymbol{k}^0|^2|\bar{\boldsymbol{u}}|^2(\partial_1\bar{u}_2 - \partial_2\bar{u}_1)^2 \\ &\le \frac{1}{c_0^2}|\boldsymbol{k}^0|^2M^2|\nabla\bar{\boldsymbol{u}}|_F^2, \end{aligned} \quad (3.29)$$

$|\boldsymbol{B}|_F$ denoting the Frobenius norm of an arbitrary matrix $\boldsymbol{B}$. It follows that

$$c^2 + b^2 + m_{\boldsymbol{u}}^2 d^2 \leq \frac{4}{c_0^2}|\boldsymbol{k}^0|^2|\nabla\bar{\boldsymbol{u}}|_F^2(1+M^2) \leq \frac{8}{c_0^2}|\boldsymbol{k}^0|^2|\nabla\bar{\boldsymbol{u}}|_F^2, \tag{3.30}$$

where we have considered that we are dealing with low Mach number flows and consequently $M << 1$. The above results allow one to bound the spectral radius of $2\frac{\mathrm{i}}{h}k_l^0[\boldsymbol{A}_l\boldsymbol{M}\boldsymbol{S}]_A$ by

$$\rho\Big(2\frac{\mathrm{i}}{h}k_l^0[\boldsymbol{A}_l\boldsymbol{M}\boldsymbol{S}]_A\Big) \leq \frac{1}{h}\frac{C_3}{c_0}|\nabla\bar{\boldsymbol{u}}|_F, \tag{3.31}$$

C_3 denoting a real constant.

Finally, the matrix in the third term of (3.21) reads

$$\boldsymbol{S}^\top\boldsymbol{M}\boldsymbol{S} = \begin{pmatrix} \beta_p(\nabla\cdot\bar{\boldsymbol{u}})^2 & 0 & 0 \\ 0 & \beta_{\boldsymbol{u}}|\partial_1\bar{\boldsymbol{u}}|^2 & \beta_{\boldsymbol{u}}\partial_1\bar{\boldsymbol{u}}\cdot\partial_2\bar{\boldsymbol{u}} \\ 0 & \beta_{\boldsymbol{u}}\partial_1\bar{\boldsymbol{u}}\cdot\partial_2\bar{\boldsymbol{u}} & \beta_{\boldsymbol{u}}|\partial_2\bar{\boldsymbol{u}}|^2 \end{pmatrix}, \tag{3.32}$$

with spectrum

$$\begin{aligned} &\mathrm{Spec}_{\boldsymbol{M}^{-1}}(\boldsymbol{S}^\top\boldsymbol{M}\boldsymbol{S}) \qquad (3.33)\\ &= \left\{\frac{m_{\boldsymbol{u}}}{2}\Big[(e+f)+\sqrt{(e-f)^2+4g^2}, \frac{1}{c_0^2}(\nabla\cdot\bar{\boldsymbol{u}})^2, \frac{m_{\boldsymbol{u}}}{2}\Big[(e+f)-\sqrt{(e-f)^2+4g^2}\right\}, \end{aligned}$$

where

$$\begin{aligned} (e+f) &= \beta_{\boldsymbol{u}}\Big[(\partial_1\bar{\boldsymbol{u}})^2 + (\partial_2\bar{\boldsymbol{u}})^2\Big] \leq \beta_{\boldsymbol{u}}|\nabla\bar{\boldsymbol{u}}|_F^2, \\ (e-f)^2 &= \beta_{\boldsymbol{u}}^2\Big[|\partial_1\bar{\boldsymbol{u}}|^2 - |\partial_2\bar{\boldsymbol{u}}|^2\Big]^2 \leq \beta_{\boldsymbol{u}}^2|\nabla\bar{\boldsymbol{u}}|_F^4, \\ 4g^2 &= 4\beta_{\boldsymbol{u}}^2(\partial_1\bar{\boldsymbol{u}}\cdot\partial_2\bar{\boldsymbol{u}})^2 \leq 4\beta_{\boldsymbol{u}}^2|\partial_1\bar{\boldsymbol{u}}|^2|\partial_2\bar{\boldsymbol{u}}|^2 \leq 4\beta_{\boldsymbol{u}}^2|\nabla\bar{\boldsymbol{u}}|_F^4. \end{aligned} \tag{3.34}$$

Therefore, the spectral radius of $\boldsymbol{S}^\top\boldsymbol{M}\boldsymbol{S}$ can be bounded as

$$\rho(\boldsymbol{S}^\top\boldsymbol{M}\boldsymbol{S}) \leq C_4 m_{\boldsymbol{u}}\beta_{\boldsymbol{u}}|\nabla\bar{\boldsymbol{u}}|_F^2 = \frac{C_4}{c_0^2}|\nabla\bar{\boldsymbol{u}}|_F^2, \tag{3.35}$$

with C_4 denoting a large enough real constant to be found again from numerical experiments.

From (3.21), (3.25), (3.31) and (3.35) we get

$$\rho(\boldsymbol{\tau}^{-1}\boldsymbol{M}\boldsymbol{\tau}^{-1}) \leq \frac{1}{h^2}\left(C_1 + C_2 M\right)^2 + \frac{1}{h}\frac{C_3}{c_0}|\nabla\bar{\boldsymbol{u}}|_F + \frac{C_4}{c_0^2}|\nabla\bar{\boldsymbol{u}}|_F^2. \tag{3.36}$$

Taking into account that $\nabla \sim \mathcal{O}(1/h)$ and redefining constants where appropriate, we can check that the bound on the $\boldsymbol{M}$-norm of the stabilization matrix behaves as

$$\rho(\boldsymbol{\tau}^{-1}\boldsymbol{M}\boldsymbol{\tau}^{-1}) \leq \frac{1}{h^2}[C_1 + C_2\mathcal{O}(M) + C_3\mathcal{O}(M^2)]. \tag{3.37}$$

Note that the discarded term involving M^2 in (3.30)-(3.31) would have give place to a term $\sim \mathcal{O}(M^3)$ in (3.37).

In order to get a simple expression for the stabilization matrix we may take it to be diagonal, $\boldsymbol{\tau} = \mathrm{diag}(\tau_p, \tau_{\boldsymbol{u}}, \tau_{\boldsymbol{u}})$. Given that the scaling matrix $\boldsymbol{M}$ in (3.15) is also diagonal, it follows that

$$\mathrm{Spec}_{\boldsymbol{M}^{-1}}(\boldsymbol{\tau}^{-1}\boldsymbol{M}\boldsymbol{\tau}^{-1}) = \left\{ \left(\frac{m_p}{\tau_p}\right)^2, \left(\frac{m_{\boldsymbol{u}}}{\tau_{\boldsymbol{u}}}\right)^2, \left(\frac{m_{\boldsymbol{u}}}{\tau_{\boldsymbol{u}}}\right)^2 \right\}. \tag{3.38}$$

We may then force every eigenvalue of $\boldsymbol{\tau}^{-1}\boldsymbol{M}\boldsymbol{\tau}^{-1}$ in (3.38) to equal the r.h.s of (3.36) and take into account the observation in (3.37). What we actually need from the stabilization parameter is to provide a constant term depending on the mesh size, a term to control the flow local mean velocity $\bar{\boldsymbol{u}}$ and a term that controls the mean velocity derivatives through $|\nabla\bar{\boldsymbol{u}}|_F^2$. Therefore, our proposal for the stabilization parameters, directly generalizing for the three dimensional case, is that of taking

$$\boldsymbol{\tau} = \begin{pmatrix} \tau_p & 0 & 0 & 0 \\ 0 & \tau_{\boldsymbol{u}} & 0 & 0 \\ 0 & 0 & \tau_{\boldsymbol{u}} & 0 \\ 0 & 0 & 0 & \tau_{\boldsymbol{u}} \end{pmatrix} \quad \text{with,}$$

$$\tau_p = \frac{\rho_0 c_0^2 h}{\left[(c_0 C_1 + C_2|\bar{\boldsymbol{u}}|)^2 + C_3 h^2 |\nabla\bar{\boldsymbol{u}}|_F^2\right]^{1/2}},$$

$$\tau_{\boldsymbol{u}} = \frac{h}{\rho_0\left[(c_0 C_1 + C_2|\bar{\boldsymbol{u}}|)^2 + C_3 h^2 |\nabla\bar{\boldsymbol{u}}|_F^2\right]^{1/2}}, \tag{3.39}$$

where use has been made of the expressions for m_p and $m_{\boldsymbol{u}}$ in (3.15).

The matrix $\boldsymbol{\tau}$ of stabilization parameters (3.39) has to be inserted into (3.13) to get the final stabilized variational formulation proposed in this article. It only remains to find the values of the constants C_1, C_2 and C_3. This will be done by means of the numerical experiments in Section 4.1. As regards the constants, it should be pointed out that there is a certain tolerance for them, in the sense that one does not necessarily need to get their optimal values as long as they are able to provide enough stabilization. For a given mesh size h, the error may be larger or smaller depending on the particular

values of the constants, but the slope of the convergence curves will remain unchanged for a wide range of values, which is what matters in fact.

Finally, note that in the case of no mean flow, $\bar{\boldsymbol{u}} = \boldsymbol{0}$, the stabilization parameters for the standard wave equation in mixed form are recovered,

$$\tau_p = Ch\sqrt{\mu_{\boldsymbol{u}}/\mu_p} \qquad \tau_{\boldsymbol{u}} = Ch\sqrt{\mu_p/\mu_{\boldsymbol{u}}}, \tag{3.40}$$

with C standing for a constant (see [49]). Likewise, if there was no reaction term, $\boldsymbol{S} = \boldsymbol{0}$, the factors $|\nabla\bar{\boldsymbol{u}}|_F^2$ would have not appeared in (3.39), and we would have recovered analogous stabilization parameters to those found for the standard wave equation in mixed form in an ALE frame of reference [89], or for the equations of wave propagation in shallow waters [54].

3.3.4 Fully discrete problem

In the above developments, the time variable has been left continuous. To proceed to the time discretization we have equally split the time interval $[0\ T]$ into N steps $0 < t^1 < t^2 < \ldots < t^n < \ldots < t^N \equiv T$ with $\Delta t := t^{n+1} - t^n$ denoting the time step size. Hereafter, g^n will stand for the evaluation of a time dependent function $g(t)$ at $t^n = n\Delta t$. Given that we are computing the aeroacoustic field close to the source region, a second order backward differentiation formula (BDF2) will prove accurate enough for the time discretization of (3.13). Identifying $\delta_t g^{n+1} := (1/2\Delta t)(3g^{n+1} - 4g^n + g^{n-1})$ allows one to write the time discrete version of (3.13) as

$$\begin{aligned}
&(\boldsymbol{\mu}\delta_t\boldsymbol{u}_h^{n+1}, \boldsymbol{v}_h) + (\boldsymbol{A}_i\partial_i\boldsymbol{u}_h^{n+1}, \boldsymbol{v}_h) + (\boldsymbol{S}\boldsymbol{u}_h^{n+1}, \boldsymbol{v}_h) \\
&+ \sum_{e=1}^{n_{el}} (\boldsymbol{\tau}\mathcal{P}[\boldsymbol{F}^{n+1} - (\delta_t\boldsymbol{u}_h^{n+1} + \boldsymbol{A}_i\partial_i\boldsymbol{u}_h^{n+1} + \boldsymbol{S}\boldsymbol{u}_h^{n+1})], \partial_i\boldsymbol{A}_i\boldsymbol{v}_h - \boldsymbol{A}_i\partial_i\boldsymbol{v}_h + \boldsymbol{S}^\top\boldsymbol{v}_h)_{\Omega_e} \\
&= (\boldsymbol{F}^{n+1}, \boldsymbol{v}_h).
\end{aligned} \tag{3.41}$$

Finally, if we choose the OSS approach for the stabilized spatial discretization it will follow that $\mathcal{P}(\delta_t\boldsymbol{u}_h) = 0$ because $\mathcal{P} = -\Pi_h$. The expanded fully discrete problem in time and space that results from accounting for (3.6) in (3.41) and that has been implemented for the numerical examples in the

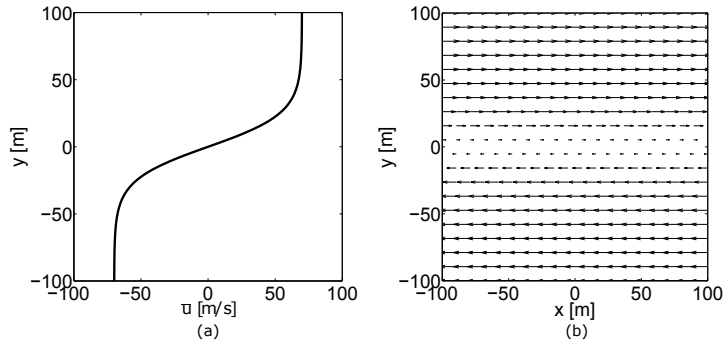

Figure 3.1: (a) Shear mean velocity profile and (b) resulting vector field for Cases 3 and 4.

forthcoming section reads

$$\frac{1}{\rho_0 c_0^2}\Big[(\delta_t p_h^{a^{n+1}}, q_h) + (\bar{\boldsymbol{u}}\cdot\nabla p_h^{a^{n+1}}, q_h) + (\nabla\cdot\bar{\boldsymbol{u}} p_h^{a^{n+1}}, q_h)\Big] + (\nabla\cdot\boldsymbol{u}_h^{a^{n+1}}, q_h)$$
$$+\sum_{e=1}^{n_{el}}(\tau_p\mathcal{P}\big[Q^{n+1} - \frac{1}{\rho_0 c_0^2}\bar{\boldsymbol{u}}\cdot\nabla p_h^{a^{n+1}} - \nabla\cdot\boldsymbol{u}_h^{a^{n+1}} - \frac{1}{\rho_0 c_0^2}\nabla\cdot\bar{\boldsymbol{u}} p_h^{a^{n+1}}\big],$$
$$-\frac{1}{\rho_0 c_0^2}\bar{\boldsymbol{u}}\cdot\nabla q_h - \nabla\cdot\boldsymbol{v}b_h + \frac{2}{\rho_0 c_0^2}\nabla\cdot\bar{\boldsymbol{u}}\ q_h)_{\Omega_e} = (Q^{n+1}, q_h), \tag{3.42a}$$
$$\rho_0(\delta_t\boldsymbol{u}_h^{a^{n+1}}, \boldsymbol{v}b_h) + \rho_0(\bar{\boldsymbol{u}}\cdot\nabla\boldsymbol{u}_h^{a^{n+1}}, \boldsymbol{v}b_h) + (\nabla p_h^{a^{n+1}}, \boldsymbol{v}b_h) + \rho_0(\boldsymbol{u}_h^{a^{n+1}}\cdot\nabla\bar{\boldsymbol{u}}, \boldsymbol{v}b_h)$$
$$+\sum_{e=1}^{n_{el}}(\tau_{\boldsymbol{u}}\mathcal{P}\big[-\rho_0\bar{\boldsymbol{u}}\cdot\nabla\boldsymbol{u}_h^{a^{n+1}} - \nabla p_h^{a^{n+1}} - \rho_0\boldsymbol{u}_h^{a^{n+1}}\cdot\nabla\bar{\boldsymbol{u}}\big],$$
$$-\rho_0\bar{\boldsymbol{u}}\cdot\nabla\boldsymbol{v}b_h - \nabla q_h + \rho_0\boldsymbol{v}b_h\nabla\cdot\bar{\boldsymbol{u}} + \rho_0\boldsymbol{v}b_h\cdot\nabla\bar{\boldsymbol{u}})_{\Omega_e} = 0. \tag{3.42b}$$

3.4 Numerical examples

3.4.1 Wave propagation in solenoidal convective and shear mean flows

The purpose of this example is twofold. On the one hand it will allow one to check the influence of the various terms appearing in the acoustic perturbation equations (3.4). On the other hand, it will help determining the values of the constants C_1, C_2 and C_3 appearing in the stabilization parameters of (3.39). Throughout section 4, the units of all quantities will be those of the SI system and will be not explicitly written.

The example consists of a squared computational domain having dimensions $\Omega = [-100, 100] \times [-100, 100]$. A time varying monopole source of

strength,

$$Q = \exp\left[-\ln(2)\frac{x^2+y^2}{9}\right]\cos(\omega t), \tag{3.43}$$

has been placed at the origin $(0,0)$ and generates acoustic waves of angular frequency $\omega = 175$. The propagation of the acoustic waves will be analyzed for different solenoidal mean velocity profiles $\bar{\boldsymbol{u}}_{\text{inc}}$ in the domain. That will reveal the importance of the distinct APE terms in (3.4). The cases that have been considered are:

- Case A.1: No mean flow, i.e., $\bar{\boldsymbol{u}}_{\text{inc}} = \mathbf{0}$. In this case the APE reduce to the standard wave equation in mixed form.
- Case A.2: A constant mean flow with $\bar{\boldsymbol{u}}_{\text{inc}} = (70, 0)$. The APE now reduce to the convective wave equation in mixed form for uniform mean flows.
- Case A.3: A solenoidal shear mean flow with the profile plotted in Fig. 3.1a resulting from equation (3.44) below. This corresponds to the convective wave equation in mixed form for the case of a non-uniform mean flow. The reaction term $\rho_0\ \boldsymbol{u}^a \cdot \nabla\bar{\boldsymbol{u}}_{\text{inc}}$ in (3.4b) is not taken into account in the simulation.
- Case A.4: The shear mean flow of Case 3 but now considering the full APE in (3.4) with all non-uniform convective and reaction terms included. This was the benchmark case proposed in [73] to test several APE formulations.

To perform all the simulations for the cases above, the computational domain has been discretized with an unstructured mesh of 87 616 triangular elements. Spurious reflections at the boundaries have been avoided by means of a simple perfectly matched layer (PML) according to the model in [166]. Two additional absorption terms αp and $\alpha^* \boldsymbol{u}$ have been respectively added to the equations (3.4a) and (3.4b). α is the attenuation coefficient and $\alpha^* := (\mu_{\boldsymbol{u}}/\mu_p)\alpha$. The attenuation factor is set to zero within the computational domain Ω, while it has been set to $\alpha = 0.0004$ in the absorbing PML surrounding Ω. The width of the PML is 50. With regard to the values of the physical parameters in (3.4), we have considered an air density of $\rho_0 = 1.14$ and a sound speed of $c_0 = 350$. The shear mean velocity for Cases A.3 and A.4 is defined by (see Fig. 3.1a),

$$\bar{\boldsymbol{u}}_{\text{inc}}(x, y) = (\bar{U}\tanh(2y/\delta), 0), \tag{3.44}$$

where $\bar{U}$ is the maximal velocity with value $\bar{U} = 70$ (Mach number $M = 0.2$) and $\delta = 50$ denotes the shear-layer thickness. The resulting mean velocity

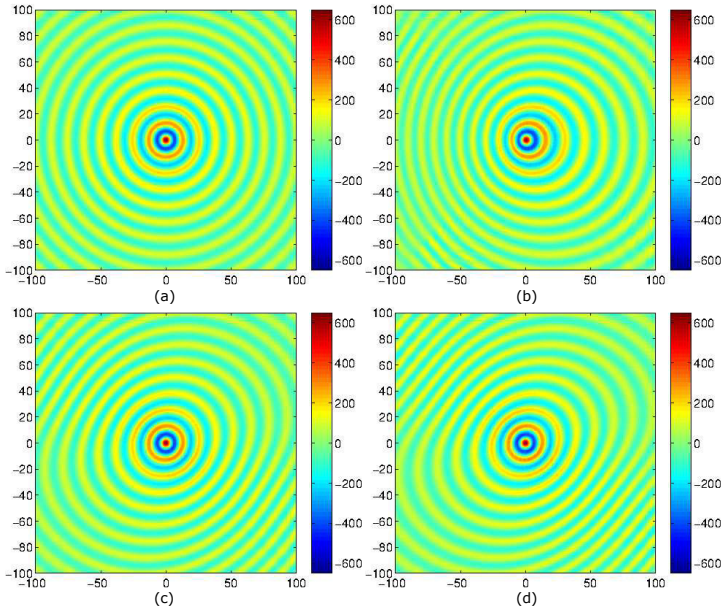

Figure 3.2: Acoustic pressure contours at time $t = 0.5$. (a) Case A.1: No mean flow. (b) Case A.2: Uniform mean flow. (c) Case A.3: Shear flow with reaction term excluded. (d) Case A.4: Shear flow with reaction term included.

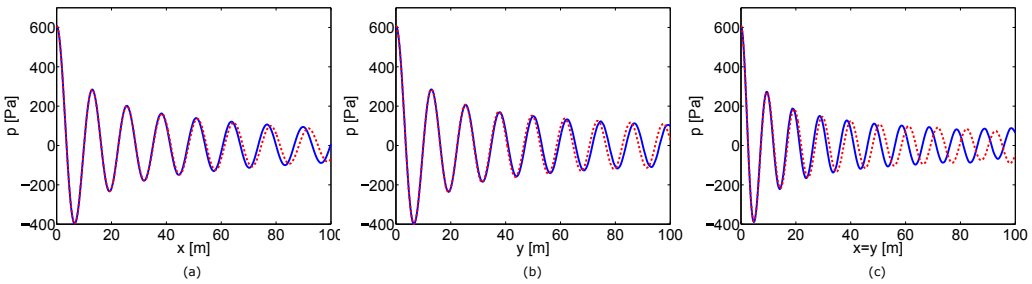

Figure 3.3: Pressure cuts at $t = 0.5$ corresponding to Fig. 3.2. Case A.3 (dashed red), Case A.4: (continuous blue). (a) x- axis. (b) y-axis. (c) $x = y$.

vector field is plotted in Fig. 3.1b. Finally, in what concerns time evolution, an incremental step of $\Delta t = 7 \times 10^{-4}$ has been chosen to discretize the interval $[0, 0.5]$.

The resulting acoustic pressure fields for Cases A.1-A.4 have been plotted in Fig. 3.2 at the time instant $t = 0.5$. As observed in Fig. 3.2a, the wavefronts simply consist of concentric circles propagating outwards for Case A.1, because there is no mean velocity in the domain. We thus recover the expected radiation pattern of a monopole source. When a uniform mean flow is imposed moving from left to right in Case A.2 (Fig. 3.2b), the front waves

travelling upstream get stretched and the wave length diminishes, whereas the opposite effect takes place for waves propagating downstream. This is nothing but the well-known Doppler effect. Cases A.3 and A.4 serve to show the importance of taking into account the reaction term in the APE. It is apparent from Figs. 3.2c and d that if one was to simulate sound propagation in a shear flow, the use of a convective mixed wave equation with non-uniform velocity (Case A.3) would lead to substantial differences when compared to the predictions made by the full APE (Case A.4). These discrepancies might be better appreciated by plotting the acoustic pressure along the positive x-axis, positive y-axis and along a diagonal cut $x = y$ in the second quadrant of the subfigures Figs. 3.2c, d (see respectively Figs. 3.3a, b and c where the dashed red line stands for Case A.3 and the blue continuous line for Case A.4).

A final plot showing the differences in wave propagation for Cases A.1-A.4 is that of Fig. 3.4. In that figure we see the time evolution of the acoustic pressure tracked at an arbitrary point A with coordinates $\boldsymbol{x}_A = (49.6, -34.1)$. The differences in amplitudes and phases between cases become again very visible. The zero pressure initial time steps correspond to the time it takes for the first wavefront to travel from the origin, where the source is placed, to A.

On the other hand, and as mentioned above, the second goal of this section is to determine the values of the constants C_1, C_2 and C_3 in the stabilization parameters of (3.39). The simulations just reported have been carried out following the numerical strategy in section 3.4, but the values for that constants were yet to be presented. Let us remark that for Case A.1, C_1 is the only constant playing a role given that $\bar{\boldsymbol{u}}_{\text{inc}} = \boldsymbol{0}$. For Cases A.2 and A.3, C_1 and C_2 get involved but not C_3 because the reaction term

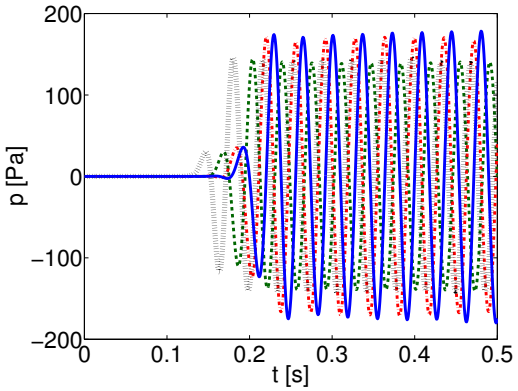

Figure 3.4: Comparison of the evolution of the pressure in the point $(49.6, -34.1)$ for Case A.1 (dashed green), Case A.2 (dotted black), Case A.3 (dot-dashed red) and Case A.4 (continuous blue).

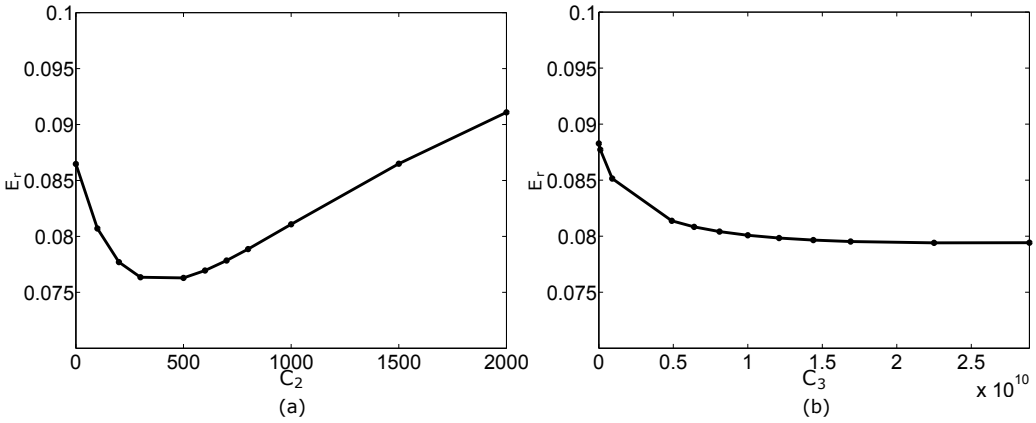

Figure 3.5: Relative error of the stabilized FEM formulation dependence on the values of the constants in the stabilization matrix. (a) Case 3: relative error dependence on C_2. (b) Case 4: relative error dependence on C_3.

is not contemplated. Finally, all constants are to be considered in Case A.4.

To find suitable values for the constants, we have compared the results of the stabilized FEM simulations with those from a reference solution computed with a very fine mesh of 420 585 elements. For such a fine mesh the contribution of the stabilization terms has been checked to be almost negligible. To proceed we have chosen to compute the relative L^2-error between the computed acoustic pressure p^a and that from the reference solution p^r. This is given by $\boldsymbol{varepsilon} = \|p^a - p^r\|_2 / \|p^r\|_2$ with $\|p^a - p^r\|_2 = \left[\int_{\Omega_{\boldsymbol{varepsilon}}} (p^a - p^r)^2 d\Omega_{\boldsymbol{varepsilon}}\right]^{1/2}$. The error is computed in the subdomain $\Omega_{\boldsymbol{varepsilon}} \subset \Omega$ so as not to contact the boundaries of Ω and avoid

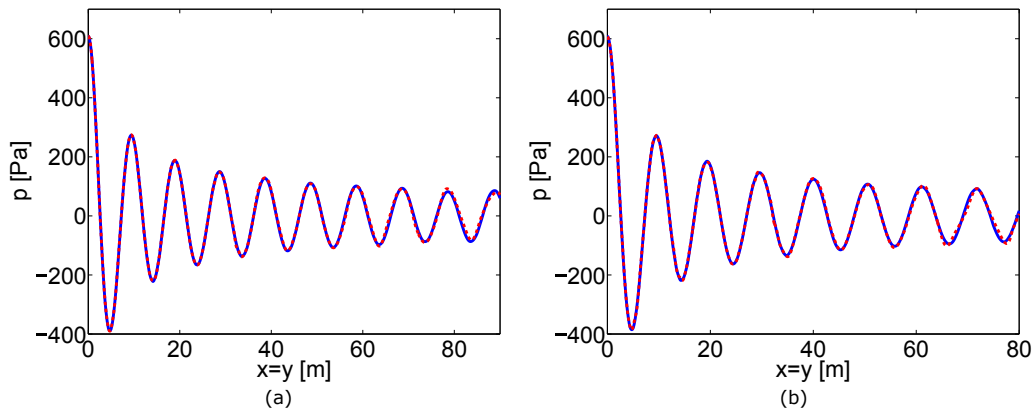

Figure 3.6: Reference acoustic pressure (blue line) versus stabilized FEM acoustic pressure (red dashed line) for the domain diagonal taking $C_1 = 100$, $C_2 = 500$ and $C_3 = 100000^2$. (a) Case A.3. (b) Case A.4.

any possible pollution that could stem from the performance of the PML. It is to be noted that we could also have included the relative error for the acoustic velocity in the process, or a weighted combination of relative errors for both, the acoustic velocity and the acoustic pressure. However, given that usually in acoustic problems the latter is the main variable of interest, we have focused on the acoustic pressure.

The value of the C_1 constant was already established in [49], where it appeared in a slightly different form. Given that for $\bar{\boldsymbol{u}}_{\text{inc}} = \mathbf{0}$ the results from [49] are to be recovered, we have fixed $C_1 = 100$ to that purpose. The constant C_2 has been selected focusing on Case A.3. For the terms in the denominator of (3.39) to have similar influence, C_2 should not surpass a value of 2 000. Having a look at the relative error plot in Fig. 3.5a we observe that an appropriate value for C_2 is $C_2 = 500$. Once fixed $C_1 = 100$ and $C_2 = 500$, we have resorted to Case A.4 to adjust the constant C_3. This constant should not exceed $150\ 000^2$, and as observed from Fig. 3.5b, the relative error get stabilized for $C_3 \approx 100\ 000^2$. As in most stabilized numerical methods, once tuned, the constants $C_1 = 100$, $C_2 = 500$ and $C_3 = 100\ 000^2$ are expected to have a rather general character and therefore to apply to many other numerical examples.

To conclude this example, we show the acoustic pressure for the stabilized FEM and reference solutions for the diagonal $x = y$ of the domain in Fig. 3.6. As observed almost no differences can be appreciated.

3.4.2 Wave propagation in non-solenoidal shear mean flows

The aim of this section is to test the reliability of the proposed FEM approach, with the stabilization constants derived in the previous subsection, when facing wave propagation in non-solenoidal mean flows. this involves dealing with the APE in (3.3). The same computational domain and boundary conditions as for cases A.1 to A.4 are contemplated but now wave propagation takes place on the following two non-solenoidal mean flows

- Case B.1: Mean flow $\bar{\boldsymbol{u}} = (\frac{1}{3}\sqrt{x^2+y^2}, \frac{1}{3}\sqrt{x^2+y^2})$.
- Case B.2: Mean flow $\bar{\boldsymbol{u}} = (\bar{U}\tanh(2y/\delta), y)$, $\bar{U} = 70$.

The results for the above two cases are shown in Fig. 3.7. Figs. 3.7a and c respectively show the velocity fields for Cases B.1 and B.2. The corresponding acoustic pressure fields are depicted in Figs. 3.7b and d.

We have computed the relative error of the proposed stabilized FEM against a reference solution obtained with the same fine mesh of the previous subsection. This has resulted in a value of $E_r = 5.6\%$ for Case B.1 and

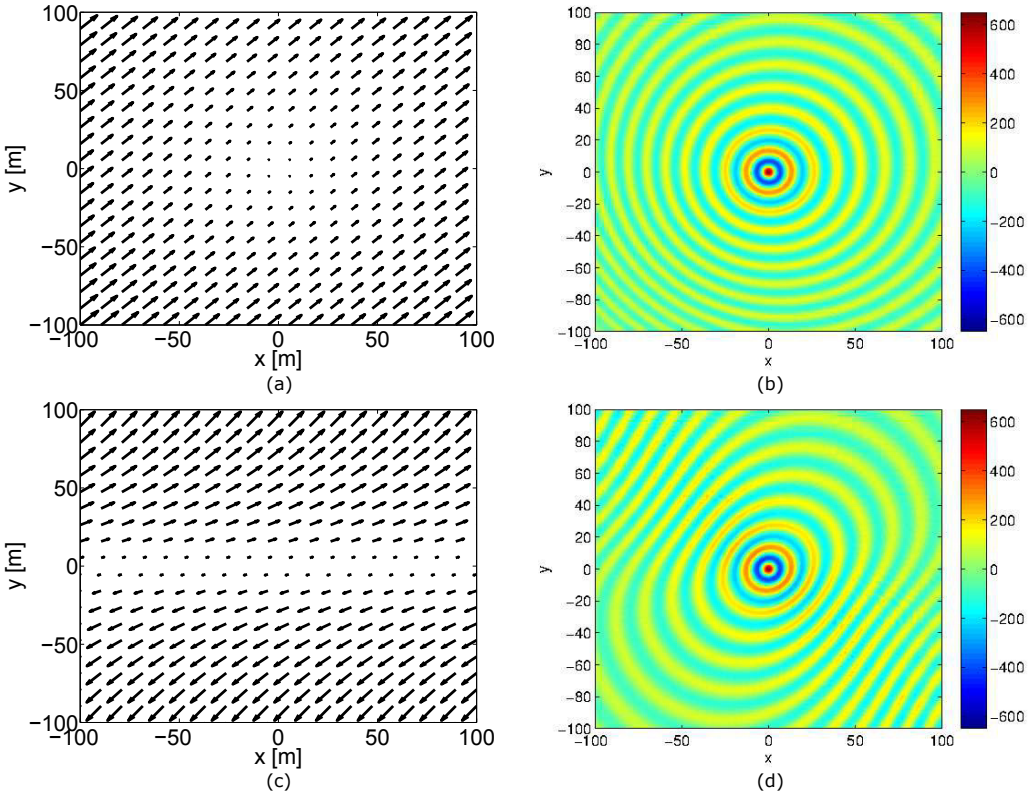

Figure 3.7: Mean velocity fields and acoustic pressure contours at time $t = 0.5$. (a) Case B.1: Velocity field. (b) Case B.1: Pressure contours. (c) Case B.2: Velocity field. (d) Case B.2: Pressure contours.

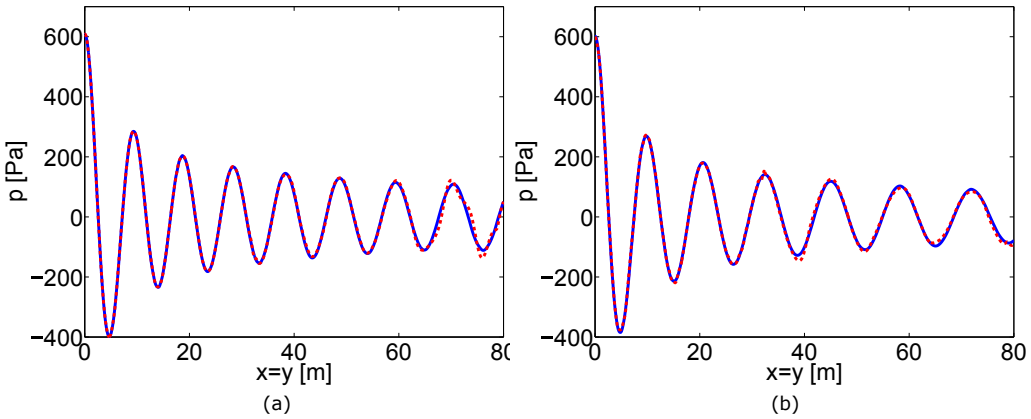

Figure 3.8: Reference acoustic pressure (blue line) versus stabilized FEM acoustic pressure (red dashed line) for the domain diagonal taking $C_1 = 100$, $C_2 = 500$ and $C_3 = 100000^2$. (a) Case B.1. (b) Case B.2.

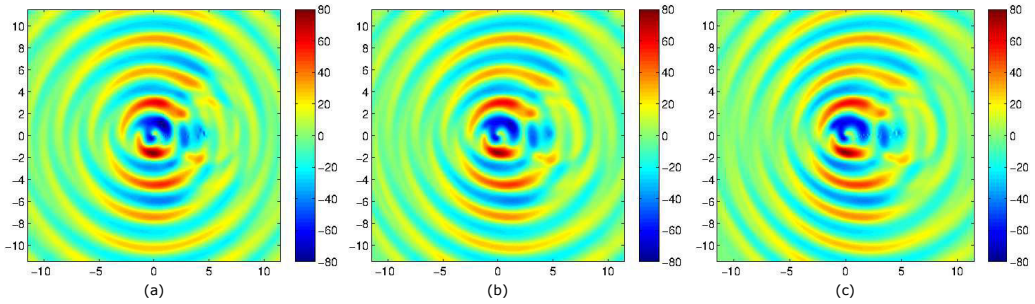

Figure 3.9: Acoustic pressure contours at time $t = 0.15$. (a) Case C.1. (b) Case C.2. (c) Case C.3.

$E_r = 8.6\%$ for Case B.2. The comparison between the acoustic pressure for the stabilized FEM and reference solution has been plotted for the positive diagonal $x = y$ in Fig. 3.8. Very slight discrepancies are found which confirms that the stabilized FEM also performs well for the tested non-solenoidal fields.

3.4.3 Aeolian tone generated by a single cylinder

As a final numerical test, we will apply the stabilized FEM approach to the APE, to a more complex situation. This consists in the classical problem of aeolian tone generation by flow past a cylinder. From a physical point of view, the aeroacoustic problem of aeolian tones is well-known and described in literature, see e.g., [107, 68] among many others. The problem consists of a flow impinging on a cylinder. For a certain range of Reynolds numbers, a wake of shedding vortices develops past the cylinder inducing lift fluctuating forces on it. That results in the emission of acoustic waves, which exhibit a dipolar radiation pattern at the acoustic far field. For low Mach numbers, the problem can be solved by first performing an incompressible CFD simulation to extract the acoustic source terms and the mean flow, which can then be inserted into the APE (3.4) to resolve the acoustic field. Our interest in this example is that of showing again the role played by the convection and reaction terms of the APE in the generated aeroacoustic pressure. Consequently, no results will be presented concerning the CFD simulation (they are rather standard and can be found elsewhere e.g., [91, 92]).

In a nutshell and as regards the CFD computation, a two-dimensional cylinder with diameter D=0.1 has been embedded in a squared computational domain of dimensions $\Omega_{CFD} = [-6, 6] \times [-6, 6]$ with an impinging flow velocity, in Cartesian coordinates, of $\boldsymbol{u}_0 = (50, 0)$ (Mach number $M \approx 0.14$ for a sound speed of $c_0 = 350$). The Reynolds number of the problem is $\mathrm{Re} = \rho_0 |\boldsymbol{u}_0| D/\mu = 1\ 000$, where μ denotes the air viscosity. The domain

Ω_{CFD} has been meshed with 295 141 linear finite elements. The incompressible Navier-Stokes equations have been solved for a time range of 0.15, using the second order BDF2 time marching scheme with a time step of 9×10^{-5}. The solution has resulted in the generation of a Von Kármán vortex street, with vortices shed at a frequency of 120.

The APE have been resolved in a larger computational domain $\Omega_{ac} = [-12, 12] \times [-12, 12]$, $\Omega_{CFD} \subset \Omega_{ac}$, using an unstructured mesh of 421 804 linear elements. The CFD and acoustic meshes coincide in the domain Ω_{CFD}. The values for the constants in the stabilization parameters found in section 4.1 have been used for the simulations. Similarly to what has been done in that subsection, the following three situations have been considered to establish the influence of the various terms in the APE,

- Case C.1: No mean flow; the APE simplifies to the wave equation in mixed form. The sources terms are obtained from the CFD computation.

- Case C.2: The APE using the mean flow and source terms from the CFD computation but neglecting the reaction term. Namely, only non-uniform convection effects are considered.

- Case C.3: The full APE taking into account non-uniform convection and reaction terms.

In Fig. 3.9 we show the acoustic pressure contour levels at the far field for each case. As observed from Fig. 3.9a, a clear dipole radiation pattern emerges with waves propagating perpendicular to the incident inlet velocity, in Case C.1. However, when convection is taken into account (Case C.2) the wavefronts propagate upstream (see Fig. 3.9b) as expected [91], the effect being more pronounced if one includes reaction (Case C.3, Fig. 3.9c).

The differences in phase and amplitude among Cases C.1-C.3 can be also very clearly appreciated if we plot one-dimensional cuts of the domain in the x, y and diagonal $x = y$ directions (see Fig. 3.10a, b and c). Again, this is also made apparent when plotting the time evolution of the acoustic pressure at three arbitrary points located at $\boldsymbol{x}_1 = (-0.2, 5.8)$, $\boldsymbol{x}_2 = (3.1, 0)$ and $\boldsymbol{x}_3 = (9, 0)$, see Figs. 3.11a, b and c.

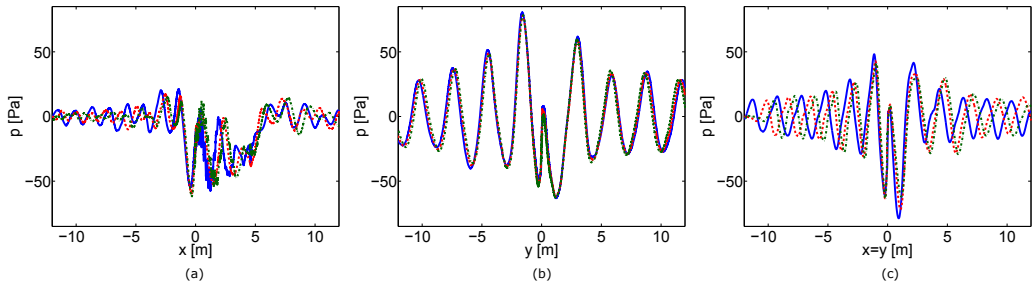

Figure 3.10: Pressure cuts at $t = 0.15$ corresponding to Fig. 3.9. Case C.1 (continuous blue), Case C.2 (dashed red line), Case C.3 (dashed-dot green line). (a) x- axis. (b) y- axis. (c) $x = y$.

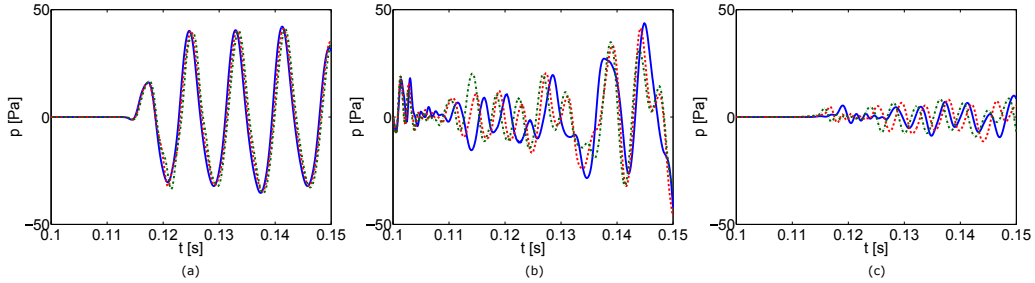

Figure 3.11: Comparison of the evolution of the pressure for Case C.1 (continuous blue), Case C.2 (dashed red line) and Case C.3 (dashed-dot green line). (a) $\boldsymbol{x}_1 = (-0.2, 5.8)$. (b) $\boldsymbol{x}_2 = (3.1, 0)$. (c) $\boldsymbol{x}_3 = (9, 0)$.

3.5 Conclusions

The FEM solution of wave operators in mixed form requires using tailored finite elements that satisfy the discrete version of the continuous problem inf-sup condition. However, these finite elements are difficult to implement and though valid for the wave equation in mixed form, it has not been tested if they could work well for more complex operators, like the ones in the acoustic perturbation equations for low Mach numbers.

In this work, we have suggested to circumvent that problem by resorting to a stabilizing variational multiscale FEM formulation for the APE. The APE acoustic pressure and acoustic particle velocity get split into large scales, which can be resolved by the computational mesh and small scales whose influence onto the former has to be modelled. A residual-based model has been chosen for that purpose, the key for its good performance being the design of the matrix of stabilization parameters. The latter has been achieved by setting the small scales equations in the wavenumber domain and using appropriate inequality bounds for its norm as well as for the APE

residual. The accomplishment of the proposed strategy has been checked by means of some numerical examples involving wave propagating in solenoidal and non solenoidal non-uniform mean flows, involving convection and shear.

Chapter 4

Unified solver for fluid dynamics and aeroacoustics in isentropic gas flows

The high computational cost of solving numerically the fully compressible Navier-Stokes equations, together with the poor performance of most numerical formulations for compressible flow in the low Mach number regime, has led to the necessity for more affordable numerical models for Computational Aeroacoustics. For low Mach number subsonic flows with neither shocks nor thermal coupling, both flow dynamics and wave propagation can be considered isentropic. Therefore, a joint isentropic formulation for flow and aeroacoustics can be devised which avoids the need for segregating flow and acoustic scales. Under these assumptions density and pressure fluctuations are directly proportional, and a two field velocity-pressure compressible formulation can be derived as an extension of an incompressible solver. Moreover, the linear system of equations which arises from the proposed isentropic formulation is better conditioned than the homologous incompressible one due to the presence of a pressure time derivative. Similarly to other compressible formulations the prescription of boundary conditions will have to deal with the backscattering of acoustic waves. In this sense, a separated imposition of boundary conditions for flow and acoustic scales which allows the evacuation of waves through Dirichlet boundaries without using any tailored damping model will be presented. Finally, the discrete formulation will be extended to an ALE frame of reference in order to reduce the complexity of the hybrid method for moving domains presented in Chapter 2.

4.1 Background

The compressibility behind the acoustics in Computational Fluid Dynamics (CFD) has been widely treated for several purposes along the history of numerical methods. Towards the 70's, the artificial compressibility method introduced in [42] was developed with the objective of reducing the computational cost of solving the incompressible Navier-Stokes equations in 3D domains. In this framework, the artificially added compressibility through a density or pressure perturbation term was not only a numerical artifact, but a term that could be easily associated to the acoustics of a low speed compressible flow. However, the artificial compressibility method did not aim to describe the acoustic scales of the flow, but to introduce a numerical relaxation parameter which allowed an easier fulfillment of the continuity condition. The main modification of the incompressible Navier-Stokes consisted in adding an artificial time derivative of the pressure to the dimensionless continuity equation, which improved the condition number of the final system to be solved. A similar method was later applied in [41] to the low speed compressible Navier Stokes equations, in which a time derivative of the primitive variables was added to the energy equation in order to reduce the big disparity between the flow velocity and the sound speed. The Chorin method was extended for both incompressible and slow compressible flows in [170] by adding similar terms to all equations in order to obtain a symmetric hyperbolic problem. In other cases such as low Mach number (M) compressible flows, the goal consisted precisely in going in the opposite direction and identifying the acoustic scales of the flow in order to remove them from the problem (see [70]), because they led to an ill-conditioning of the system and to the backscattering of sound waves into the computational domain.

While the addition of a certain amount of compressibility has made the calculation of incompressible flows easier without taking into account the consequent acoustic field, the inclusion of compressibility in the flow formulation has been a drawback for calculating acoustics when dealing with low speed flows. The conservative compressible flow equations are considered the complete representation of the aeroacoustic problem because they describe directly all flow and acoustic scales without any need for modeling, which in terms of Computational Fluid Dynamics (CFD) is called Direct Numerical Simulation (DNS) [21], and in acoustics is referred as Direct Noise Computation (DNC) [18]. However, as stated above, this formulation performs poorly for Mach numbers tending to zero due to the huge difference between flow velocity and wave propagation speed, which causes convergence problems. In order to avoid the bad conditioning of the problem, a series of hybrid methods, which segregate the acoustics from the CFD, were devel-

oped. The so called acoustic analogies resolve the acoustic scales by means of an inhomogeneous wave equation where the source term that represents the aerodynamic noise comes from a previous flow calculation. The pioneer work in this field is presented in [130]. This method has been progressively extended to include diffraction by solid boundaries [65] and moving surfaces [178]. Other hybrid methods, such as the incompressible-acoustic split method presented in [99, 160] enrich the incompressible flow equations with a variable density linked to pressure perturbations. Then, the time derivative of this perturbed density is translated into isentropic fluctuations of velocity and pressure that are propagated using a purely acoustic compressible solver after subtracting the incompressible component of the flow field. In a similar way, some formulations propagate the near field flow information to the far field with the Linearized Euler Equations (LEE) [33, 19, 158] or with the acoustic perturbation equations [74, 125, 97], which consist in an acoustic filtering of the LEE source term. All these methods allow a considerable flexibility, for example the use of a different discretization for each problem, as well as different flow and acoustic models. However, these models are based on assumptions and the subsequent approximation errors need to be properly assessed. In some cases, acoustic source terms need to be modeled and might not be straightforward to implement in a finite element code. Moreover, the segregated calculation of the flow and acoustic components only assumes a one-way coupling from flow to acoustics, but not the other way around.

The formulation proposed in this work aims for a simplification of Computational Aeroacoustics (CAA) of isentropic compressible flows and proposes a general framework that can be applied to any geometry, spatial discretization or flow regime below the transonic range. It consists in a compressible formulation with primitive variables without solving for the energy equation, since the flow is considered to be isentropic, which after condensing the density field becomes a system of equations in terms of the velocity and the pressure, like in incompressible flow solvers. As a consequence, the implementation cost is very low when one departs from an already implemented incompressible flow solver. Also, the computational cost is reduced with respect to other methodologies due to the following reasons: getting rid of the fully compressible approach and solving only for velocity and pressure, solving all scales at once without acoustic analogies and improving the condition number of the system for the incompressible limit. This formulation provides two important advantages respect to the acoustic analogies and other hybrid methods presented in the previous paragraph: first, it takes into account the acoustic feedback on the flow scales and second, the validity of the acoustic field will not depend on the motion of the flow or the presence of obstacles. These are precisely the main advantages of a DNC.

In fact, for flows with $M \to 0$ this solver should converge to the solution of a DNC, but with a much lower computational cost. The only drawback of such a unified system will be, again like in a DNC, the lack of visualization of the acoustic fluctuations at the near field, where the aerodynamic scales are totally dominant and the wave propagation cannot be extracted like in [154] or [96]. As in all compressible flow models, an adequate equation of state needs to be chosen, in this case relating only density and pressure. For simplicity the ideal gas law has been used to close the problem, but the formulation can be easily extended to any other equation of state.

Since the present chapter aims at solving both aerodynamics and acoustics scales in a single calculation, the prescription of compatible and accurate boundary conditions for both components of the solution has been an important aspect of this work. From a numerical point of view, the imposition of boundary conditions can be performed as in the incompressible case, avoiding the difficulties found in compressible flows. However, omitting the acoustic scales in the treatment of the external boundaries leads to undesired wave reflections which affect the accuracy and the stability of the unified solver. Therefore, a new method including the combined imposition of essential boundary conditions in a weak sense on the mean flow variables [53], and a Sommerfeld boundary condition for the acoustic component of the pressure will be presented [71]. This combination will allow the acoustic wave to leave the domain through boundaries where the mean flow has been prescribed a certain boundary condition.

As stated above, the present formulation has been implemented as an update of an already existent FEM incompressible flow solver, but is not restricted to this numerical framework. In fact, [177] presents a CAA formulation based on the Lattice-Boltzmann Method (LLM) for isentropic flows, although in this case flow and acoustic scales are segregated. Linear elements have been used for simplicity, but the method can be also automatically applied to high-order grids leading to a decrease of the approximation error, as long as the chosen element is stable. In this sense, stability is provided by the Variational Multiscale Method (VMS), which in turn models the scales that are not captured by the spatial discretization (subgrid scales) in form of turbulent dissipation [60, 94].

The chapter is organized as follows: a detailed presentation of the isentropic compressible equations is shown in Section 4.2. The details of the aforementioned prescription of boundary conditions are presented in Section 4.3, and the stabilized time-discrete finite element formulation is derived in Section 4.4. Then, this formulation is adapted to ALE references for cases with moving domains in Section 4.5. Finally, numerical results are presented in Section 4.6: three cases consisting in a 2D flow around a cylinder, a 3D flow around a NACA0012 airfoil and a 2D open cavity will be presented and

benchmarked against the Lighthill analogy [130] with incompressible flow, the Ffowcs Williams Hawkings (FWH) acoustic analogy [178] using compressible flow and a DNS, respectively. This analysis will allow to show the performance of the present method in its whole application range. Furthermore, the oscillating airfoil simulated in Chapter 2 will be simulated again for benchmarking both ALE formulations.

4.2 Problem formulation

4.2.1 The differential problem

The present work focuses in the study of the aerodynamic and acoustic behavior of an ideal gas undergoing a reversible thermodynamical process, which is a realistic hypothesis in most aeroacoustic problems without heat transfer or shocks. This initial assumption allows a drastic simplification of the compressible Navier-Stokes equations, since the energy equation does not need to be solved and the primitive variables of the problem can be used. Moreover, a general formulation can be derived for both slow and high speed isentropic flows taking into account the following equalities (see e.g. [144]):

$$\frac{p_0}{p} = \left(1 + \frac{\gamma - 1}{2}\mathrm{M}^2\right)^{\frac{\gamma}{\gamma-1}}, \tag{4.1}$$

$$\frac{\rho_0}{\rho} = \left(1 + \frac{\gamma - 1}{2}\mathrm{M}^2\right)^{\frac{1}{\gamma-1}}, \tag{4.2}$$

where γ is the adiabatic constant of the gas, p and ρ are the total pressure and density fields including perturbations caused by the compressibility of the medium, whereas p_0 and ρ_0 are the same fields at stagnation conditions [144]. M is the Mach number, defined as:

$$\mathrm{M} := \frac{|\mathbf{u}|}{c_0}, \tag{4.3}$$

where $|\mathbf{u}|$ is either the modulus of the pointwise velocity (or a characteristic value of it if one wants to define a global Mach number) and c_0 is the speed of sound in an ideal gas, defined as $c_0 = \sqrt{\frac{\gamma R T_0}{\mathcal{M}}}$, where T_0 is the temperature field at stagnation, R [J/K-mol] is the universal gas constant and $\mathcal{M}$ [kg/mol] is the molar mass of the gas. From Eq. (5.1) the following equality between ρ and p can be easily obtained:

$$\frac{p_0}{p} = \left(\frac{\rho_0}{\rho}\right)^{\gamma}. \tag{4.4}$$

Then, differentiating with respect to time both sides of Eq. (4.4) and using the equation of state for an ideal gas, $p_0 = \frac{\rho_0 R T_0}{\mathcal{M}}$, the next expression connecting pressure and density time derivatives can be found:

$$\partial_t p = \frac{p_0}{\rho_0}\gamma\left(1+\frac{\gamma-1}{2}\mathrm{M}^2\right)^{-1}\frac{\partial\rho}{\partial t} = \frac{RT_0}{\mathcal{M}}\gamma\left(1+\frac{\gamma-1}{2}\mathrm{M}^2\right)^{-1}\partial_t\rho. \tag{4.5}$$

The final time derivative of the equation of state for a low speed gas flow can be approximated as

$$\partial_t p \approx c_0^2\partial_t\rho, \tag{4.6}$$

the approximation error being $\mathcal{O}\left(\mathrm{M}^2\right)$. Otherwise the speed of sound c has to be computed as follows:

$$c^2 = c_0^2\left(1+\frac{\gamma-1}{2}\mathrm{M}^2\right)^{-1}, \tag{4.7}$$

and then the following equation can be used:

$$\partial_t p = c^2\partial_t\rho. \tag{4.8}$$

The same procedure can be applied to the pressure gradient, obtaining the same relationship with respect to the density gradient. This explicit connection between pressure and density variations allows one to greatly simplify the compressible Navier-Stokes equations, since density perturbations can be expressed in terms of pressure. It is important to highlight that the limit $\mathrm{M}\to 0$ will lead to a problem which will be very similar to the one resulting from the artificial compressibility method and will contain the acoustic scales of the flow. This is remarkable if it is compared to other non-isentropic formulations for low Mach numbers (see for instance [10]), where density variations are linked exclusively to temperature oscillations, and as a consequence no acoustics are captured.

Let us consider a computational domain $\Omega\subset\mathbb{R}^d$ (where $d=2,3$ is the number of space dimensions) with a domain boundary $\Gamma=\partial\Omega$ and let $(0,T)$ be the time interval of analysis. The isentropic compressible equations are then:

$$\rho\partial_t\mathbf{u}+\rho\left(\mathbf{u}\cdot\nabla\right)\mathbf{u}-\mu\nabla^2\mathbf{u}-\frac{1}{3}\mu\nabla\left(\nabla\cdot\mathbf{u}\right)+\nabla p=\mathbf{0}\text{ in }\Omega, \tag{4.9}$$

$$\partial_t\rho+\mathbf{u}\cdot\nabla\rho+\rho\nabla\cdot\mathbf{u}=0\text{ in }\Omega, \tag{4.10}$$

where $\mathbf{u}$ is the velocity and μ the dynamic viscosity. Boundary and initial conditions need to be appended to this problem. Using Eq. (4.5) $\partial_t\rho$ can be expressed in terms of $\partial_t p$ and the continuity equation becomes

$$\frac{1}{c^2}\partial_t p+\frac{1}{c^2}\mathbf{u}\cdot\nabla p+\rho\nabla\cdot\mathbf{u}=0\text{ in }\Omega, \tag{4.11}$$

where $c(\mathbf{x}, t)$ is given by Eq. (4.7) and $\mathbf{x}$ is the spatial coordinate vector. Despite all simplifications, the previous equation still depends on the function c and two density dependent terms remain in the momentum equation. Calculating these two fields as implicit functions of $[\mathbf{u}, p]$ would increase the complexity of the new scheme with new non-linearities. In this sense, equations (5.1) and (4.7) will be used for closing the problem and obtaining a formulation which only depends on the velocity and pressure fields.

4.2.2 Weak formulation

The next step consists in deriving the variational formulation of the previous problem. Let us denote with $\langle \cdot, \cdot \rangle_\omega$ the integral of the product of two functions in the domain ω, with the subscript omitted when $\omega = \Omega$. Let V and Q be the functional spaces where for each time t the velocity and pressure solutions live, respectively, with appropriate regularity that we will not analyze here. Then, defining the velocity and pressure test functions $\mathbf{v} \in V$ and $\rho q \in Q$, the variational formulation can be written in terms of the forms:

$$\begin{aligned} B([\mathbf{u}, p], [\mathbf{v}, \rho q]) =& \langle \rho \mathbf{v}, \partial_t \mathbf{u} \rangle + \langle \rho \mathbf{v}, (\mathbf{u} \cdot \nabla)\, \mathbf{u} \rangle + \mu \langle \nabla \mathbf{v}, \nabla \mathbf{u} \rangle \\ &+ \frac{1}{3} \mu \langle \nabla \cdot \mathbf{v}, \nabla \cdot \mathbf{u} \rangle - \langle \nabla \cdot \mathbf{v}, p \rangle \\ &+ \left\langle \frac{1}{c^2} q, \partial_t p \right\rangle + \left\langle \frac{1}{c^2} q, \mathbf{u} \cdot \nabla p \right\rangle + \langle \rho q, \nabla \cdot \mathbf{u} \rangle, \qquad (4.12) \\ \tilde{B}_{\mathrm{B}}([\mathbf{u}, p], \mathbf{v}) =& - \langle \mathbf{v}, \mathbf{n} \cdot \sigma(\mathbf{u}, p) \rangle_\Gamma, \qquad (4.13) \end{aligned}$$

where the stress tensor is defined as $\sigma(\mathbf{u}, p) = -p\mathbf{I} + \mu \nabla \mathbf{u} + \frac{1}{3} \mu\, (\nabla \cdot \mathbf{u})\, \mathbf{I}$. The Galerkin weak form of the problem prior to applying boundary conditions can be written as follows: for all time $t > 0$, find $\mathbf{u}(t) \in V$ and $p(t) \in Q$, with appropriate regularity in time, such that:

$$B([\mathbf{u}, p], [\mathbf{v}, \rho q]) + \tilde{B}_{\mathrm{B}}([\mathbf{u}, p], \mathbf{v}) = 0 \qquad (4.14)$$

for all $\mathbf{v} \in V$ and $\rho q \in Q$. Moreover, initial conditions need to be appended. Boundary conditions will be defined in the following section, proposing a new formulation for the form $\tilde{B}_{\mathrm{B}}$. This will give rise to a decomposition of the form $\tilde{B}_{\mathrm{B}} = B_{\mathrm{B}} - L_{\mathrm{B}}$, with B_{B} depending on the unknowns and L_{B} on the boundary data, so that it can be moved to the right-hand-side of (4.14).

4.3 Imposition of boundary conditions

4.3.1 Mean and acoustic components

Although the intricate prescription of boundary conditions of the fully compressible formulation is avoided in the present problem, new challenges arise

which need to be accounted for. Given that flow and acoustic scales need to be resolved together, an appropriate boundary condition for the acoustic component of the pressure must be used. The main objective of this boundary condition is to avoid the sound waves being backscattered by the external boundaries into the computational domain. There are several numerical methods which deal with this problem, see for instance the reviews in [79] and [87]. Here we highlight some of the most relevant ones. In [169] a non-reflecting boundary condition (NRBC) was presented for the Euler equations in multi-dimensional domains, modeling the waves using the characteristic equations. However, the identification of waves is not so straightforward in the Navier-Stokes equations and the assumption of one-dimensional flow on the boundaries had to be made [145]. This method yields proper results in boundaries where the solution is homogeneous and known, such as the inlet. In [150], [151] and [180] the method was extended using low Mach number asymptotics in order to account for viscous and transverse effects on the wave. Another family of methods are the so called Perfectly Matched Layer (PML) methods, see [26] and [109], which can work under near-field conditions and thus allow for smaller computational domains to be used. These methods use an auxiliary domain beyond the outer boundaries which absorbs the incident waves without reflecting them back. A third alternative for the non-reflection of waves is the use of radiative and outflow conditions developed in [168] and extended in [31]. Similarly to the PML method, these works also consider a secondary domain, but in this case a modified set of equations minimizing reflection is solved at the far-field.

The treatment of the waves must be compatible with the flow velocity boundary conditions. This is of most importance on Dirichlet boundaries where the velocity needs to be prescribed. This need has motivated the development of a method for a unified prescription of flow and non-reflecting boundary conditions, which will be presented next. The method is able to deal with subsonic flows solved in arbitrary geometries, and following the aim of being a general formulation, it is compatible with any non-reflecting model for the acoustic waves, which will not be part of the work scope. The development of the method starts by splitting the two fields of the problem into mean variables $\bar{\mathbf{u}}$ and $\bar{p}$, and oscillatory components $\mathbf{u}'$ and p', as follows:

$$\begin{aligned} \mathbf{u}\left(\mathbf{x},t\right) =& \bar{\mathbf{u}}\left(\mathbf{x},t\right) + \mathbf{u}'\left(\mathbf{x},t\right), \\ p\left(\mathbf{x},t\right) =& \bar{p}\left(\mathbf{x},t\right) + p'\left(\mathbf{x},t\right), \end{aligned} \tag{4.15}$$

where

$$\begin{aligned} \bar{\mathbf{u}}\left(\mathbf{x},t\right) :=& \frac{1}{T_w}\int_{t-T_w}^{t} \mathbf{u}\left(\mathbf{x},s\right) ds \\ \bar{p}\left(\mathbf{x},t\right) :=& \frac{1}{T_w}\int_{t-T_w}^{t} p\left(\mathbf{x},s\right) ds \end{aligned} \tag{4.16}$$

and T_w is an appropriate time window. The mean flow variables are allowed to evolve during the calculation and they do not necessary need to be homogeneous along the boundary, but high frequency variations of these variables are not allowed because they would interfere with $[\mathbf{u}', p']$, which can be identified as the acoustic fluctuations. In other words, eq. (4.16) acts as a low pass filter that attenuates signals beyond a certain cutoff frequency that is determined by T_w.

4.3.2 Split boundary conditions

In order to treat flow and acoustic boundary conditions in an appropriate way, the boundary Γ has been divided into three disjoint subsets Γ_S, Γ_L and Γ_O, which will refer to the solid boundaries where velocity is prescribed to zero, the lateral walls and the outflow, respectively. Whereas the first and the latter ones have a clear physical meaning, Γ_L is defined for numerical convenience: it is composed of any outer boundary with at least one component of the velocity prescribed to a known value, which means that it also encompasses the inlet boundaries, see Fig. 4.1. The upper and lower walls belong to Γ_L because they have been assumed to be a mere truncation of the computational domain. This artificial truncation of the domain, which is performed with the objective of limiting the computational cost, does not assume that the affected boundaries are part of the outflow because this may not properly represent the physics of the flow and could even lead to numerical instabilities. Therefore, the flow needs to be confined without affecting the outward propagation of the waves. This boundary definition has been used for the two cases presented in Section 4.6.

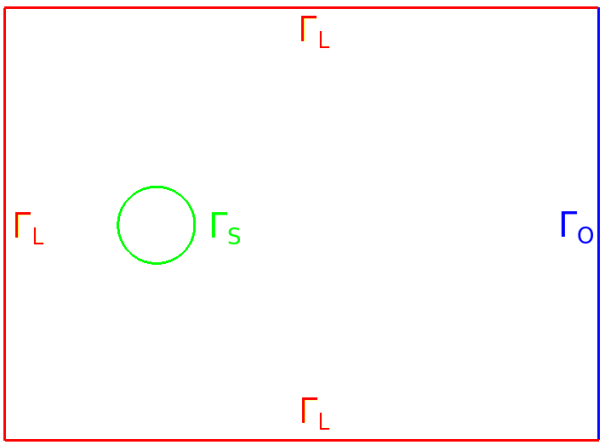

Figure 4.1: Schematic definition of domain boundaries.

On Γ_L and Γ_O, the far-field conditions assume that the acoustic scales are dominant. This means that a naive approach using a zero traction boundary

condition would lead to reflection of the waves into the domain. Therefore, a non-reflecting numerical model must be applied on these boundaries, see for example [71].

The proposed methodology for applying compatible flow and acoustic boundary conditions on Γ_L and Γ_O is based on a weak or weighted prescription of the Dirichlet conditions together with the use of a Sommerfeld type boundary condition. The boundary conditions for the problem can be formulated as described next.

On the solid boundary Γ_{S}, where the velocity is known and the incident waves are expected to reflect, we enforce:

$$\mathbf{u} = \bar{\mathbf{u}} + \mathbf{u}' = \mathbf{u}_{\mathrm{S}} \text{ on } \Gamma_{\mathrm{S}},$$

where $\mathbf{u}_{\mathrm{S}}$ is the prescribed velocity on the solid boundary.

On the truncation boundary Γ_L, several conditions are going to be enforced: firstly, the mean value of the velocity is going to be prescribed to the inlet (or truncation) boundary velocity $\mathbf{u}_L$:

$$\bar{\mathbf{u}} = \mathbf{u}_L \quad \text{on } \Gamma_L.$$

Secondly, a Sommerfeld-like boundary condition for the fluctuating part of the velocity and pressure fields is prescribed:

$$\mathbf{n} \cdot \mathbf{u}' = -\frac{1}{\rho c}\mathbf{n} \cdot [\mathbf{n} \cdot \sigma(\mathbf{u}', p')] \quad \text{on } \Gamma_L,$$

where $\mathbf{n}$ is the unit outward normal to Γ_L. Let also $\mathbf{m}$ be any unit vector tangent to it. The fluctuating tractions in the tangential direction are prescribed to zero:

$$\mathbf{m} \cdot [\mathbf{n} \cdot \sigma(\mathbf{u}', p')] = 0 \text{ on } \Gamma_L.$$

Finally, on the outflow boundary Γ_O, the following conditions are going to be applied:

$$\mathbf{n} \cdot \sigma(\bar{\mathbf{u}}, \bar{p}) = \mathbf{t}_O \quad \text{on } \Gamma_O,$$

which enforces the mean value tractions to the prescribed value $\mathbf{t}_O$. Regarding the fluctuating values, the same approach used for Γ_L is used, now with a Sommerfeld-like condition in the normal direction and zero traction prescribed in the tangential directions:

$$\begin{aligned} \mathbf{n} \cdot \mathbf{u}' &= -\frac{1}{\rho c}\mathbf{n} \cdot [\mathbf{n} \cdot \sigma(\mathbf{u}', p')] \quad \text{on } \Gamma_O, \\ \mathbf{m} \cdot [\mathbf{n} \cdot \sigma(\mathbf{u}', p')] &= 0 \qquad\qquad\qquad\qquad\quad \text{on } \Gamma_O. \end{aligned}$$

Note that:

- Γ_{S} is a classical Dirichlet-type boundary. Velocity test functions will vanish there and the condition $\mathbf{u} = \mathbf{u}_{\mathrm{S}}$ can be prescribed in a strong way.

- Γ_L is a boundary where Dirichlet-type boundary conditions are prescribed for $\bar{\mathbf{u}}$ and mixed boundary conditions for $\mathbf{u}'$, namely the normal component and the tangent associated stress. Both will be prescribed weakly.

- Γ_O is a boundary where Neumann-type boundary conditions are prescribed for $\bar{\mathbf{u}}$ and mixed boundary conditions for $\mathbf{u}'$, the same as on Γ_L. All these conditions will be prescribed weakly.

- For inviscid flows, the condition on the normal component of $\mathbf{u}'$ reduces to Sommerfeld's condition $p' = \rho c\,(\mathbf{u}' \cdot \mathbf{n})$. Obviously, other non-reflecting boundary conditions could be used.

Let us see how to prescribe these boundary conditions in the variational form of the problem. Let us start by noting that

$$\begin{aligned}
-\langle \mathbf{v}, \mathbf{n} \cdot \sigma\,(\mathbf{u}, p)\rangle_{\Gamma} &= -\langle \mathbf{v}, \mathbf{n} \cdot \sigma\,(\mathbf{u}, p)\rangle_{\Gamma_L} - \langle \mathbf{v}, \mathbf{n} \cdot \sigma\,(\mathbf{u}, p)\rangle_{\Gamma_O} \\
&= -\langle \mathbf{v}, \mathbf{n} \cdot \sigma\,(\bar{\mathbf{u}}, \bar{p})\rangle_{\Gamma_L} - \langle \mathbf{v}, \mathbf{n} \cdot \sigma\,(\mathbf{u}', p')\rangle_{\Gamma_L} \\
&\quad - \langle \mathbf{v}, \mathbf{n} \cdot \sigma\,(\bar{\mathbf{u}}, \bar{p})\rangle_{\Gamma_O} - \langle \mathbf{v}, \mathbf{n} \cdot \sigma\,(\mathbf{u}', p')\rangle_{\Gamma_O} \\
&= -\langle \mathbf{v}, \mathbf{n} \cdot \sigma\,(\bar{\mathbf{u}}, \bar{p})\rangle_{\Gamma_L} + \langle \rho c \mathbf{v} \cdot \mathbf{n}, \mathbf{u}' \cdot \mathbf{n}\rangle_{\Gamma_L} \\
&\quad - \langle \mathbf{v}, \mathbf{t}_O\rangle_{\Gamma_O} + \langle \rho c \mathbf{v} \cdot \mathbf{n}, \mathbf{u}' \cdot \mathbf{n}\rangle_{\Gamma_O}.
\end{aligned} \tag{4.17}$$

Note that no contribution on Γ_{S} has been included, since in this boundary usual Dirichlet boundary conditions are applied and the test functions vanish on it. We still need to prescribe $\bar{\mathbf{u}} = \mathbf{u}_L$, which will be done through penalization using Nitsche's method [122]. In the spirit of this method, it is convenient to symmetrize the boundary terms. Taking this into account we define the boundary terms, which can be written as $B_{\mathrm{B}}([\mathbf{u}, p], [\mathbf{v}, q]) - L_{\mathrm{B}}([\mathbf{v}, q])$, with

$$\begin{aligned}
B_{\mathrm{B}}([\mathbf{u}, p], [\mathbf{v}, q]) &:= -\langle \mathbf{v}, \mathbf{n} \cdot \sigma\,(\bar{\mathbf{u}}, \bar{p})\rangle_{\Gamma_L} - \langle \bar{\mathbf{u}}, \mathbf{n} \cdot \sigma\,(\mathbf{v}, q)\rangle_{\Gamma_L} + \beta \frac{\mu_p}{l_p} \langle \mathbf{v}, \bar{\mathbf{u}}\rangle_{\Gamma_L} \\
&\quad + \langle \rho c \mathbf{v} \cdot \mathbf{n}, \mathbf{u}' \cdot \mathbf{n}\rangle_{\Gamma_L} + \langle \rho c \mathbf{v} \cdot \mathbf{n}, \mathbf{u}' \cdot \mathbf{n}\rangle_{\Gamma_O}, \\
L_{\mathrm{B}}([\mathbf{v}, q]) &:= -\langle \mathbf{u}_L, \mathbf{n} \cdot \sigma\,(\mathbf{v}, q)\rangle_{\Gamma_L} + \beta \frac{\mu_p}{l_p} \langle \mathbf{v}, \mathbf{u}_L\rangle_{\Gamma_L} + \langle \mathbf{v}, \mathbf{t}_O\rangle_{\Gamma_O},
\end{aligned} \tag{4.18}$$

where β, μ_p, l_p are numerical parameters, the first one dimensionless, the second one with units of viscosity and the latter with units of length. We are still at the continuous level. When a finite element approximation in

space is performed, h being the element size, one can show that μ_p, l_p can be taken as $\mu_p = \mu + |\mathbf{u}|h$, and $l_p = h$ [52].

The only ingredient missing in the formulation is the definition of the outflow traction $\mathbf{t}_O$. Assuming that Γ_O is placed in a far-field region, where $\bar{p} \approx 0$ and $\nabla \bar{\mathbf{u}} \approx 0$, then the natural condition to be imposed is $\mathbf{t}_O = \mathbf{0}$.

4.3.3 Domain truncation

The truncation of the domain is a problematic issue when dealing with acoustic waves. Sometimes, especially in case of low speed flows, the far field conditions are reached within a small distance of the solid objects causing the perturbation. In these cases the truncation of the domain will only depend on the measure of the largest wavelength. Therefore, in such scenarios the present formulation can be applied in a general way without further artifacts. However, when convection becomes dominant stagnation conditions may be found far away from the perturbation, which results in a high computational cost if the full near-field domain needs to be simulated. Moreover, many times the Sommerfeld non-radiating boundary condition is compromised, since it assumes an orthogonal incidence of the wave with the external boundary.

An example illustrating this situation is depicted in Fig. 4.2. In this case a M = 0.4 flow over a wing profile is calculated departing from a fully developed incompressible flow solution. Before any wave reaches the boundary, the outlet is already reflecting the noise produced by the vortices passing through it, see Fig. 4.2.

In the second numerical example shown in Section 4.6, this problem has been solved by adding a spherical PML based on [167] in an artificial outlet domain Ω_{PML}, see Fig. 4.3. For this, we define the finite element contribution of the PML layer in a new bilinear form B_{PML}:

$$B_{\text{PML}}([\mathbf{u}, p], [\mathbf{v}, q]) := (\mathbf{v}, \alpha^* \mathbf{u}) + (q, \rho \alpha p) \tag{4.19}$$

where α is defined as

$$\alpha(r) = 0.4 \frac{(r - r_0)^2}{(r_f - r_0)^3} (-2r + 3r_f - r_0) \quad \text{in } \Omega_{\text{PML}},$$
$$\alpha(r) = 0 \quad \text{in } \Omega \setminus \Omega_{\text{PML}}, \tag{4.20}$$

where $\alpha^* = \alpha \rho^2 c^2$ and r_0 and r_f are the small and big radius of the PML, respectively.

Taking the previous considerations into account, the final problem to be solved consists of finding $[\mathbf{u}, p]$ such that

$$B([\mathbf{u}, p], [\mathbf{v}, q]) + B_{\text{PML}}([\mathbf{u}, p], [\mathbf{v}, q]) + B_{\text{B}}([\mathbf{u}, p], [\mathbf{v}, q]) = L_{\text{B}}([\mathbf{v}, q]) \tag{4.21}$$

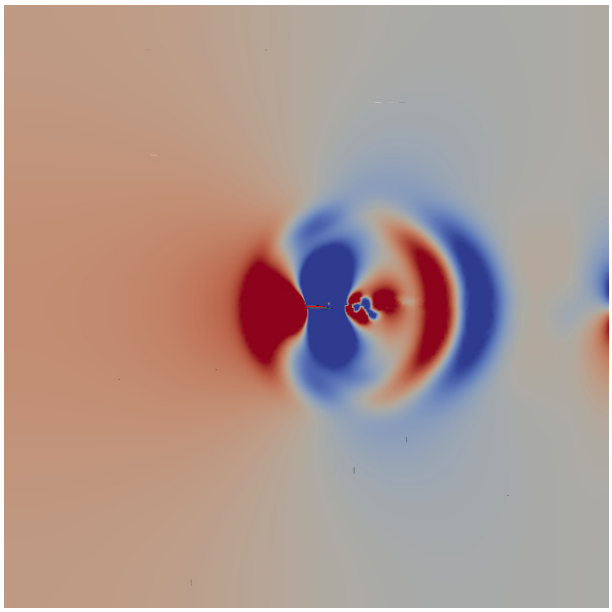

Figure 4.2: Reflection of the sound generated by vortices approaching the outflow.

for all test functions $[\mathbf{v}, q]$.

Unlike in Section 4.3, the importance of absorbing both hydrodynamic and acoustic scales on the outlet justifies the application of the PML to the whole variables $[\mathbf{u}_h^{n+1}, p_h^{n+1}]$. The performance of this numerical tool will be presented in Section 4.6.

4.4 Numerical approximation

In this section we present the finite element formulation for the space approximation of the isentropic Navier-Stokes equations, including the stabilization terms required for obtaining a stable formulation when using equal velocity-pressure interpolations, in particular linear-linear (P_1/P_1) elements, as well as the time discretization using finite differences.

Let us consider a finite element partition of the domain Ω of size h, and use this letter as subscript to denote finite element functions and spaces. Only conforming finite element approximations will be considered in what follows. Let $V_h \subset V$ be the finite approximation space for the discrete velocity field and let us also define $Q_h \subset Q$, the pressure approximation space.

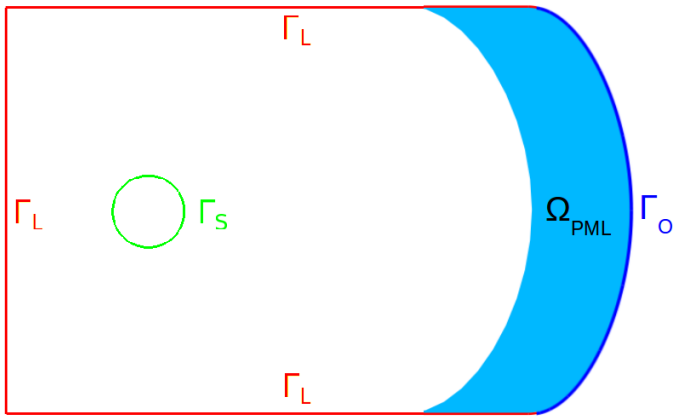

Figure 4.3: A PML is attached to the original outlet of the domain Ω.

4.4.1 Time discretization

Concerning the time integration, the monolithic approach for solving the incompressible Navier-Stokes equations consists in building a system with both velocity and pressure degrees of freedom, which leads to the coupled calculation of the momentum and mass equations in one single step. To approximate the first order time derivatives, a second order backward finite difference scheme (BDF2) has been used. Let us partition the time interval $[0, T]$ into N equal time steps of size $\delta t := t^{n+1} - t^n$ so that $0 \equiv t^0 < t^1 < \ldots < t^n < \ldots < t^N \equiv T$. Given a generic time dependent function $g(t)$, the following notation will be used for the BDF2 approximation to the first time derivative:

$$\partial_t g|_{t^{n+1}} \approx \delta_t g^{n+1} := \frac{1}{\delta t}\left(\frac{3}{2}g^{n+1} - 2g^n + \frac{1}{2}g^{n-1}\right), \tag{4.22}$$

where g^n denotes the evaluation of g at time step t^n.

Obviously other time integration schemes could be used, both implicit and explicit. The latter would require mass lumping to avoid the solution of linear systems using a finite element approximation (see below); this is easy only for linear elements. Moreover, implicit time integration allows reaching the incompressible limit. We therefore favor the use of implicit integrators, as BDF2.

4.4.2 Discrete boundary conditions

At an arbitrary time step of the numerical simulation, the final fully discretized implicit scheme in space and time can be derived using the finite

element formulation described below. Moreover, the mean flow values must be expressed according to the chosen integration scheme and the penalty parameters of the weak essential condition on Γ_L must be defined. We do this as follows:

- As mentioned above, μ_p, l_p can be taken as $\mu_p = \mu + |\mathbf{u}|h,\ l_p = h$ [52].

- If the temporal window presented at Eq. (4.16) is defined at a discrete level as $T_w = N_w \delta t$ and we use the trapezoidal rule for the integration, then the mean values can be expressed as follows:

$$\bar{\mathbf{u}}_h^{n+1} = \frac{\delta t}{T_w}\left(\frac{1}{2}\mathbf{u}_h^{n+1} + \sum_{k=n-N_w+2}^{n} \mathbf{u}_h^k + \frac{1}{2}\mathbf{u}_h^{n-N_w+1}\right). \tag{4.23}$$

This expression of the mean flow values keeps the temporal integration implicit and second order accurate. Bearing in mind the (usually) sharp initial pressure transient and the absence of a minimally developed mean flow, it is important to run several time steps (N_w) before using the present formulation in order to obtain representative mean flow variables. The same procedure is applied to p and the fluctuating components will be also expressed from now on in terms of the full variables evaluated at t^{n+1}. The trapezoidal rule in eq. (4.23) can be viewed as a particular realization of a causal finite impulse response (FIR) filter of order $N_w + 1$. By modifying the coefficients that multiply the discrete velocities, one could design a time scheme that filters the frequencies higher than a given cutoff value.

4.4.3 Finite element approximation

For clarity, the formulation will be arranged in five forms: B, B_{B}, B_{PML}, L_{B} and B_{S}; the latter corresponds to the stabilization terms and will be presented next. The final formulation reads as follows: from known $\mathbf{u}_h^{n-2}$, $\mathbf{u}_h^{n-1}$ and $\mathbf{u}_h^n$, compute the compressible velocity and pressure at time step t^{n+1}, $\left[\mathbf{u}_h^{n+1}, p_h^{n+1}\right] \in V_h \times Q_h$, such that

$$\begin{aligned} B^{n+1}([\mathbf{u}_h, p_h], [\mathbf{v}_h, q_h]) + B_{\mathrm{PML}}^{n+1}([\mathbf{u}_h, p_h], [\mathbf{v}_h, q_h]) + B_{\mathrm{B}}^{n+1}([\mathbf{u}_h, p_h], [\mathbf{v}_h, q_h]) \\ + B_{\mathrm{S}}^{n+1}([\mathbf{u}_h, p_h], [\mathbf{v}_h, q_h]) = L_{\mathrm{B}}^{n+1}([\mathbf{v}_h, q_h]), \end{aligned} \tag{4.24}$$

for all test functions, where

$$
\begin{aligned}
B^{n+1}([\mathbf{u}_h, p_h], [\mathbf{v}_h, q_h]) = &\left\langle \rho^{n+1}\mathbf{v}_h, \delta_t \mathbf{u}_h^{n+1} \right\rangle + \left\langle \rho^{n+1}\mathbf{v}_h, \left(\mathbf{u}_h^{n+1}\cdot\nabla\right)\mathbf{u}_h^{n+1} \right\rangle \\
&+ \mu \left\langle \nabla\mathbf{v}_h, \nabla\mathbf{u}_h^{n+1} \right\rangle + \frac{1}{3}\mu \left\langle \nabla\cdot\mathbf{v}_h, \nabla\cdot\mathbf{u}_h^{n+1} \right\rangle \\
&- \left\langle \nabla\cdot\mathbf{v}_h, p_h^{n+1} \right\rangle + \left\langle \frac{1}{\left(c^2\right)^{n+1}} q_h, \delta_t p_h^{n+1} \right\rangle \\
&+ \left\langle \frac{1}{\left(c^2\right)^{n+1}} q_h, \mathbf{u}_h^{n+1}\cdot\nabla p_h^{n+1} \right\rangle + \left\langle \rho^{n+1} q_h, \nabla\cdot\mathbf{u}_h^{n+1} \right\rangle . \qquad (4.25)
\end{aligned}
$$

Note that this expression involves both the unknowns at time step $n+1$ and at previous time steps. For the rest of the terms in (4.24), the superscript $n+1$ indicates that both the unknowns and the data are evaluated at time step $n+1$.

As mentioned before, the condensation of ρ^{n+1} and c^{n+1} is essential for keeping the complexity of the formulation low. They are evaluated with the converged unknowns of the problem at t^{n+1}, as the implicit scheme requires:

$$
\begin{aligned}
\rho^{n+1} &= \rho_0 \left(1 + \frac{\gamma-1}{2}\frac{|\mathbf{u}_h^{n+1}|^2}{c_0^2}\right)^{\gamma-1}, \\
\left(c^2\right)^{n+1} &= c_0^2 \left(1 + \frac{\gamma-1}{2}\frac{|\mathbf{u}_h^{n+1}|^2}{c_0^2}\right)^{-1}. \qquad (4.26)
\end{aligned}
$$

We have included the evaluation of ρ^{n+1} and c^{n+1} in the non-linearity loop in a fixed point manner, that is say, when computing the unknowns at a certain iteration we use the values of ρ^{n+1} and c^{n+1} at the previous one, and once the unknowns are computed we update them. Note that they are required at the integration points within each finite element domain. To simplify the notation, since it is understood that ρ and c are only evaluated at t^{n+1}, from now on they will be referred as ρ and c instead of ρ^{n+1} and c^{n+1}.

Next, the bilinear form B_{B}^{n+1} and the linear form L_{B}^{n+1} can be easily obtained using (4.18):

$$
\begin{aligned}
B_{\mathrm{B}}^{n+1}([\mathbf{u}_h, p_h], [\mathbf{v}_h, q_h]) = &-\langle \mathbf{v}_h, \mathbf{n}\cdot\sigma_h\left(\bar{\mathbf{u}}_h^{n+1}, \bar{p}_h^{n+1}\right)\rangle_{\Gamma_L} \\
&- \langle \bar{\mathbf{u}}_h^{n+1}, \mathbf{n}\cdot\sigma_h\left(\mathbf{v}_h, q_h\right)\rangle_{\Gamma_L} + \beta\frac{\mu_p}{l_p}\langle \mathbf{v}_h, \bar{\mathbf{u}}_h^{n+1}\rangle_{\Gamma_L} + \langle \rho c \mathbf{v}_h\cdot\mathbf{n}, \mathbf{u}_h'^{n+1}\cdot\mathbf{n}\rangle_{\Gamma_L\cup\Gamma_O}, \\
L_{\mathrm{B}}^{n+1}([\mathbf{v}_h, q_h]) = &\,\beta\frac{\mu_p}{l_p}\langle \mathbf{v}_h, \mathbf{u}_L^{n+1}\rangle_{\Gamma_L} - \langle \mathbf{u}_L^{n+1}, \mathbf{n}\cdot\sigma_h\left(\mathbf{v}_h, q_h\right)\rangle_{\Gamma_L},
\end{aligned}
$$

where we have assumed that $\mathbf{t}_O = \mathbf{0}$. Applying the definition of the mean values presented in Eq. (4.23) and expressing the fluctuating components in

terms of the problem unknowns, B_{B}^{n+1} can be rewritten as follows:

$$
\begin{aligned}
B_{\mathrm{B}}^{n+1}([\mathbf{u}_h,p_h],[\mathbf{v}_h,q_h]) &= -\frac{1}{2N_w}\langle \mathbf{v}_h, \mathbf{n}\cdot\sigma_h\left(\mathbf{u}_h^{n+1},p_h^{n+1}\right)\rangle_{\Gamma_L} \\
&- \frac{1}{2N_w}\langle \mathbf{u}_h^{n+1}, \mathbf{n}\cdot\sigma_h\left(\mathbf{v}_h,q_h\right)\rangle_{\Gamma_L} + \left(1-\frac{1}{2N_w}\right)\langle \rho c\mathbf{v}_h\cdot\mathbf{n}, \mathbf{u}_h^{n+1}\cdot\mathbf{n}\rangle_{\Gamma_L\cup\Gamma_O} \\
&+ \frac{\beta}{2N_w}\frac{\mu_p}{l_p}\langle \mathbf{v}_h,\mathbf{u}_h^{n+1}\rangle_{\Gamma_L} + \frac{\beta}{N_w}\frac{\mu_p}{l_p}\Big[\sum_{k=n-N_w+2}^{n}\langle \mathbf{v}_h,\mathbf{u}_h^{k}\rangle_{\Gamma_L} - \frac{1}{2}\langle \mathbf{v}_h,\mathbf{u}_h^{n-N_w+1}\rangle_{\Gamma_L}\Big] \\
&- \frac{1}{N_w}\sum_{k=n-N_w+2}^{n}\langle \mathbf{v}_h, \mathbf{n}\cdot\sigma_h\left(\mathbf{u}_h^{k},p_h^{k}\right)\rangle_{\Gamma_L} \\
&+ \frac{1}{2N_w}\langle \mathbf{v}_h, \mathbf{n}\cdot\sigma_h\left(\mathbf{u}_h^{n-N_w+1},p_h^{n-N_w+1}\right)\rangle_{\Gamma_L} \\
&- \frac{1}{N_w}\Big[\sum_{k=n-N_w+2}^{n}\langle \mathbf{u}_h^{k}, \mathbf{n}\cdot\sigma_h\left(\mathbf{v}_h,q_h\right)\rangle_{\Gamma_L} - \frac{1}{2}\langle \mathbf{u}_h^{n-N_w+1}, \mathbf{n}\cdot\sigma_h\left(\mathbf{v}_h,q_h\right)\rangle_{\Gamma_L}\Big] \\
&- \frac{1}{N_w}\sum_{k=n-N_w+2}^{n}\langle \rho c\mathbf{v}_h\cdot\mathbf{n}, \mathbf{u}_h^{k}\cdot\mathbf{n}\rangle_{\Gamma_L\cup\Gamma_O} - \frac{1}{2N_w}\langle \rho c\mathbf{v}_h\cdot\mathbf{n}, \mathbf{u}_h^{n-N_w+1}\cdot\mathbf{n}\rangle_{\Gamma_L\cup\Gamma_O}. \\
L_{\mathrm{B}}^{n+1}([\mathbf{v}_h,q_h]) &= \beta\frac{\mu_p}{l_p}\langle \mathbf{v}_h,\mathbf{u}_L^{n+1}\rangle_{\Gamma_L} - \langle \mathbf{u}_L^{n+1}, \mathbf{n}\cdot\sigma_h\left(\mathbf{v}_h,q_h\right)\rangle_{\Gamma_L}.
\end{aligned}
$$

Note that several terms of B_{B}^{n+1} can be computed with values of velocities and pressure of previous time steps, and therefore moved to the right-hand-side in the final equation.

When a PML is mandatory, B_{PML}^{n+1} must be included in the formulation. Using (4.19) the discrete bilinear form for the PML can be easily derived:

$$
B_{\mathrm{PML}}^{n+1}([\mathbf{u}_h,p_h],[\mathbf{v}_h,q_h]) = \alpha^*\left(\mathbf{v}_h,\mathbf{u}_h^{n+1}\right)_{\Omega_{\mathrm{PML}}} + \alpha\left(q_h,\rho p_h^{n+1}\right)_{\Omega_{\mathrm{PML}}}. \quad (4.27)
$$

The last ingredient for a robust and consistent formulation consists in applying an appropriate stabilization for the convective terms and for the fulfillment of the velocity-pressure inf-sup condition [117], since equal interpolation elements are being used. In the present case, the Algebraic Subgrid Scale (ASGS) method for incompressible flows presented in [45] has been taken as reference and extended to isentropic flows. This is the simplest version of Variational Multiscale (VMS) finite element methods (see [51] for a review). The only care that needs to be taken when designing the stabilization terms is that the continuity equation now has two more additional terms compared to the case of incompressible flows that need to be taken into account, both in the residual of this equation and in the operator applied to

the test functions that multiplies this residual. The final result is:

$$
\begin{aligned}
&B_{\mathrm{S}}^{n+1}\left([\mathbf{u}_h, p_h], [\mathbf{v}_h, q_h]\right) \\
&\quad = \sum_K \tau_{1,K} \big\langle \rho \mathbf{u}_h^{n+1} \cdot \nabla \mathbf{v}_h + \nabla q_h, \rho \delta_t \mathbf{u}_h^{n+1} + \rho \mathbf{u}_h^{n+1} \cdot \nabla \mathbf{u}_h^{n+1} - \nabla \cdot \sigma_h^{n+1} \big\rangle_K \\
&\quad + \sum_K \tau_{2,K} \big\langle \rho \nabla \cdot \mathbf{v}_h + \frac{1}{c^2} \mathbf{u}_h^{n+1} \cdot \nabla q_h, \\
&\qquad \rho \nabla \cdot \mathbf{u}_h^{n+1} + \frac{1}{c^2} \mathbf{u}_h^{n+1} \cdot \nabla p_h^{n+1} + \frac{1}{c^2} \delta_t p_h^{n+1} \big\rangle_K,
\end{aligned} \tag{4.28}
$$

where K denotes a generic element domain, summation is done over all elements of the finite element mesh, and $\tau_{1,K}$ and $\tau_{2,K}$ are suitable stabilization parameters defined in each element [47], that we compute as:

$$
\tau_{1,K} = \left[c_1 \frac{\nu}{h^2} + c_2 \frac{|\mathbf{u}_h^{n+1}|_K}{h} \right]^{-1}, \qquad \tau_{2,K} = \frac{h^2}{c_1 \tau_{1,K}},
$$

$|\mathbf{u}_h^{n+1}|_K$ being the mean Euclidean norm of the velocity in element K. The algorithmic constants c_1 and c_2 depend on the polynomial order of the interpolation. We set them to $c_1 = 4$ and $c_2 = 2$ for linear elements. Note that in (4.33) we have not considered operator associated to the stresses applied to the test functions multiplying the residual of the momentum equation. Likewise, in order to keep the presentation concise we have not considered neither time dependent subscales [58], nor orthogonal subgrid scales [47], although we favor these two options.

4.5 Unified flow and acoustics isentropic compressible solver using an ALE frame of reference

In Chapter 2 it has been show how the ALE formulation of Lighthill's analogy increases its numerical complexity because it does not allow using the irreducible second order wave equation and requires solving it in a set of two stabilized equations [89], which affects the computational cost in regard to the static case [96]. On the contrary, the ALE formulation for the incompressible flow equations, which has also been reviewed in Chapter 2, does not add a relevant degree of complexity to the static problem, for which it makes sense to extend the isentropic compressible formulation for being used in moving domains. Moreover, it will allow validating the results corresponding to the rotating airfoil obtained with the hybrid method.

4.5.1 Continuous problem

Unlike the problem presented in Section 2.3.3, the present formulation will not be decomposed into an incident and a diffracted problem, since it would involve the solution of two CFD problems. Using the notation defined in Chapter 2, the continuous isentropic compressible equations using an ALE frame of reference with appropriate initial and boundary conditions will read

$$\partial_t \mathbf{u} - \nu \Delta \mathbf{u} - \frac{1}{3}\nu \nabla(\nabla \cdot \mathbf{u}) + (\mathbf{u} - \mathbf{u}_{\text{dom}}) \cdot \nabla \mathbf{u} + \nabla p = \mathbf{f} \quad \text{in } \Omega,\ t > 0, \tag{4.29a}$$

$$\frac{1}{\rho c^2}\partial_t p + \frac{1}{\rho c^2}(\mathbf{u} - \mathbf{u}_{\text{dom}}) \cdot \nabla p + \nabla \cdot \mathbf{u} = 0 \quad \text{in } \Omega,\ t > 0, \tag{4.29b}$$

$$\mathbf{u}(\boldsymbol{x}, 0) = \mathbf{u}_0(\boldsymbol{x}) \quad \text{in } \Omega,\ t = 0, \tag{4.29c}$$

$$\mathbf{u}(\boldsymbol{x}, t) = \mathbf{u}_S(\boldsymbol{x}, t) + \mathbf{u}_{\text{dom}}(\boldsymbol{x}, t) \quad \text{on } \Gamma_S,\ t > 0, \tag{4.29d}$$

$$\bar{\mathbf{u}}(\boldsymbol{x}, t) = \mathbf{u}_L(\boldsymbol{x}, t) + \mathbf{u}_{\text{dom}}(\boldsymbol{x}, t) \quad \text{on } \Gamma_L,\ t > 0, \tag{4.29e}$$

$$\mathbf{n} \cdot \mathbf{u}' = -\frac{1}{\rho c}\mathbf{n} \cdot [\mathbf{n} \cdot \sigma(\mathbf{u}', p')] \quad \text{on } \Gamma_L,\ t > 0, \tag{4.29f}$$

$$\mathbf{m} \cdot [\mathbf{n} \cdot \sigma(\mathbf{u}', p')] = 0 \quad \text{on } \Gamma_L,\ t > 0, \tag{4.29g}$$

$$\mathbf{n} \cdot \sigma(\bar{\mathbf{u}}, \bar{p}) = \mathbf{t}_O(\boldsymbol{x}, t) \quad \text{on } \Gamma_O,\ t > 0, \tag{4.29h}$$

$$\mathbf{n} \cdot \mathbf{u}' = -\frac{1}{\rho c}\mathbf{n} \cdot [\mathbf{n} \cdot \sigma(\mathbf{u}', p')] \quad \text{on } \Gamma_O,\ t > 0, \tag{4.29i}$$

$$\mathbf{m} \cdot [\mathbf{n} \cdot \sigma(\mathbf{u}', p')] = 0 \quad \text{on } \Gamma_O,\ t > 0. \tag{4.29j}$$

Like in the Eulerian case, c and ρ will be condensated taking profit from the equation of ideal gas.

4.5.2 Weak formulation

The derivation of the continuous variational form of the momentum and continuity equations in an ALE frame of reference, whose terms will be grouped in a form $B^{ALE}([\mathbf{u}, p], [\mathbf{v}, q])$, will only contain one difference respect

to the Eulerian formulation presented in the static case: the velocity and pressure convective terms will be affected by the advection of the mesh. Note that the boundary terms grouped together in the form $B_B([\mathbf{u},p],[\mathbf{v},q])$ will not change because the mesh velocity only affects the Dirichlet value on Γ_S, which is not present anymore. However, $\bar{\mathbf{u}} = \mathbf{u}_L$ still needs to be prescribed, which is done through penalization using Nitsche's method [122] and will be affected by the mesh velocity. In the spirit of this method, it is convenient to symmetrize the boundary terms. The known terms will then grouped in the form $L_B^{ALE}(\mathbf{v},q)$ and sent to the RHS. Using the same notation of Chapter 2 the variational formulation can be written as follows:

$$\begin{aligned} &B^{ALE}\left([\mathbf{u},p],[\mathbf{v},q]\right) = \langle\rho\mathbf{v},\partial_t\mathbf{u}\rangle + \langle\rho\mathbf{v},\left(\left(\mathbf{u}-\mathbf{u}_{\text{dom}}\right)\cdot\nabla\right)\mathbf{u}\rangle + \mu\langle\nabla\mathbf{v},\nabla\mathbf{u}\rangle \\ &+\frac{1}{3}\mu\langle\nabla\cdot\mathbf{v},\nabla\cdot\mathbf{u}\rangle - \langle\nabla\cdot\mathbf{v},p\rangle + \langle\frac{1}{c^2}q,\partial_t p\rangle + \langle\frac{1}{c^2}q,\left(\mathbf{u}-\mathbf{u}_{\text{dom}}\right)\cdot\nabla p\rangle \\ &+\langle\rho q,\nabla\cdot\mathbf{u}\rangle, \end{aligned} \tag{4.30a}$$

$$\begin{aligned} &L_{\text{B}}^{ALE}([\mathbf{v},q]) := -\langle\mathbf{u}_L+\mathbf{u}_{\text{dom}},\mathbf{n}\cdot\sigma\left(\mathbf{v},q\right)\rangle_{\Gamma_L} + \beta\frac{\mu_p}{l_p}\langle\mathbf{v},\mathbf{u}_L+\mathbf{u}_{\text{dom}}\rangle_{\Gamma_L} \\ &+\langle\mathbf{v},\mathbf{t}_O\rangle_{\Gamma_O}, \end{aligned} \tag{4.30b}$$

for all $\mathbf{v}\in V$ and $\rho q\in Q$. $\beta,\mu_p,\ l_p$ are numerical parameters, the first one dimensionless, the second one with units of viscosity and the latter with units of length. We are still at the continuous level. When a finite element approximation in space is performed, h being the element size, one can show that μ_p, l_p can be taken as $\mu_p = \mu + |\mathbf{u}-\mathbf{u}_{\text{dom}}|h$, and $l_p = h$ [52]. Moreover, initial conditions need to be appended. Finally, the variational problem to be solved will be

$$B^{ALE}\left([\mathbf{u},p],[\mathbf{v},q]\right) + B_B([\mathbf{u},p],[\mathbf{v},q]) = L_{\text{B}}^{ALE}([\mathbf{v},q]) \tag{4.31}$$

4.5.3 Fully discrete problem

At a discrete level, after discretizing using finite elements of size h and a BDF2 time integrator like in the previous cases, the problem to be solved at $t=(n+1)\delta t$ will be

$$\begin{aligned} B^{ALE}\left([\mathbf{u}_h^{n+1},p_h^{n+1}],[\mathbf{v}_h,q_h]\right) + B_B([\mathbf{u}_h^{n+1},p_h^{n+1}],[\mathbf{v}_h,q_h]) \\ +B_S^{ALE}([\mathbf{u}_h^{n+1},p_h^{n+1}],[\mathbf{v}_h,q_h]) = L_B^{ALE}([\mathbf{v}_h,q_h]) \end{aligned} \tag{4.32}$$

However, the solver must finally have two equations and two variables, for which all mean flow and acoustic components must be expressed in terms of $(\mathbf{u}_h^{n+1},p_h^{n+1})$. In order to keep the presentation consice, the full development has been omitted. The only relevant modification has to do with the stabilization method, which has to be expressed in the ALE reference modifying

the residual and the convective stabilization operators:

$$B_S^{ALE}\left(\left[\mathbf{u}_h^{n+1}, p_h^{n+1}\right], [\mathbf{v}_h, q_h]\right) = \sum_K \tau_{1,K}\big\langle(\rho\mathbf{u}_h^{n+1} - \mathbf{u}_{\text{dom}})\cdot\nabla\mathbf{v}_h + \nabla q_h,$$
$$\rho\delta_t\mathbf{u}_h^{n+1} + \rho(\mathbf{u}_h^{n+1} - \mathbf{u}_{\text{dom}})\cdot\nabla\mathbf{u}_h^{n+1} - \nabla\cdot\sigma_h^{n+1}\big\rangle_K$$
$$+\sum_K \tau_{2,K}\big\langle\rho\nabla\cdot\mathbf{v}_h + \frac{1}{c^2}(\mathbf{u}_h^{n+1} - \mathbf{u}_{\text{dom}})\cdot\nabla q_h,$$
$$\rho\nabla\cdot\mathbf{u}_h^{n+1} + \frac{1}{c^2}(\mathbf{u}_h^{n+1} - \mathbf{u}_{\text{dom}})\cdot\nabla p_h^{n+1} + \frac{1}{c^2}\delta_t p_h^{n+1}\big\rangle_K, \tag{4.33}$$

where K denotes a generic element domain, summation is done over all elements of the finite element mesh, and $\tau_{1,K}$ and $\tau_{2,K}$ are suitable stabilization parameters defined in each element [47], that we compute as:

$$\tau_{1,K} = \left[c_1\frac{\nu}{h^2} + c_2\frac{|\mathbf{u}_h^{n+1} - \mathbf{u}_{\text{dom}}|_K}{h}\right]^{-1}, \qquad \tau_{2,K} = \frac{h^2}{c_1\tau_{1,K}}.$$

4.6 Results

For a proper validation of the present formulation two different scenarios have been taken as reference. First, a 2D problem consisting in a low speed Re = 1000 flow around a cylinder has been calculated with the isentropic compressible equations for comparing the CFD results and the acoustic propagation to those provided by an incompressible solver and the Lighthill analogy [90], and to those obtained when using a compressible flow formulation with primitive variables presented in [20]. Second, a M = 0.4 flow around a 3D NACA 0012 airfoil has been calculated in order to evaluate the performance of the formulation against a compressible flow solver and the Ffowcs Williams & Hawkings (FWH) acoustic analogy. The main advantage of the isentropic compressible formulation is that it can be treated numerically like the incompressible formulation, although the flow regime might not be in the incompressible range anymore. From the point of view of an end user, the only further requirement consists in introducing the four following parameters: the gas universal constant $R = 8.31$ J/KÂůmol, the molar mass, the sound propagation speed of the working gas and the bulk temperature. In both cases the values of air at room temperature have been considered ($\mathcal{M} = 28.97$ g/mol, $c_0 = 343$ m/s and $T_0 = 293.15$ K).

4.6.1 Aerodynamic sound radiated by flow past a cylinder. M = 0.0583.

The first benchmark case consists in a 2D flow around a cylinder of diameter $D = 0.3$, which allows evaluating the aeolian tones of a low Mach viscous

flow [90]. The incident velocity of 20 leads to a Reynolds and Mach numbers at the far field (away from the cylinder) of Re = 1000 and M = 0.0583 for a sound speed of $c_0 = 343$ (all units are in SI). The problem has been solved in an unstructured mesh of nearly 1 million triangular linear elements using equal interpolation for velocity and pressure, with a size of $3 \times 10^{-3} D$ near the cylinder surface. The case has been run up to 1.5 s with a time step $\delta t = 1 \times 10^{-3}$ s, departing from an initial incompressible solution in order to ease the initial convergence of the iterative solver. For the weak imposition of boundary conditions it has been enough taking a penalty parameter $\beta = 1$.

The original case in [90] was computed with the incompressible Navier-Stokes equations and Lighthill's analogy, which is a realistic approach for this flow range. However, one of the main goals of this work consists in showing that, given a low Mach number and a fine enough discretization, the present formulation converges to the solution of a Direct Numerical Simulation. For this reason, the case has been also computed with the formulation in [20], which despite a high computational cost manages to overcome the poor performance of compressible conservative schemes in the incompressible range.

Regarding the flow solution, the first result to be analyzed is the vortex shedding frequency and the dispersive error of the wave propagation along the domain. In order to filter the main frequency mode from the noise produced by secondary vortices, three points located on the perpendicular direction to the flow have been selected. Point 1 is located just below the cylinder, point 3 lays near the lower boundary of the domain and point 2 in the middle between 1 and 3. Table 5.1 presents the vortex shedding frequency computed with the pressure time history for all three formulations at the three chosen locations. The obtained ranges of values show that, in spite of being near the incompressible limit and using the same spatial discretization and the same temporal integrator, the dispersive error of the isentropic approximation is similar to that of the fully compressible solver and much smaller than the incompressible one.

Solver/Point	1	2	3
Incompressible	15.601	15.723	15.898
Isentropic compressible	15.576	15.601	15.625
Fully compressible	15.775	15.779	15.855

Table 4.1: Vortex shedding frequency (Hz) at four different points.

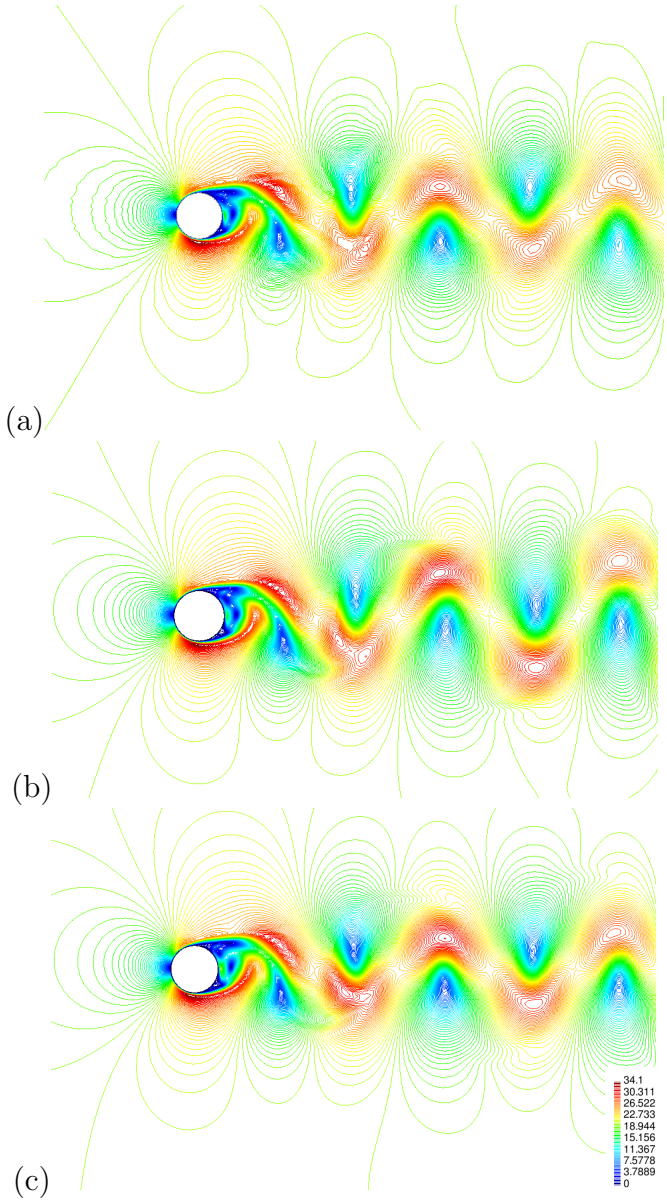

Figure 4.4: DNS compressible flow velocity (a), incompressible flow velocity (b), isentropic compressible flow velocity (c).

The fully developed velocity profiles are compared in Fig. 4.4. This very good fitting between all three velocity profiles shows the possibility of replacing the incompressible solvers when their convergence is not satisfactory even if the acoustics are not relevant, as well as the fully compressible formulation when dealing with low speed flows. Moreover, it confirms the good performance of the weakly imposed inlet condition. Of course, one may think that, despite this benefit, the compressibility brings the big drawback of waves being reflected by the boundaries and polluting the flow solution.

However, Fig. 4.5 shows that this inconvenience is completely resolved by the previously presented boundary conditions as no reflections are observed on the external boundaries. This plot also validates qualitatively the acoustic propagation at the far field. The present formulation is capable of capturing the anisotropy of the aeolian tones as well as the amplitude of the acoustic waves. On the other hand, Fig. 4.6 aims for a quantitative validation of the phenomenon. In this sense, the wave propagation obtained with the isentropic compressible solver reproduces with small error the solution of both incompressible and fully compressible formulations, from which we can conclude that the method converges to a DNC at the low Mach range.

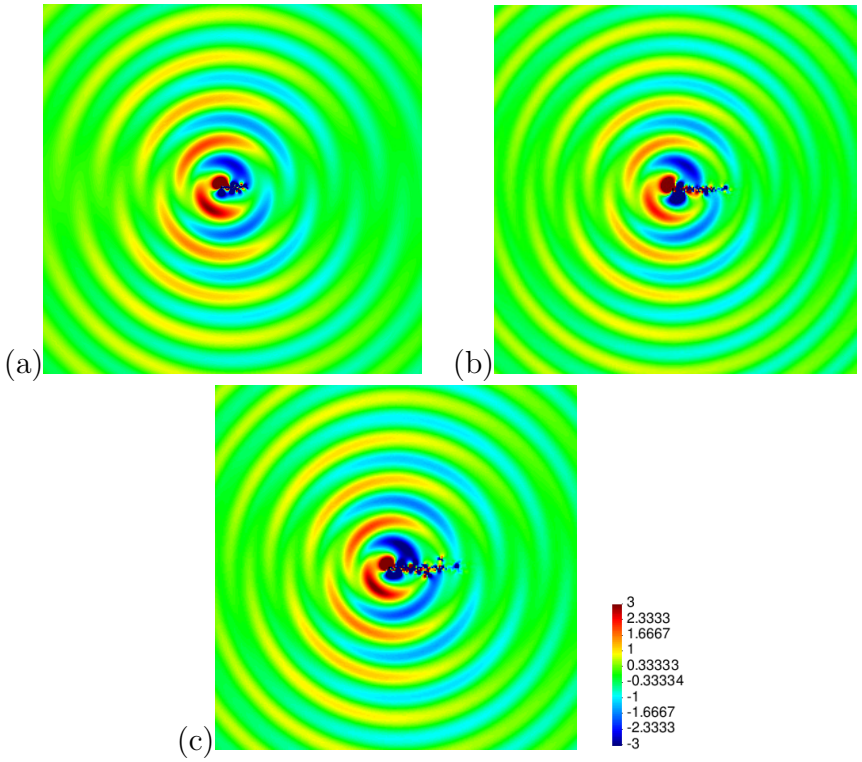

Figure 4.5: DNS compressible flow pressure (a), acoustic pressure calculated with the incompressible Lighthill analogy (b), isentropic compressible flow pressure (c).

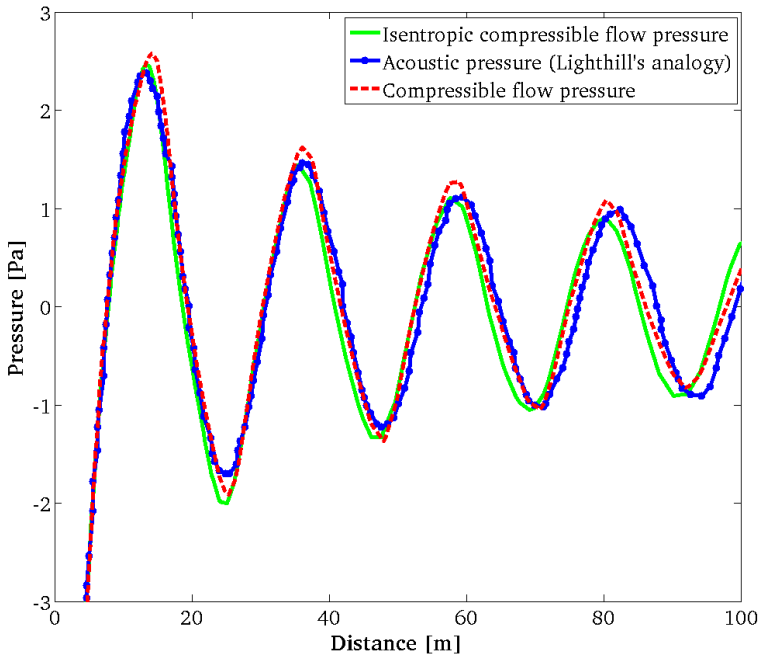

Figure 4.6: Wave propagation at 90 degrees with respect to the flow direction.

A very important issue which has been already highlighted in the Introduction is the computational cost of the formulation in comparison to the state-of-the-art incompressible and fully compressible approaches using primitive variables. Table 5.2 shows the number of non-linearity iterations and the cost per iteration using a Biconjugate Gradients linear solver without any preconditioning. This non-optimized configuration has been chosen because it has yielded convergence for all three formulations. The results reveal the poor performance of monolithic incompressible schemes in problems of this size ($\sim 360,000$ elements) due to the divergence-free condition, as well as a huge cost saving respect to the fully compressible approach, which has needed a ten times smaller time step for reaching convergence.

Solver	# Picard iterations	Cost/iteration (s)
Incompressible	10	65.0
Isentropic compressible	4	2.3
Fully compressible	4	3.8

Table 4.2: Computational cost for all three formulations using the same linear solver and no preconditioner.

4.6.2 Aerodynamic sound radiated by flow past an airfoil. $\mathbf{M} = 0.4$.

The simulation of turbulent compressible flows is a challenging problem that, from the CFD point of view, has been often approached with the Reynolds Averaged Navier-Stokes equations (RANS) [118] for reducing the computational cost. This case intends to show that the present formulation is capable of facing large-sized problems involving high-speed subsonic turbulent flows with a Large Eddy Simulation (LES), which a priori might sound too demanding for a fully compressible monolithic solver. The selected benchmark case consists in a 3D flow around a NACA 0012 airfoil with an angle of attack of 5 [179], with a Reynolds number based on the airfoil chord ($d = 0.1524$) $\mathrm{Re}_c = 408000$ and an incident Mach number $\mathrm{M} = 0.4$. The problem has been solved in an unstructured mesh of nearly 20 million tetrahedral linear elements using equal interpolation for velocity and pressure, with a size of 4×10^{-4} on the leading edge and 6.5×10^{-4} on the rest of the airfoil surface (all units are in SI). The case has been run up to 0.050 s with a time step $\delta t = 10^{-5}$ s, departing from an initial incompressible solution in order to ease the initial convergence of the iterative solver. For the weak imposition of boundary conditions a penalty parameter $\beta = 125$ has been taken. Unlike the previous low-speed flow, the present case generates an airjet that cannot be dissipated before reaching the outlet, for which a PML has been placed in this region. On the external boundaries the flow field has been prescribed separately following the method presented in Section 4.3.

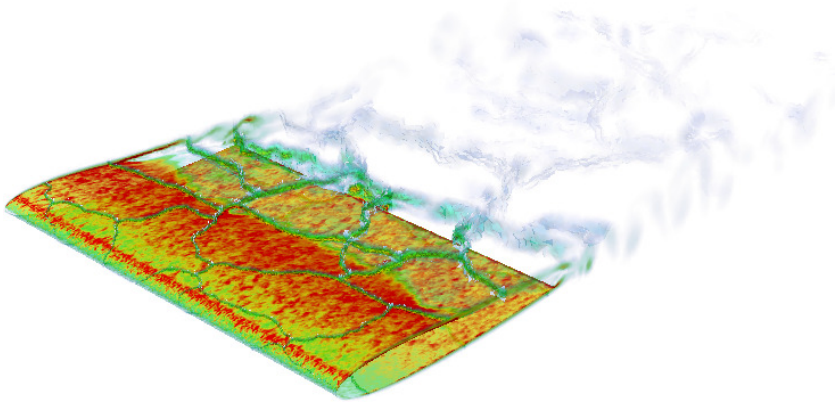

Figure 4.7: Vorticity profile on the airfoil.

The original case in [179] was computed with a compressible Large Eddy Simulation (LES) for the flow scales and the Ffowcs Williams & Hawkings (FWH) acoustic analogy for the acoustic component [178]. Since the object of the present work does not consist in assessing the performance of the solver in specific mesh typologies or in reproducing all the details of a particular

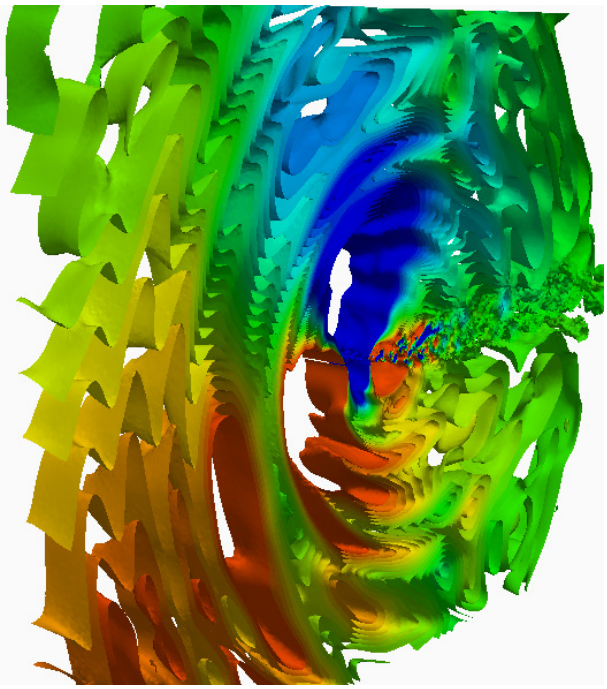

Figure 4.8: Pressure isosurfaces.

problem, but in establishing a general framework for the calculation of a wide range of flows, the goal of this analysis has been restricted to the following points: the suitability of the present isentropic compressible formulation for reproducing the mean flow patterns at M = 0.4, the proper propagation of the captured acoustic modes, and finally the validation of the proposed boundary conditions.

Figs. 4.7 and 4.8 show the calculated vorticity profile on the airfoil and the pressure isosurfaces with the corresponding wave propagation, respectively. Due to the highly aerodynamic character of this profile, the validation of the formulation in regard to the mean flow variables is very dependent to a proper description of the boundary layer. A wall-law with both buffer and logarithmic regions has been prescribed on the airfoil and the result in Fig. 4.9a has been obtained. Although the mean velocity field values are properly reproduced, the boundary layer still suffers an early detachment from the airfoil. In order to analyze in what extent the mesh element size, and not the formulation, was the reason for this discrepancy, the same problem has been run in a 2D section of the original profile using a much finer grid. Fig. 4.9b shows that the element size around the wall was indeed the cause of the early boundary layer detachment.

The same dependence on the mesh resolution can be found when capturing the acoustic modes. However, in this case the lack of accuracy does

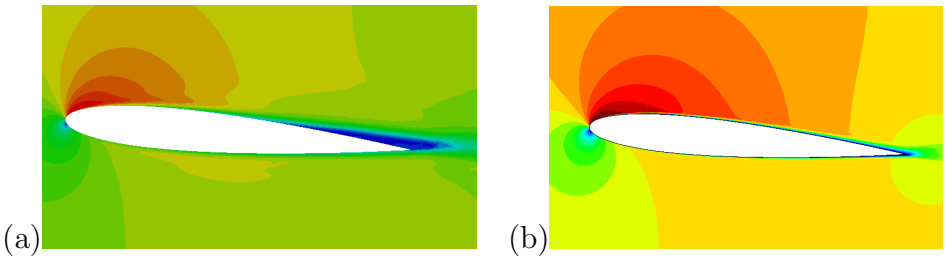

Figure 4.9: Contours of time-averaged flow velocity calculated in a 3D domain (a), in a 2D domain (b).

not affect the description of the acoustic scales generated by the interaction between the fluid and the airfoil, but its propagation to the far-field. The proper description of the wave requires dimensioning the element size at the far-field according to the smallest relevant wavelength, which would suppose an unaffordable problem size for a monolithic numerical approach. Fig. 4.10a shows how the wave propagation in the nearest region around the airfoil is not visible due to the presence of the much larger aerodynamic scale, but beyond a certain point it arises with the same pattern of the solution calculated with the FWH acoustic analogy in [179]. These challenges can only be approached with a manufactured structured mesh, which optimizes the spatial discretization according to the expected solution using elements with a high aspect ratio. Nevertheless, these methods are not part of the scope of the work.

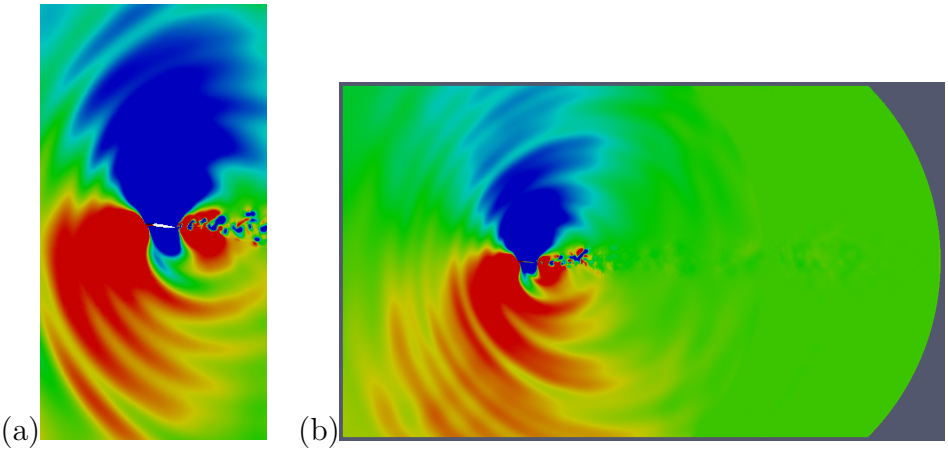

Figure 4.10: Calculated pressure at the near-field (a), at the far-field (b)

The behavior of waves abandoning the domain is one of the main concerns in compressible flow calculations. In the previous case, due to the low Mach and Reynolds regime, the size of the near-field region under influence of the flow perturbations was very small compared to the domain size,

for which the separated prescription of boundary conditions considering a mean flow component and an acoustic variation was conceptually very clear. However, in the present case real far-field stagnation conditions cannot be reached within a reasonably big domain and the aerodynamics pressure field is not yet uniform on the external boundaries, see Fig. 4.2. In spite of this theoretical drawback, the method manages to separate the two scales properly by updating the mean value at each time step, which allows the waves to cross Γ_L without any spurious reflection, see Fig. 4.10b. Furthermore, the implemented PML on the outlet completely absorbs the incoming waves as well as the noise produced by the airjet. It can be also observed how the flow pressure field is not exactly flat on Γ_L but no spurious reflections appear. This is possible because the present method is able to account for variations in the mean flow variables, but they must be smooth enough so they do not interfere with the acoustic field, otherwise spurious reflections may appear. Therefore, the truncation of the domain is not so immediate in this case since it must be assessed in advance that the far-field variations are acceptable, keeping always the computational cost in mind. It could be argued that this compromise could be avoided by using a PML on all external boundaries. Unfortunately this is only possible in solvers that compute the acoustic and the flow scales separately. In compressible formulations where the full set of variables is solved in a single calculation, like the present one, the inlet cannot be in contact with a PML. Moreover, the use of a global PML on all other external boundaries can lead to an unaffordable computational cost in big 3D cases with large wavelengths, for which the use of a non-radiating boundary condition has been prioritized.

4.6.3 Flow past an open cavity. $\mathbf{M} = 0.7$.

The acoustic feedback to the flow, which is one of the advantages of using unified solvers, has not been assessed yet. For this reason we next present a simulation of cavity noise. The case of a 2D flow past an open cavity ($M = 0.7$ and $Re = 41.000$) is considered. Periodic vortices are formed just downstream the leading edge of the cavity. When they impinge the trailing edge, an acoustic pulse is generated that propagates upstream and triggers flow instabilities, which result in flow separation at the leading edge. An acoustically driven feedback loop is thus established. We have compared the results to those provided by an equivalent DNS [83] for a more accurate and quantitative validation. This case is characterized by an inlet velocity $U = 245$ m/s and a rectangular cavity with a length $L = 5.18$ mm and a depth $D = 2.54$ mm. The mesh used to discretize the computational domain has $391,000$ linear elements and the time step size has been taken as 2×10^{-7}.

At M = 0.7 the acoustic scales are not negligible anymore respect to

the flow oscillations like in the previous cases, and its feedback to the flow motion in the cavity becomes an important factor. This phenomenon affects in turn the subsequent wave propagation, for which it can be assumed that the coupling between scales is much stronger and the advantage of using a unified compressible solver is far more evident than in the two past scenarios. Fig. 4.11 shows vorticity and pressure isosurfaces in the cavity for four different times during a complete shedding period. These sequences can be directly compared to those presented in [83] because the same scaling has been used for both fields, and it can be concluded that the present formulation manages to reproduce the same flow patterns that were obtained with the DNS.

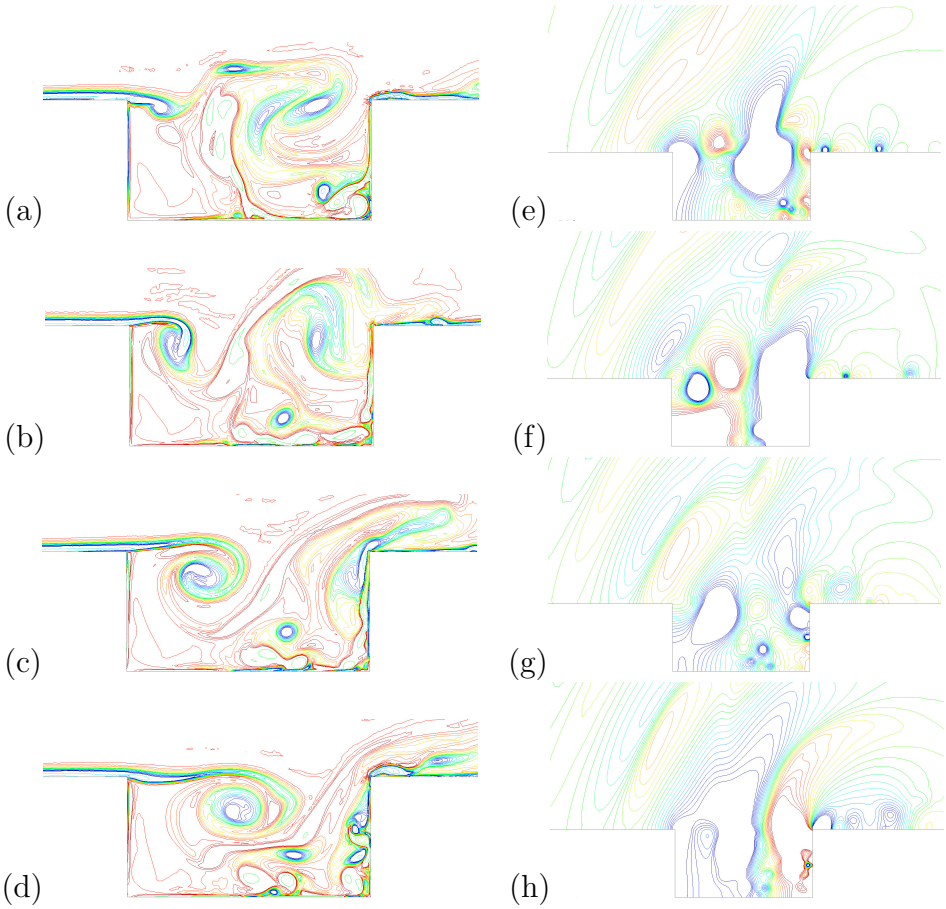

Figure 4.11: Vorticity (a-d) and pressure (e-h) isosurfaces at four different moments during the main oscillation period [83].

Unlike the previous open geometries, the partial confinement of the flow in the cavity increases the non-linearity of the problem because the propagation of the exiting waves is clearly affected by the unsteadiness of the flow. In this sense, Figs. 4.12 and 4.13 show that the acoustic component of the

solution is also properly described by the isentropic solver. On the one hand, the main oscillation mode is found at the same Strouhal number $St = 0.68$ and a similar slope is obtained for the pressure frequency spectrum at the beginning of the acoustic region outside the cavity. On the other, the further wave propagation to the far field is also properly described by the present method, see Fig. 4.13 and [83].

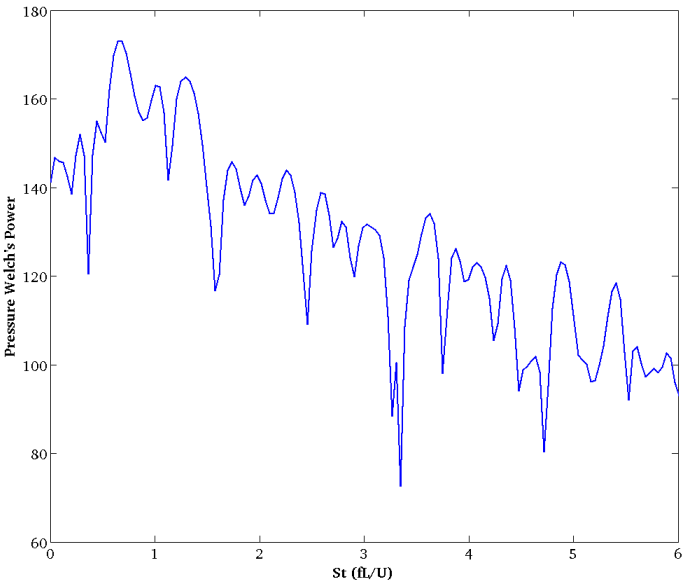

Figure 4.12: Welch's power spectrum computed with the flow pressure field at the beginning of the acoustic region.

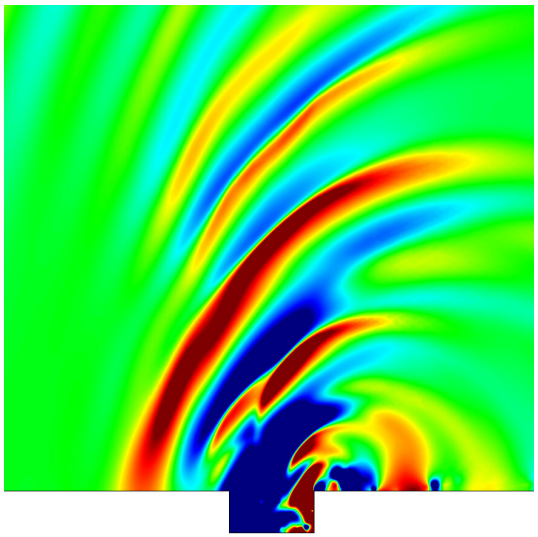

Figure 4.13: Pressure wave propagation.

4.6.4 Aeroacoustics of an oscillating 2D NACA0012 airfoil. $\mathbf{M} = 0.1$

As anticipated in Chapter 2, the same case has been computed again with the ALE extension of the isentropic compressible flow formulation. In this case, the pressure has not been split into two components because it would lead to the excessive cost of computing to full CFD problems. However, it will be very useful for validating the previously obtained flow velocity and total acoustic pressure. Regarding the former, Fig. 4.14 shows the velocity profile around the airfoil at the same positions of Fig. 4.14, obtaining very similar results. The latter though shows relevant differences, see Fig. 4.15. Although the oscillation ranges and the growing noise found in Fig. 2.15 are also obtained in this case, in all three positions the wave propagation looks cleaner because no offset interferes with the acoustic scales.

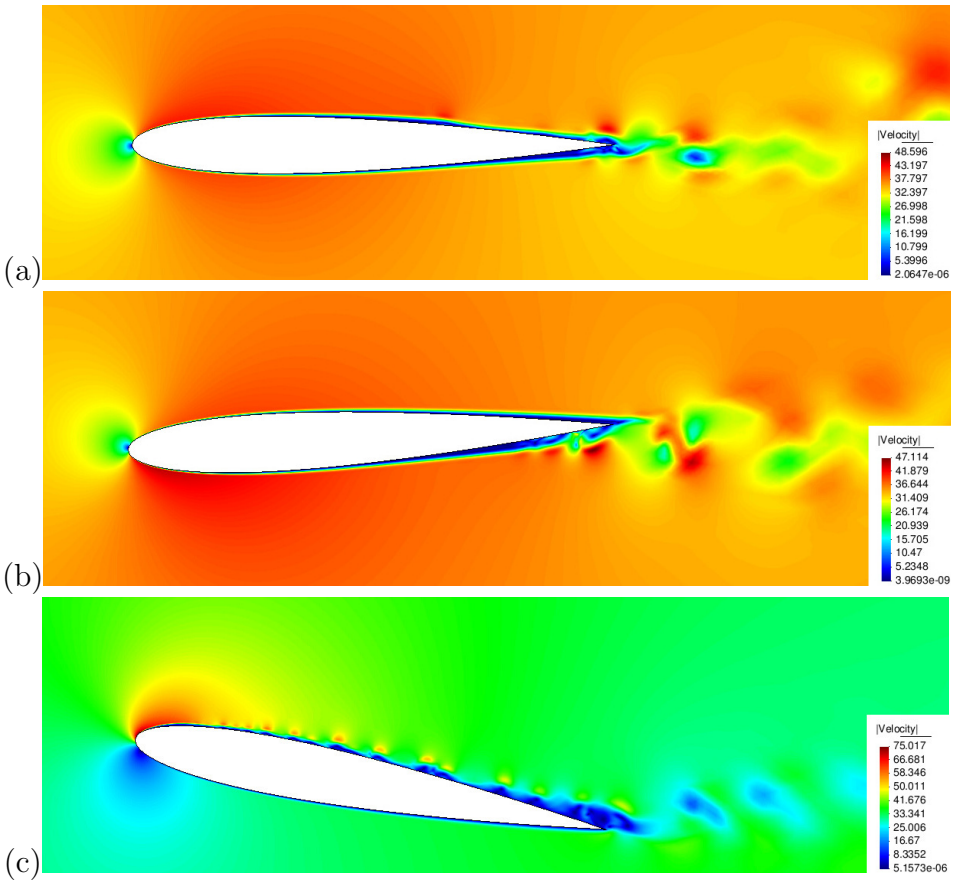

Figure 4.14: Velocity profiles at three different positions of the airfoil.

However, when pressure time histories and frequency spectra at the same four points are compared, the methods look much more consistent, see Figs. 4.16 and 2.20. Only one major discrepancy needs to be mentioned:

the noise in the wake region downstream. Whereas the isentropic compressible solver yields a very low acoustic propagation in this area, Lighthill's analogy clearly overestimates the diffraction of high frequency sound at $P3$. This disagreement might be caused by the lack of validity of this method in regions where the flow is not uniform, like turbulent jets.

4.7 Conclusions

The presented finite element formulation offers a simplified framework for dealing with subsonic adiabatic gas flows without facing the numerical inconveniences and the high computational cost of the state-of-the-art compressible flow formulations. The minimal implementation cost when departing from a monolithic incompressible solver makes this approach very attractive for solving aeroacoustic problems where heat transfer can be neglected. Moreover, its validation against the incompressible Navier-Stokes equations for a low-Mach regime has shown its suitability in problems where acoustics are not relevant. On the other hand, it has been also shown that the present formulation converges to a DNC when dealing with low speed flows.

The developed numerical method has successfully reproduced the acoustics of the incompressible Lighthill analogy and the FWH analogy with compressible flow, as well as the acoustic feedback to the flow of a DNS. The full subsonic range, from M = 0.058 to M = 0.7, has been covered and therefore, one of the main goals of this research, the development of a general numerical framework for all isentropic gas flows, has been successfully accomplished. In this sense, the presentation of a novel method for prescribing separate boundary conditions for the aerodynamic and the acoustic components strives in the same direction of offering a general solution to the problem of spurious wave reflection in aeroacoustic calculations. On the most problematic boundary for such cases, the inlet, this formulation manages to prescribe an incoming velocity while being transparent to the exiting acoustic waves. Moreover, it is compatible with any kind of non-radiating boundary condition and can be combined with a PML on the outlet in case of highly convective jets.

Finally, the ALE extension of the isentropic formulation has reduced the complexity of the aeroacoustic problem in moving domains in comparison to the method presented in Chapter 2. Apart from validating the results obtained with the hybrid method, it has yielded a better representation of the acoustic field and, as expected, a more accurate propagation in the turbulent flow region.

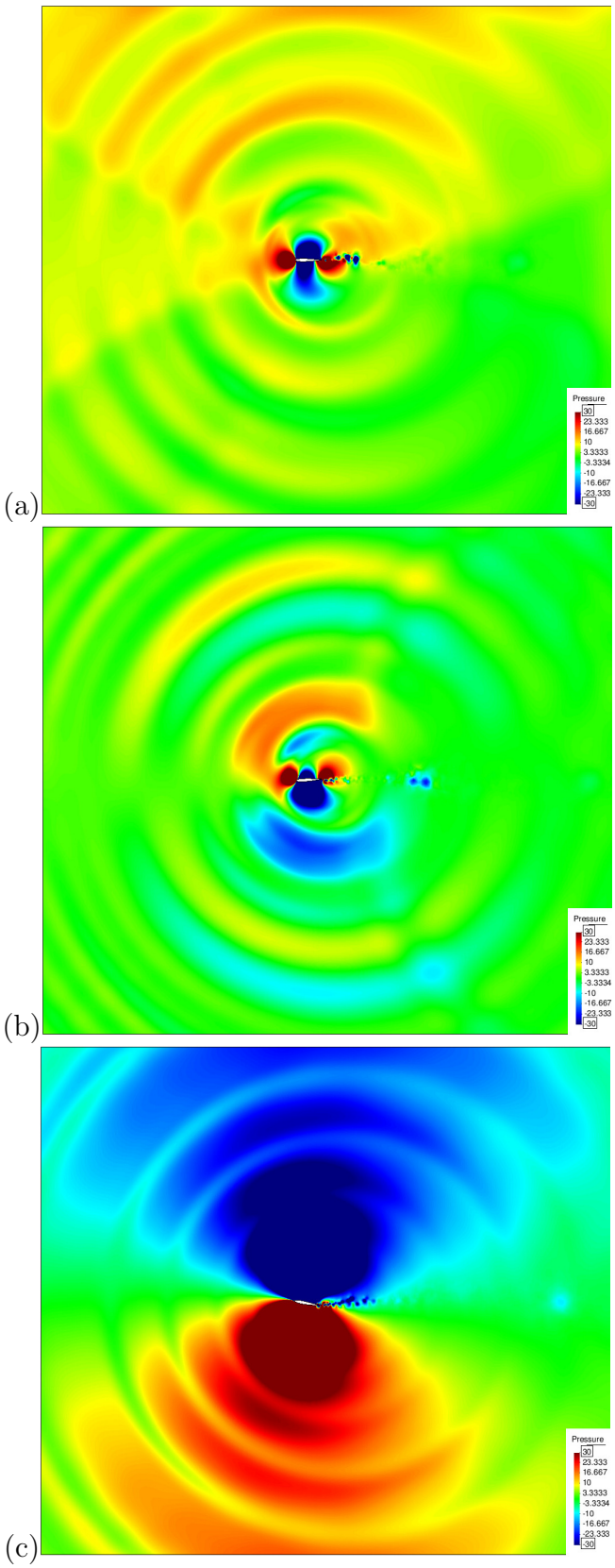

Figure 4.15: Pressure profiles at three different positions of the airfoil.

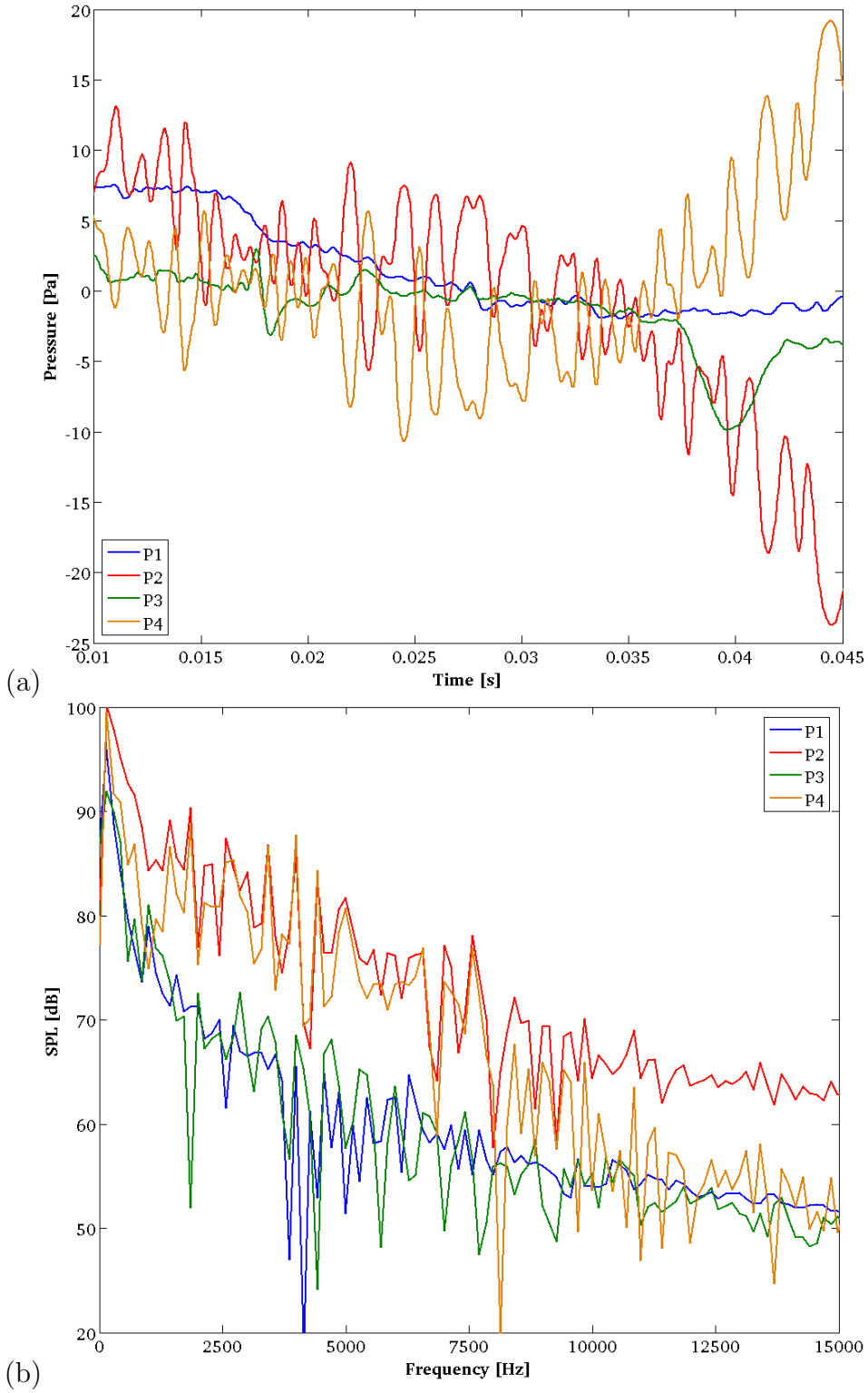

(a)

(b)

Figure 4.16: Pressure time history (a) and frequency spectrum (b) at the four selected points.

Chapter 5

Interpolation with restrictions between finite element meshes for flow problems in an ALE setting

The need for remeshing when computing flow problems in domains suffering large deformations has motivated the implementation of a tool which allows the proper transmission of information between finite element meshes. Since the Lagrangian projection of results from one mesh to another is a dissipative method, a new conservative interpolation method has been developed. A series of constraints, such as the conservation of mass or energy, are applied to the interpolated arrays through Lagrange multipliers in an error minimization problem, so that the resulting array satisfies these physical properties while staying as close as possible to the original interpolated values in the L^2 norm. Unlike other conservative interpolation methods which require a considerable effort in mesh generation and modification, the proposed formulation is mesh independent and is only based on the physical properties of the field being interpolated. Moreover, the performed corrections are neither coupled with the main calculation nor with the interpolation itself, for which reason the computational cost is very low.

5.1 Background

The interpolation of numerical solutions between computational meshes is a well known procedure with multiple applications, for example the transmission of arrays in case of problems with evolving domains, coupling between different physical problems or computational codes, initialization or update of boundary conditions or visualization of results. In some of these cases,

a simple Lagrangian interpolation within the elements is acceptable, but in other scenarios the non-conservative character of the interpolation operation can cause considerable dissipation and other kinds of numerical error. This has led to the development of multiple methods for the transmission of information between meshes in finite element computations.

The accurate projection of transmission conditions between two subdomains was the main motivation for the development of an interpolation method based on the conservation of relevant magnitudes, [104], which has already been applied to the fixed mesh ALE method by [55]. In this chapter, the projection of vector fields corresponding to the transmission conditions between subdomains in a domain decomposition problem is constrained by the conservation of mass in a weak sense and by the conservation of the L^2 norm of the solution along the boundary. The application of these restrictions is performed by solving an optimization problem with constraints controlled by Lagrange multipliers which enforce that the distance between the interpolated and the corrected solutions is minimum in the L^2 norm and that the restrictions are fulfilled. This concept is the background of the formulation presented in this work.

The pioneer works on conservative interpolation between computational meshes were an answer to the needs regarding the domain deformation in ALE (Arbitrary Lagrangian Eulerian) calculations, where the computational nodes of the mesh may either remain fixed as in the Eulerian configuration or can be prescribed an arbitrary velocity, [67]. The techniques for achieving the conservation of certain magnitudes during the interpolation process consisted in either building a new mesh by locally modifying the original one, or interpolating the results to a new random grid after computing the intersections between both meshes. The first case corresponds to the local rezoning, which normally takes place at every time step but at a low computational cost. An example of such an algorithm is presented by [136], a second order accurate scheme which divides the new cells taking into account the intersections with the old ones and guarantees the conservation of the mass fluxes along the edges of the finite volumes in 2D. This method was extended to 3D domains by [82]. On the other hand, global remapping does not assume any relation between the original and the target mesh, for which reason these algorithms deal with the whole domain and increase the computational cost, although they might be used less often during the simulation. In this sense, [152] and [69] present a remapping method which computes the intersection volume between meshes with a surface integral and builds the interpolated field performing an area-weight averaging. On the other hand, some disciplines such as weather forecast use conservative numerical methods in a semi-Lagrangian frame of reference which require the tracking of the trajectory and the interpolation of the convection velocity to an

Eulerian frame of reference. An area-weighted interpolation is also used to prevent loss of accuracy by [157]. The concept of interpolation with constraints is presented by [38] for finite volumes and finite differences, where the integration weights and the interpolation coefficients are forced to fulfill certain conditions. [1] propose a P1 exact, mass conservative interpolation scheme which also fulfills the maximum principle by reconstructing the mass field and its gradient with the elemental intersections between both meshes. Another popular technique developed recently is the common-refinement or the supermesh, [121], [77] and [76]. It consists in the construction of an intermediate mesh as a union of the original and the target meshes in order to allow an efficient Galerkin projection of the results, which minimizes the L^2 norm of the interpolation error. An important method regarding the formulation that will be presented in this work is that of [40]. It is not based on grid operations or algorithms but on the physics of the problem, in this case the shallow water equations. The unknown velocity on the target mesh is expressed as an L^2 projection of the old one plus a correction factor defined in terms of the gradient of a scalar function (pseudo-pressure), which leads to an elliptic problem of the projected velocity correction. Additionally, this method yields local mass conservation without changing the vorticity of the velocity field.

As stated before, one of the main fields of application of conservative interpolation methods is the transmission of loads between interfaces belonging to non coincident meshes. This scenario happens in coupled problems such as fluid-structure interaction or in domain decomposition methods. In the first case, [37] propose the conservation of the load along the interface with a node-projection scheme. On the other hand, [75] use a quadrature-projection of the loads, which involves the transmission of the integration points to the target mesh, and finally the local version of the common-refinement [121], being this last one the only whose error is independent of the degree of mismatching between meshes. A comparison between them can be found in [119], where the common-refinement method is recommended due to its general good performance with a reasonable computational cost. In the case of non-conforming domain decomposition methods, one of the most extended methods of conservative interpolation is the mortar element, [27].

An alternative approach to the remeshing problem is that presented by [39], which presents a method for a homogeneous distortion of moving computational meshes by preventing those elements located near the boundaries to collapse. This is achieved by solving a virtual structural problem on the mesh and giving the problematic elements a higher Young modulus in order to reach a uniform mesh displacement field. For problems involving moderate deformations leading to high local mesh distortion, this method avoids remeshing, whereas for large deformations it would reduce the remeshing

frequency. For this reason, it is foreseen as a complementary tool to the present work.

The presented methodology overcomes the typical difficulties related to the described conservative schemes. First of all, the method is valid for all discretizations and is independent of the degree of coincidence between them. Moreover, neither algorithms related to the mesh, such as rezoning, nor computation of local integrals are performed, for which reason the computational cost will be low and only dependent on the size of the meshes. Another important property is that, unlike many of the aforementioned methods, the conservation is achieved interpolating directly the solution values instead of fluxes at overlapping boundaries. Although the conservation of magnitudes will be global and not satisfied locally, the procedure presented in this work allows to enforce conservation conditions of a general form which may not be restricted to mass and momentum conservation.

5.2 Formulation

5.2.1 The concept

Let us consider a finite element partition $\mathcal{T}_{h,1}$ of a domain $\Omega \subset \mathbb{R}^d$, $d \geq 1$, and a discrete solution $u_{h,1}$ of an arbitrary problem defined in the subspace of functions $\mathcal{V}_{h,1} \subset \mathcal{V}$, where $\mathcal{V}$ is the space of functions where the continuous solution lives. For the sake of conciseness, we will consider scalar functions in this section. Given another finite element partition $\mathcal{T}_{h,2}$ of the same domain, the objective is to construct $u_{h,2}$ from $u_{h,1}$ with the same approximation properties to the continuous solution as $u_{h,1}$. We will call $u_{h,2}$ the interpolation of $u_{h,1}$ on $\mathcal{T}_{h,2}$ (see Fig. 5.1), and $\mathcal{V}_{h,2}$ the corresponding finite element space.

In order to simplify the notation for the rest of the chapter, the finite element functions will be expressed in terms of the shape functions of each finite element partition, which will be denoted as $\{N_n^a\}$, where $n = 1, 2$ refers to the mesh and the superscript to the nodes, so that a will run from 1 to the number of nodes of each mesh. Denoting by U_n^a the corresponding nodal values and assuming a standard Lagrangian interpolation, we may write

$$u_{h,n} = \sum_a N_n^a U_n^a, \quad n = 1, 2,$$

where summation is understood to run over the set of nodal values.

Let us describe two simple possibilities to compute $u_{h,2}$.

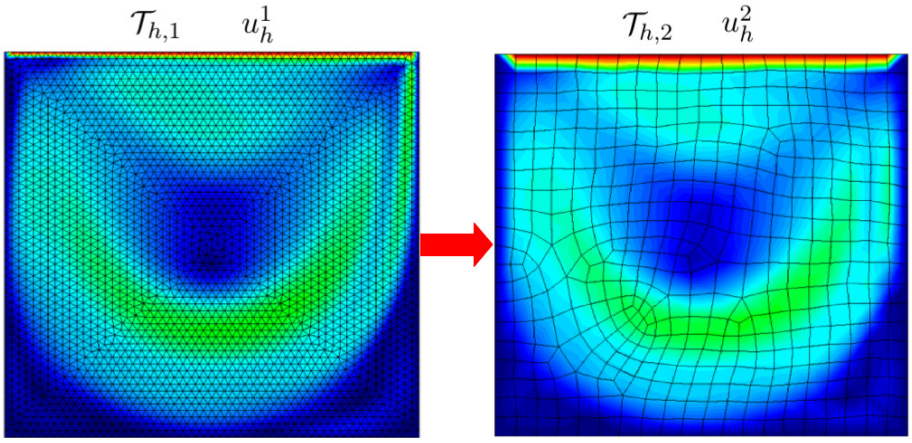

Figure 5.1: Interpolation of a finite element solution between two computational meshes.

Option 1: L^2 projection

The interpolation $u_{h,2}$ might consist in an L^2 projection of $u_{h,1}$ onto $\mathcal{V}_{h,2}$. This is equivalent to minimize the functional $J(v_{h,2}) = \frac{1}{2}\|v_{h,2} - u_{h,1}\|^2_{L^2(\Omega)}$, and leads to the problem: find $u_{h,2} \in \mathcal{V}_{h,2}$ such that

$$\int_\Omega u_{h,2} v_{h,2} = \int_\Omega u_{h,1} v_{h,2},$$

for all test functions $v_{h,2} \in \mathcal{V}_{h,2}$. Using the shape functions and nodal values, the problem to be solved becomes:

$$\sum_b \int_\Omega N_2^a N_2^b U_2^b = \sum_c \int_\Omega N_2^a N_1^c U_1^c, \tag{5.1}$$

for all nodes a of $\mathcal{T}_{h,2}$. Let us call $\mathbf{U}_n$ the array of nodal values of $u_{h,n}$, M_2 the standard mass matrix of $\mathcal{T}_{h,2}$ and $\mathbf{P}_{21}$ the array whose components appear in the right-hand-side of Eq. (5.1). The solution to this equation can thus be written as

$$\mathbf{U}_2 = M_2^{-1}\mathbf{P}_{21}.$$

Apart from the cost of solving this algebraic system, the algorithmic difficulty of this method is the evaluation of the components of $\mathbf{P}_{21}$. Suppose that numerical integration associated to $\mathcal{T}_{h,2}$ is used, with integration points $\{\mathbf{x}_2^g\}$ and associated weights $\{w_2^g\}$. Then

$$\sum_c \int_\Omega N_2^a N_1^c U_1^c \approx \sum_c \sum_g w_2^g N_2^a(\mathbf{x}_2^g) N_1^c(\mathbf{x}_2^g) U_1^c$$

The difficulty is the evaluation of $N_1^c(\mathbf{x}_2^g)$. This requires finding the element domain $K_1 \in \mathcal{T}_{h,1}$ where $\mathbf{x}_2^g$ belongs. If node c belongs to this element K_1, then $N_1^c(\mathbf{x}_2^g)$ can be computed from interpolation. Otherwise, it is zero.

Option 2: standard Lagrangian interpolation

The method described above requires the solution of a system of equations, which may be inconvenient from a computational point of view, even if it is easy to invert the mass matrix. A simpler alternative is to obtain the nodal values of $u_{h,2}$ simply by interpolation, i.e.,

$$U_2^a = \sum_b N_1^b(\mathbf{x}_2^a) U_1^b,$$

where $\mathbf{x}_2^a$ are the coordinates of node a. This is a node of $\mathcal{T}_{h,2}$, whereas $\{N_1^b\}$ are the shape functions of $\mathcal{T}_{h,1}$. Therefore, one needs to find the element $K_1 \in \mathcal{T}_{h,1}$ where $\mathbf{x}_2^a$ belongs, and then proceed to interpolate as in the previous approach.

Interpolation with restrictions

The approach described above has the drawback of being non-conservative and very diffusive, which is precisely what the application of certain restrictions aims to compensate. However, it is more flexible and easier to parallelize, whereas the L^2 projection, in spite of yielding a smaller interpolation error, is not completely conservative either and in some cases the mass and other quantities should be corrected as well. Therefore, the idea we propose consists in obtaining $\tilde{u}_{h,2} \in \mathcal{V}_{h,2}$ that satisfies two important features:

- It must remain the nearest solution to $u_{h,2}$ in the L^2 norm, $u_{h,2}$ being obtained from a standard Lagrangian interpolation, for example.
- It must fulfill some physical properties of $u_{h,1}$, which could involve for example the conservation of a set of magnitudes.

In order to describe the second point, let us define the restriction operators (forms). When applied to the finite element functions, these operators give a scalar result corresponding to a relevant magnitude of the physical problem being calculated. We write them as

$$R_{n,i} : \mathcal{V}_{h,n} \longrightarrow \mathbb{R}, \tag{5.2}$$

where the subindex $n = 1, 2$ refers either to the donor 1 or to the target mesh 2, and $i = 1, ..., m$ is the restriction counter. Operators $R_{n,i}$ can be written in terms of their nodal values, so that

$$R_{n,i}(u_{h,n}) = \sum_a R_{n,i}^a U_n^a,$$

where $R^a_{n,i} = R_{n,i}(N^a_n)$ for linear restrictions and $R^a_{n,i}$ may depend on $\mathbf{U}_n$ in the case of non-linear ones.

Since it has been stated that the restriction consists in conserving the value of these selected magnitudes, the following equalities must hold:

$$\sum_a R^a_{2,i}\tilde{U}^a_2 = \sum_b R^b_{1,i}U^b_1, \quad i = 1, \ldots, m, \tag{5.3}$$

where $\tilde{U}_2$ denotes the nodal values associated to $\tilde{u}_{h,2}$. The computational domain Ω remains the same for all stages of the process, since the interpolation process is completely static although the simulation considers a dynamic domain. In some cases, only a part of the domain needs to be interpolated, for example in case of fluid-structure interaction (FSI) problems, where the values at the interface must be exchanged between both subdomains. This scenario will not be considered in the present work.

Although this method is only presented for some particular flow problems, it can be extended to other physical problems. For example, the formulation could be extended to flows with free surfaces in a straightforward way by restricting the constraints to the flow subdomain, which would require subelemental integration, [55]. Problems in which the restrictions are inequalities rather than equalities could also be treated by embedding the scheme in a iterative loop that requires to solve a sequence of problems with equality constraints, as it is done in optimization; these inequality restrictions are found for example in plasticity problems, where the stresses are required to be admissible, [34]. This last example requires a further extension consisting in posing the restriction in terms of variables defined at the numerical integration points, such as internal variables like plastic multipliers or damage; it is only required to be able to express these variables in terms of the nodal unknowns of the problem and proceed as we propose here.

At this point it is important to distinguish the current method from the mortar method, [27]. Unlike the present method, the mortar method consists in a domain decomposition technique which performs a L^2 projection along an interface between non-matching grids satisfying adequate matching conditions. The restriction of these fluxes might be performed with Lagrange multipliers. In our case, the interpolation is performed point by point and the restrictions affect the whole domain.

5.2.2 Application to linear restrictions

Let us develop the concept introduced above in the case in which the restrictions are linear functionals. For example, bearing in mind that one of the main issues in the numerical computations of incompressible flows is the conservation of mass, it is reasonable to formulate a problem with this linear restriction.

The restrictions can be enforced through Lagrange multipliers $\boldsymbol{\lambda} = (\lambda_1, \ldots, \lambda_m) \in \mathbb{R}^m$. Given $u_{h,2} \in \mathcal{V}_{h,2}$, the interpolation of $u_{h,1} \in \mathcal{V}_{h,1}$ on $\mathcal{T}_{h,2}$, let us define the following functional $L : \mathcal{V}_{h,2} \times \mathbb{R}^m \longrightarrow \mathbb{R}$:

$$L(v_{h,2}, \boldsymbol{\mu}) = \frac{1}{2} \left\| \sum_a N_2^a (V_2^a - U_2^a) \right\|^2_{L^2(\Omega)} - \sum_{i=1}^m \mu_i \left(\sum_a R_{2,i}^a V_2^a - \sum_b R_{1,i}^b U_1^b \right), \tag{5.4}$$

where V_2^a are the nodal values of $v_{h,2}$, $\boldsymbol{\mu} \in \mathbb{R}^m$ is an admissible set of Lagrange multipliers and the subscript in the norm indicates that it is the $L^2(\Omega)$ one. Then the solution that minimizes the distance to the interpolated values and imposes the restrictions will be:

$$[\tilde{u}_{h,2}, \boldsymbol{\lambda}] = \arg \inf_{v_{h,2} \in \mathcal{V}_{h,2}} \sup_{\boldsymbol{\mu} \in \mathbb{R}^m} \left[L\left(v_{h,2}, \boldsymbol{\mu}\right) \right]. \tag{5.5}$$

This is a saddle point problem. A necessary and sufficient condition for it to be well posed is that the finite element space $\mathcal{V}_{h,2}$ and $\mathbb{R}^m$ satisfy the appropriate inf-sup condition. This in particular restricts the number of Lagrange multipliers. However, since m is usually very small, we have not encountered any stability problem.

The equations to be solved are obtained by differentiation of the functional L with respect to the unknowns:

$$\frac{\partial L}{\partial V_2^b} = 0 \Longrightarrow \sum_a \int_\Omega N_2^b N_2^a \tilde{U}_2^a - \sum_{i=1}^m \lambda_i R_{2,i}^b = \sum_a \int_\Omega N_2^b N_2^a U_2^a, \quad \text{for all } b, \tag{5.6}$$

$$\frac{\partial L}{\partial \mu_i} = 0 \Longrightarrow \sum_a R_{2,i}^a \tilde{U}_2^a = \sum_b R_{1,i}^b U_1^b, \quad \text{for all } i. \tag{5.7}$$

These two equations can be arranged into the following algebraic system:

$$\begin{bmatrix} M_2 & -R_2^T \\ R_2 & 0 \end{bmatrix} \begin{bmatrix} \tilde{\mathbf{U}}_2 \\ \boldsymbol{\lambda} \end{bmatrix} = \begin{bmatrix} M_2 \mathbf{U}_2 \\ R_1 \mathbf{U}_1 \end{bmatrix},$$

where R_n are the matrices of the linear restriction operators, $n = 1, 2$.

In order to avoid solving the full linear system, which can be expensive and requires to add the Lagrange multiplier unknowns to the solver, we can solve first the Schur complement problem for the Lagrange multipliers, and later compute the nodal values $\tilde{\mathbf{U}}_2$:

$$R_2 M_2^{-1} R_2^T \boldsymbol{\lambda} = R_1 \mathbf{U}_1 - R_2 \mathbf{U}_2, \tag{5.8}$$

$$\tilde{\mathbf{U}}_2 = \mathbf{U}_2 + M_2^{-1} R_2^T \boldsymbol{\lambda}. \tag{5.9}$$

Note that system (5.8) is of small size $m \times m$. The only difficulty for solving this problem is the calculation of M_2^{-1}. This is trivial if the mass matrix M_2 is approximated by a diagonal matrix. If not, the problem can be solved using iterative methods, each iteration of which requiring the solution of a system of equations with matrix M_2; it is known that these systems can be solved with a small computational cost.

5.2.3 Non-linear restrictions

The same idea can be applied in the case in which the restrictions are non-linear, i.e., mappings $R_{n,i}$ in (5.2) are non-linear. Let us assume that we write them as

$$R_{n,i}(v_{h,n}) = \sum_a R^a_{n,i}(\mathbf{V}_n) V^a_n,$$

with the components $R^a_{n,i}(\mathbf{V}_n)$ depending of the nodal values $\mathbf{V}_n$. We consider now the functional

$$\begin{aligned} L(v_{h,2}, \boldsymbol{\mu}) = \frac{1}{2} \left\| \sum_a N^a_2 (V^a_2 - U^a_2) \right\|^2_{L^2(\Omega)} \\ - \sum_{i=1}^m \mu_i \left(\sum_a R^a_{2,i}\left(\mathbf{V}_2\right) V^a_2 - \sum_b R^b_{1,i}\left(\mathbf{U}_1\right) U^b_1 \right). \end{aligned} \tag{5.10}$$

The optimization of this functional leads to the equations:

$$\begin{aligned} \frac{\partial L}{\partial V^b_2} = 0 \Longrightarrow \ & \sum_a \int_\Omega N^b_2 N^a_2 \tilde{U}^a_2 - \sum_{i=1}^m \lambda_i \left(R^b_{2,i}(\tilde{\mathbf{U}}_2) + \sum_a \frac{\partial R^a_{2,i}(\tilde{\mathbf{U}}_2)}{\partial \tilde{U}^b_2} \tilde{U}^a_2 \right) \\ & = \sum_a \int_\Omega N^b_2 N^a_2 U^a_2, \quad \text{for all } b, \end{aligned} \tag{5.11}$$

$$\frac{\partial L}{\partial \mu_i} = 0 \Longrightarrow \ \sum_a R^a_{2,i}(\tilde{\mathbf{U}}_2) \tilde{U}^a_2 = \sum_b R^b_{1,i}(\mathbf{U}_1) U^b_1, \quad \text{for all } i. \tag{5.12}$$

This is a non-linear system that needs to be linearized. Let us use a superscript between parenthesis to denote the iteration counter. Using a fixed point method for (5.11) and a fixed-point or Newton-Raphson linearization

for (5.12) we have that

$$\sum_a \int_\Omega N_2^b N_2^a \tilde{U}_2^{a,(k)} - \sum_{i=1}^m \lambda_i^{(k)} \left(R_{2,i}^b(\tilde{\mathbf{U}}_2^{(k-1)}) + \sum_a \frac{\partial R_{2,i}^a(\tilde{\mathbf{U}}_2^{(k-1)})}{\partial \tilde{U}_2^b} \tilde{U}_2^{a,(k-1)} \right)$$
$$= \sum_a \int_\Omega N_2^b N_2^a U_2^a, \quad \text{for all } b, \tag{5.13}$$

$$\sum_b \left(R_{2,i}^b(\tilde{\mathbf{U}}_2^{(k-1)}) + \gamma \sum_a \frac{\partial R_{2,i}^a(\tilde{\mathbf{U}}_2^{(k-1)})}{\partial \tilde{U}_2^b} \tilde{U}_2^{a,(k-1)} \right) \tilde{U}_2^{b,(k)}$$
$$= \sum_b R_{1,i}^b(\mathbf{U}_1) U_1^b + \gamma \sum_a \frac{\partial R_{2,i}^a(\tilde{\mathbf{U}}_2^{(k-1)})}{\partial \tilde{U}_2^b} \tilde{U}_2^{a,(k-1)} \tilde{U}_2^{b,(k-1)}, \quad \text{for all } i. \tag{5.14}$$

For $k = 1$ the algorithm can be initialized taking $\tilde{\mathbf{U}}_2^{(0)} = \mathbf{U}_2$. The Newton-Raphson linearization for (5.12) corresponds to $\gamma = 1$, whereas a fixed-point (Picard's) method is obtained for $\gamma = 0$. Note that a Newton-Raphson linearization of (5.11) would imply a modification of the term multiplying $\tilde{U}_2^{a,(k)}$ in(5.13).

Let us introduce matrix $\hat{R}_2(\tilde{\mathbf{U}}_2)$, of components

$$\hat{R}_{2,i}^b(\tilde{\mathbf{U}}_2) = \sum_a \frac{\partial R_{2,i}^a(\tilde{\mathbf{U}}_2)}{\partial \tilde{U}_2^b} \tilde{U}_2^a.$$

We can now write (5.13)-(5.14) as

$$\begin{bmatrix} M_2 & -R_2^T - \hat{R}_2^T(\tilde{\mathbf{U}}_2^{(k-1)}) \\ R_2 + \gamma \hat{R}^T(\tilde{\mathbf{U}}_2^{(k-1)}) & 0 \end{bmatrix} \begin{bmatrix} \tilde{\mathbf{U}}_2^{(k)} \\ \boldsymbol{\lambda} \end{bmatrix} =$$
$$\begin{bmatrix} M_2 \mathbf{U}_2 \\ R_1 \mathbf{U}_1 + \gamma \hat{R}^T(\tilde{\mathbf{U}}_2^{(k-1)}) \tilde{\mathbf{U}}_2^{(k-1)} \end{bmatrix}.$$

The matrix of this system can be made symmetric only if $\gamma = 1$.

As for the linear problem, we could proceed to compute first $\boldsymbol{\lambda}$ by solving the corresponding Schur complement system, and then compute $\tilde{\mathbf{U}}_2$.

5.3 Implementation

The implemented interpolator is based on a search octree method which has been extended for MPI parallel computing. This algorithm builds cubic boxes around the selected entities (points, elements or subdomains) and organizes them hierarchically in a way that the search can proceed forwards

and backwards recursively without having to apply brute force every time, [133]. First of all, an octree of subdomains links each node of the target mesh with the processor containing this coordinate at the old mesh. Each subdomain has its own octree of elements that finds the element of the old mesh which corresponds to a node of the new one. Once all connections have been made and communicated between processors, all arrays of the physical problem can be projected to the target mesh by performing a Lagrangian interpolation within the found element. Finally, the obtained array can go through the optimization problem with restrictions in a completely independent subroutine (see Fig. 5.2).

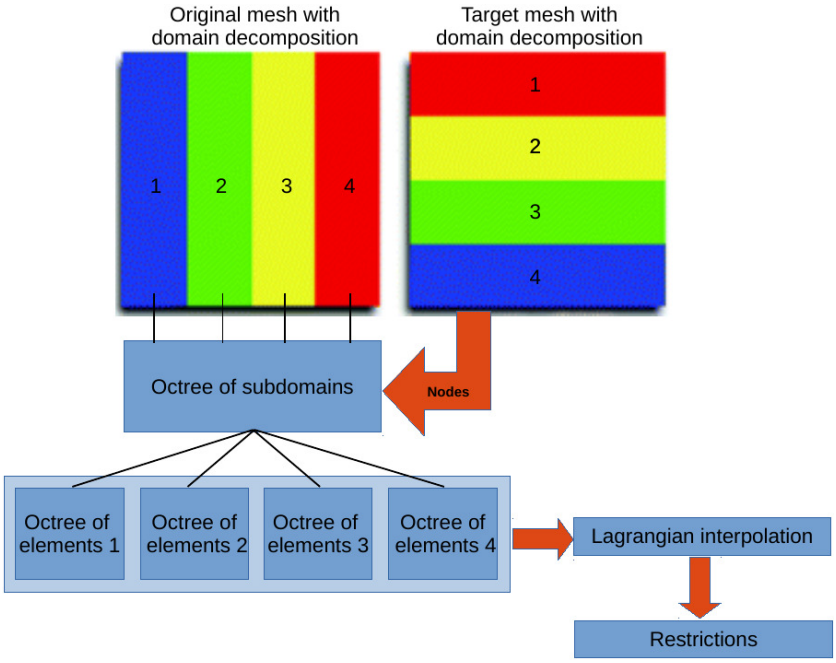

Figure 5.2: Scheme showing the computational implementation of the interpolation method. Example with 4 subdomains.

5.4 Application to the incompressible Navier-Stokes equations

The presented formulation has been applied to the incompressible Navier-Stokes equations solved in an ALE frame of reference. Our motivation to develop the formulation described here is to use it as a first step towards a complete ALE aeroacoustics calculation using Lighthill's acoustic analogy, [130], with incompressible flow and 3D dynamic realistic vocal tract geometries. The simulation of syllables with a CFD code represents a challenge

in regard to the accuracy of the interpolation of velocity and pressure fields during the remeshing stages. If we consider the numerical calculation of the syllable [as], sharp gradients are expected to appear when the upper inscissors approach the lower teeth, which combined with the large deformation of the domain from the initial open position to the final closed configuration, makes a conservative interpolation method extremely necessary in order to prevent the propagation of important numerical error sources.

5.4.1 Continuous problem

The incompressible Navier-Stokes equations model the motion of isentropic, low-speed viscous flows which do not involve relevant compressibility effects. These are to be solved in a computational domain $\Omega \subset \mathbb{R}^d$ (where $d = 2, 3$ is the number of space dimensions) with boundary $\partial\Omega$ and prescribed initial and boundary conditions. Splitting $\partial\Omega$ into two disjoint sets $\partial\Omega = \Gamma_D \cup \Gamma_N$, the mathematical problem to be faced reads

$$\begin{aligned}
&\partial_t \mathbf{u} - \nu\Delta\mathbf{u} + \mathbf{u}\cdot\nabla\mathbf{u} + \nabla p = \mathbf{f} && \text{in } \Omega,\ t > 0,\\
&\nabla\cdot\mathbf{u} = 0 && \text{in } \Omega,\ t > 0,\\
&\mathbf{u}(\mathbf{x}, 0) = \mathbf{u}_0(\mathbf{x}) && \text{in } \Omega,\ t = 0,\\
&\mathbf{u}(\mathbf{x}, t) = \mathbf{u}_D(\mathbf{x}, t) && \text{on } \Gamma_D,\ t > 0,\\
&\mathbf{n}\cdot\boldsymbol{\sigma}(\mathbf{x}, t) = \mathbf{t}_N(\mathbf{x}, t) && \text{on } \Gamma_N,\ t > 0,
\end{aligned}$$

where $\mathbf{u}$ is the velocity, p the pressure, $\mathbf{f}$ the vector of body forces, ν the kinematic viscosity, $\mathbf{u}_0$ the velocity initial condition, $\mathbf{u}_D$ the velocity Dirichlet condition, $\mathbf{n}$ the exterior unit normal to $\partial\Omega$, $\boldsymbol{\sigma} = -p\mathbf{I} + \nu\mathbf{n}\cdot\nabla\mathbf{u}$ and $\mathbf{t}_N$ the prescribed (pseudo-)traction.

Let $\mathcal{V}_D$ the space of vector functions with components in $H^1(\Omega)$ and equal to $\mathbf{u}_D$ on Γ_D, and $\mathcal{V}_0$ the analogous space of functions vanishing on Γ_D. Let also $\mathcal{Q} = L^2(\Omega)$, being the mean of these functions zero if Γ_N is empty. Let $\langle\cdot,\cdot\rangle_\omega$ be the integral of the product of two functions in the domain ω (with the subscript omitted when $\omega = \Omega$) and $(\cdot,\cdot)$ the $L^2(\Omega)$-inner product. The weak form of the Navier-Stokes equations can be written as follows: for all time $t > 0$, find $\mathbf{u}(t) \in \mathcal{V}_D$ and $p(t) \in \mathcal{Q}$, with appropriate regularity in time, such that

$$\begin{aligned}
(\partial_t\mathbf{u}, \mathbf{v}) + \langle\mathbf{u}\cdot\nabla\mathbf{u}, \mathbf{v}\rangle + \nu(\nabla\mathbf{u}, \nabla\mathbf{v}) - (p, \nabla\cdot\mathbf{v}) &= \langle\boldsymbol{f}, \mathbf{v}\rangle + \langle\boldsymbol{t}_N, \mathbf{v}\rangle_{\Gamma_N},\\
(q, \nabla\cdot\mathbf{u}) &= 0,
\end{aligned}$$

for all $\mathbf{v} \in \mathcal{V}_0$ and $q \in \mathcal{Q}$, and supplemented with the weak form of the initial conditions.

When the domain Ω is time dependent, this dependency can be taken into account using an ALE formulation. If $\mathbf{u}_{\text{dom}}$ is the velocity of the points

in Ω, the only modification that needs to be introduced to the previous equations is the replacement of the advection velocity in the convective term by $\mathbf{u} - \mathbf{u}_{\text{dom}}$.

5.4.2 Finite element approximation and time integration using a monolithic scheme

Let us consider a finite element partition of the domain Ω of size h, and use this letter as subscript to denote finite element functions and spaces. Only conforming finite element approximations will be considered in what follows.

Concerning the time integration, the monolithic approach for solving the incompressible Navier-Stokes equations consists in building a linearized system with both velocity and pressure degrees of freedom, which leads to the coupled calculation of the momentum and mass equations in one single step. To approximate the first order time derivative, a third order backward finite difference scheme (BDF3) has been used. Let us partition the time interval $[0, T]$ into N equal time steps of size $\delta t := t^{n+1} - t^n$ so that $0 \equiv t^0 < t^1 < \ldots < t^n < \ldots < t^N \equiv T$. Given a generic time dependent function $g(t)$, the following notation will be used for the BDF3 approximation to the first time derivative:

$$\partial_t g|_{t^{n+1}} \approx \delta_t g^{n+1} := \frac{1}{\delta t}\left(\frac{11}{6}g^{n+1} - 3g^n + \frac{3}{2}g^{n-1} - \frac{1}{3}g^{n-2}\right),$$

where g^n denotes evaluation of g at time step t^n. At an arbitrary time step of the numerical simulation, the final fully discretized implicit scheme in space and time reads as follows. From known $\mathbf{u}_h^{n-2}$, $\mathbf{u}_h^{n-1}$ and $\mathbf{u}_h^n$, compute the incompressible velocity and pressure at time step t^{n+1}, $\left[\mathbf{u}_h^{n+1}, p_h^{n+1}\right] \in \mathcal{V}_{D,h} \times \mathcal{Q}_h$, such that

$$\begin{aligned}\left(\delta_t \mathbf{u}_h^{n+1}, \mathbf{v}_h\right) + \langle \mathbf{u}_h^{n+1} \cdot \nabla \mathbf{u}_h^{n+1}, \mathbf{v}_h \rangle + \nu \left(\nabla \mathbf{u}_h^{n+1}, \nabla \mathbf{v}_h\right) - \left(p_h^{n+1}, \nabla \cdot \mathbf{v}_h\right) \\ + \left(q_h, \nabla \cdot \mathbf{u}_h^{n+1}\right) = \langle \mathbf{f}^{n+1}, \mathbf{v}_h \rangle + \langle \mathbf{t}_N^{n+1}, \mathbf{v}_h \rangle_{\Gamma_N},\end{aligned} \tag{5.15}$$

for all test functions $[\mathbf{v}_h, q_h] \in \mathcal{V}_{0,h} \times \mathcal{Q}_h$. This is the standard Galerkin approximation of the problem. Stabilization is required to deal with convection-dominated flows. Likewise, the pressure and velocity spaces have to satisfy an adequate inf-sup condition or, otherwise, a stabilization technique is also required. In our calculations we use the approach described in [47].

5.4.3 Examples of restrictions for incompressible flows

Let $\mathbf{u}_{h,1}$ be the velocity computed from (5.15) at a certain time step and with a mesh $\mathcal{T}_{h,1}$. Suppose now that Ω is remeshed and the new finite

element partition is $\mathcal{T}_{h,2}$. Using the notation of the previous section, if $\mathbf{u}_{h,1} = \sum_a N_1^a \mathbf{U}_1^a$, the straightforward interpolation will produce $\mathbf{u}_{h,2} = \sum_b N_2^b \mathbf{U}_2^b$. From this, we wish to compute now $\tilde{\mathbf{u}}_{h,2}$, an approximation to $\mathbf{u}_{h,2}$ satisfying certain restrictions.

The imposition of restrictions is obviously problem-dependent. In the case of the incompressible Navier-Stokes equations, we will consider *conservation of mass, conservation of kinetic energy and conservation of linear momentum*. The first and last restrictions are linear, whereas the second is non-linear (quadratic). They can be written as:

$$\int_\Omega \nabla \cdot \tilde{\mathbf{u}}_{h,2} = \int_\Omega \nabla \cdot \mathbf{u}_{h,1}, \tag{5.16}$$

$$\int_\Omega |\tilde{\mathbf{u}}_{h,2}|^2 = \int_\Omega |\mathbf{u}_{h,1}|^2, \tag{5.17}$$

$$\int_\Omega \tilde{\mathbf{u}}_{h,2} = \int_\Omega \mathbf{u}_{h,1}. \tag{5.18}$$

Note that density can be cancelled in all these conditions, as well as the factor 1/2 of the kinetic energy in (5.17). The mass conservation equation (5.16) is crucial; even if we may assume $\mathbf{u}_{h,1}$ to be mass-conserving, i.e., the right-hand-side of (5.16) to be zero, this property cannot be guaranteed for $\mathbf{u}_{h,2}$, and therefore it may be very important to explicitly impose it.

Let λ_1, λ_2 and λ_{2+j}, $j = 1, \ldots, d$, be the Lagrange multipliers to enforce (5.16), (5.17) and (5.18), respectively. In this case, the Lagrangian functional to be minimized, whose generic expression is (5.10), is given by

$$\begin{aligned} L(\mathbf{v}_{h,2}, \boldsymbol{\mu}) = {} & \frac{1}{2} \int_\Omega \left(\sum_a N_2^a (\mathbf{V}_2^a - \mathbf{U}_2^a) \right)^2 \\ & - \mu_1 \int_\Omega \left(\sum_a \sum_{j=1}^d \partial_j N_2^a V_{2,j}^a - \sum_b \sum_{j=1}^d \partial_j N_1^b U_{1,j}^b \right) \\ & - \mu_2 \int_\Omega \left[\left(\sum_a N_2^a \mathbf{V}_2^a \right)^2 - \left(\sum_b N_1^b \mathbf{U}_1^b \right)^2 \right] \\ & - \sum_{j=1}^d \mu_{2+j} \int_\Omega \left(\sum_a N_2^a V_{2,j}^a - \sum_b N_1^b U_{1,j}^b \right). \end{aligned} \tag{5.19}$$

The restrictions have been expressed in terms of the velocity nodal values, that now are vectors whose components have been identified with subscript j.

Now we can proceed as in the general case, taking the derivatives of L with respect to the nodal unknowns and the Lagrange multipliers to obtain

the optimality conditions, and then linearizing the resulting non-linear problem, the non-linearity being due to the imposition of conserving the kinetic energy.

The optimality conditions read:

$$\begin{aligned}
\frac{\partial L}{\partial V_{2,j}^b} = 0 \Longrightarrow \quad & \sum_a \int_\Omega N_2^b N_2^a \tilde{U}_{2,j}^a - \lambda_1 \int_\Omega \partial_j N_2^b - 2\lambda_2 \sum_a \int_\Omega N_2^b N_2^a \tilde{U}_{2,j}^a \\
& - \lambda_{2+j} \int_\Omega N_2^b \quad = \sum_a \int_\Omega N_2^b N_2^a U_{2,j}^a, \quad \text{for all } b,\ j = 1, \ldots, d, \\
\frac{\partial L}{\partial \mu_1} = 0 \Longrightarrow \quad & \int_\Omega \sum_a \sum_{j=1}^d \partial_j N_2^a \tilde{U}_{2,j}^a = \int_\Omega \sum_b \sum_{j=1}^d \partial_j N_1^b U_{1,j}^b, \\
\frac{\partial L}{\partial \mu_2} = 0 \Longrightarrow \quad & \int_\Omega \left(\sum_a N_2^a \tilde{\mathbf{U}}_2^a \right)^2 = \int_\Omega \left(\sum_b N_1^b \mathbf{U}_1^b \right)^2, \\
\frac{\partial L}{\partial \mu_{2+j}} = 0 \Longrightarrow \quad & \int_\Omega \sum_a N_2^a \tilde{U}_{2,j}^a = \int_\Omega \sum_b N_1^b U_{1,j}^b, \quad j = 1, \ldots, d.
\end{aligned}$$

Using the notation introduced for the general case, a Newton-Raphson linearization of the problem yields:

$$\begin{aligned}
& \sum_a \int_\Omega N_2^b N_2^a \tilde{U}_{2,j}^{a,(k)} - \lambda_1^{(k)} \int_\Omega \partial_j N_2^b - 2\lambda_2^{(k)} \sum_a \int_\Omega N_2^b N_2^a \tilde{U}_{2,j}^{a,(k-1)} - \lambda_{2+j}^{(k)} \int_\Omega N_2^b \\
& \quad = \sum_a \int_\Omega N_2^b N_2^a U_{2,j}^a, \quad \text{for all } b,\ j = 1, \ldots, d, \\
& \int_\Omega \sum_a \sum_{j=1}^d \partial_j N_2^a \tilde{U}_{2,j}^{a,(k)} = \int_\Omega \sum_b \sum_{j=1}^d \partial_j N_1^b U_{1,j}^b, \\
& 2 \sum_{a,b} \sum_{j=1}^d \int_\Omega N_2^b N_2^a \tilde{U}_{2,j}^{a,(k-1)} \tilde{U}_{2,j}^{b,(k)} = \int_\Omega \left(\sum_b N_1^b \mathbf{U}_1^b \right)^2 + \int_\Omega \left(\sum_a N_2^a \tilde{\mathbf{U}}_2^{a,(k-1)} \right)^2, \\
& \int_\Omega \sum_a N_2^a \tilde{U}_{2,j}^{a,(k)} = \int_\Omega \sum_b N_1^b U_{1,j}^b, \quad j = 1, \ldots, d.
\end{aligned}$$

In the case of a Picard's scheme for the third equation, it would read

$$\sum_{a,b} \sum_{j=1}^d \int_\Omega N_2^b N_2^a \tilde{U}_{2,j}^{a,(k-1)} \tilde{U}_{2,j}^{b,(k)} = \int_\Omega \left(\sum_b N_1^b \mathbf{U}_1^b \right)^2.$$

Let $R_{n,1}$ and $R_{n,3}$ be the matrices that arise from the imposition of the conservation of mass and linear momentum, respectively, on mesh n,

$n = 1, 2$. Let also $\boldsymbol{\lambda}_3 = (\lambda_3, \ldots, \lambda_{2+d})$. Using Picard's linearization for the conservation of kinetic energy, the system to be solved at each iteration is

$$\begin{bmatrix} M_2 & -R_{2,1}^T & -2M_2\tilde{\mathbf{U}}_2^{(k-1)} & -R_{2,3}^T \\ R_{2,1} & 0 & 0 & 0 \\ (\tilde{\mathbf{U}}_2^{(k-1)})^T M_2 & 0 & 0 & 0 \\ R_{2,3} & 0 & 0 & 0 \end{bmatrix} \begin{bmatrix} \tilde{\mathbf{U}}_2^{(k)} \\ \lambda_1 \\ \lambda_2 \\ \boldsymbol{\lambda}_3 \end{bmatrix} = \begin{bmatrix} M_2\mathbf{U}_2 \\ R_{1,1}\mathbf{U}_1 \\ \mathbf{U}_1^T M_1 \mathbf{U}_1 \\ R_{1,3}\mathbf{U}_1 \end{bmatrix}.$$

As a measure of convergence of this iterative scheme, we have used precisely the kinetic energy of $\tilde{\mathbf{U}}_2$. In general, convergence is quite fast, but it can deteriorate when dealing with fields with sharp gradients and highly non-coincident meshes. Convergence can be improved using under-relaxation.

As in the general case, the Lagrange multipliers can be solved first from a Schur complement system, which is trivially constructed if M_2 is approximated by a diagonal matrix.

5.4.4 Time integration using a fractional step scheme and pressure interpolation

Instead of using the monolithic approach to integrate in time the Navier-Stokes equations, one can use a fractional step scheme, in which the calculation of the velocity and the pressure are segregated. The interest of this approach is well known; in particular, it is known that the computational cost is drastically reduced, particularly for problems with many degrees of freedom. In general, within each time step fractional step schemes consist in the computation of a non divergence-free velocity in a first stage and a Poisson problem for the pressure in a second step; finally, the velocity is corrected in order to fulfill the incompressibility condition and consistency (see [11] for a review).

Let us consider the simplest backward Euler discretization of the Navier-Stokes equations combined with a second order fractional step method. Supposing that there are only Dirichlet conditions, the equations to be solved are:

$$\begin{aligned} &\frac{1}{\delta t}\left(\hat{\mathbf{u}}_h^{n+1} - \mathbf{u}_h^n, \mathbf{v}_h\right) + \langle \hat{\mathbf{u}}_h^{n+1} \cdot \nabla \hat{\mathbf{u}}_h^{n+1}, \mathbf{v}_h \rangle + \nu\left(\nabla \hat{\mathbf{u}}_h^{n+1}, \nabla \mathbf{v}_h\right) - (p_h^n, \nabla \cdot \mathbf{v}_h) \\ &\quad = \langle \boldsymbol{f}^{n+1}, \mathbf{v}_h \rangle, \\ &\left(\nabla p_h^{n+1}, \nabla q_h\right) = (\nabla p_h^n, \nabla q_h) + \frac{1}{\delta t}\left(\nabla \cdot \hat{\mathbf{u}}_h^{n+1}, q_h\right), \\ &\frac{1}{\delta t}\left(\mathbf{u}_h^{n+1} - \hat{\mathbf{u}}_h^{n+1}, \mathbf{v}_h\right) + \left(\nabla p_h^{n+1}, \mathbf{v}_h\right) - (\nabla p_h^n, \mathbf{v}_h) = 0, \end{aligned}$$

where $\hat{\mathbf{u}}$ is the non-solenoidal intermediate velocity. Once again, the stabilization terms needed for using equal interpolation for the velocity and pressure fields have been omitted for the sake of simplicity.

An important particularity of the second order fractional step scheme presented is that the momentum equation uses the pressure field of the previous time step. If the computational domain is remeshed at a certain time step, not only the velocity, but also the pressure must be interpolated to the target mesh when the calculation restarts. In order to ensure an accurate interpolation, the conservation of the L^2-norm of the pressure can be imposed as a restriction. Proceeding as described for the general case, the calculation of the pressure nodal values $\tilde{\mathbf{P}}_2$ from $\mathbf{P}_2$, computed from the standard interpolation of $\mathbf{P}_1$, consists in the optimization of the functional:

$$L(q_{h,2}, \boldsymbol{\mu}) = \frac{1}{2} \left\| \sum_a N_2^a (Q_2^a - P_2^a) \right\|^2_{L^2(\Omega)} - \mu \int_\Omega \left(\sum_{a,b} Q_2^b N_2^b N_2^a Q_2^a - \sum_{c,d} P_1^d N_1^d N_1^c P_1^c \right), \tag{5.20}$$

where we have assumed that functions in the pressure spaces are interpolated also with the shape functions $\{N_i^a\}$, $i = 1, 2$.

Now we can proceed as for the velocity interpolation with restrictions, obtaining the optimality conditions for (5.20), linearizing them, solving for the optimal Lagrange multiplier λ from a Schur complement problem and, finally, obtaining $\tilde{\mathbf{P}}_2$ as a correction of $\mathbf{P}_2$ with λ known. Details are omitted.

5.5 Numerical results

5.5.1 Method validation: interpolation between identical translated meshes

Before proceeding to analyze the correction performed by the restrictions on the interpolated field in common application cases, such ALE calculations, a first case consisting in an analytical solution is presented to assess the dissipation caused by the non-conservative interpolation and the efficiency of the compensation introduced by the present method. This function is interpolated from an original structured mesh of bilinear elements with dimensionless size $h = 0.025$ covering the domain $\Omega = [0, 1] \times [0, 1]$ to an identical mesh which has been shifted to the right with elements of size $h/2$, so the old and the new nodes do not coincide at all, see [35]. Afterwards, the function is interpolated back to the original mesh, repeating this sequence up to 20 times. The analytical solution is given by $\boldsymbol{u} = (u_x, u_y)$, with

$$u_x = 2x^2 y \left(x - 1\right)^2 \left(y - 1\right) \left(2y - 1\right),$$
$$u_y = -2y^2 x \left(y - 1\right)^2 \left(x - 1\right) \left(2x - 1\right).$$

Original value	0.013650
After Interp. without restrictions	0.013621
Interp. with restrictions	0.013653

Table 5.1: Maximum values of $|\boldsymbol{u}|$ at the first interpolation stage.

Original value	0.013650
After Interp. without restrictions	0.012244
Interp. with restrictions	0.013261

Table 5.2: Maximum values of the final norm of $|\boldsymbol{u}|$.

Since $\boldsymbol{u}|_\Gamma = \mathbf{0}$, where $\Gamma = \partial\Omega$, only the conservation of momentum and L^2 norm are applied. Table 5.1 shows the evolution of the maximum of $|\boldsymbol{u}|$ during the first interpolation process: after a 2% loss caused by the point-by-point interpolation, the correction brings the maximum back to its original value with a small overflow. In spite of the benefit, this scenario shows that this global method does not respect the local features of the solution, such as peak values. However, this deviations are very small and new spurious peaks are not possible because the method enforces that the final solution remains the nearest possible to the interpolated one. The same happens with the sign preservation and the monotonicity of the solution, since the method does not enforce them explicitly and some unwanted sign changes might appear at points where the function or its derivative are very close to zero. Nonetheless, these errors will be always negligible for the same reason.

Next, the accumulation of the interpolation error along the whole sequence and its compensation are analyzed. After the 20th interpolation the dissipation is considerable as it can be seen in the following series of plots of $|\boldsymbol{u}|$, see Fig 5.3, which use the same scale in order to reflect the degradation of the solution. Fig. 5.3d and Table 5.2 show how the imposition of momentum and L^2 norm conservation compensate most of the dissipation.

5.5.2 Flow around a cylinder

In order to show the benefit of the presented formulation in a straightforward way, a simple Re = 500 flow around a cylinder benchmark case has been computed with the monolithic approach of the incompressible Navier-Stokes equations in a static domain and a fine finite element mesh (see [93] for more details). During 2000 time steps, 5 equispaced interpolations to a coarse mesh have been performed in two different ways: without applying any restrictions and enforcing the conservation of mass, momentum and kinetic energy to the velocity field. After each interpolation, the results have been projected back to the original mesh after only one time step, in

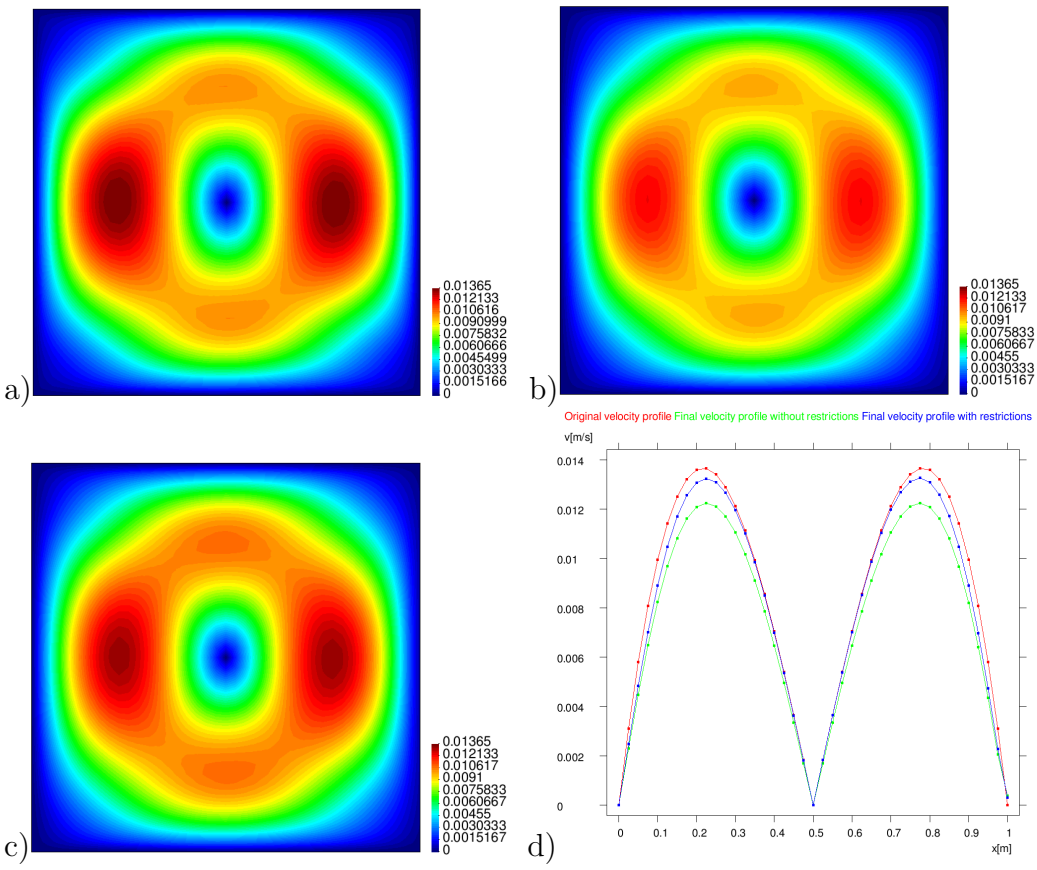

Figure 5.3: a) Original profile of $|\boldsymbol{u}|$, b) final profile of $|\boldsymbol{u}|$ after interpolating without restrictions, c) final profile of $|\boldsymbol{u}|$ after interpolating with restrictions, d) Superposition of the previous profiles at $y = 0.5$.

order to avoid further distortion of the solution than that caused by the interpolation error. This procedure allows the comparison of the results to a reference case which undergoes the same interpolation stages, but projecting the velocity field always to the same, slightly moved, fine mesh. Therefore, in this case no accuracy losses are expected other than those due to the interpolation between meshes and the results can be considered as ideal for our purpose. The mesh parameters of the simulation are listed in Table 5.3.

In spite of the small differences expected for only five bidirectional interpolations in an overall run of 2000 time steps, a considerable phase error between the reference curve and the solution computed without applying restrictions can be clearly observed in Fig. 5.4, which shows the last steps of the velocity time history. On the other hand, the red curve, corresponding to the velocity interpolated with restrictions, nearly fits the reference solution. This proves that the imposition of the restrictions leads to a reduction of the interpolation error and its propagation.

Mesh	Fine	Coarse
#elements	63,413	13,860
#nodes	32,445	7,079
Element type	Stabilized P1/P1	Stabilized P1/P1

Table 5.3: Parameters for the flow over a cylinder example.

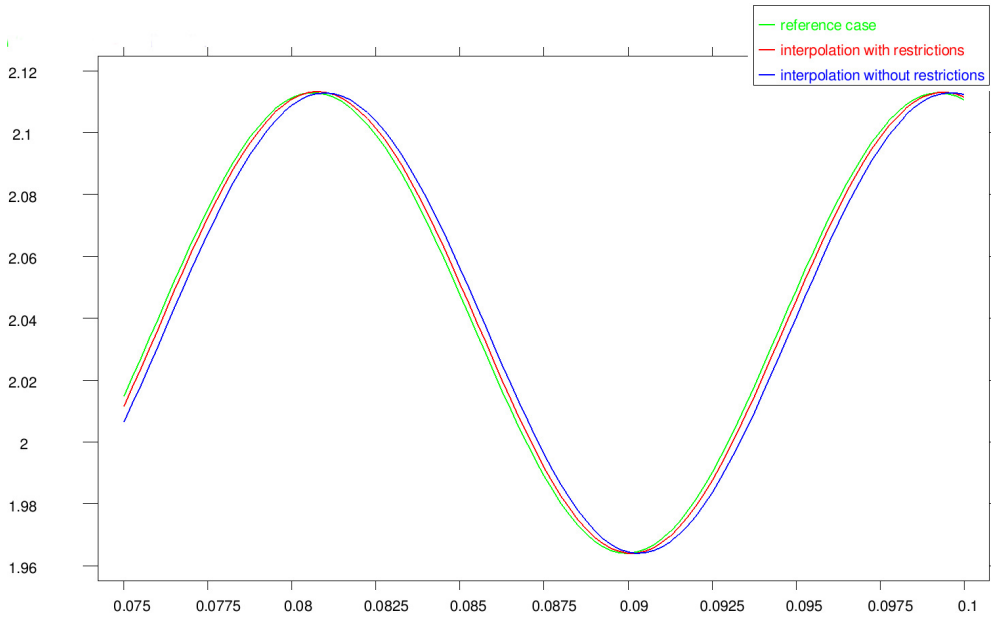

Figure 5.4: Time history of the last time steps of the velocity field.

5.5.3 A problem in aero-acoustics using an ALE description and remeshing

Following the practical motivation of this work, a preliminary case representing the syllable [as] is presented next. It consists in an air flux (density 1.2 kg/m^3 and viscosity $1.5{\cdot}10^{-5}$ Pa s) flowing through a constriction in a simplified 2D geometry based on the 3D simplified model of a vocal tract, [43]. The computation starts from a developed flow computed with the incompressible Navier-Stokes equations on the initial open configuration corresponding to the phoneme [a], (see Fig. 5.6). The upper part of the vocal tract has been prescribed an initial velocity ramp followed by a constant vertical velocity of -5 m/s until the final position corresponding to the fricative sound is reached, which happens after a total closure path of 5.15 cm at $t = 0.012$ s. During this dynamic phase an ALE frame of reference is used and a total of 7 remeshing stages are performed due to the fast distortion of the elements. Moreover, the domain velocity and the closure itself change the flow characteristics, for which reason the time step has been changed progressively

from the initial value $\delta t = 10^{-5}$ s to a final size of $\delta t = 2.5 \cdot 10^{-6}$ s. The computational domain, from now on referred as Ω, with an inlet velocity of $(2.4, 0)$ m/s, rigid walls with a non-slip condition except the vertical outlet boundary, has been discretized with two different finite element meshes (see Fig. 5.5), whereas the time integration scheme is BDF3 in all cases. Therefore, three time components of the velocity are interpolated in order to guarantee a smooth and accurate restart of the computation on the new mesh.

It will be shown how the accuracy of the interpolation, and hence the impact of the restrictions, depend, as expected, on the degree of coincidence between the donor and the target mesh. Therefore, the same case will be run twice: first interpolating always to a similar mesh as usual, and then going from the original fine mesh to a coarse mesh and vice-versa. This scenario might not be usual in ALE calculations, but is indeed common in the computation of coupled problems with two or more different meshes, such as FSI and aero-acoustics, where the acoustic source term arising from the CFD calculation can be projected to a coarser mesh for the less demanding wave equation, [125]. The results will be also analyzed from both a static and a dynamic point of view. In the first one, the effect of the restrictions within the interpolation will be assessed, whereas the latter will focus on the propagation of the interpolation error along a complete simulation.

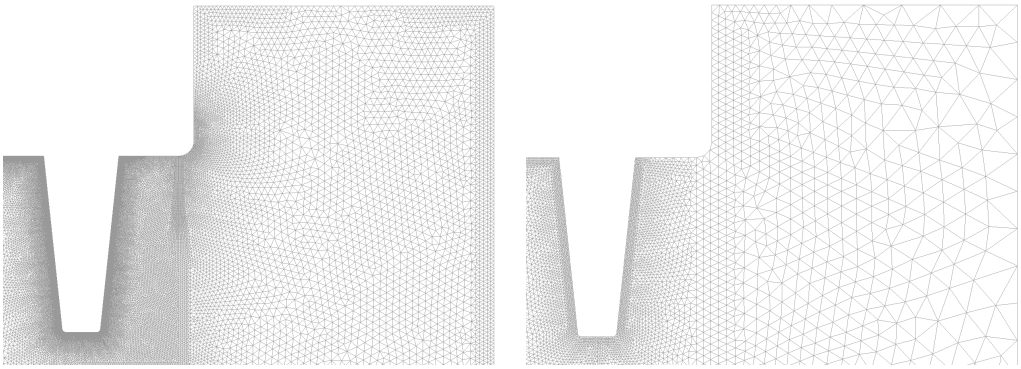

Figure 5.5: Original fine mesh (left) and coarse mesh used at the first interpolation (right). Dimensions in mm.

Monolithic scheme

As stated above, the presented case has been run twice for analyzing the dependence of the formulation on the degree of coincidence between meshes. In both cases the following restrictions for the velocity field of the incompressible Navier-Stokes equations have been applied together: conservation of mass, conservation of momentum in x and y, and conservation of kinetic

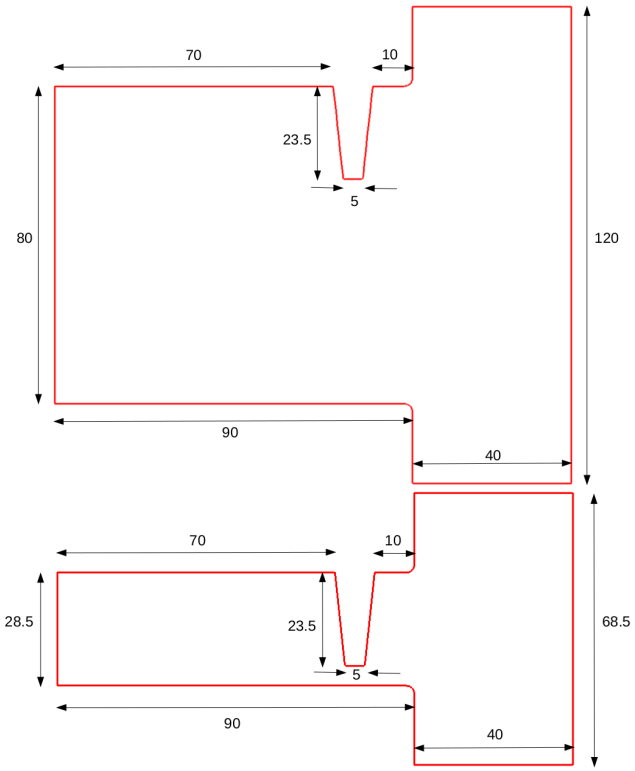

Figure 5.6: Initial geometry corresponding to phoneme [a] (top), final geometry corresponding to phoneme[s] (bottom).

energy. On the other hand, when they are applied separately the compensation performed by each one turns to be nearly the same, for which reason the decoupled case will not be presented. Moreover, this fact reveals that the non-diagonal terms of the system matrix, which force the simultaneous fulfillment of all restrictions, scarcely modify the values of the Lagrange multipliers and only compensate the linearization. A direct solver has been used in order to better evaluate the interpolation error at the remeshing stages and its propagation, since it provides the exact discrete solution of the problem.

Static analysis This subsection intends to illustrate the performance of the restrictions in a single interpolation. The procedure is called static because the projection of results takes place in a fixed domain. Table 5.5 summarizes the corrections performed by each restriction in all the remeshing stages from the initial geometry [a] to the final configuration [s] in the aforementioned two different cases: projection to a similar fine mesh ($F \to F$) and intercalation of coarse meshes ($F \to C$ or $C \to F$). It shows the amount of mass as well as the deviation percentage of momentum and kinetic energy

Initial mesh	Fine	Coarse
#elements	254,907	16,784
#nodes	131,058	8,706
Element type	Stabilized P1/P1	Stabilized P1/P1
max. size	0.001	0.005
min. size	10^{-5}	$2 \cdot 10^{-4}$

Table 5.4: Mesh parameters for the aero-acoustics example.

# interp	1	1	2	2	3	3
	$F \to F$	$F \to C$	$F \to F$	$C \to F$	$F \to F$	$F \to C$
Mass	8.4e-5	0.029	1.0e-5	1.7e-4	3.4e-6	0.014
MomX (%)	0.029	0.542	0.034	0.022	0.027	0.174
MomY (%)	4.3e-4	0.004	0.002	1.8e-4	4.9e-3	0.113
Kinet. (%)	0.027	0.328	0.049	0.031	0.079	0.514

4	4	5	5	6	6	7	7
$F \to F$	$C \to F$	$F \to F$	$F \to C$	$F \to F$	$C \to F$	$F \to F$	$F \to C$
5.0e-5	5.7e-4	1.8e-4	9.2e-3	2.5e-4	1.3e-3	2.9e-4	0.052
0.031	0.016	0.040	0.332	0.052	0.022	0.026	1.263
9.3e-3	4.3e-3	3.7e-3	0.145	4.9e-3	8.0e-3	0.013	0.069
0.101	0.062	0.143	1.208	0.201	0.116	0.267	1.908

Table 5.5: Corrections performed by each restriction at all interpolation stages.

that needs to be compensated at each interpolation when all restrictions are applied together. First of all, the first interpolation to the coarse mesh with restrictions will be compared to that without them and to the equivalent ideal projection to a similar fine mesh, in order to check how far this method can compensate a non-accurate interpolation. Later on, the most critical interpolation will be carefully analyzed by evaluating the contribution of the restrictions, not only as a whole, but seeing how they perform individually.

It can be clearly seen, as expected, that the interpolations going from a fine mesh to a coarse one ($F \to C$) are far more inaccurate than the others due to the low degree of coincidence between nodes. If we consider the first interpolation, which departs from the same solution in both cases, an interesting analysis regarding the peak value can be derived. The current formulation does not conserve explicitly the peak value, since this would require local restrictions, which are not part of the scope of this global method. However, the injection of mass, energy and momentum by the imposition of restrictions performs indeed a correction on the peak values which have been shaved by the interpolation. Table 5.6 shows the maximum values of the ve-

Original value	29.637	
Target mesh	fine	coarse
Interp. without restrictions	29.591	29.397
Interp. with restrictions	29.600	29.435

Table 5.6: Maximum values of the velocity norm at the first remeshing stage

locity norm, which appear around the obstacle, at the first remeshing stage.

Although the resulting peak value after applying the restrictions will mostly depend on the capability of the mesh of capturing local sharp gradients, which is not always possible given a low degree of coincidence between meshes and a coarse resolution of the target mesh, the method manages to restore partially the lost peaks, above all in the coarse solution, which needs a greater correction than the fine one.

The last interpolation to the coarse mesh is clearly the most critical one. The losses of mass and momentum are considerable, but the most remarkable fact is the loss of kinetic energy, which nearly reaches the 2%. The next series of plots show the correction performed by each restriction separately and all together to the velocity field in Fig. 5.7, which corresponds to the last remeshing stage at the final geometry, (see Fig. 5.6).

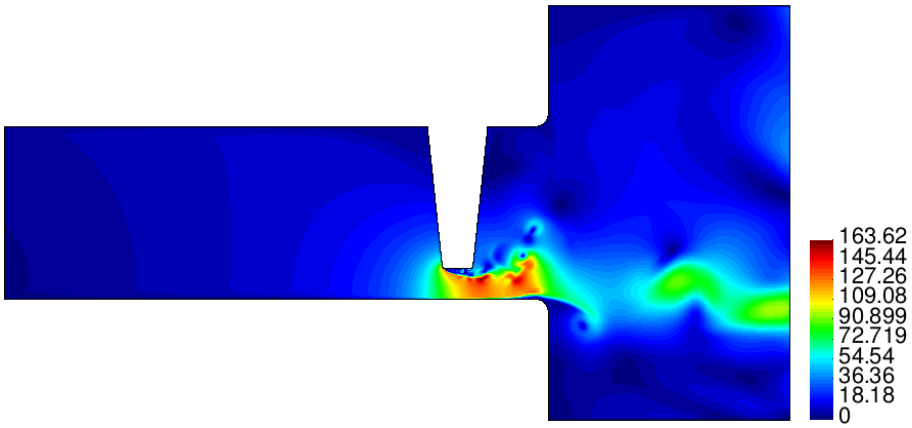

Figure 5.7: Velocity field before the last interpolation to the coarse mesh.

Fig. 5.8 shows the non-conservative interpolation of the velocity field to the coarse mesh. For a better tracking of the whole process, the same scaling has been used. The conservation of mass is achieved by injecting fluid through the only open boundary, the outlet, as shown in (Fig. 5.9), taking into account the divergence theorem. Then, the mass is diffused into the bulk by a consistent mass matrix. However, the correction is essentially restricted to the boundary nodes because it must also satisfy that the final solution remains the nearest possible to the interpolated field. The correction

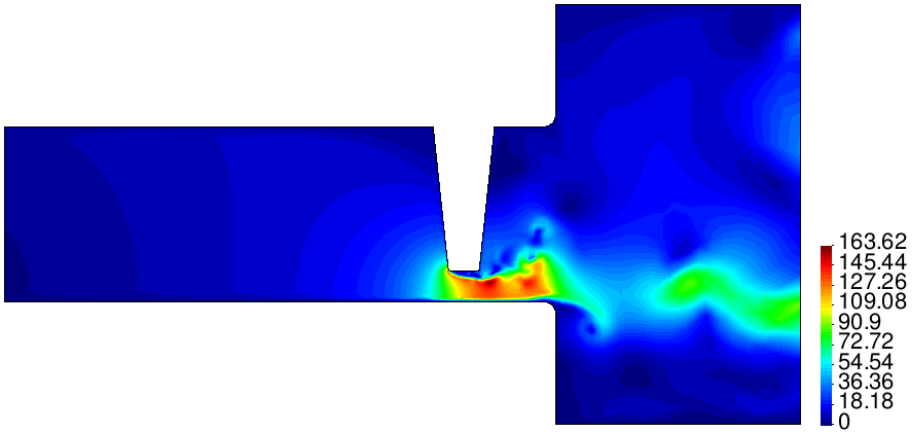

Figure 5.8: Velocity field after the last interpolation to the coarse mesh before being corrected by the restrictions.

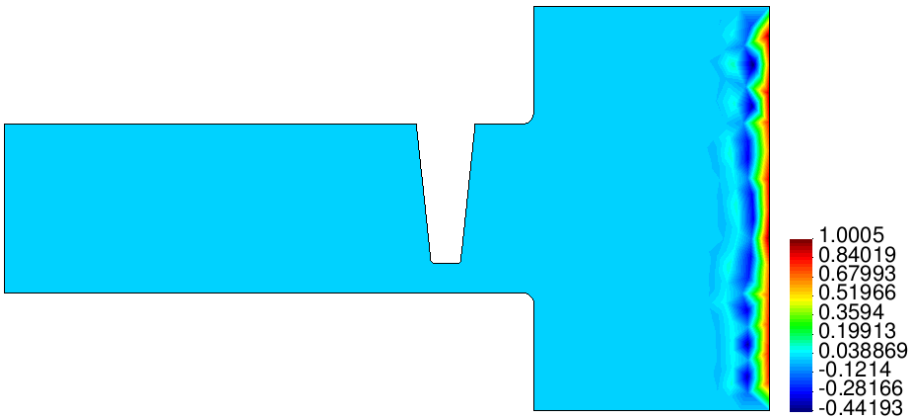

Figure 5.9: Correction of the velocity field performed by the conservation of mass.

of momentum follows a mesh dependent discontinuous pattern, since the corresponding restriction operator is the integral of the shape functions at the nodes (see Fig. 5.10). On the other hand, the correction of the kinetic energy follows perfectly the motion of the flow because it can be understood as the conservation of the velocity L^2 norm. Bearing in mind that this correction has a quadratic effect, the injection of kinetic energy will be proportional to the velocity field in order to minimize the relative variation of the solution (see Fig. 5.11). The total correction scale (see Fig. 5.12) shows the key importance of this method when dealing with highly non-coincident grids, a typical scenario that can be found in some coupled problems, otherwise the solution could get distorted in just one time step. Finally, Fig. 5.13 shows the final velocity field after applying the previous correction, which recovers most of the flow features of the original field that hat been lost during the

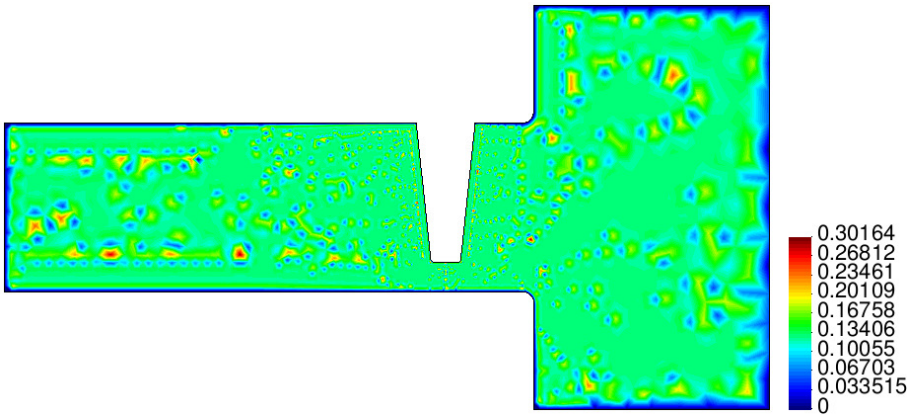

Figure 5.10: Correction of the velocity field performed by the conservation of momentum.

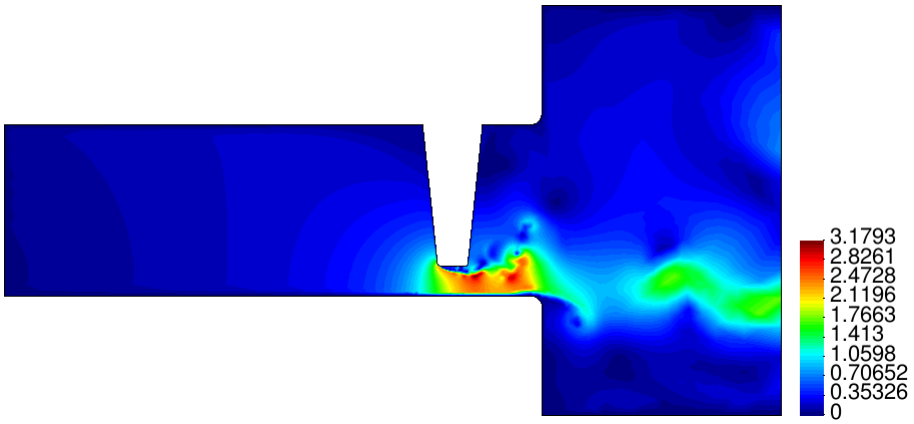

Figure 5.11: Correction of the velocity field performed by the conservation of kinetic energy.

non-conservative interpolation, (see Figs. 5.7 and 5.8).

Dynamic analysis. Up to now, only the static transmission of information between two meshes has been analyzed. However, the most important features are the degradation of the results and the accumulation of error during a dynamic calculation when no restrictions are applied, as well as the global effect of the restrictions along the simulation. It is not easy to quantify the benefit just by adding the effect of the successive application of the restrictions because after losing mass, momentum and energy at one interpolation, the numerical solution of the Navier-Stokes equations is computed again and this interpolation error is partially compensated by the imposition of the incompressibility condition as well as by the injection of momentum and kinetic energy coming from the inlet boundary condition.

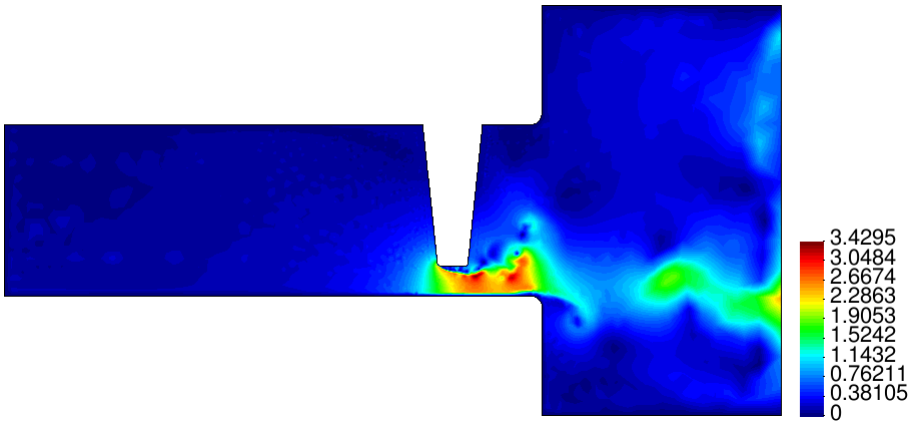

Figure 5.12: Total correction of the velocity when applying all restrictions together.

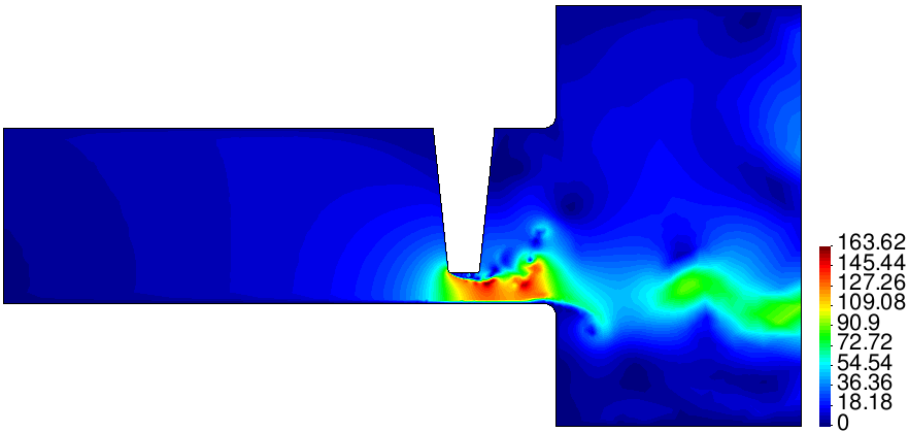

Figure 5.13: Final velocity field after applying all restrictions.

For this reason, if we did not apply the restrictions and we measured the losses at the last interpolation, these values would not reveal the accumulated error, but just a frozen picture of the accuracy of a single interpolation. Instead, the accumulation of error arises from an interpolated value which does not fulfill the physical problem features and that is later propagated when the computation restarts.

In this case, only interpolations to similar fine meshes have been considered. Unlike the previous case, the numerical error cannot be assessed comparing the velocity before and after the interpolation stage, since the high degree of coincidence between meshes avoids a visible dissipation. The matter of study here is the accumulation of this error, hence the time histories of the velocity at a point under the tooth $(78.7, 5.33)$ mm during the last two stages of the simulation, (see Figs. 5.15 and 5.16), and the final velocity

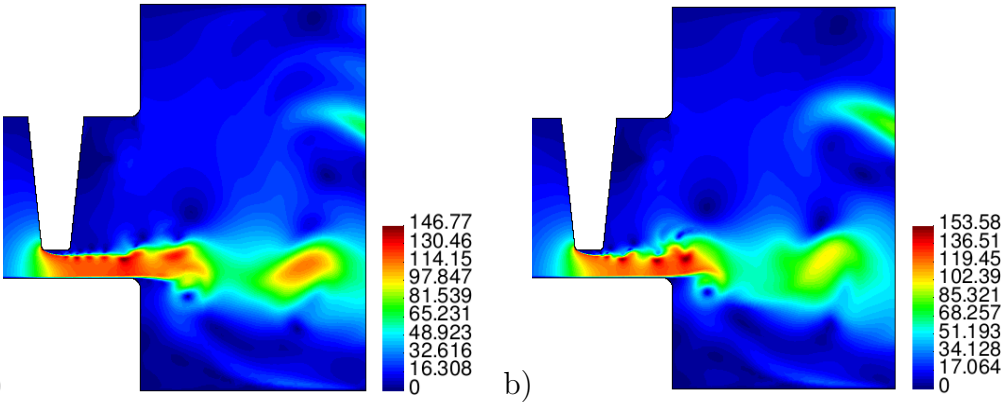

a) b)

Figure 5.14: Final velocity profile applying no restrictions (a), final velocity profile applying all restrictions (b)

fields at the configuration [s] have been compared, (see Fig. 5.14). In spite of keeping the same mean value, the solutions start diverging when the first vortices go across the analyzed point. Between interpolations 5 and 6 the tooth is approximating its final position but the flow under the obstacle has not yet experimented important oscillations and the two solutions show a good agreement. However, at the following stage between interpolations 6 and 7, just before reaching the final position, the sudden presence of sharp velocity gradients amplifies the propagation of the initial interpolation error, leading to different peak values and to a considerable phase change. The impact of the application of the restrictions in the oscillating solution can be clearly observed in Fig. 5.17, where the Fast Fourier Transform of both velocity time histories has been computed.

Second order fractional step scheme

The same case as for the monolithic scheme is now solved using a fractional step scheme. The same computational meshes have also been used. The problem has been computed again three times: without restrictions, with only velocity restrictions and with velocity and pressure restrictions as presented in Section 5.4, in order to evaluate the benefits of the interpolation procedure applied to the pressure field (see Fig. 5.18).

Once again, in spite of showing some similar patterns, the solutions yield significant discrepancies regarding the peak value and the phase of oscillation. Unlike the monolithic case, the solutions with and without restrictions diverge at the stage between interpolations 5 and 6. Fig. 5.19 shows that the red solution starts oscillating earlier than the blue one. In this case, the solution without enforcing the pressure constraint has not been plotted because it coincides perfectly with the solution applying all restrictions. On

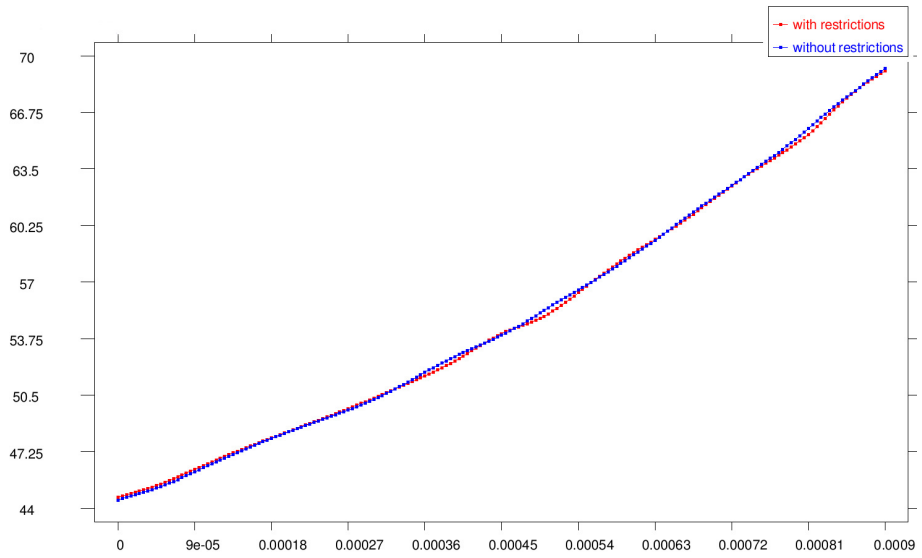

Figure 5.15: Time history of the velocity between interpolations 5 and 6.

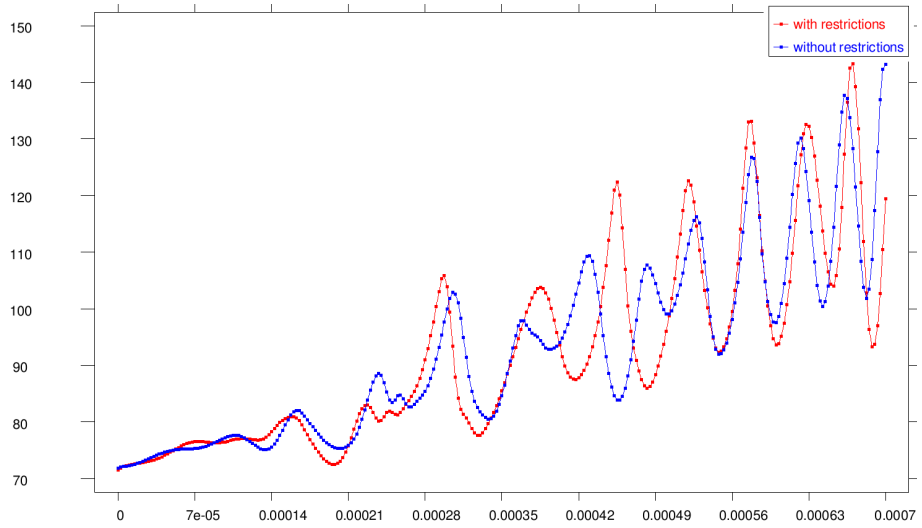

Figure 5.16: Time history of the velocity between interpolations 6 and 7.

the other hand, at the following stage (Fig. 5.20), these two solutions finally diverge once sharp gradients appear at the analyzed point below the tooth, which shows that the enforcement of the pressure L^2 norm conservation is as important as the velocity restrictions to prevent phase error.

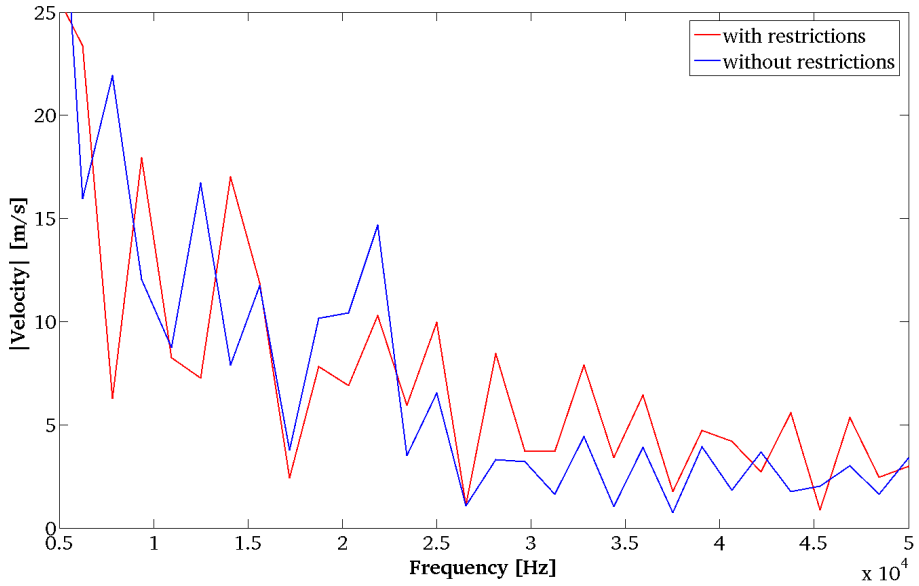

Figure 5.17: FFT of the velocity between interpolations 6 and 7.

5.6 Conclusions

The presented formulation has proved to be very effective in compensating the interpolation error when using two highly non-coincident computational grids, where it was already expected that the loss of mass, momentum and kinetic energy would be relevant in flow problems. It has also turned to be of crucial importance in scenarios, such as in Arbitrary Lagrangian Eulerian calculations, where the interpolations take place between similar fine meshes. In this case, the effect of the restrictions on the interpolated array is not so relevant but the accumulation and propagation of this theoretically small error due to the non-conservative interpolation turns to be relevant indeed after several thousands of time steps. One of the most important factors regarding the accuracy of the interpolation between meshes is the presence of sharp gradients as well as the mesh resolution and coincidence to capture them. Although this is a global method, it also manages to partially restore the lost peaks in the interpolated field.

The method has been applied successfully to the solution of the incompressible Navier-Stokes equations. In this case, the most relevant restriction is the conservation of kinetic energy. It has also been proved that the propagation of interpolation error when using a non-conservative interpolation becomes considerable after several hundreds of time steps. Although the mean value is conserved, the oscillation pattern becomes clearly divergent when the vorticity increases. In a similar way, for second order fractional schemes the conservation of the pressure L^2 norm has turned to be necessary

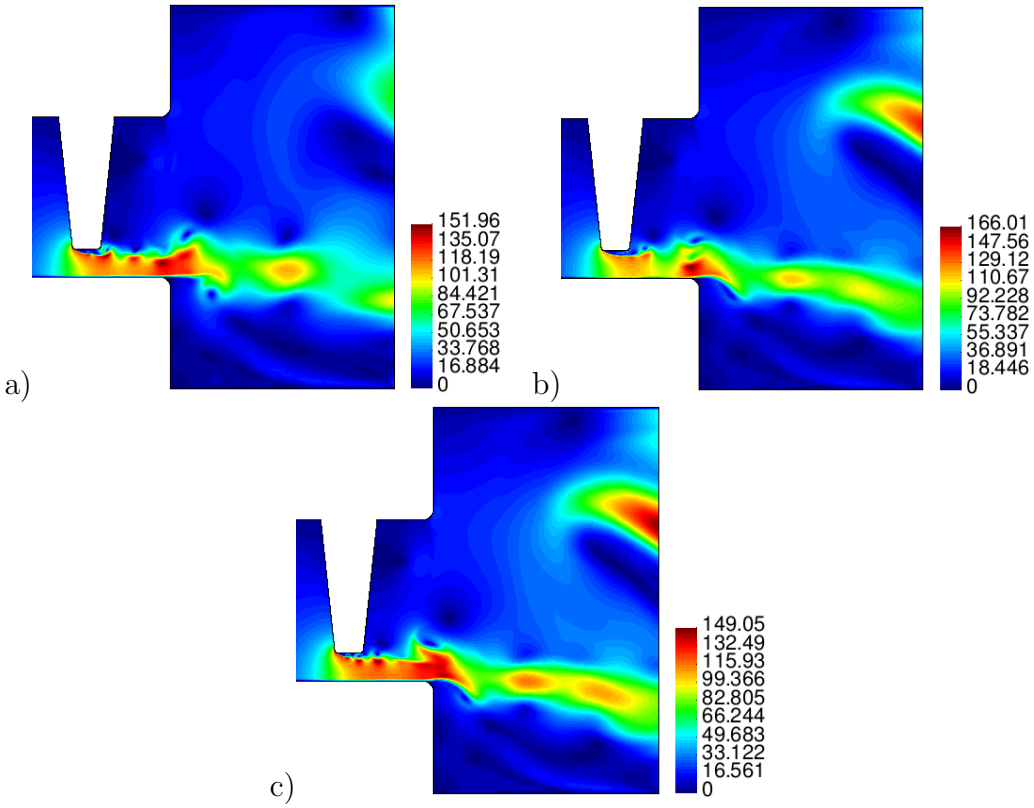

Figure 5.18: Final velocity profile applying no restrictions (a), final velocity profile applying only velocity restrictions (b), final velocity profile applying all restrictions (c)

to prevent phase error.

From a computational point of view, the method yields a fast convergence and a very low computational cost, and is flexible enough for being easily extended to other physical problems, like acoustics, with other restrictions to be imposed. In the present context, this tool would allow dealing with complex vocal tract deformation in cases of dynamic phonation, where the elastic problem solved in the previous chapters for minimizing the distortion of the elements [39] might not be robust enough.

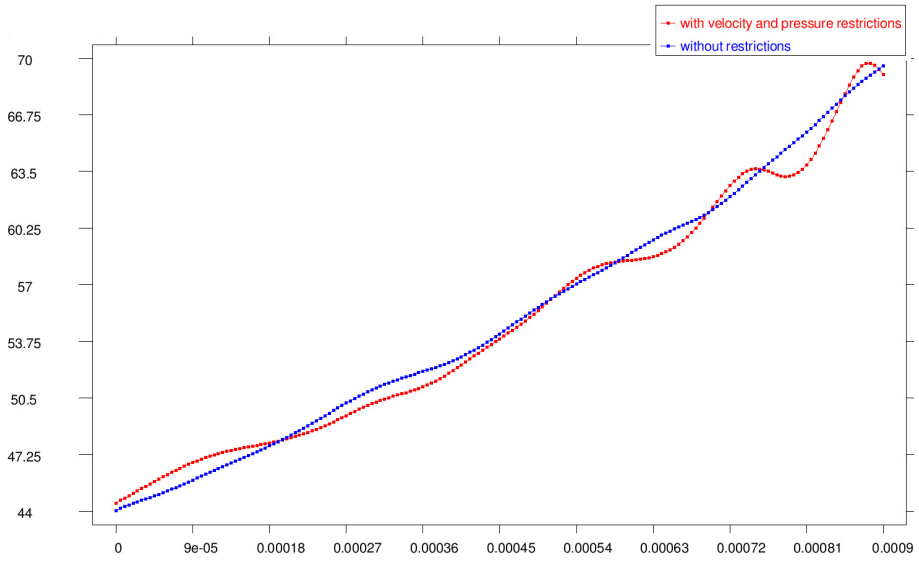

Figure 5.19: Time history of the velocity between interpolations 5 and 6.

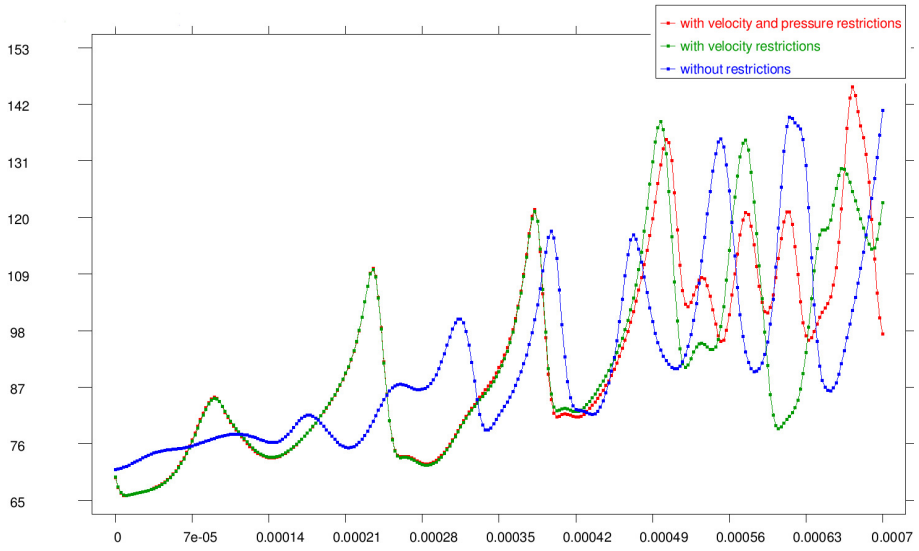

Figure 5.20: Time history of the velocity between interpolations 6 and 7.

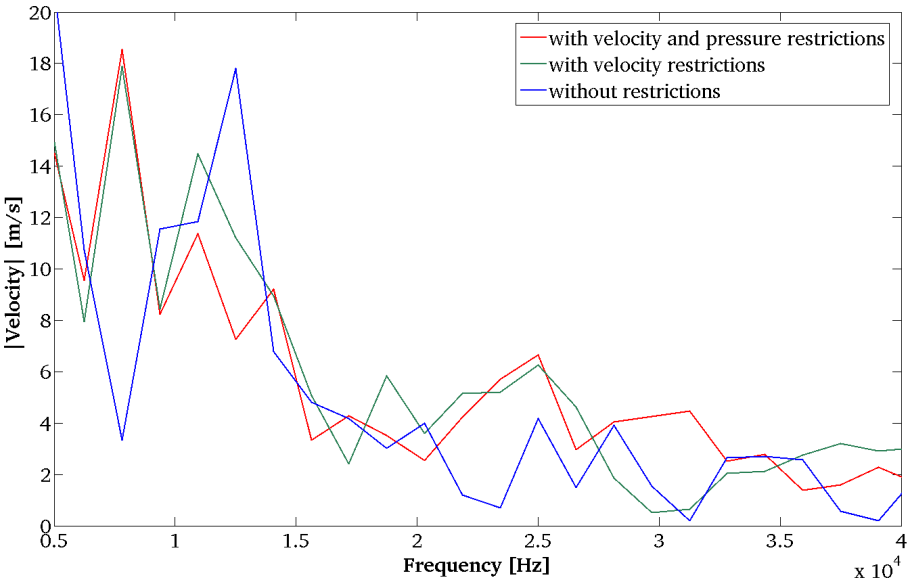

Figure 5.21: FFT of the velocity between interpolations 6 and 7.

Chapter 6

Computational aeroacoustics to identify sound sources in the generation of sibilant /s/

A sibilant fricative /s/ is generated when the turbulent jet in the narrow channel between the tongue blade and the hard palate is deflected downwards through the space between upper and lower incisors, and impinges the space between the lower incisors and the lower lip. The flow eddies in that region become a source of direct aerodynamic sound, which is also diffracted by the upper incisors and radiated outwards. The numerical simulation of these phenomena is complex. The spectrum of an /s/ typically peaks between $4 - 10$ kHz, which implies that very fine computational meshes to capture the eddies producing such high frequencies are needed. In this work, a large-scale computation of the aeroacoustics of /s/ has been performed for a realistic vocal tract geometry, resorting to two different acoustic analogies. A stabilized finite element method that acts as a large eddy simulation model has been adopted to solve the flow dynamics. Also, a numerical strategy has been implemented which allows determining, in a single computational run, the separate contributions from the direct turbulent sound and the sound diffracted by the upper incisors, to the radiated sibilant /s/. Results are presented for points located close to the lip opening showing the relative influence of the sources of sound depending on frequency.

6.1 Background

In this work, we aim at better understanding the generation and radiation mechanisms of sibilant /s/, by means of computational aeroacoustics (CAA) performed on a realistic vocal tract geometry. In particular, we are interested in determining the separate acoustic contributions to points near the lip

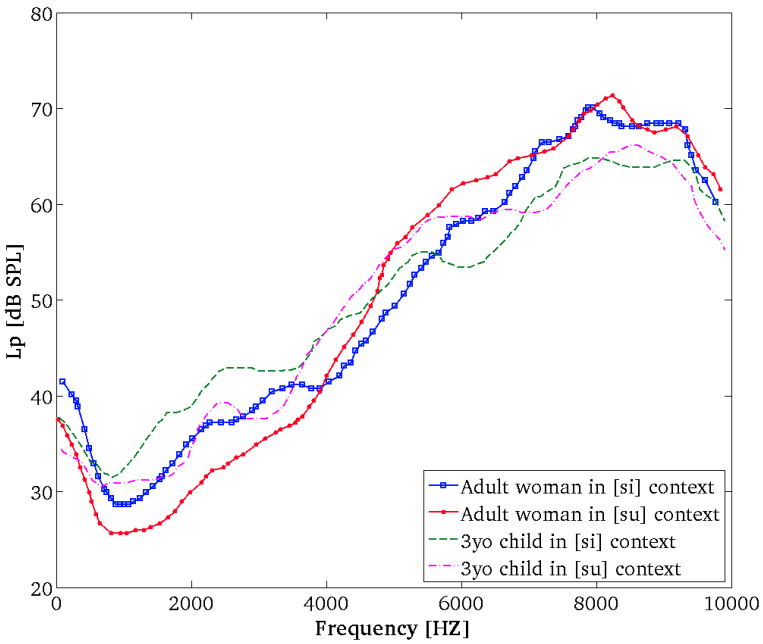

Figure 6.1: Welch averaged power spectral density for the measurements with subject utterances in [141].

opening from the flow noise generated in that region, and from its diffraction by the upper incisors.

The sibilant fricative /s/ is produced when the turbulent jet leaving the glottis is accelerated in the constriction between the tongue blade and the hard palate, passes through the space between upper and lower incisors, and impinges the cavity between the lower incisors and the lower lip. This results in the generation of aerodynamic noise, which in turn gets diffracted by the incisors and radiated outwards. The emitted sound has a characteristic wide-band spectral content which can be observed in Fig. 6.1, where we reproduce the measurements of uttered sibilants in [141]. Recordings with a microphone and a digital spectrograph were provided in that reference for the pronunciation of /s/ in the context of phonemes /si/ and /su/. Sibilant /s/ was recorded for an adult woman and also for a three year old child. The curves in the figure correspond to the sound pressure level of the Welch averaged power spectral density of the recorded acoustic pressure [120]. As observed, strong differences can be appreciated at low frequencies, yet the general trends of the spectra are similar. They all exhibit a decay from low frequencies to a dip between $\sim 1-3$ kHz, followed by a strong level increase with frequency up to $\sim 8-9$ kHz, and two peaks whose locations change depending on each realization. The latter can be clearly distinguished for the measurements corresponding to phoneme /si/, and to a less extent for

the adult woman when pronouncing phoneme /su/. It should be remarked that there are significant variations between the spectral shapes of speakers reported in literature, because of morphological differences. Yet the general trends described before can be recognized in most sibilant measurements [141, 159, 14, 140, 120].

A detailed analytical model to describe the physics behind the production of /s/ was proposed in [106]. In that model, the diffraction of the sound generated by the turbulent boundary layer (TBL) attached to the incisors was considered as the main noise contributor. A compact Green's function that accounted for a simplified geometry of the incisors and the vocal tract was deduced and convolved with a theoretical model for the wall pressure wavenumber-frequency spectrum [107], to predict the acoustic pressure at the far-field. More recently, in [181] large eddy simulations (LES) have been presented on a 3D realization of the geometry in [106], and lately compared it with a realistic one in [164]. Those works reported that it is actually in the cavity between the lower incisors and the lower lip where most of the aeroacoustic source terms concentrate. The simulations in the present work, also with a realistic vocal tract, support that conclusion. In addition, they will essentially show that for points in the vicinity of the mouth, the direct aerodynamic sound contribution from the eddies within the lower incisors-lips cavity dominate the acoustic spectrum at low frequencies, whereas diffraction by the upper incisors governs the high frequency range of the spectrum. As regards the numerical simulations of sibilants, we note that although the articulators are constantly in movement during speech [86], stationary vocal tract walls are always assumed in computational models for simplicity.

To validate the above assertions, the numerical strategy in [96] has been implemented. We note that in most hybrid approaches to CAA a two step procedure is followed (see e.g., [17]). First, an LES computation is carried out by means of a finite element (FEM) (or a finite volume) approach, to obtain the aerodynamic noise source terms. Secondly, these terms are input into an acoustic analogy that is solved using an integral formulation (see e.g., [65, 178]), which becomes discretized by a boundary element method (BEM). Yet, the proposal in [96] relies on different grounds. The method only makes use of a single FEM code that allows one to solve, in a single computational run, an LES for the incompressible Navier-Stokes equations, a first wave equation for the direct flow noise contribution, and a second wave equation for the sound diffracted by the incisors. This procedure circumvents an inconsistency related to the numerical solution of Curle's dipolar integral term for low Mach numbers [65], given that the total pressure to be input in that integral cannot be obtained from an incompressible LES simulation [138, 96].

In this work, the focus will be placed on the acoustic results of the above

strategy rather than on the LES ones, which will be only described qualitatively, together with the implemented FEM strategy. It is to be noted that 3D LES simulations of flow passing around teeth-shaped obstacles to better understand the underlying physics of /s/ were already reported in [176, 175] and in [43]. Simulations of flow passing through simplified geometries with constrictions of different sizes had also been conducted in [44]. The work in [142] also resorted to LES to analyze the flow dynamics of /s/ in a realistic vocal tract geometry. As said before, more recently, [181, 164] presented simulations on a 3D realization of the geometry in [106] and compared it with realistic ones. On the other hand, the LES in the present work has been solved with the stabilized FEM method in [58], which behaves as an implicit LES model (see e.g., [156, 88]). In implicit LES methods, the additional terms included in the equations to avoid numerical instabilities simultaneously act as a turbulence model. These have been proven succesful on well-known benchmark turbulent tests for the strategy in [58], (see e.g., [149, 60, 57]), as well as through analytical reasoning [94].

In what concerns the acoustic formulations to get the contributions from the direct flow noise in the lower incisors-lips cavity, and from the between-incisors diffraction, one should ideally resort to approaches that could account for the unsteady flow acoustics in the vocal tract. The most relevant ones for that purpose are probably the linearized Euler equations (see e.g., [16]), or some of its source filtered counterparts to leave aside the vorticity and entropy modes, like the acoustic perturbation equations (APE), see [73]. In [111], a low Mach number for the APE was introduced (see [97] for a full numerical solution retaining all terms). In the case of very low Mach number flows, like those encountered in voice production, the APE in [111] can be further simplified to the acoustic analogy in [154]. The wave operator in this analogy is just the standard wave equation, like in Lighthill's analogy [130], yet the double time derivative of the incompressible pressure field is used as the source term, instead of the double divergence of the Reynolds tensor of the incompressible velocity field. It can be shown that this allows the filtering of some pseudosound at the flow region (the term pseudosound refers to pressure fluctuations indistinguishable by a single microphone from proper sound, see, e.g., [62]). In this piece of research both Lighthill's and the analogy in [154] will be employed.

To end this introductory section, we would like to remark that aside from static vowel sounds, for which a large literature is available (see e.g., [171, 167, 163, 6, 172, 78, 29, 9, 5, 4, 30]), few works can be found in literature addressing the numerical simulation of other speech sounds. The reason for that is probably the complex physics beneath their generation and the associated high computational cost. An exception that has received some recent attention is that of vowel-vowel utterances in [89]. Also, attention

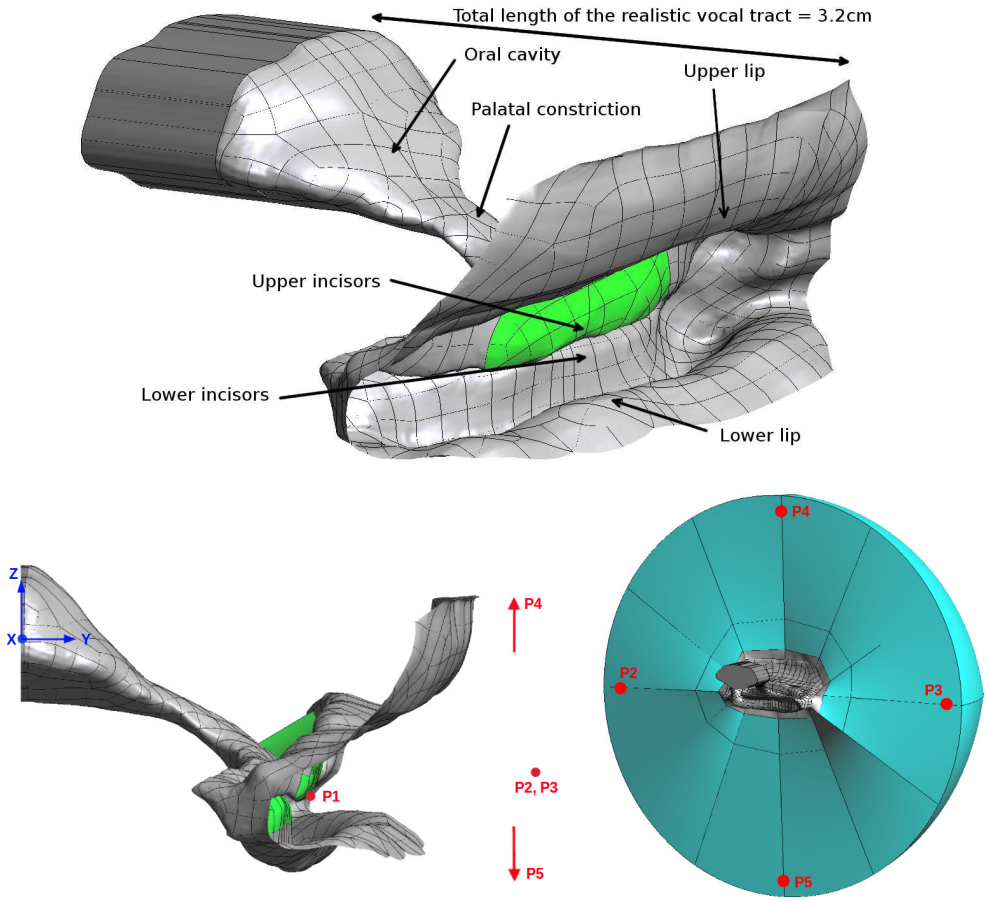

Figure 6.2: 3D realistic vocal tract geometry for /s/ with upper incisors highlighted in green. Measuring points P2 and P3 are placed at the far-field in the x direction, and P4 and P5 in the z direction.

has been paid to some unvoiced sounds (see e.g., [127]) and in particular to fricative sounds. Related to the present work, we shall cite [3] where different computational fluid dynamics (CFD) formulations were tested for fricative //, using realistic two (2D) and three (3D) dimensional vocal tract geometries. That study compared the performance of a compressible CFD simulation, an incompressible LES and a Reynolds averaged Navier-Stokes (RANS) approach. Though a rather coarse mesh was used, the study arrived at some interesting conclusions. As expected, the RANS simulation provided no reliable results but the compressible CFD and incompressible LES combined with an acoustic analogy yielded proper outputs. Another interesting and unexpected result was that although the flow field from 2D simulations did not match at all with the 3D one, that was not the case for the 2D acoustic pressure field, which was quite similar to the 3D one.

This chapter is organized as follows. The methodology that has been followed to perform the simulations is detailed in Sec. 6.2, which includes a description of the realistic vocal tract geometry for sibilant /s/, the formulation of the acoustic analogies and the splitting strategy between turbulent and diffracted sound that has been implemented. It also outlines the numerical strategy used to solve the involved partial differential equations and includes specific details on how the numerical simulations have been run. The results of the latter are presented in Sec. 6.3, with special emphasis on the characteristics of the generated aerodynamic sound. In Sec. 6.4 the same scenario is calculated with the isentropic compressible approach presented in Chapter 4, and the corresponding results are compared to the ones obtained in Sec. 6.3. Conclusions close the chapter in Sec. 6.5.

6.2 Methodology

6.2.1 Vocal tract model

The vocal tract geometry used for the simulations was obtained from a cone-beam CT scan (CB MercuRay, 512 slices of 512 pixel $\times$ 512 pixel grid with accuracy ± 0.1 mm) in [174] and [81], from which a physical replica was constructed. The geometry (see Fig. 6.2) corresponds to an adult male Japanese native speaker with normal dentition (angle Class I) without any speech disorder, in normal sitting position. The subject was instructed to sustain phoneme [s] at a medium loudness (with a flow rate $\sim$ 21 l/min) during 10 s. The entire vocal tract was imaged, but only the portion containing the main tongue constriction and all structures downstream of it, including the lip horn ($\sim$ 32 mm), was reconstructed for the replica, see Fig. 6.2. This simplification intends to focus on the region of the vocal tract where the generating mechanisms take place, as in [106]. This includes the constricted passage between the tongue blade and the hard palate (the section with minimum area has a hydraulic diameter of 2.1 mm), the lower and upper incisors (highlighted in green in the figure) and the lips. According to [174], the initial flow conditions upstream (geometry and Reynolds number) do have an influence on the modulation of the acoustic spectrum of fricatives, but do not play an essential role in the physiological mechanisms that lead to the generation of this phoneme.

6.2.2 Problem formulation

Acoustic analogies

As said in the Introduction, in this work the celebrated Lighthill acoustic analogy [130] and the analogy in [154] will be used. For low Mach numbers,

Lighthill's tensor can be well approximated by the double divergence of the Reynolds tensor of the incompressible velocity field. If one considers a computational domain Ω_v with outer boundary Γ_∞, and a rigid body embedded in it with boundary Γ_w and external normal $\boldsymbol{n}$, the Lighthill acoustic analogy problem reads (see Fig. 6.3),

$$\frac{1}{c_0^2}\frac{\partial^2 p}{\partial t^2} - \nabla^2 p = \rho_0 \left(\nabla \otimes \nabla\right) : \left(\boldsymbol{u}^0 \otimes \boldsymbol{u}^0\right) \text{ in } \Omega_v, \tag{6.1a}$$

$$\frac{\partial p}{\partial \boldsymbol{n}} = -\frac{1}{c_0}\frac{\partial p}{\partial t} \text{ on } \Gamma_\infty,\ t > 0, \tag{6.1b}$$

$$\frac{\partial p}{\partial \boldsymbol{n}} = 0 \text{ on } \Gamma_w,\ t > 0, \tag{6.1c}$$

$$p = 0,\ \frac{\partial p}{\partial t} = 0 \text{ in } \Omega_v,\ t = 0. \tag{6.1d}$$

In Eq. (6.1), $p(\boldsymbol{x}, t)$ stands for the acoustic pressure fluctuations and $\boldsymbol{u}^0(\boldsymbol{x}, t)$ for the incompressible velocity field obtained e.g., from a CFD computation. ρ_0 stands for the flow density, c_0 for the speed of sound and $\otimes$ for the tensor product. In the second line, (6.1b) introduces a Sommerfeld non-reflecting condition on Γ_∞ and in the third one, (6.1c) expresses a rigid wall assumption for the immersed body. The initial conditions are set in (6.1d). The source term $\rho_0 \left(\nabla \otimes \nabla\right) : \left(\boldsymbol{u}^0 \otimes \boldsymbol{u}^0\right)$ in Eq. (6.1) is often rewritten as $\rho_0 \left(\nabla \otimes \boldsymbol{u}^0\right) : \left(\nabla \otimes \boldsymbol{u}^0\right)^\top$ for computations ($\top$ denotes transpose), given that $\nabla \cdot \boldsymbol{u}^0 = 0$ (see e.g., [93]).

With regard to the acoustic analogy in [154], it can be obtained from the low Mach APE equations in [111], by simply neglecting the mean velocity field and combining the momentum and continuity equations to get the scalar wave equation for the acoustic pressure. Alternatively, the analogy was originally derived from the following straightforward reasoning. Taking the divergence of the Navier-Stokes momentum conservation equation results in the Poisson equation $\nabla^2 p^0 = -\rho_0 \left(\nabla \otimes \nabla\right) : \left(\boldsymbol{u}^0 \otimes \boldsymbol{u}^0\right)$, which allows one to replace Eq. (6.1a) with

$$\frac{1}{c_0^2}\frac{\partial^2 p}{\partial t^2} - \nabla^2 p = -\nabla^2 p^0. \tag{6.2}$$

This equation is interesting for the following reason. It is well known that the acoustic pressure predicted by Lighthill's analogy is only valid far away from the source region, where no flow motion occurs. If one needs to determine the acoustic pressure field close to the generation area it becomes necessary to filter out the *pseudosound* due to non-acoustic pressure fluctuations. In the case of a flow with very small mean convection velocity, [154] proposed to do so by splitting the pressure into its incompressible *pseudosound*, $p^0(\boldsymbol{x}, t)$,

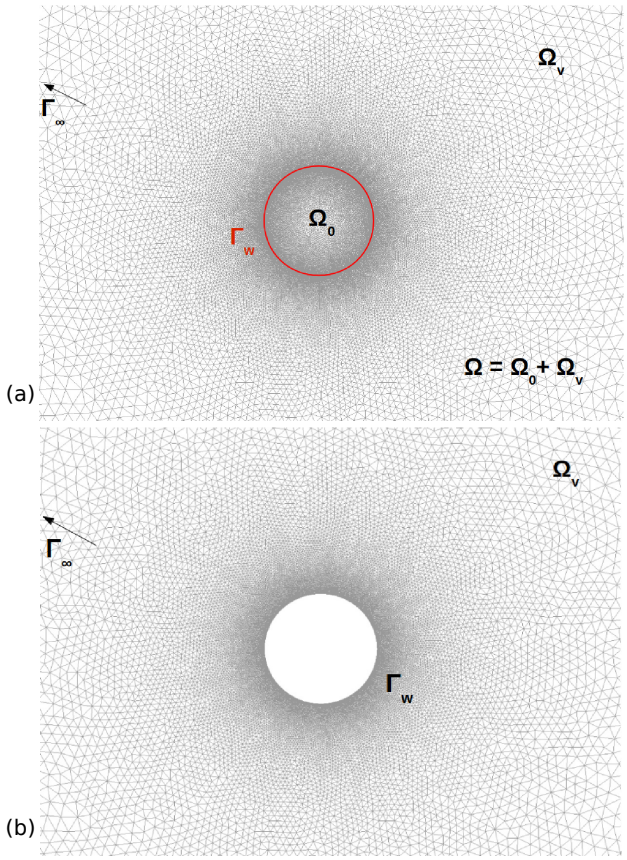

Figure 6.3: Domains for computing (a) the incident acoustic pressure and (b) the diffracted acoustic pressure in the proposed splitting strategy for aeroacoustics.

and acoustic, $p^a(\boldsymbol{x}, t)$, components, i.e., $p(\boldsymbol{x}, t) = p^0(\boldsymbol{x}, t) + p^a(\boldsymbol{x}, t)$. Inserting this factorization in Eq. (6.2) results in the following wave equation for the acoustic pressure fluctuations

$$\frac{1}{c_0^2}\frac{\partial^2 p^a}{\partial t^2} - \nabla^2 p^a = -\frac{1}{c_0^2}\frac{\partial^2 p^0}{\partial t^2}, \tag{6.3}$$

which is to be supplemented with the boundary and initial conditions (6.1b)-(6.1d), now for $p^a(\boldsymbol{x}, t)$.

Quadrupole and dipole contributions to the acoustic pressure

To determine the contributions to the utterance of /s/ from the quadrupole noise generated by the turbulent jet exiting the mouth, and from the dipole noise due to the acoustic pressure diffraction by the upper incisors, one could

typically resort, as said before, to Curle's formulation [65]. However, in the case of low Mach number flows a severe difficulty appears when trying to account for the rigid body (e.g., the incisors) contribution to the far field. The reason is that the surface integral in Curle's formulation involves the total pressure, which includes both the incompressible and acoustic fluctuations. Obviously, the later cannot be obtained from an incompressible CFD simulation.

Though recently some proposals have been made to at least partially mitigate that problem in the framework of integral formulations (see e.g. [138]), in [96], a very different approach was suggested. The approach considers that the acoustic dipole distribution of Curle's surface integral corresponds, in fact, to the diffraction of the turbulent noise generated by the jet flow [84]. On the one hand, the proposed methodology circumvents the total pressure difficulty in Curle's surface term. On the other hand, it avoids the need to resort to integral formulations, and one can obtain the flow field in the vocal tract, the noise generated by the jet flow at the lip opening, and the noise contribution from the incisors in a single computational run.

The cornerstone of the method consists in splitting the acoustic pressure, $p(\boldsymbol{x},t)$ in Eq. (6.1) (the same holds for $p^a(\boldsymbol{x},t)$ in Eq. (6.3)), into incident and diffracted components $p(\boldsymbol{x},t) = p_i(\boldsymbol{x},t) + p_d(\boldsymbol{x},t)$. This leaves one with two wave equations, one for $p_i(\boldsymbol{x},t)$ and the other one for $p_d(\boldsymbol{x},t)$, which are solved subsequently in slightly different domains (see Fig. 6.3). The procedure goes as follows. Once an acoustic source term $s(\boldsymbol{x},t)$ is obtained from an incompressible CFD computation, for instance,

$$s(\boldsymbol{x},t) = \begin{cases} \rho_0 \left(\nabla \otimes \nabla\right) : \left(\boldsymbol{u}^0 \otimes \boldsymbol{u}^0\right) \\ -c_0^{-2}\ \partial^2 p^0 / \partial t^2, \end{cases} \tag{6.4}$$

$s(\boldsymbol{x},t)$ is used as the inhomogeneous term in the wave equation for the incident pressure component,

$$\frac{1}{c_0^2}\frac{\partial^2 p_i}{\partial t^2} - \nabla^2 p_i = s \text{ in } \Omega \tag{6.5a}$$

$$\frac{\partial p_i}{\partial \boldsymbol{n}} = -\frac{1}{c_0}\frac{\partial p_i}{\partial t} \text{ on } \Gamma_\infty,\ t > 0 \tag{6.5b}$$

$$p_i = 0,\ \frac{\partial p_i}{\partial t} = 0 \text{ in } \Omega,\ t = 0, \tag{6.5c}$$

with $\Omega := \Omega_v \cup \Omega_0$, Ω_0 being the volume occupied by the rigid body (see Fig. 6.3a). In other words, the problem is solved as if the rigid body (in our case the incisors) was absent. After having computed $p_i(\boldsymbol{x},t)$, the rigid body is inserted again in the computational domain, which leaves one with

Ω_v (see Fig. 6.3b). The diffracted pressure $p_d(\boldsymbol{x}, t)$ is then obtained knowing the value of the incident pressure on the boundary Γ_w of the rigid body, that is to say, solving

$$\frac{1}{c_0^2}\frac{\partial^2 p_s}{\partial t^2} - \nabla^2 p_s = 0 \text{ in } \Omega_v \tag{6.6a}$$

$$\frac{\partial p_s}{\partial \boldsymbol{n}} = -\frac{\partial p_i}{\partial n} \text{ on } \Gamma_w,\ t > 0 \tag{6.6b}$$

$$\frac{\partial p_s}{\partial \boldsymbol{n}} = -\frac{1}{c_0}\frac{\partial p_s}{\partial t} \text{ on } \Gamma_\infty,\ t > 0 \tag{6.6c}$$

$$p_s = 0,\ \frac{\partial p_s}{\partial t} = 0 \text{ in } \Omega_v,\ t = 0. \tag{6.6d}$$

Note that the summation of problems Eqs. (6.5) and (6.6) recovers the original Lighthill analogy in Eq.(6.1) or that in Eq. (6.3), depending on the selected source term in (6.4).

When applied to the production of /s/, Eq. (6.5) will provide the incident acoustic contribution $p_i(\boldsymbol{x}, t)$ from the jet flow exiting the mouth to the total sibilant sound, whereas the contribution from the aerodynamic sound diffracted by the incisors will be given by the solution $p_s(\boldsymbol{x}, t)$ to Eq. (6.6). In this work the factorization into incident and diffracted components has been performed for Lighthill's analogy and only total values for the acoustic pressure are given for that in [154]. However, the strategy could have also been applied to the latter.

6.2.3 Numerical strategy

All the partial differential equations in this work have been solved using the method of lines, i.e. the spatial discretization has been carried out with the finite element method (FEM), while the finite difference method have been adopted for the time discretization. A custom developed software has been used for all computations.

As regards the incompressible Navier-Stokes equations, it is well known that the Galerkin FEM solution suffers from strong instabilities for convection dominated flows and for small time steps at the beginning of evolutionary processes. Moreover, the spatial discrete problem has to satisfy an inf-sup compatibility condition that implies using different interpolation spaces for the incompressible pressure and velocity fields. An efficient way to circumvent all these difficulties is to resort to residual-based stabilized variational multiscale (VMS) methods, see [114, 117]. The unknown variables in the problem weak form become split into large components, resolvable by the finite element mesh, and subgrid scales whose effects onto the large

ones have to be modeled. In this work the subscales have been chosen orthogonal to the finite element space and the stabilization parameters have been obtained from a Fourier analysis of the subgrid scale equation, see the orthogonal subgrid scale (OSS) method in [47, 58]. As mentioned in the Introduction, the OSS method acts as an implicit LES model. The stabilized variational Navier-Stokes equations for the problem at hand have been solved using the second order fractional step scheme presented in [50]. A backward differentiation formula of order three (BDF3) has been used for the time discretization.

At each discrete time step, the acoustic source terms in Eq. (6.4) are computed by postprocessing the incompressible pressure and velocity output from the fluid dynamics computation. In the case of Lighthill's analogy, the acoustic waves for the incident and diffracted acoustic pressure, Eqs. (6.5)-(6.6), are then solved. The contribution analysis has not been performed for the analogy in [154] as it would have yielded very similar results to those of Lighthill (see Sec. 6.3.2 below). Therefore, only Eq. (6.3) has been solved in this case.

From a computational point of view, the spatial discretization of the wave equation poses no particular problem given that the Laplacian of the acoustic pressure gives rise to a coercive term in the variational form of the problem. Therefore, the main difficulty with the numerical solution of the wave equation arises from the time discretization, which should prevent numerical dissipation as a wave propagates. Given that the focus in this work is on the aerodynamic acoustic pressure at points only a few wavelengths from the mouth, a BDF2 scheme proves accurate enough to approximate the time derivatives in the wave equation and its boundary conditions. Another issue to consider is that of imposing a proper non-reflecting condition at the outer boundary of the computational domain. This often requires the use of a perfectly matched layer (PML) formulation. However, the outward propagating waves in the present simulations are nearly spherical and impinge in the normal direction to the radiation boundary, which makes a PML unnecessary. Spurious reflections have then been avoided by simply imposing the Sommerfeld condition in [72], which has been tested in a wide range of problems and geometries.

Interested readers are referred to [96] and references therein for a full detailed description of the numerical strategy that has been just outlined.

6.2.4 Numerical simulations

To perform the numerical simulations the vocal tract in Fig. 6.2 has been set in a circular, rigid, flat baffle. A hemispherical domain has been attached to it to allow the flow to emanate from the mouth and the acoustic waves to

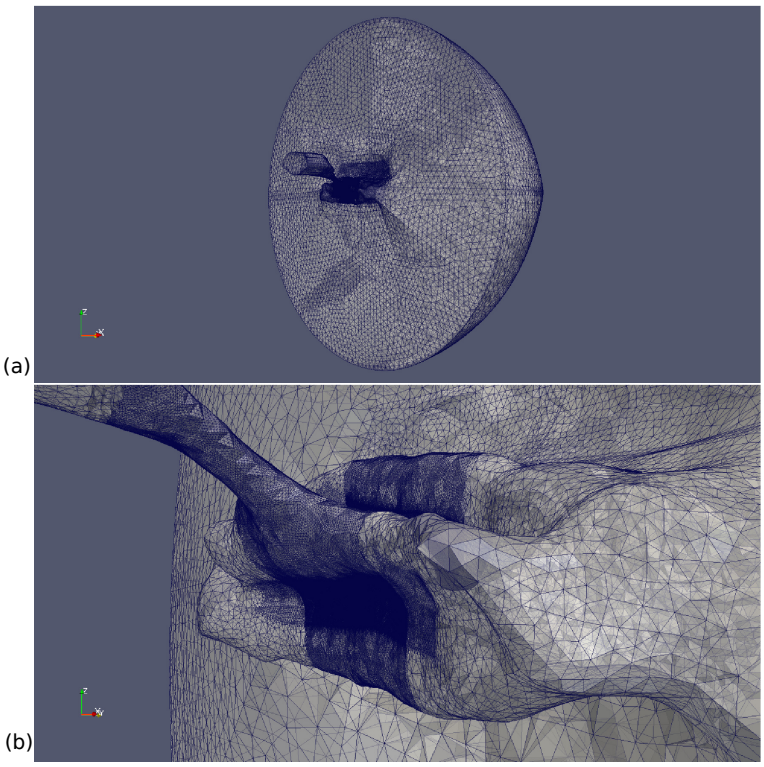

Figure 6.4: (a) Meshed computational domain including the vocal tract geometry and the far field (b) Zoom of the refined mesh region.

propagate outwards (see Fig. 6.4a).

The following boundary conditions have been applied to solve the incompressible Navier-Stokes equations. A velocity of 2.4 m/s has been prescribed at the inlet section. This has been scaled from the blower in [174] and corresponds to a Reynolds number of Re = 8850, according to the inlet section diameter. Non-slip conditions have been applied to the whole vocal tract and baffle surfaces, while the hemispherical surface has been considered an open boundary, [43]. As regards the acoustic computations, the vocal tract and baffle have been assumed rigid, whereas as mentioned, a non-reflecting boundary condition has been applied at the hemispherical boundary and at the flow inlet. The first order Sommerfeld boundary condition in [72] does not lead to any spurious reflection in the present example. The following values have been taken for the physical parameters appearing in the equations: an air density of $\rho_0 = 1.2\ \mathrm{kg/m^3}$, a kinematic viscosity of $\nu = 1.5 \times 10^{-5}\ \mathrm{m^2/s}$ and a sound speed of $c_0 = 343\ \mathrm{m/s}$.

At low Mach numbers, M, an eddy of characteristic size l essentially radiates sound of wavelength $\lambda \sim \mathcal{O}(l/M)$. Taking into account that the

Mach number according to the inlet velocity is $M \sim 0.007$ (though it can locally reach values up to $M \sim 0.23$), and that frequencies up to 12 kHz are to be captured to reproduce the physics of /s/, very fine spatial meshes are required for the simulations. In this work a computational mesh of 45 million linear tetrahedral elements with equal interpolation for all variables has been used (see Fig. 6.4a and b for a general view and mesh refinement details). The mesh size ranges from $h = 0.025$ mm close to the incisors, where the smallest turbulent flow scales are expected, to $h = 2.5$ mm outside the mouth. The latter guarantees having about twelve nodes per wavelength at 12 kHz ($\lambda \sim 30$ mm).

As explained in the previous section, a total of three equations are solved in the same finite element computational run (four if the acoustic analogy in [154] gets included). Performing such computations with very large size models, as the one in this work, is complex. To that purpose a domain decomposition with an MPI distributed memory scheme has been carried out so as to run the problem at the MareNostrum computer cluster, of the Barcelona Supercomputing Centre (BSC). A period of 10.8 ms with a time step of $\Delta t = 5 \times 10^{-6}$ s has been simulated. This suffices to reach a statistical stationary state. The computational run has lasted $\sim$ 30 hours using 256 processors. A Biconjugate Gradients solver with Pilut preconditioner of the Hypre library has been used to solve the FEM algebraic matrix systems, all of them integrated in PETSc.

6.3 Results

6.3.1 Flow field and acoustic sources

The qualitative results from the CFD simulation confirm the general theoretical framework describing the mechanisms of /s/ generation, and provide some further insight to it as well. The jet flow is strongly accelerated in the constriction between the tongue blade and the hard palate, to which the flow is diverted, (see Fig. 6.5a). These phenomena can be explained with the velocity profile shown at Fig. 6.5b, where it can be observed how the tongue also closes the tract in the transversal direction, forcing the flow to concentrate in a small section of the path before impacting the upper incisors. The flow is greatly accelerated again at the inter-teeth space reaching local Mach numbers of $M \sim 0.2$. Eddies are shed past the upper incisors and impinge on the lower lips. A strong turbulent flow is generated in the cavity between the lower incisors and lower lip, where most sound sources concentrate. This is shown in Fig. 6.5c where a snapshot of Lighthill's source term, $\rho_0 \left(\nabla \otimes \nabla\right) : \left(\boldsymbol{u}^0 \otimes \boldsymbol{u}^0\right)$, is presented. The strongest quadrupole sources can be found in the direct path between the edge of the upper incisors, where

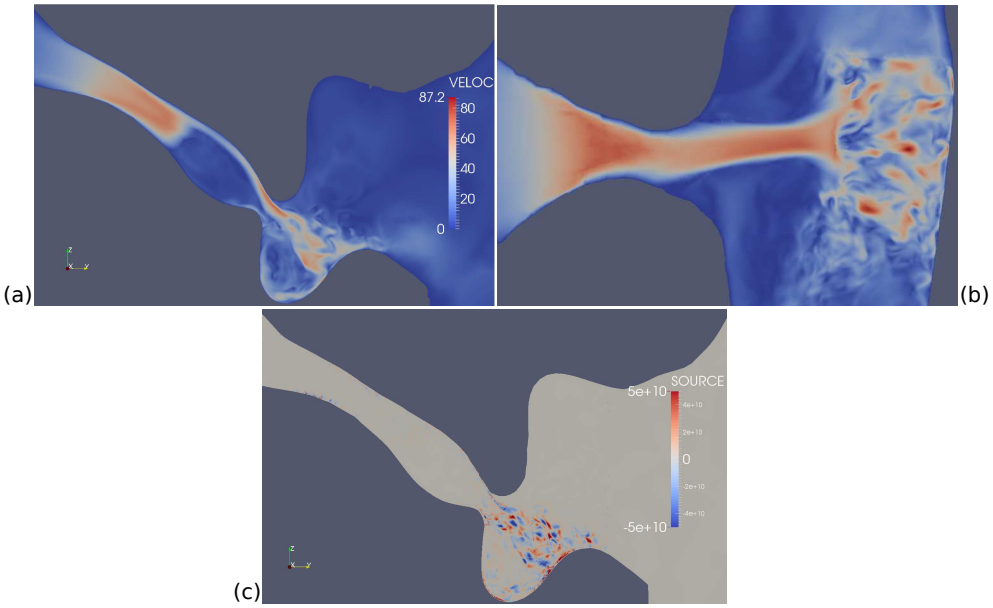

Figure 6.5: Snapshot of (a) flow velocity profile in [m/s] on the vertical midplane cut, (b) flow velocity profile on a plane tangent to the tract and (c) Lighthill's acoustic source term at t=0.0108 s in [kg m^{-3}s^{-2}].

flow separation takes place, and the top side of the lower lips.

To check that the LES is able to capture all turbulent scales down to the inertial subrange, the incompressible pressure spectrum in time E_{pp} at an arbitrary point placed just in front of the upper incisors, at coordinates $P1 = (0, 0.0205, -0.012)^\top$, has been plotted in Fig. 6.6, using a log-log scale. The origin of coordinates is placed at the center of the flat section leading to the realistic vocal tract geometry in Fig. 6.2. According to Kolmogorov's theory for isotropic turbulence, the energy spectrum at the inertial subrange behaves as $E \sim k^{-5/3}$ while the pressure spectrum behaves as $E_{pp} \sim k^{-7/3}$ (see e.g., [147]). Taylor's hypothesis of frozen turbulence allows one to show the latter also exhibits the same power dependence with frequency, namely $E_{pp} \sim f^{-7/3}$. Note that, at the near field, the assumptions of fully developed isotropic turbulence do not apply due to the presence of walls. However, it is observed in Fig. 6.6 that the present CFD simulation manages to reproduce the behavior of the pressure spectrum at the inertial subrange, therefore showing that the stabilized FEM formulation, combined with the fine computational mesh, corresponds to a large eddy simulation approach.

Quantitative details on the flow dynamics simulation are left out of the scope of this work, which essentially focus on the generated aerodynamic sound results to be presented in the next subsection.

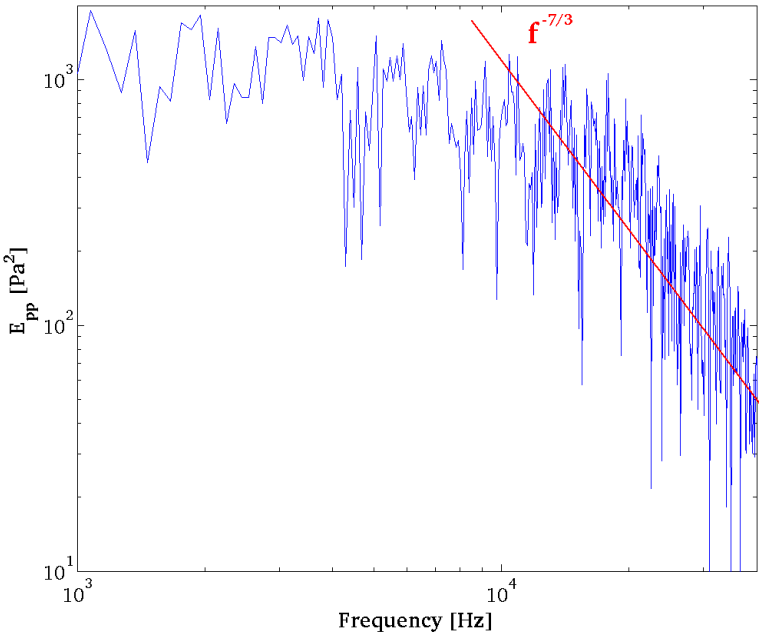

Figure 6.6: Spectrum of the incompressible pressure at a near field point showing the right $f^{-7/3}$ dependence at the turbulent inertial subrange.

6.3.2 Incident and diffracted sound contributions to the acoustic field

On the one hand, the quadrupole sources depicted in Fig. 6.5b directly radiate sound which propagates outside the mouth. On the other hand, this sound is partially diffracted by the upper incisors and also becomes radiated outwards. As said before, this second mechanism is sought to be the predominant one at the far-field [106, see e.g.,]. However, it will be shown that the incident quadrupole radiation cannot be neglected for points in the vicinity of the mouth.

The numerical strategy in Sec. 6.2.2 has been applied to compute the contributions from the direct quadrupolar sound and the dipolar diffracted one. Before proving more deeply the quantitative results, a snapshot showing the spherical acoustic wavefronts emanating from the mouth is shown in Fig. 6.7a, whereas a mid-cut showing the propagation of the acoustic waves resulting from the between-incisors diffraction is presented in Fig. 6.7b, for illustrative purposes.

Several time history occurrences for the acoustic pressure at two points respectively located close and far from the mouth exit are presented in Fig. 6.8. The first one is point $P1$, already introduced in the previous Sec. 6.3.2, whereas the second one is not affected by the flow emanating

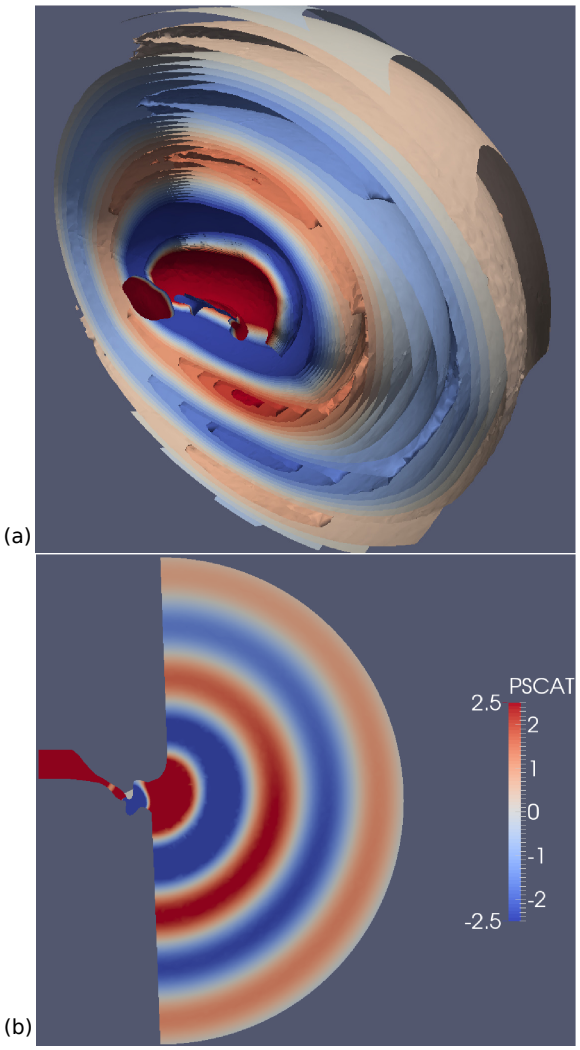

Figure 6.7: (a) Total acoustic pressure isosurfaces and (b) mid-cut showing diffracted pressure wavefronts. Units in [Pa]

from the mouth and is placed at $P5 = (0, 0.035, -0.085)^\top$, see Figure 6.2. Figure 6.8a presents the incident and diffracted contributions to point $P1$ using Lighthill's acoustic analogy. As known, Lighthill's analogy is not valid for points in the source region so the strong fluctuations from the incident contribution in Fig. 6.8a (dashed blue line) correspond to pseudosound rather than to acoustic fluctuations. These are one order of magnitude higher than the acoustic contribution from the incisors' diffraction (red continuous line). The contributions for point $P5$ are presented in Fig. 6.8b. In this case Lighthill's acoustic analogy is perfectly valid to compute the generated aerodynamic acoustic pressure. As observed, at $P5$ the acoustic pressure from

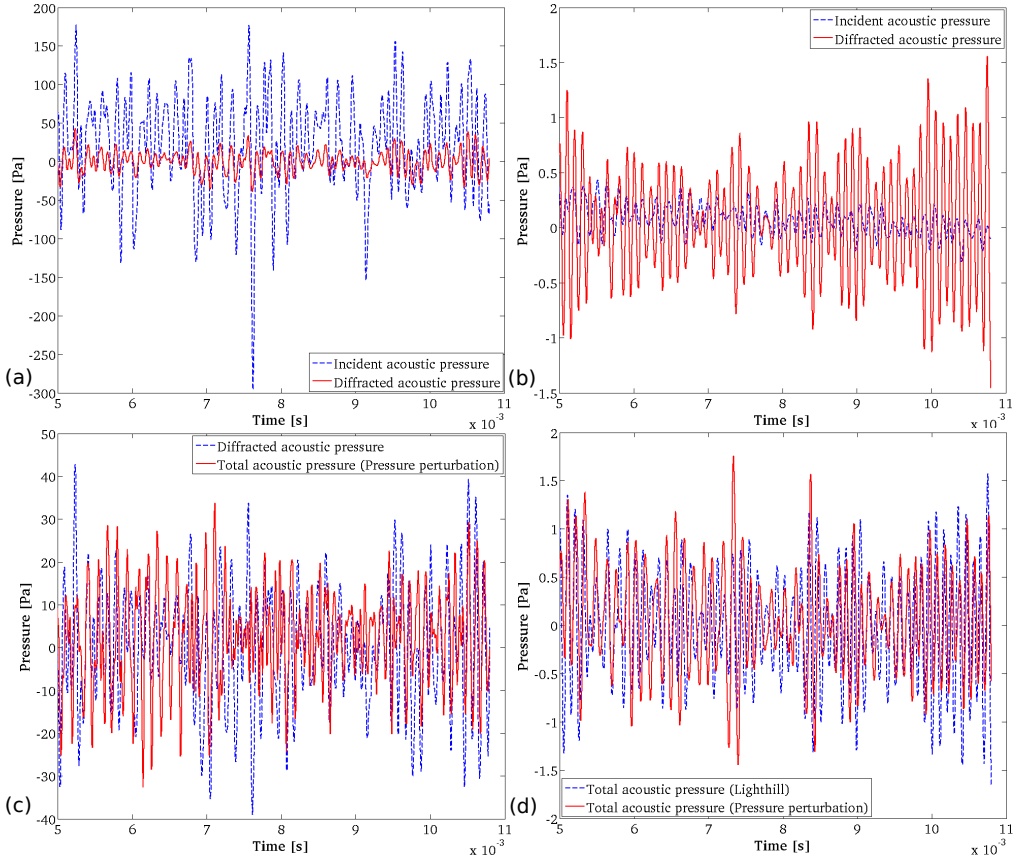

Figure 6.8: Time evolution of the acoustic pressure. (a) Incident pseudosound (dashed blue) and diffracted (continuous red) components at the near field point $P1$ from Lighthill's analogy, (b) incident turbulent (dashed blue) and incisor diffracted (continuous red) contributions to the far field point $P5$, (c) Incisors' diffracted contribution using Lighthill's analogy (dashed blue) versus total acoustic pressure (continuous red) using the analogy in [154] at the near field and (d) total acoustic pressure at the far field using Lighthill's analogy (dashed blue) and the analogy in [154] (continuous red).

the diffracted component is clearly higher than that provided by the direct turbulent flow contribution. In Fig. 6.8c, a comparison is presented between the contribution of the incisors' diffraction to point $P1$ (dashed blue line), already plotted in Fig. 6.8a, and the total acoustic pressure (continuous red line) computed with the acoustic analogy in [154]. Both contributions have amplitudes of the same order showing that the analogy in Eq. (6.3) is capable of filtering the pseudosound and extracting the acoustic component from the pressure fluctuations, at very low Mach numbers. When evaluated at

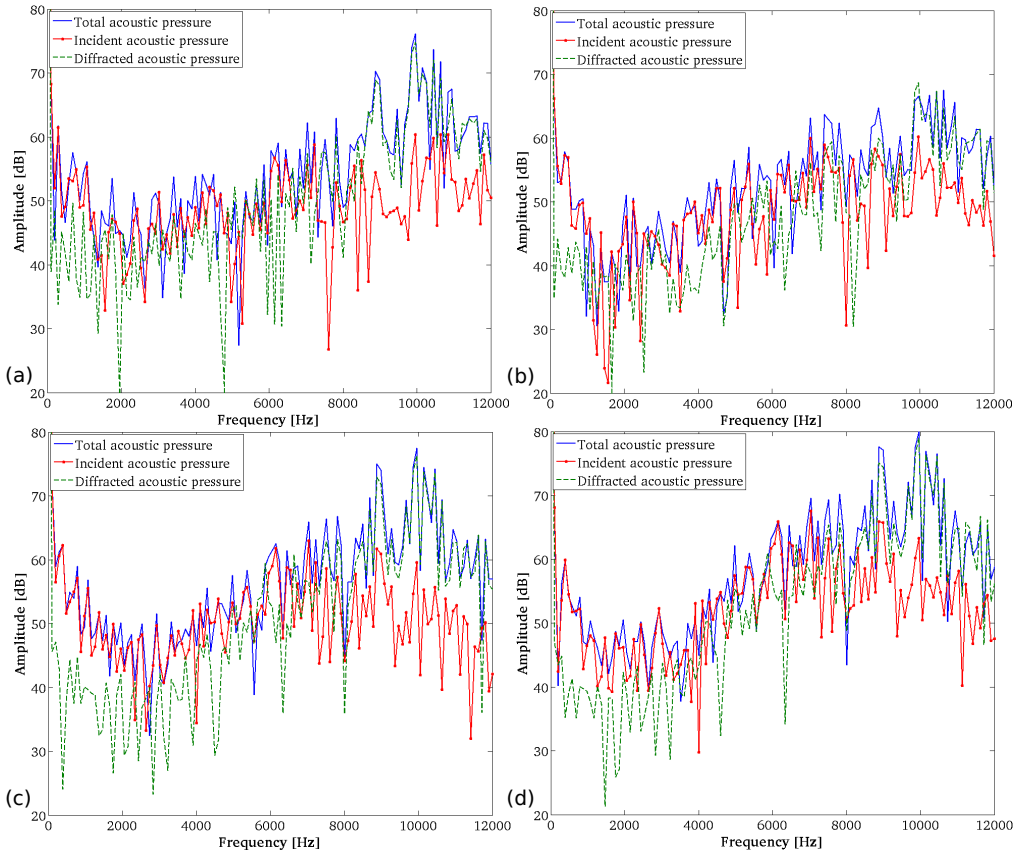

Figure 6.9: Spectra of the incident, diffracted and total components of the acoustic pressure at the far field. (a) Point $P2$, (b) Point $P3$, (c) Point $P4$, (d) Point $P5$.

a point outside the acoustic source region like $P5$, both, Lighthill's analogy in Eq. (6.1a) and Eq. (6.3) should yield almost the same results. This is what is observed in Fig. 6.8d where the time evolution for the total acoustic pressure at $P5$ using both analogies is plotted. The two curves in the figure show very similar trends in terms of amplitude and phase.

The spectra in dB (ref. 2×10^{-5} Pa) at four points well separated from the flow exiting the mouth are plotted in Fig. 6.9. Figs. 6.9a-d respectively correspond to the following points:
$P2 = (-0.075, 0.035, -0.0125)^\top$,
$P3 = (0.075, 0.035, -0.0125)^\top$,
$P4 = (0, 0.035, 0.06)^\top$ and
$P5$, see Figure 6.2.

The figures contain the total acoustic pressure at these points, together with the contributions from the incident turbulent aerodynamic noise and

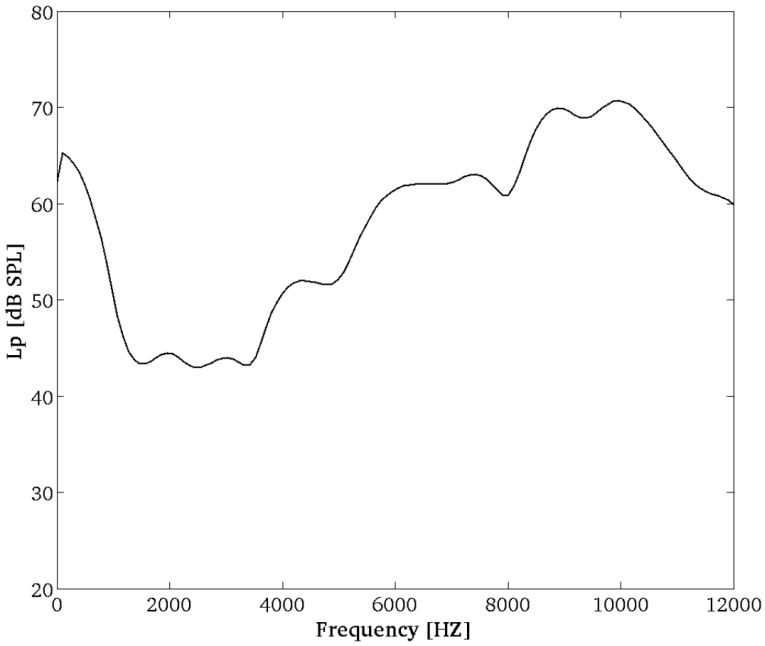

Figure 6.10: Welch averaged power spectral density level at point P3.

from the sound diffracted by the incisors. As regards the total acoustic pressure, very similar tendencies can be appreciated in all figures. The spectra first decrease with frequency and exhibit a dip close to 2 kHz; then they increase linearly showing two marked peaks close to 9 kHz and 10 kHz and finally they decrease again with frequency. As regards the contributions, it can be checked that in the range up to 2 kHz the incident turbulent component clearly dominates. The size of the incisors are small compared to the acoustic wavelengths at those frequencies so diffraction is not so important. However, as frequency increases the situation changes and both the incident and diffracted components contribute the same from 2 kHz to $\sim$ 8 kHz, with a slight predominance of the former. Above $\sim$ 8 kHz the turbulent contribution begins to decay and the spectra become mostly justified by the diffracted component. Again, this is logical given that for smaller wavelengths the diffraction effects become more important. In addition, more wavelengths are needed to reach the target points and dipolar sources become more effective. For a fixed distance, the conditions of far-field are sooner satisfied at higher frequencies, where the diffracted component is predicted to dominate [106].

The spectra for the total acoustic pressure in Figs. 6.9a-d basically exhibit the same spectral trend as those described in the Introduction for Fig. 6.1. To better appreciate this point, the level of the Welch averaged power spectral density at $P3$ has been plotted, after proper scaling, in Fig. 6.10. A

comparison with Fig. 6.1 reveals that, despite considering different speakers (woman and child) and scenarios (the reconstructed geometry portion is obtained for sustained /s/ whereas the speech measurements are reported for syllables), and taking into account that in [80] it is shown that the constriction degree is greater for sustained phonemes than for phonemes in a syllable context, qualitative good agreement is observed for spectral features. The essentials of sibilant /s/ (see [120]) are well-recovered, namely the dip at mid frequencies followed by a positive spectral slope, the frequency position of the spectral peaks and the dynamic amplitude. Given the lack of experimental data with the exact configuration of the numerical simulations, the authors believe, however, that the recovery of the essential spectral features for /s/ validates in a first way that its underlying physics is being well-captured.

6.4 Numerical simulation of sibilant /s/ using the isentropic compressible flow equations

The simulation of this phoneme using an LES based on the isentropic compressible approach presented in Chapter 4 is the last stage of the present work. Bearing in mind taht the same flow configuration, geometry, spatial and temporal discretizations of the incompressible approach have been used, the compressible flow solution should converge to the one obtained in Sec. 6.3. Therefore, we do not expect to find new information regarding the flow dynamics, but regarding the acoustics, we must remember that the present case, unlike Lighthill's analogy, considers the wave propagation in turbulent regions.

Another relevant aspect of this chapter is to show that this compressible approach can be applied to complex phonation problems. As expected, the computational cost increases drastically respect to the segregated incompressible approach (Fractional Step Method) and the convergence of the solver becomes much more difficult. In order solve these two challenges simultaneously, a field-split preconditioner has been used iterating up to the monolithic solution. Otherwise, the time step reduction for converging would have led to an excessive computation time.

Like in Sec. 6.3, the analysis begins with the flow dynamic scales. Fig. 6.11 shows a profile of the developed flow velocity, which turns to be qualitatively very similar to the incompressible flow motion shown in Fig. 6.5. Despite this apparent consistency, the pressure frequency spectrum at $P1$, see Fig. 6.12, does not exactly reproduce the same turbulence pattern obtained in Fig. 6.6. Although several similarities can be found, the dissipative region of the turbulence model is much more important in the present case, and this will

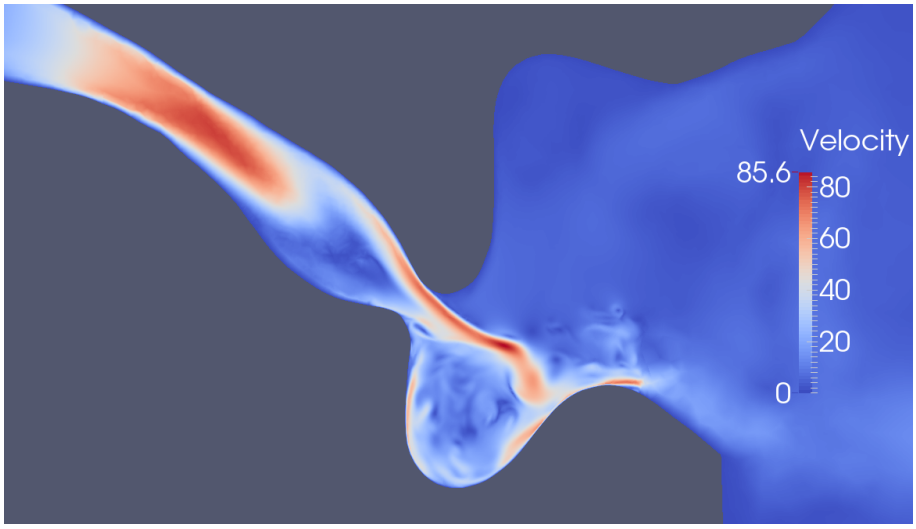

Figure 6.11: Velocity profile using the isentropic compressible flow equations.

affect in a certain way the acoustic propagation.

The analysis of the acoustic scales generates an interesting room for discussion and research. Although the acoustic propagation of this approach should converge to that of a Direct Noise Calculation (DNC) for such a low Mach regime, Fig. 6.13 shows that, despite following a similar pattern, the acoustic signal at the far-field has suffered a much higher dissipation than the Lighthill counterpart, see Fig. 6.7. One could argue that the propagation of a solution in regions with coarse meshes requires the deployment of high-order spatial discretizations, above all in compressible flow schemes. Taking into account the dissipative character of the VMS turbulence model, the effect of the Algebraic Subgrid-Scale(ASGS) stabilization method on the wave dissipation is an important factor to be considered, bearing in mind that the second order wave equation of Lighthill's analogy does not include any stabilization term. A possible solution to this problem would be the Orthogonal Subgrid-Scale (OSS) method [47], known to be less dissipative than the ASGS, together with the dynamic terms of the sub-scale problem [56]. Another encouraging alternative can be found in the non-residual based stabilized method Split-OSS [36], which gets rid of the cross terms and eases the convergence of highly non-linear problems.

In spite of the previous discrepancy regarding dissipation, the pressure frequency spectrum at all the selected points of the far-field in Fig. 6.14 does not show relevant differences respect to Fig. 6.9. In fact, the differential characteristics of each location described by Lighthill's analogy are properly reproduced by the present formulation: $P3$ has again the flattest spectrum with the lowest intensity, whereas $P5$ has the steepest and loudest.

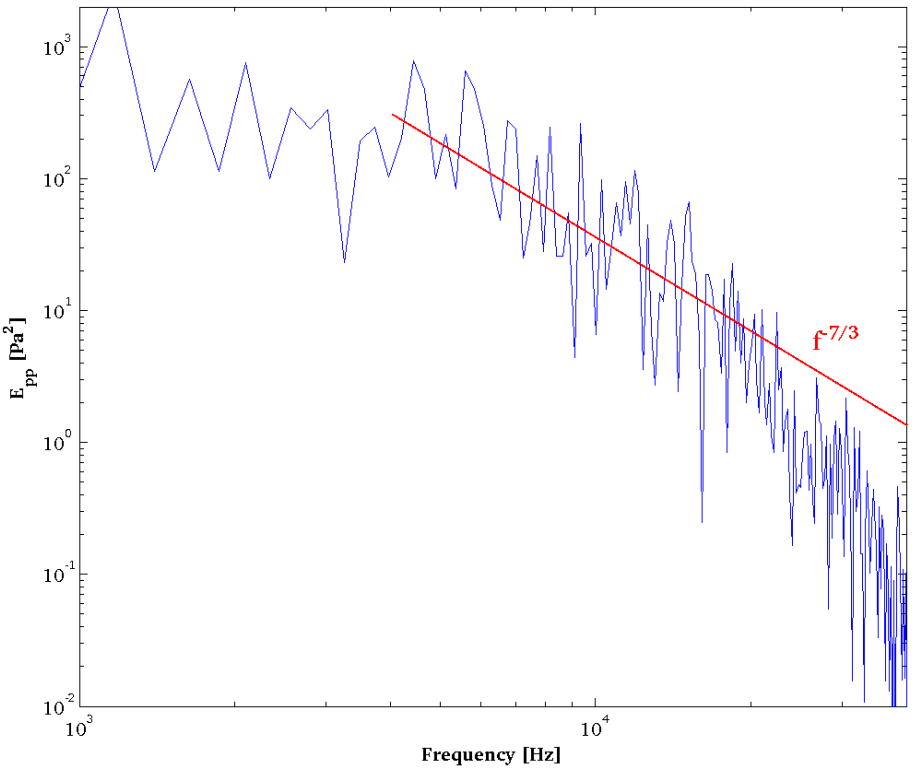

Figure 6.12: Spectrum of the compressible pressure at a near field point showing the right $f^{-7/3}$ dependence at the turbulent inertial subrange.

6.5 Conclusions

In this work a large-scale numerical simulation of the aeroacoustics of a single example of sibilant fricative /s/ has been carried out. Lighthill's acoustic analogy and an analogy that allows filtering pseudosound to some extent at the source region have been implemented. A stabilized finite element method which acts as an implicit large eddy simulation model has been used to solve the incompressible Navier-Stokes equations. The acoustic field has been resolved resorting to a splitting strategy that allows one to obtain the contributions from the incident turbulent sound and the sound diffracted by the upper incisors in a single computational run.

The spectra from the contributions to the total acoustic pressure at points located close to the mouth exit (yet out of the flow wake) reveal a significant different behavior depending on the frequency range. At the lowest side of the spectrum, the acoustic pressure level decreases and the incident turbulent sound directly emanating from eddies in the cavity between incisors and lips dominates. This is the case up to ~ 2 kHz. From ~ 2 kHz to $\sim 8-9$ kHz, the level strongly increases and the contributions from both the

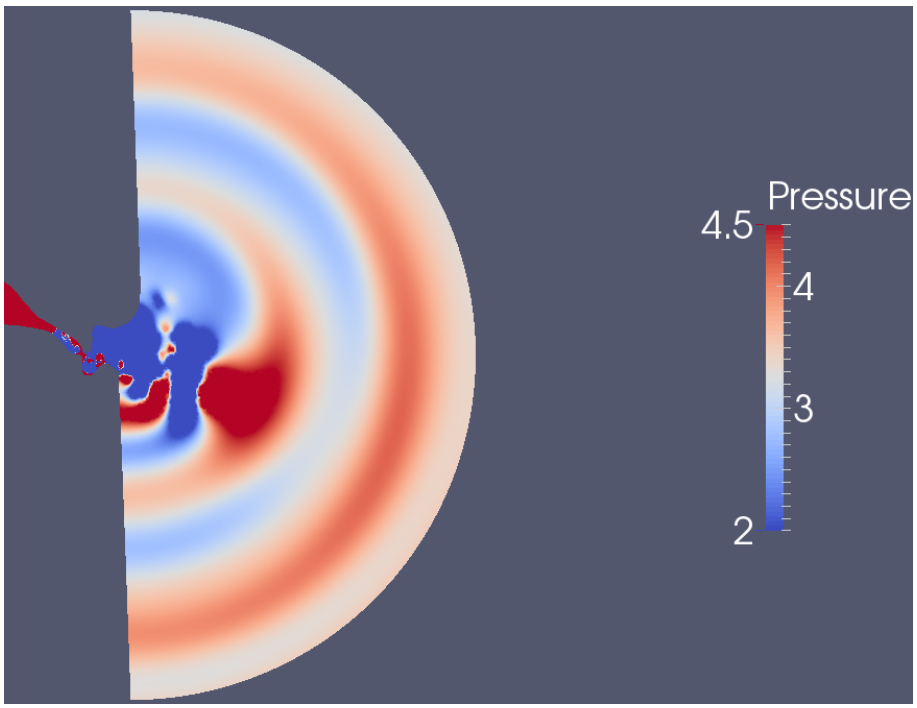

Figure 6.13: Pressure wave propagation using the isentropic compressible flow equations.

sound diffracted by the upper incisors and from turbulence are very similar. At higher frequencies the diffracted sound becomes dominant. Though one should bear in mind that the results reported in this work correspond to a single vocal tract geometry extracted from a subject while uttering a particular realization of /s/, and therefeore lack of general validity, comparisons with subject recordings in literature seem to validate the main trends of the obtained results.

The final computational run using the isentropic compressible approach has reached an important milestone: the aeroacoustic simulation of a turbulent unvoiced sound. The method has proved to be consistent with the incompressible approach in the solution of the flow dynamics and the acoustics, except for its excessive dissipation, which might be probably caused by the stabilization method.

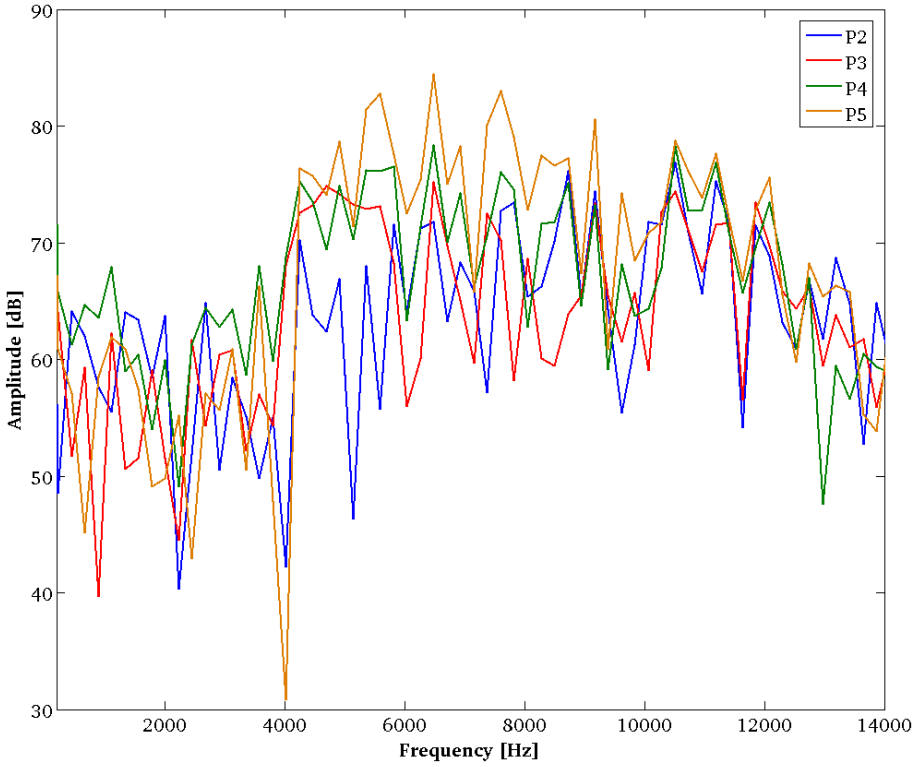

Figure 6.14: Spectra of the compressible pressure at $P5$.

Chapter 7

Conclusions and future work

A series of aeroacoustic formulations, ranging from incompressible uniform to isentropic compressible flows, have been proposed as an alternative to fully compressible schemes with the aim of simulating human phonation problems in HPC environments with an affordable computational cost. The first approach has consisted in decomposing Lighthill's analogy in two different problems corresponding to the quadrupolar sources (noise generated by the vorticity of the flow) and to the dipolar ones (sound radiated by solid walls). Although this artifact does not change the assumptions of the original problem, it has proved to be very useful for evaluating the contribution of solid boundaries in the generation of sound. A benchmark of the aeolian tones has been calculated with this method and the results have revealed that, as expected, the dipolar component reaches its maximum intensity at the perpendicular direction of the flow and is much more relevant at the far field than the quadrupolar one. In the same direction, a simplified 3D vocal tract calculation of the phoneme /s/ has reached the same conclusion obtained with analytical models [106], that the main contributors to the phoneme /s/ are the upper incisors. Moreover, the dipolar acoustic profile shows the same behavior of the purely acoustic pressure obtained with the second order acoustic perturbation equation [154], for which it can be concluded that the method can also be understood as an acoustic filtering of Lighthill's analogy, since the incompressible flow oscillations that do not propagate are mainly captured by the quadrupolar component.

The second step has consisted in developing a stabilized finite element formulation of the Acoustic Perturbation Equations [74, 125, 97], which are the result of an acoustic filtering of the Linearized Euler Equations (LEE) [33, 19, 158]. The main improvement regarding the description of the physical problem lays on the consideration of non-uniform mean flows, which extends the validity of the acoustic solution to the near field or perturbed region. In this sense, the aeolian tones solution appears convected by the flow and totally filtered from flow oscillations, hence it can be concluded

that this method overcomes all simplifications of Lighthill when using incompressible flow. In spite of the optimum result, the high implementation and computational costs of this option have motivated a third alternative which yields a high accuracy with less complexity. Instead of extending an incompressible formulation, the problem has been approached as a simplification of a compressible solver, which assumes that both flow and acoustics behave as isentropic processes. The two-field unified solver, together with the developed method for prescribing compatible flow and acoustic boundary conditions in a weak sense, has shown a great robustness in a wide range of subsonic flows and has converged to a DNS at a very low Mach number.

The extension to dynamic domains has also been approached from two sides: on one hand, the aforementioned splitting of the acoustic pressure has been applied to the stabilized ALE formulation of Lighthill's analogy in [89], and on the other, the isentropic compressible solver has been extended to an ALE frame of reference. In spite of some discrepancies, the methods have proved to be consistent and have shown the readiness of the computational platform to face the aeroacoustic simulation of dynamic voice sounds. Bearing in mind the expected large deformation in some phonation scenarios, a conservative remeshing strategy has also been presented. The solution of a small optimization problem with restrictions imposing the conservation of relevant magnitudes has compensated the loss of relevant information during the Lagrangian interpolation of results. Moreover, it has avoided the solution of a global system of equations.

Finally, the simulation of the fricative phoneme /s/ with several incompressible acoustic formulations and the isentropic compressible approach has proved the suitability of the presented numerical framework for representing all relevant physical phenomena involved in the generation and propagation of this sound. Both compressible and incompressible LES succeed in reproducing a physical pattern for turbulence, and the local refinement of the mesh has succeeded in capturing all relevant flow scales. The acoustic models which complement the incompressible flow solver provide a valid solution at the far-field, where the results have been validated against the measurements performed in an equivalent mechanical replica [81]. Moreover, the identification of quadrupolar and dipolar sources has confirmed the results obtained with the simplified geometry regarding the contribution of the upper incisors.

The present thesis has presented a basis towards a complete computational platform for the simulation of human voice in HPC environments. However, there are still some crucial tasks to be done, specially in the field of biomechanics. The multiphysics code FEMUSS has recently been upgraded with some relevant features, such as a Fluid-Structure-Interaction (FSI) solver and several solid constitutive models, which will allow the cal-

culation of phonemes involving deformation of tissues, e.g. /r/, or the behavior of the vocal folds in the generation of vowels. However, the most difficult challenge corresponds to the simulation of syllables and other dynamic sounds, which requires the inclusion of realistic deformation mappings and the coupling with a mesher that automatically generates new grids on the deformed domain when the distortion of the elements reaches a certain threshold. Furthermore, a suitable contact model for different kind of materials (teeth, palate, lips, tongue) should be implemented.

Bearing in mind the difficulties and uncertainties that arise from a fully coupled human phonation simulation, an alternative research line has been envisaged and is already ongoing. It consists in a drastic simplification of the simulation by getting rid of the CFD and thus reducing the computational cost to a minimum, even for large-scale cases. In a first step, the reduction will be applied only partially to the simulation of voiced fricatives and syllables departing from an unvoiced fricative. At this stage, the basic CFD simulation of the phoneme /s/ will be complemented with the propagation of a known glottal pulse corresponding to the characteristic vocal fold vibration of the backflow in voiced sounds such as /z/. In the case of syllables, the source term to be propagated by the wave operator will be a glottal pulse representing the desired vowel, like in [7, 8], together with a simplified deformation mapping. In a second phase, the CFD will be completely replaced by the direct propagation of a tailored distribution of quadrupoles near the incisors, emulating the turbulent sound sources captured in the presented simulations. Although this approach will not be part of the CAA framework anymore, it might be very useful for obtaining real-time simulations for any vocal tract geometry. An alternative to this approach is the Reduced Order Model technique (ROM) applied to CFD calculations, which has been recently implemented in the FEMUSS code yielding promising results.

Bibliography

[1] F. Alauzet and M. Mehrenberger. P1-conservative solution interpolation on unstructured triangular meshes. *International Journal for Numerical Methods in Engineering*, 84(13):1552–1588, 2010.

[2] V. Allampalli, R. Hixon, M. Nallasamy, and S. D. Sawyer. High-accuracy large-step explicit Runge-Kutta (HALE-RK) schemes for computational aeroacoustics. *J. Comput. Phys.*, 228(10):3837 – 3850, 2009.

[3] P. Anderson, S. Green, and S. Fels. Modeling fluid flow in the airway using CFD with a focus on fricative acoustics. In *Proc. 1st*, pages 146–154, 2009.

[4] M. Arnela, R. Blandin, S. Dabbaghchian, O. Guasch, F. Alías, X. Pelorson, A. Van Hirtum, and O. Engwall. Influence of lips on the production of vowels based on finite element simulations and experiments. *J. Acoust. Soc. Am.*, 139(5):2852–2859, 2016.

[5] M. Arnela, S. Dabbaghchian, R. Blandin, O. Guasch, O. Engwall, A. Van Hirtum, and X. Pelorson. Influence of vocal tract geometry simplifications on the numerical simulation of vowel sounds. *J. Acoust. Soc. Am.*, 140(3):1707–1718, 2016.

[6] M. Arnela and O. Guasch. Finite element computation of elliptical vocal tract impedances using the two-microphone transfer function method. *J. Acoust. Soc. Am.*, 133(6):4197–4209, 2013.

[7] M. Arnela and O. Guasch. Finite element computation of elliptical vocal tract impedances using the two-microphone transfer function method. *The Journal of the Acoustical Society of America*, 133(6):4197–4209, 2013.

[8] M. Arnela and O. Guasch. Two-dimensional vocal tracts with three-dimensional behavior in the numerical generation of vowels. *The Journal of the Acoustical Society of America*, 135(1):369–379, 2014.

[9] M. Arnela, O. Guasch, and F. Alías. Effects of head geometry simplifications on acoustic radiation of vowel sounds based on time-domain finite-element simulations. *J. Acoust. Soc. Am.*, 134(4):2946–2954, 2013.

[10] M. Avila, J. Principe, and R. Codina. A finite element dynamical nonlinear subscale approximation for the low mach number flow equations. *J. Comput. Physics.*, 230(22):7988–8009, 2011.

[11] S. Badia and R. Codina. Algebraic pressure segregation methods for the incompressible Navier-Stokes equations. *Archives of Computational Methods in Engineering*, 15:1–52, 2007.

[12] S. Badia, R. Codina, and H. Espinoza. Stability, convergence, and accuracy of stabilized finite element methods for the wave equation in mixed form. *SIAM Journal on Numerical Analysis*, 52(4):1729–1752, 2014.

[13] S. Badia, R. Codina, and H. Espinoza. Stability, convergence and accuracy of stabilized finite elements methods for the wave equation in mixed form. *SIAM J. Numer. Anal.*, 52:1729–1752, 2014.

[14] P. Badin. Fricative consonants-acoustic and x-ray measurements. *Journal of phonetics*, 19(3-4):397–408, 1991.

[15] J. Baiges and R. Codina. A variational multiscale method with subscales on the element boundaries for the Helmholtz equation. *Int. J. Numer. Meth. Engrg.*, 93(6):664–684, 2013.

[16] C. Bailly and C. Bogey. Contributions of computational aeroacoustics to jet noise research and prediction. *Int. J. Comput. Fluid Dyn.*, 18(6):481–491, 2004.

[17] C. Bailly, C. Bogey, and X. Gloerfelt. Some useful hybrid approaches for predicting aerodynamic noise. *C. R. Mec.*, 333(9):666–675, 2005.

[18] C. Bailly, C. Bogey, and O. Marsden. Progress in Direct Noise Computation. *Noise Notes*, 9(3):31–48, 2010.

[19] C. Bailly and D. Juve. Numerical solution of acoustic propagation problems using linearized Euler equations. *AIAA journal*, 38(1):22–29, 2000.

[20] C. Bayona, J. Baiges, and R. Codina. Solution of low Mach number aeroacoustic flows using a variational multi-scale finite element formulation of the compressible Navier-Stokes equations written in primitive variables. *Submitted*.

[21] C. A. Bayona Roa, J. Baiges, and R. Codina. Variational multi-scale finite element approximation of the compressible Navier-Stokes equations. *International Journal of Numerical Methods for Heat & Fluid Flow*, 26(3/4):1240–1271, 2016.

[22] Y. Bazilevs, V. Calo, J. Cottrell, T. Hughes, A. Reali, and G. Scovazzi. Variational multiscale residual-based turbulence modeling for large eddy simulation. *Comput. Methods Appl. Mech. Engrg.*, 197(1–4):173–201, 2007.

[23] E. Bécache, P. Joly, and C. Tsogka. An analysis of new mixed finite elements for the approximation of wave propagation problems. *SIAM J. Numer. Anal.*, 37(4):1053–1084, 2000.

[24] E. Bécache, P. Joly, and C. Tsogka. Fictitious domains, mixed finite elements and perfectly matched layers for 2-D elastic wave propagation. *J. Comput. Acoust.*, 9(3):1175–1201, 2001.

[25] E. Bécache, P. Joly, and C. Tsogka. A new family of mixed finite elements for the linear elastodynamic problem. *SIAM J. Numer. Anal.*, 39(6):2109–2132, 2002.

[26] J.-P. Berenger. A perfectly matched layer for the absorption of electromagnetic waves. *Journal of Computational Physics*, 114(2):185–200, 1994.

[27] C. Bernardi. A new nonconforming approach to domain decomposition: the mortar element method. *Nonliner Partial Differential Equations and Their Applications*, 1994.

[28] M. Billaud, G. Gallice, and B. Nkonga. A simple stabilized finite element method for solving two phase compressible–incompressible interface flows. *Computer Methods in Applied Mechanics and Engineering*, 200(9):1272–1290, 2011.

[29] R. Blandin, M. Arnela, R. Laboissière, X. Pelorson, O. Guasch, A. Van Hirtum, and X. Laval. Effects of higher order propagation modes in vocal tract like geometries. *J. Acoust. Soc. Am.*, 137(2):832–843, 2015.

[30] R. Blandin, A. Van Hirtum, X. Pelorson, and R. Laboissière. Influence of higher order acoustical propagation modes on variable section waveguide directivity: Application to vowel [α]. *Acta Acust. united Ac.*, 102(5):918–929, 2016.

[31] C. Bogey and C. Bailly. Three-dimensional non-reflective boundary conditions for acoustic simulations: far field formulation and validation test cases. *Acta Acustica united with Acustica*, 88(4):463–471, 2002.

[32] C. Bogey, C. Bailly, and D. Juvé. Numerical simulation of sound generated by vortex pairing in a mixing layer. *AIAA J.*, 38(12):2210–2218, 2000.

[33] C. Bogey, C. Bailly, and D. Juvé. Computation of flow noise using source terms in linearized Euler equations. *AIAA journal*, 40(2):235–243, 2002.

[34] D. Brancherie, P. Villon, A. Ibrahimbegovi´ c, A. Rassineux, and P. Breitkopf. Transfert de champs par approximation diffuse avec conservation de l'énergie. *European Journal of Computational Mechanics/Revue Européenne de Mécanique Numérique*, 15(1-3):107–118, 2006.

[35] P. Bussetta, R. Boman, and J.-P. Ponthot. Efficient 3d data transfer operators based on numerical integration. *International Journal for Numerical Methods in Engineering*, 102(3-4):892–929, 2015.

[36] E. Castillo and R. Codina. Finite element approximation of the viscoelastic flow problem: A non-residual based stabilized formulation. *Computers & Fluids*, 142:72–78, 2017.

[37] J. R. Cebral and R. Lohner. Conservative load projection and tracking for fluid-structure problems. *AIAA journal*, 35(4):687–692, 1997.

[38] G. Chesshire and W. D. Henshaw. A scheme for conservative interpolation on overlapping grids. *SIAM Journal on Scientific Computing*, 15(4):819–845, 1994.

[39] G. Chiandussi, G. Bugeda, and E. Oñate. A simple method for automatic update of finite element meshes. *Communications in Numerical Methods in Engineering*, 16(1):1–19, 2000.

[40] S. Chippada, C. N. Dawson, M. L. Martinez, and M. F. Wheeler. A projection method for constructing a mass conservative velocity field. *Computer Methods in Applied Mechanics and Engineering*, 157(1):1–10, 1998.

[41] D. Choi and C. L. Merkle. Application of time-iterative schemes to incompressible flow. *AIAA journal*, 23(10):1518–1524, 1985.

[42] A. J. Chorin. A numerical method for solving incompressible viscous flow problems. *Journal of Computational Physics*, 2(1):12–26, 1967.

[43] J. Cisonni, K. Nozaki, A. Van Hirtum, X. Grandchamp, and S. Wada. Numerical simulation of the influence of the orifice aperture on the flow around a teeth-shaped obstacle. *Fluid Dynamics Research*, 45(2):025505, 2013.

[44] J. Cisonni, K. Nozaki, A. Van Hirtum, and S. Wada. A parameterized geometric model of the oral tract for aero acoustic simulation of fricatives. *IJIEE*, 1(3):223, 2011.

[45] R. Codina. On stabilized finite element methods for linear systems of convection–diffusion-reaction equations. *Comput. Methods Appl. Mech. Engrg.*, 188(1):61–82, 2000.

[46] R. Codina. Stabilized finite element approximation of transient incompressible flows using orthogonal subscales. *Comput. Methods Appl. Mech. Engrg.*, 191:4295–4321, 2002.

[47] R. Codina. Stabilized finite element approximation of transient incompressible flows using orthogonal subscales. *Computer Methods in Applied Mechanics and Engineering*, 191(39):4295–4321, 2002.

[48] R. Codina. Finite element approximation of the hyperbolic wave equation in mixed form. *Computer Methods in Applied Mechanics and Engineering*, 197(13):1305–1322, 2008.

[49] R. Codina. Finite element approximation of the hyperbolic wave equation in mixed form. *Comput. Methods Appl. Mech. Engrg.*, 197(13–16):1305–1322, 2008.

[50] R. Codina and S. Badia. On some pressure segregation methods of fractional-step type for the finite element approximation of incompressible flow problems. *Comput. Methods Appl. Mech. Engrg.*, 195(23):2900–2918, 2006.

[51] R. Codina, S. Badia, J. Baiges, and J. Principe. *Variational Multiscale Methods in Computational Fluid Dynamics,* in Encyclopedia of Computational Mechanics. John Wiley & Sons Ltd., to appear.

[52] R. Codina and J. Baiges. Approximate imposition of boundary conditions in immersed boundary methods. *International Journal for Numerical Methods in Engineering*, 80(11):1379–1405, 2009.

[53] R. Codina and J. Baiges. Weak imposition of essential boundary conditions in the finite element approximation of elliptic problems with non-matching meshes. *International Journal for Numerical Methods in Engineering*, 104(7):624–654, 2015.

[54] R. Codina, J. González-Ondina, G. Díaz-Hernández, and J. Principe. Finite element approximation of the modified boussinesq equations using a stabilized formulation. *Int. J. Numer. Meth. Fluids*, 57(9):1249–1268, 2008.

[55] R. Codina, G. Houzeaux, H. Coppola-Owen, and J. Baiges. The fixed-mesh ale approach for the numerical approximation of flows in moving domains. *Journal of Computational Physics*, 228(5):1591–1611, 2009.

[56] R. Codina and J. Principe. Dynamic subscales in the finite element approximation of thermally coupled incompressible flows. *International journal for numerical methods in fluids*, 54(6-8):707–730, 2007.

[57] R. Codina, J. Principe, and M. Ávila. Finite element approximation of turbulent thermally coupled incompressible flows with numerical subgrid scale modelling. *International Journal of Numerical Methods for Heat & Fluid Flow*, 20(5):492–516, 2010.

[58] R. Codina, J. Principe, O. Guasch, and S. Badia. Time dependent subscales in the stabilized finite element approximation of incompressible flow problems. *Comput. Methods Appl. Mech. Engrg.*, 196(21):2413–2430, 2007.

[59] R. Codina, J. Principe, O. Guasch, and S. Badia. Time dependent subscsales in the stabilized finite element approximation of incompressible flow problems. *Comput. Methods Appl. Mech. Engrg.*, 196(21–24):2413–2430, 2007.

[60] O. Colomés, S. Badia, R. Codina, and J. Principe. Assessment of variational multiscale models for the large eddy simulation of turbulent incompressible flows. *Comput. Methods Appl. Mech. Engrg.*, 285:32–63, 2015.

[61] D. Crighton. Basic principles of aerodynamic noise generation. *Prog. Aerosp. Sci.*, 16(1):31–96, 1975.

[62] D. Crighton, A. Dowling, J. F. Williams, M. Heckl, and F. Leppington. Modern methods in analytical acoustics. *Journal of Fluid Mechanics*, 318:410–412, 1996.

[63] S. Crow. Aerodynamic sound emission as a singular perturbation problem. *Stud. Appl. Math.*, 49 (1):21–44, 1970.

[64] G. Cunha and S. Redonnet. On the signal degradation induced by the interpolation and the sampling rate reduction in aeroacoustics hybrid methods. *Int. J. Numer. Meth. Fluids*, 71(7):910–929, 2013.

[65] N. Curle. The influence of solid boundaries upon aerodynamic sound. *Proc. R. Soc. Lond. A*, 231(1187):505–514, 1955.

[66] P. Doak. Acoustic radiation from a turbulent fluid containing foreign bodies. *Proc. R. Soc. Lond. A*, 254(1276):129–146, 1960.

[67] J. Donea, A. Huerta, J. P. Ponthot, and A. Rodriguez-Ferran. Arbitrary Lagrangian-Eulerian methods, vol. 1: Fundamentals, E. Stein, R. de Borst & T. J. R. Hugues. Encyclopedia of Computational Mechanics, 2004.

[68] P. Drazin. *Introduction to Hydrodynamic Stability*. Cambridge Texts in Applied Mathematics, Cambridge University Press, 2002.

[69] J. K. Dukowicz and J. W. Kodis. Accurate conservative remapping (rezoning) for arbitrary lagrangian-eulerian computations. *SIAM Journal on Scientific and Statistical Computing*, 8(3):305–321, 1987.

[70] D. R. Durran. A physically motivated approach for filtering acoustic waves from the equations governing compressible stratified flow. *Journal of Fluid Mechanics*, 601:365–379, 2008.

[71] H. Espinoza, R. Codina, and S. Badia. A Sommerfeld non-reflecting boundary condition for the wave equation in mixed form. *Computer Methods in Applied Mechanics and Engineering*, 276:122–148, 2014.

[72] H. Espinoza, R. Codina, and S. Badia. A Sommerfeld non-reflecting boundary condition for the wave equation in mixed form. *Comput. Methods Appl. Mech. Engrg.*, 276:122–148, 2014.

[73] R. Ewert and W. Schröder. Acoustic perturbation equations based on flow decomposition via source filtering. *J. Comput. Phys.*, 188(2):365–398, 2003.

[74] R. Ewert and W. Schröder. Acoustic perturbation equations based on flow decomposition via source filtering. *Journal of Computational Physics*, 188(2):365–398, 2003.

[75] C. Farhat, M. Lesoinne, and P. Le Tallec. Load and motion transfer algorithms for fluid/structure interaction problems with non-matching discrete interfaces: Momentum and energy conservation, optimal discretization and application to aeroelasticity. *Computer methods in applied mechanics and engineering*, 157(1):95–114, 1998.

[76] P. E. Farrell and J. R. Maddison. Conservative interpolation between volume meshes by local galerkin projection. *Computer Methods in Applied Mechanics and Engineering*, 200(1):89–100, 2011.

[77] P. E. Farrell, M. D. Piggott, C. C. Pain, G. J. Gorman, and C. R. Wilson. Conservative interpolation between unstructured meshes via supermesh construction. *Computer Methods in Applied Mechanics and Engineering*, 198(33):2632–2642, 2009.

[78] M. Fleischer, S. Pinkert, W. Mattheus, A. Mainka, and D. Mürbe. Formant frequencies and bandwidths of the vocal tract transfer function are affected by the mechanical impedance of the vocal tract wall. *Biomechanics and modeling in mechanobiology*, 14(4):719–733, 2015.

[79] P. Fosso, H. Deniau, N. Lamarque, T. Poinsot, et al. Comparison of outflow boundary conditions for subsonic aeroacoustic simulations. *International Journal for Numerical Methods in Fluids*, 68(10):1207–1233, 2012.

[80] Y. Fujiso, K. Nozaki, and A. Van Hirtum. Estimation of minimum oral tract constriction area in sibilant fricatives from aerodynamic data. *The Journal of the Acoustical Society of America*, 138(1):EL20–EL25, 2015.

[81] Y. Fujiso, K. Nozaki, and A. Van Hirtum. Towards sibilant physical speech screening using oral tract volume reconstruction: Some preliminary observations. *Appl. Acoust.*, 96:101–107, 2015.

[82] R. Garimella, M. Kucharik, and M. Shashkov. An efficient linearity and bound preserving conservative interpolation (remapping) on polyhedral meshes. *Computers & fluids*, 36(2):224–237, 2007.

[83] X. Gloerfelt, C. Bailly, and D. Juve. Computation of the noise radiated by a subsonic cavity using direct simulation and acoustic analogy. *AIAA paper*, 2226(7), 2001.

[84] X. Gloerfelt, F. Pérot, C. Bailly, and D. Juvé. Flow-induced cylinder noise formulated as a diffraction problem for low Mach numbers. *J. Sound Vib.*, 287(1):129–151, 2005.

[85] M. Goldstein. A generalized acoustic analogy. *J. Fluid Mech.*, 488:315–333, 2003.

[86] V. L. Gracco and A. Lofqvist. Speech motor coordination and control: evidence from lip, jaw, and laryngeal movements. *Journal of Neuroscience*, 14(11):6585–6597, 1994.

[87] V. Granet, O. Vermorel, T. Léonard, L. Gicquel, and T. Poinsot. Comparison of nonreflecting outlet boundary conditions for compressible solvers on unstructured grids. *AIAA journal*, 48(10):2348–2364, 2010.

[88] V. Gravemeier. The variational multiscale method for laminar and turbulent flow. *Arch. Computat. Methods Eng.*, 13(2):249–324, 2006.

[89] O. Guasch, M. Arnela, R. Codina, and H. Espinoza. A stabilized finite element method for the mixed wave equation in an ALE framework with application to diphthong production. *Acta Acust. united Ac.*, 102(1):94–106, 2016.

[90] O. Guasch and R. Codina. An algebraic subgrid scale finite element method for the convected helmholtz equation in two dimensions with applications in aeroacoustics. *Comput. Methods Appl. Mech. Engrg.*, 196(45):4672–4689, 2007.

[91] O. Guasch and R. Codina. An algebraic subgrid scale finite element method for the convected helmholtz equation in two dimensions with applications in aeroacoustics. *Comput. Methods Appl. Mech. Engrg.*, 196(45–48):4672–4689, 2007.

[92] O. Guasch and R. Codina. Computational aeroacoustics of viscous low speed flows using subgrid scale finite element methods. *J. Comput. Acoust.*, 17(3):309–330, 2009.

[93] O. Guasch and R. Codina. Computational aeroacoustics of viscous low speed flows using subgrid scale finite element methods. *Journal of Computational Acoustics*, 17(03):309–330, 2009.

[94] O. Guasch and R. Codina. Statistical behavior of the orthogonal subgrid scale stabilization terms in the finite element large eddy simulation of turbulent flows. *Comput. Methods Appl. Mech. Engrg.*, 261:154–166, 2013.

[95] O. Guasch, A. Pont, J. Baiges, and R. Codina. Concurrent finite element simulation of incident and diffracted flow noise in computational aeroacoustics. In *InterNoise2015*, San Francisco, California, USA, August 2015.

[96] O. Guasch, A. Pont, J. Baiges, and R. Codina. Concurrent finite element simulation of quadrupolar and dipolar flow noise in low Mach number aeroacoustics. *Comput. Fluids*, 133:129–139, 2016.

[97] O. Guasch, P. Sánchez-Martín, A. Pont, J. Baiges, and R. Codina. Residual-based stabilization of the finite element approximation to the acoustic perturbation equations for low mach number aeroacoustics. *International Journal for Numerical Methods in Fluids*, 82(12):839–857, 2016.

[98] I. Harari. A survey of finite element methods for time-harmonic acoustics. *Comput. Methods Appl. Mech. Engrg.*, 195(13):1594–1607, 2006.

[99] J. Hardin and D. Pope. An acoustic/viscous splitting technique for computational aeroacoustics. *Theoretical and Computational Fluid Dynamics*, 6(5-6):323–340, 1994.

[100] G. Hauke. A symmetric formulation for computing transient shallow water flows. *Comput. Methods Appl. Mech. Engrg.*, 163 (1-4):111–122, 1998.

[101] R. Hill and J. Wilczak. Pressure structure functions and spectra for locally isotropic turbulence. *J. Fluid Mech.*, 296:247–269, 1995.

[102] J. Hoffman, J. Jansson, R. V. de Abreu, N. C. Degirmenci, N. Jansson, K. Müller, M. Nazarov, and J. H. Spühler. Unicorn: Parallel adaptive finite element simulation of turbulent flow and fluid–structure interaction for deforming domains and complex geometry. *Computers & Fluids*, 80:310–319, 2013.

[103] J. Hoffman and C. Johnson. A new approach to computational turbulence modeling. *Comput. Methods Appl. Mech. Engrg.*, 195(23):2865–2880, 2006.

[104] G. Houzeaux and R. Codina. Transmission conditions with constraints in finite element domain decomposition methods for flow problems. *Commun. Numer. Meth. Engrg.*, 17(3):179–190, 2001.

[105] M. Howe. The generation of sound by aerodynamic sources in an inhomogeneous steady flow. *J. Fluid Mech.*, 67(03):597–610, 1975.

[106] M. Howe and R. McGowan. Aeroacoustics of [s]. *Proc. R. Soc. A*, 461:1005–1028, 2005.

[107] M. S. Howe. *Acoustics of fluid-structure interactions*. Cambridge university press, 1998.

[108] M. S. Howe. *Theory of vortex sound*, volume 33. Cambridge University Press, 2003.

[109] F. Q. Hu. A perfectly matched layer absorbing boundary condition for linearized Euler equations with a non-uniform mean flow. *Journal of Computational Physics*, 208(2):469–492, 2005.

[110] F. Q. Hu. Development of PML absorbing boundary conditions for computational aeroacoustics: A progress review. *Comput. Fluids*, 37(4):336–348, 2008.

[111] A. Hueppe and M. Kaltenbacher. Spectral finite elements for computational aeroacoustics using acoustic perturbation equations. *J. Comput. Acoust.*, 20(02):1240005, 2012.

[112] A. Huerta and W. Liu. Viscous flow with large free surface motion. *Comput. Methods Appl. Mech. Engrg.*, 69:277–324, 1988.

[113] T. Hughes. Multiscale phenomena: Green's function, the dirichlet-to-neumann formulation, subgrid scale models, bubbles and the origins of stabilized formulations. *Comput. Methods Appl. Mech. Engrg.*, 127:387–401, 1995.

[114] T. Hughes. Multiscale phenomena: Green's functions, the dirichlet-to-neumann formulation, subgrid scale models, bubbles and the origins of stabilized methods. *Comput. Methods Appl. Mech. Engrg.*, 127(1):387–401, 1995.

[115] T. Hughes, G. FeijÃşo, L. Mazzei, and J. Quincy. The variational multiscale method, a paradigm for computational mechanics. *Comput. Methods Appl. Mech. Engrg.*, 166:3–24, 1998.

[116] T. Hughes, W. Liu, and T. Zimmermann. Lagrangian-eulerian finite-element formulation for compressible viscous flows. *Comput. Methods Appl. Mech. Engrg.*, 29:329–349, 1981.

[117] T. J. Hughes, G. R. Feijóo, L. Mazzei, and J.-B. Quincy. The variational multiscale method. A paradigm for computational mechanics. *Computer Methods in Applied Mechanics and Engineering*, 166(1-2):3–24, 1998.

[118] M. C. Iorio, L. M. Gonzalez, and A. Martínez-Cava. Global stability analysis of a compressible turbulent flow around a high-lift configuration. *AIAA Journal*, 2015.

[119] R. K. Jaiman, X. Jiao, P. H. Geubelle, and E. Loth. Assessment of conservative load transfer for fluid-solid interface with non-matching meshes. *International Journal for Numerical Methods in Engineering*, 64(15):2014–2038, 2005.

[120] L. M. Jesus and C. H. Shadle. A parametric study of the spectral characteristics of european portuguese fricatives. *J. Phonetics*, 30(3):437–464, 2002.

[121] X. Jiao and M. T. Heath. Common-refinement-based data transfer between non-matching meshes in multiphysics simulations. *International Journal for Numerical Methods in Engineering*, 61(14):2402–2427, 2004.

[122] M. Juntunen and R. Stenberg. Nitsche,s method for general boundary conditions. *Mathematics of Computation*, 78(267):1353–1374, 2009.

[123] B. Kaltenbacher, M. Kaltenbacher, and I. Sim. A modified and stable version of a perfectly matched layer technique for the 3-d second order wave equation in time domain with an application to aeroacoustics. *J. Comput. Phys.*, 235:407–422, 2013.

[124] M. Kaltenbacher, M. Escobar, S. Becker, and I. Ali. Numerical simulation of flow-induced noise using les/sas and lighthill's acoustic analogy. *Int. J. Numer. Meth. Fluids*, 63(9):1103–1122, 2010.

[125] M. Kaltenbacher, S. Zörner, A. Hüppe, and P. Sidlof. 3d numerical simulations of human phonation. In *Proceedings of the 11th World Congress on Computational Mechanics-WCCM XI*, 2014.

[126] M. Krane. Aeroacoustic production of low-frequency unvoiced speech sounds. *J. Acoust. Soc. Am.*, 118(1):410–427, 2005.

[127] M. Krane. Aeroacoustic production of low-frequency unvoiced speech sounds. *J. Acoust. Soc. Am.*, 118(1):410–427, 2005.

[128] O. Labbé, C. Peyret, G. Rahier, and M. Huet. A CFD/CAA coupling method applied to jet noise prediction. *Comput. Fluids*, 86(0):1 – 13, 2013.

[129] H. P. Langtangen and G. Pedersen. Computational models for weakly dispersive nonlinear water waves. *Comput. Methods Appl. Mech. Engrg.*, 160 (3-4):337–358, 1998.

[130] M. J. Lighthill. On sound generated aerodynamically. i. general theory. *Proceedings of the Royal Society of London. Series A. Mathematical and Physical Sciences*, 211(1107):564–587, 1952.

[131] G. Lilley. *On the noise radiated from a turbulent high speed jet, in Computational Aeroacoustics, J.C. Hardin and M.Y. Hussaini (Eds.).* Springer Verlag, 1993.

[132] L. Liu, X. Li, and F. Q. Hu. Nonuniform-time-step explicit Runge-Kutta scheme for high-order finite difference method. *Comput. Fluids*, 105(0):166 – 178, 2014.

[133] R. Löhner. Robust, vectorized search algorithms for interpolation on unstructured grids. *Journal of computational Physics*, 118(2):380–387, 1995.

[134] M. B. M. Walkley and. A finite element method for the two-dimensional extended Boussinesq equations. *Int. J. Numer. Meth. Fluids*, 39(10):865–885, 2002.

[135] W. Mansur and C. Brebbia. Numerical implementation of the boundary element method for two dimensional transient scalar wave propagation problems. *Applied Mathematical Modelling*, 6(4):299–306, 1982.

[136] L. G. Margolin and M. Shashkov. Second-order sign-preserving conservative interpolation (remapping) on general grids. *Journal of Computational Physics*, 184(1):266–298, 2003.

[137] P. Martínez-Lera and C. Schram. Correction techniques for the truncation of the source field in acoustic analogies. *J. Acoust. Soc. Am.*, 124(6):3421–3429, 2008.

[138] P. Martínez-Lera, C. Schram, H. Bériot, and R. Hallez. An approach to aerodynamic sound prediction based on incompressible-flow pressure. *J. Sound Vib.*, 333(1):132–143, 2014.

[139] W. Möhring. On vortex sound at low Mach number. *J. Fluid Mech.*, 85(04):685–691, 1978.

[140] S. S. Narayanan, A. A. Alwan, and K. Haker. An articulatory study of fricative consonants using magnetic resonance imaging. *J. Acoust. Soc. Am.*, 98(3):1325–1347, 1995.

[141] S. Nittrouer, M. Studdert-Kennedy, and R. S. McGowan. The emergence of phonetic segmentsevidence from the spectral structure of fricative-vowel syllables spoken by children and adults. *Journal of Speech, Language, and Hearing Research*, 32(1):120–132, 1989.

[142] K. Nozaki. Numerical simulation of sibilant [s] using the real geometry of a human vocal tract. In *High Performance Computing on Vector Systems 2010*, pages 137–148. Springer, 2010.

[143] A. A. Oberai, F. Roknaldin, and T. J. R. Hughes. Computation of trailing-edge noise due to turbulent flow over an airfoil. *AIAA J.*, 40(11):2206–2216, 2002.

[144] P. H. Oosthuizen and W. E. Carscallen. *Introduction to compressible fluid flow*. CRC Press, 2013.

[145] T. J. Poinsot and S. Lele. Boundary conditions for direct simulations of compressible viscous flows. *Journal of Computational Physics*, 101(1):104–129, 1992.

[146] A. Pont, R. Codina, and J. Baiges. Interpolation with restrictions between finite element meshes for flow problems in an ale setting. *Int. J. Numer. Meth. Engrg.*, 2016.

[147] S. Pope. *Turbulent Flows*. Cambridge University Press, 2000.

[148] A. Powell. Theory of vortex sound. *J. Acoust. Soc. Am.*, 36(1):177–195, 1964.

[149] J. Principe, R. Codina, and F. Henke. The dissipative structure of variational multiscale methods for incompressible flows. *Comput. Methods Appl. Mech. Engrg.*, 199(13):791–801, 2010.

[150] R. Prosser. Improved boundary conditions for the direct numerical simulation of turbulent subsonic flows I. Inviscid flows. *Journal of Computational Physics*, 207(2):736–768, 2005.

[151] R. Prosser. Towards improved boundary conditions for the DNS and LES of turbulent subsonic flows. *Journal of Computational Physics*, 222(2):469–474, 2007.

[152] J. D. Ramshaw. Conservative rezoning algorithm for generalized two-dimensional meshes. *Journal of Computational Physics*, 59(2):193–199, 1985.

[153] J. Ristorcelli. A closure for the compressibility of the source terms in Lighthill's acoustic analogy. Technical Report ICASE Report 97-44, NASA/CR-1997-201738, 1997.

[154] M. Roger. The acoustic analogy some theoretical background. *Lecture series-van Kareman Institute for fluid dynamics*, 2:A1–A32, 2000.

[155] M. Roger. *Aeroacoustics: Some theoretical background–The acoustic analogy, J. Anthoine and T. Colonius (Eds.)*, volume LS 2006-05. Von Karman Institute, Rhode-St-Genese, 2006.

[156] P. Sagaut. *Large eddy simulation for incompressible flows: an introduction*. Springer Science & Business Media, 2006.

[157] J. S. Scroggs and F. H. M. Semazzi. A conservative semi-lagrangian method for multidimensional fluid dynamics applications. *Numerical Methods for Partial Differential Equations*, 11(5):445–452, 1995.

[158] J. H. Seo and Y. J. Moon. Linearized perturbed compressible equations for low Mach number aeroacoustics. *Journal of Computational Physics*, 218(2):702–719, 2006.

[159] C. H. Shadle. The effect of geometry on source mechanisms of fricative consonants. *J. Phonetics*, 19:409–424, 1991.

[160] W. Z. Shen and J. N. Sørensen. Aeroacoustic modelling of low-speed flows. *Theoretical and Computational Fluid Dynamics*, 13(4):271–289, 1999.

[161] S. A. Slimon, M. C. Soteriou, and D. W. Davis. Development of computational aeroacoustics equations for subsonic flows using a mach number expansion approach. *J. Comput. Phys.*, 159(2):377–406, 2000.

[162] M. Speed, D. T. Murphy, and D. M. Howard. Three-dimensional digital waveguide mesh simulation of cylindrical vocal tract analogs. *IEEE Trans. Audio Speech Lang. Process.*, 21(2):449–455, 2013.

[163] M. Speed, D. T. Murphy, and D. M. Howard. Three-dimensional digital waveguide mesh simulation of cylindrical vocal tract analogs. *IEEE Trans. Audio Speech Lang. Process.*, 21(2):449–455, 2013.

[164] S. W. T. Yoshinaga, K. Nozaki. *A relationship between simplified and realistic vocal tract geometries for Japanese sibilant fricatives.*

[165] H. Takemoto, S. Adachi, P. Mokhtari, and T. Kitamura. Acoustic interaction between the right and left piriform fossae in generating spectral dips. *J. Acoust. Soc. Am.*, 134(4):2955–2964, 2013.

[166] H. Takemoto, P. Mokhtari, and T. Kitamura. Acoustic analysis of the vocal tract during vowel production by finite-difference time-domain method. *J. Acoust. Soc. Am.*, 128(6):3724–3738, 2010.

[167] H. Takemoto, P. Mokhtari, and T. Kitamura. Acoustic analysis of the vocal tract during vowel production by finite-difference time-domain method. *The Journal of the Acoustical Society of America*, 128(6):3724–3738, 2010.

[168] C. K. Tam and Z. Dong. Radiation and outflow boundary conditions for direct computation of acoustic and flow disturbances in a nonuniform mean flow. *Journal of Computational Acoustics*, 4(02):175–201, 1996.

[169] K. W. Thompson. Time dependent boundary conditions for hyperbolic systems. *Journal of Computational Physics*, 68(1):1–24, 1987.

[170] E. Turkel. Preconditioned methods for solving the incompressible and low speed compressible equations. *Journal of Computational Physics*, 72(2):277–298, 1987.

[171] T. Vampola, J. Horácek, and J. Svec. FE modeling of human vocal tract acoustics. Part I: Production of czech vowels. *Acta Acust. united Ac.*, 94(5):433–447, 2008.

[172] T. Vampola, J. Horácek, and J. Svec. Modeling the influence of piriform sinuses and valleculae on the vocal tract resonances and antiresonances. *Acta Acust. united Ac.*, 101(3):594–602, 2015.

[173] T. Vampola, J. HorÃąček, and J. G. Švec. FE modeling of human vocal tract acoustics. Part I: Production of czech vowels. *Acta Acust. united Ac.*, 94(5):433–447, 2008.

[174] A. Van Hirtum, Y. Fujiso, and K. Nozaki. The role of initial flow conditions for sibilant fricative production. *J. Acoust. Soc. Am.*, 136(6):2922–2925, 2014.

[175] A. Van Hirtum, X. Grandchamp, J. Cisonni, K. Nozaki, and H. Bailliet. Numerical and experimental exploration of flow through a teeth-shaped nozzle. *Adv. Appl. Fluid Mech.*, 11:87–117, 2012.

[176] A. Van Hirtum, X. Grandchamp, X. Pelorson, K. Nozaki, and S. Shimojo. LES and" in vitro" experimental validation of flow around a teeth-shaped obstacle. *Int. J. Appl. Mech.*, 2(02):265–279, 2010.

[177] E. Vergnault, O. Malaspinas, and P. Sagaut. Noise source identification with the lattice boltzmann method. *The Journal of the Acoustical Society of America*, 133(3):1293–1305, 2013.

[178] J. F. Williams and D. L. Hawkings. Sound generation by turbulence and surfaces in arbitrary motion. *Phil. Trans. Roy. Soc. A*, 264(1151):321–342, 1969.

[179] W. R. Wolf and S. K. Lele. Trailing edge noise predictions using compressible les and acoustic analogy. In *Proceedings of the 17th*

AIAA/CEAS Aeroacoustics Conference, AIAA Paper, volume 2784, pages 1–25, 2011.

[180] C. S. Yoo and H. G. Im. Characteristic boundary conditions for simulations of compressible reacting flows with multi-dimensional, viscous and reaction effects. *Combustion Theory and Modelling*, 11(2):259–286, 2007.

[181] T. Yoshinaga, N. Koike, K. Nozaki, and S. Wada. Study on production mechanisms of sibilants using simplified vocal tract model. In *INTER-NOISE and NOISE-CON Congress and Conference Proceedings*, volume 250, pages 5662–5669. Institute of Noise Control Engineering, 2015.